UNIVERSIDAD NACIONAL AUTÓNOMA DE MÉXICO

PROGRAMA DE MAESTRÍA Y DOCTORADO EN CIENCIAS QUÍMICAS

INTERACCIONES NO COVALENTES DE FTALOCIANINAS METÁLICAS CON NANOTUBOS DE CARBONO

TESIS

PARA OPTAR POR EL GRADO DE

DOCTORA EN CIENCIAS

PRESENTA

M. en C. LINA MARCELA BOLÍVAR PINEDA

Dr. Vladimir Bassiouk Endokimenko
INSTITUTO DE CIENCIAS NUCLEARES

Dra. Petra Rudolf
ZERNIKE INSTITUTE FOR ADVANCED MATERIALS

Ciudad de México. Abril 2023

UNIVERSIDAD NACIONAL AUTÓNOMA DE MÉXICO

PROGRAMA DE MAESTRÍA Y DOCTORADO EN CIENCIAS QUÍMICAS

“INTERACCIONES NO COVALENTES DE FTALOCIANINAS METÁLICAS CON NANOTUBOS DE CARBONO”

T E S I S
PARA OPTAR POR EL GRADO DE

DOCTORA EN CIENCIAS

P R E S E N T A

M. en C. Lina Marcela Bolívar Pineda

Dr. Vladimir Bassiouk Endokimenko
INSTITUTO DE CIENCIAS NUCLEARES

Dra. Petra Rudolf
ZERNIKE INSTITUTE FOR ADVANCED MATERIALS

Ciudad de México. Abril 2023

Comité tutor

Dr. Ernesto Rivera García
Dr. Gustavo A. Zelada Guillén

Comité evaluador

Presidente Dr. Carlos Amador Bedolla
Vocal Dra. Lioudmila Fomina
Vocal Dra. Rubicelia Vargas Fosada
Vocal Dra. María del Pilar Carreón Castro
Secretario Dr. Ernesto Rivera García

university of groningen

Non-covalent interactions of metal phthalocyanines with carbon nanotubes

PhD thesis

to obtain the degree of PhD at the
University of Groningen
on the authority of the
Rector Magnificus Prof. C. Wijmenga
and in accordance with
the decision by the college of Deans

and

to obtain the degree of PhD of the
Universidad Nacional Autónoma de México
on the authority of the
Rector E. Graue Wiechers
and in accordance with
the decision of the General Meeting of the
Master and Doctoral Program of Chemical Sciences

Double PhD degree

This thesis will be defended in public on

Tuesday 13 June 2023 at 16:15 hours

by

Lina Marcela Bolivar Pineda

born on 07 July 1993
in Garzón, Colombia

Supervisors
Prof. V. Bassiouk
Prof. P. Rudolf

Assessment committee
Prof. S.S. Faraji
Prof. P. Ayala
Prof. M. Quintana Ruiz
Prof. E. Rivera García

To my ray of light: **Dad.**

+Rafael Bolivar Cruz (1953-2020)

NON–COVALENT INTERACTIONS OF METAL PHTHALOCYANINES WITH CARBON NANOTUBES

Lina Marcela Bolivar Pineda
PhD. Thesis
Universidad Nacional Autónoma de México
University of Groningen

The work presented in this thesis was performed in the Nanomaterials Laboratory (Intituto de Ciencias Nucleares-ICN) of the Universidad Nacional Autónoma de México (Mexico) and the Surfaces and Thin Films Group (Zernike Institute for Advanced Materials) of the University of Groningen (the Netherlands). The research work was funded by CONACYT (Consejo Nacional de Ciencia y Tecnología), the Universidad Nacional Autónoma de México (UNAM, grants DGPA-IN203219 and IN103622) and the Faculty of Science and Engineering (RUG).

Acknowledgments

In this section I would like to express my gratitude to those who contributed to this PhD path.

To the Universidad Nacional Autónoma de México and its master's and doctoral programme in chemical sciences for the opportunity of admission to the PhD, and at the same time for allowing me to be part of the double degree programme with the University of Groningen, Netherlands. UNAM opened the doors of Mexico and the world to me.

To Consejo Nacional de Ciencia y Tecnología (CONACYT) for the CVU 736504 scholarship, granted for the completion of my PhD.

To the Dirección General de Asuntos de Personal Académico for the economic resources granted through the DGAPA-UNAM IN103622 and IN203219 projects and the Programa de Apoyo a los Estudios de Posgrado (PAEP) and the Instituto de Ciencias Nucleares to participate in two events: (i) 32nd International Conference on Diamond and Carbon materials and (ii) IX Simposio de Química Aplicada (IX SIQUIA) y I Congreso Internacional de Nanoquímica, Nanofísica y Nanomedicina (I CINNN).

To the University of Groningen, for accepting me to be part of their double doctoral degree programme in the Faculty of Science and Engineering at the Zernike Institute for Advanced Materials for the scholarship granted during my stay in the Netherlands and for the financial support for the participation in national and international conferences.

To my advisors, Prof. Vladimir A. Basiuk and Prof. Petra Rudolf for giving me the opportunity to work in their research groups: nanomaterials and thin films and surface, respectively. For their support, trust, dedication, patience and for the thousand advice during my stay in the postgraduate course. Admiration for them.

To the Institute of Applied Sciences and Technology (ICAT with its acronym in Spanish Instituto de Ciencias Aplicadas y Tecnología) of the UNAM, for the use of the Raman equipment at the Spectroscopic Characterisation University Laboratory (LUCE, Laboratorio Universitario de Caracterizacción Espectroscópica).

Special thanks to Dr Victor Meza from ICN-UNAM for his support in the infrared, Raman, and SEM techniques during my stay in Mexico, to Dr Dominic Gerlach in the XPS machine, to Václav Ocelik for the training support in SEM and STEM measurements, to Ing. Jacob Baas for the training in XDR, SQUID and the sublimation equipment of the RUG-ZERNIKE, to Dr Wesley Browne for the measurements of Raman and UV-Visible spectroscopy and EPR, additional for the advice to analyse and discuss the results and to Dr Théophile Pelras for the TEM images and the knowledge acquired in this technique. From them I not only learnt techniques, but I also got to know a part of their country, their culture.

To my tutorial committee at UNAM, Dr Ernesto Rivera and Dr Gustavo Zelada, and the

members of the extended committee Dra. Patricia Guadarrama Acosta, Instituto de Investigaciones en Materiales, UNAM, Dra. Rubicelia Vargas Fosada, UAM-Iztapalapa for their comments, corrections, and contributions to this research.

To my group mates from Mexico and Groningen, Mónica Sinecio, Carlos Mendoza, Diego Guzman, Diego Acevedo, Diego Jaramillo, Dinorah Rodríguez, Carolina Ibarra, Aaron Mendoza, Brenda Carreño, Denisse Cruz, Yindi Zhu, Giovanna Feraco, Xiaojing Liu, Zhiying Dan and Wenbo Lu for making the research time more enjoyable with the daily gossip and teamwork. Thanks to them I learned a bit more about Colombia, Mexico, Ecuador, and China. It was a pleasure to share with them.

To my Colombian friends that I met in Mexico, Claudia Villamizar, Sebastián Rocha, Andrea Cadena, Andrés Marmolejo and Fernanda Cordoba, the flavours of our country present in each of them, and to my Mexican friends who taught me to love the country of the tacos, Susana Marin and Ingrid Martínez.

To my friends Leidy González, Mercy Artunduaga, Johannes Ramírez, and Diego Barrera for listening to me, supporting me, and giving me advice. The guiding experience and wisdom.

To Sebastián Arenas for being part of my life, for always being by my side no matter the distance, for that hug that day when a part of me started a journey to eternity.

To my family, here the list is long, but it tops the list, my grandparents Reynaldo and Gertrudis, love, happiness, and health for them; my mother, Enismenia, my brothers, cousins, nieces, godmothers and uncles, my inspiration and my motivation, every achievement is for and because of them.

At these last lines, knowing he won't read it, to my dad, Rafael. What a fall and what a loss his departure leaves, but I rise in honour of him for his humble and noble love.

I learned:

A cardboard with an academic degree does not define us as a good person.
Hug before you leave home, you don't know if you'll be back, or you don't know who won't be there.

THANKS MEXICO AND THE NETHERLANDS

Table of content

List of abbreviations

ANT	Armchair single-walled carbon nanotubes
ANT_SW-P	Armchair nanotube with a Stone-Wales defect with (7,7) junction parallel to the tube axis
ANT_SW-T	Armchair nanotube with a Stone-Wales defect with (7,7) junction tilted to the tube axis
CNTs	Carbon nanotubes
CVD	Chemical vapor deposition
DFT	Density functional theory
DTA	Differential thermal analysis
EDS	Energy-dispersive X-ray spectroscopy
EPR	Electron paramagnetic resonance spectroscopy
FTIR	Fourier-transform infrared spectroscopy
H_2Pc+SWCNT	Free-base phthalocyanine + single-walled carbon nanotubes
HOMO	Highest occupied molecular orbital
$LnPc_2$	Lanthanide bisphthalocyanine (Ln= Y, La, Gd, Tb and Lu)
$LnPc_2$+SWCNT	Lanthanide bisphthalocyanine + Single-walled carbon nanotubes hybrids
LUMO	Lowest unoccupied molecular orbital
MM	Mechanic molecular
MPc	Metal phthalocyanine (M=Mn, Fe, Co and Ni; Pc=monophthalocyanine)
MPc_2	Rare-earth bisphthalocyanine (M= Y, La, Gd, Tb and Lu)
MPc+ANT	Metal monophthalocyanine + armchair nanotubes hybrids
MPc+SWCNT	Metal monophthalocyanine + single-walled carbon nanotubes hybrids
MPc_2+SWCNT	Rare-earth bisphthalocyanine + single-walled carbon nanotubes hybrids
MPc+SWCNT_SW	Hybrid systems with carbon nanotubes that have Stone-Wales defect
MvK	Mars and Van Krevelen mechanic
MWCNTs	Multi-walled carbon nanotubes
MPc+ZNT	Metal monophthalocyanine + zigzag nanotubes hybrids
OER	Oxygen evolution reaction
PBE	Perdew Burke Ernzerhof functional
Pcs	Phathalocyanines
Pc+CNT	Phathalocyanines + carbon nanotubes
SEM	Scanning electron microscopy
SW	Stone-Wales defect
SWCNTs	Single-walled carbon nanotubes
TGA	Thermogravimetric analysis

TEM	Transmission electron microscopy
XPS	X-ray photoelectron spectroscopy
ZNT	Zigzag single-walled carbon nanotubes
ZNT_SW-P	Zigzag nanotube with a Stone-Wales defect with (7,7) junction perpendicular to the tube axis
ANT_SW-T	Zigzag nanotube with a Stone-Wales defect with (7,7) junction tilted to the tube axis

Summary

Hybrid materials consisting of carbon nanotubes and organic macrocycles such as phthalocyanines are of great interest due to the synergistic combination of the properties of both components, which significantly increases their potential for technological application. To obtain these hybrid materials, covalent and non-covalent methods of functionalisation nanotubes with phthalocyanines are widely used. Non-covalent functionalisation is an attractive approach to improve the interfacial properties of nanotubes, as the graphitic structure is not altered. This approach relies on the supramolecular interaction of the components via hydrogen bonds, electrostatic and van der Waals forces, as well as π-π interactions, with the latter playing the most crucial role.

Phthalocyanines have the ability to coordinate with different metal ions such as transition metal and rare earth ions. Depending on the oxidation state, size of the metal ionic radius and number of coordinated phthalocyanine ligands, these macrocycles are classified into single-, double-, triple- and quadruple-decker phthalocyanines. Phthalocyanines are characterised by their high thermal stability, tendency to self-assemble nature, and low solubility in conventional solvents. While the solubility of phthalocyanines improves with the addition of substituents, their stability decreases. In view of the above, this project focused on π-π interactions between unsubstituted metal phthalocyanines and single-walled carbon nanotubes.

The phthalocyanines used for non-covalent functionalisation or adsorption on carbon nanotubes were manganese, iron, cobalt, and nickel monophthalocyanines as a representative set of the 3*d* transition metal phthalocyanines, and the rare earth metal bisphthalocyanine with yttrium, lanthanum, gadolinium, terbium, and lutetium. In contrast to bisphthalocyanines, monophthalocyanines are commercially available. Consequently, the solvothermal method was used as a new strategy for the synthesis of bysphthalocyanines. The identified characteristics of the bisphthalocyanines were confirmed by infrared, Raman, UV-Visible and paramagnetic resonance spectroscopy, corroborating that they are neutral and free radical [$M^{3+}(Pc^{-2})$ $(Pc^{\bullet-})$].

The adsorption of phthalocyanines on the surface of nanotubes is challenging due to the low solubility and dispersion of both components, as well as their tendency to agglomerate. Nevertheless, one-step sublimation or gas-phase functionalisation of nanotubes with Fe, Co, and Ni monophthalocyanines was proposed as an alternative to conventional methods using solvents with high boiling points. As for manganese phthalocyanine and rare earth bisphthalocyanines (Y, La, Gd and Tb), which are more soluble, deposition on the nanotubes was achieved by refluxing in butanol.

According to scanning and transmission electron microscopy images the non-covalent interactions between nanotubes and phthalocyanines on the surface of individual nanotubes and single-walled nanotube agglomerates or bundles. On the other hand, the dispersion of the modified nanotubes depends on the polarity of the solvent and the coordinated metal. Although the hybrids remain in the form of agglomerates, these are smaller in size than those of pristine

nanotubes and can be relatively homogeneously dispersed in isopropanol, which is slightly polar. Furthermore, the electronic structure of the nanotubes after functionalisation was not altered, and no additional covalent bonds or structural defects were formed in the nanotube wall during the adsorption process, as confirmed by Raman and X-ray photoelectron spectroscopy results.

The nanotube + monophthalocyanines hybrids were used as electrocatalysts for the oxygen evolution reaction involved in the electrolysis of water. The hybrids were evaluated in alkaline medium in two concentrations, (0.1 and 1 M) potassium hydroxide. The functionalised carbon nanotubes show an increase in catalytic activity over the pristine nanotubes, with nanotubes decorated with nickel and cobalt phthalocyanines being the most active.

The self-assembly of mono-phthalocyanines on the surface of a carbon nanotube was studied by molecular mechanics with the MM+ force field. The results suggest that self-assembly of the molecules occurs in a combined short and long helix arrangement.

Density functional theory (based on the DMol^3 module of the Materials Studio software) was used to analyse the electronic properties of the non-covalent hybrids, structural changes of mono- and bisphthalocyanines after adsorption on the nanotubes, the influence of chirality, diameter, length and structural defects of the single-walled nanotubes on the formation of the hybrids, as well as the nature of the central metal atoms of the macrocycles.

Determination of the influence of nanotube defects on the structural characteristics and electronic properties of the hybrids was done by modelling the adsorption of cobalt and nickel phthalocyanines on two models of nanotubes of different chirality, armchair and zigzag with a Stone-Wales defect incorporated in different orientations in the graphitic lattice of the nanotube. The obtained data were compared with the homologous hybrids with nanotubes without defect using the same calculation methodology, the PBE functional with Grimme dispersion correction and DNP basis set.

After deposition on the nanotube surface, the flat cobalt and nickel macrocycles undergo bending distortion to increase the contact area with the nanotube wall. The degree of distortion depends on the chirality and diameter of the nanotube, as well as the orientation of the defect. The presence of the Stone-Wales defect leads to a variation in the distribution of the HOMO-LUMO frontier orbitals in all hybrids, but to different degrees, depending on the system: for most of them, the pattern of perfect nanotube hybrids with HOMO and LUMO located mainly on the nanotube is maintained. The spin density in the open-shell hybrids, that is, with the cobalt phthalocyanine, is located in the central metal independently of the chirality of the nanotubes and the defect. Such a distribution was evident in the hybrids with the perfect zigzag nanotubes.

Prior to the simulation of the interaction of the armchair and zigzag nanotubes models with the bisphthalocyanines, the calculation conditions were optimised to obtain a structure of each bisphthalocyanine closest to the structure deduced by X-ray diffraction. In this part of the

project, the effect of the DN, DND and DNP basis sets on the systems with yttrium bisphthalocyanine was evaluated. The lanthanum, gadolinium, and lutetium bisphthalocyanine hybrids were optimised with the DN basis set. Compared to monophthalocyanines, the double-decker phthalocyanines were found to be not flat, but to have a domed structure and to undergo additional distortion when interacting with nanotubes. The bending is higher when the bisphthalocyanines interacted with the smaller diameter nanotube model. The HOMO-LUMO distribution, the HOMO-LUMO bandgap energy and the spin density depend on the central coordinating atom and the chirality of the nanotube. In the case of the yttrium bispthalocyanine hybrids, there is no significant influence of the size of the base set. As a general trend, it was observed that the HOMO-LUMO bandgap energy in hybrids with armchair nanotubes increases linearly with the number of lanthanide electrons, while with zigzag nanotubes the trend is less obvious. The spin density was found on the ligands when the molecules were on the surface of the armchair nanotube. For adsorption on a zigzag nanotube, it was on both components except for the lanthanum bisphthalocyanine hybrid where was localized only in the nanotube.

Finally, a carbonaceous material obtained in the purification process of the free-base phthalocyanine H_2Pc through sublimation was characterised and identified as nitrogen-doped carbon nanofibers from the oxidative pyrolysis of the macrocycle. These nanofibers were at least as thermally stable as graphene and defect-free nanotubes, with a final decomposition temperature of 827 °C in an air atmosphere.

Resumen

Los materiales híbridos formados por nanotubos de carbono y macrociclos orgánicos como las ftalocianinas son de gran interés debido a la combinación sinérgica de las propiedades de ambos componentes, que aumentan significativamente las capacidades tecnológicas para su aplicación. Para obtener estos materiales híbridos, se utilizan ampliamente métodos de funcionalización covalente y no covalente de los nanotubos con las ftalocianinas. La funcionalización no covalente es un enfoque atractivo para mejorar las propiedades interfaciales de los nanotubos, ya que la estructura grafítica no es alterada. Este enfoque se basa en la interacción supramolecular de los componentes mediante puentes de hidrógeno, fuerzas electroestáticas y de van der Waals, así como las interacciones π-π, siendo estás las que desempeñan el papel más importante.

Las ftalocianinas tienen la capacidad de coordinar con diferentes iones metálicos como de transición y tierras raras. Dependiendo del estado de oxidación, tamaño de radio iónico del metal y del número de ligandos de ftalocianinas coordinados, estos macrociclos se clasifican en mono, bis, tris and tretaftalocianinas. Las ftalocianinas se caracterizan por su alta estabilidad térmica, su naturaleza de autoensamblaje y su baja solubilidad en disolventes convencionales. La solubilidad de las ftalocianianas mejora con la incorporación de sustituyentes, sin embargo, su estabilidad disminuye. Teniendo en cuenta lo mencionado, el objetivo de este proyecto se centró en la interacción π-π entre las ftalocianinas metálicas no sustituidas y nanotubos de carbono de pared sencilla.

Las ftalocianinas utilizadas para la funcionalización no covalente o adsorción en los nanotubos de carbono fueron monoftalocianinas de manganeso, hierro, cobalto y níquel como conjunto representativo de las ftalocianinas metálicas de transición *3d* y de los metales de tierras raras, las bisftalocianinas de itrio, lantano, gadolinio, terbio y lutecio. Las monoftalocianinas se encuentran disponible comercialmente en contraste con las bisftalocianinas. En consecuencia, se empleó el método solvotermal como nueva estrategia de síntesis de este último conjunto. Las características propias de las bisftalocianinas fueron identificadas por espectroscopia infrarroja, Raman, UV-Visible y resonancia paramagnética, corroborando que las bisftalocianinas son neutras y con un radical libre [$M^{3+}(Pc^{-2})\ (Pc^{\bullet -})$].

La adsorción de las ftalocianinas en la superficie de los nanotubos es un desafío debido a la baja solubilidad y dispersión de ambos componentes y su tendencia a la aglomeración. Sin embargo, se propuso como alternativa a los métodos convencionales que usan disolventes con altos puntos de ebullición, la funcionalización en un solo paso por sublimación o fase de gas de las monoftalocianinas metálicas de Fe, Co y Ni. En cuánto, a la ftalocianina de manganeso y a las bisftalocianinas de tierras raras (Y, La, Gd y Tb) que son más solubles, se logra la deposición en los nanotubos por reflujo en butanol.

Las interacciones no covalentes entre los nanotubos y las ftalocianinas de acuerdo con las imágenes de microscopia electrónica de barrido y transmisión, se puede generar tanto en la

superficie de los nanotubos individuales como en la superficie de los aglomerados o paquetes de nanotubos de pared sencilla. Por otro lado, la dispersión de los nanotubos modificados depende de la polaridad del disolvente y del metal central de coordinado. A pesar de que los híbridos permanecen en forma de aglomerados, estos son de menor tamaño que el de los nanotubos prístinos y se visualiza una dispersión relativamente homogénea en isopropanol, que es notablemente polar. Además, la estructura electrónica de los nanotubos después de la funcionalización no fue alterada, no se formó ningún enlace covalente adicional o defectos estructurales en la pared de los nanotubos durante el proceso de adsorción, según los resultados de espectroscopia Raman y de fotoelectrones de rayos X.

Los híbridos de nanotubos y monoftalocianinas fueron utilizados como electrocalizadores para la reacción de evolución de oxígeno, implícita en la electrolisis del agua. Los híbridos fueron evaluados en medio alcalino en dos concentraciones 0.1 y 1.0 M de hidróxido de potasio. Los nanotubos de carbono funcionalizados muestran un aumento en la actividad catalítica que los nanotubos prístinos, siendo los nanotubos con las ftalocianinas de níquel y cobalto los de mejor desempeño.

El autoensamblaje de las monoftalocianinas en la superficie de un nanotubo de carbono se estudió por mecánica molecular con el campo de fuerza MM+ y los resultados sugieren que el autoensamble de las moléculas se da en una geometría combinada de hélices corta y larga.

Se utilizó la teoría de funcionales de la densidad para analizar las propiedades electrónicas de los híbridos no covalentes, cambios estructurales de las mono y bisftalocianinas después de su adsorción en los nanotubos, influencia de la quiralidad, diámetro, longitud y defectos estructurales de los nanotubos de pared sencilla en la formación de los híbridos, así como la naturaleza de los átomos metálicos centrales de los macrociclos.

La influencia de los defectos de los nanotubos de carbono en las características estructurales y propiedades electrónicas de los híbridos formados con ftalocianinas, se llevó a cabo con el modelado molecular de los híbridos con ftalocianinas de cobalto y níquel sobre la superficie de dos modelos de nanotubos de carbono de distinta quiralidad; silla y zigzag. Los dos modelos de nanotubos tienen un defecto Stone-Wales incorporado en diferentes orientaciones en la red grafítica. Los datos obtenidos se compararon con los híbridos homólogos con nanotubos sin defecto empleando la misma metodología de cálculo: funcional PBE con corrección de dispersión de Grimme y el conjunto base DNP.

Los macrociclos de Co y Ni planos después de su deposición en la superficie de los nanotubos sufren una distorsión de flexión para aumentar su área de contacto con la pared del nanotubo. El grado de distorsión depende de la quiralidad y diámetro del nanotubo, así como de la orientación del defecto. La presencia del defecto Stone-Wales da lugar a una variación en la distribución de orbitales frontera HOMO-LUMO en todos los híbridos, pero en distinto grado, dependiendo del sistema. Para la mayoría de ellos, se mantiene el patrón de los híbridos con nanotubos perfectos con HOMO y LUMO localizados principalmente en el nanotubo. La diferencia de energía entre HOMO y LUMO (banda prohibida) disminuye con la presencia del

defecto estructural para casi todos los híbridos modelados. La densidad de spin en los híbridos de capa abierta, es decir con la ftalocianiana de cobalto se ubica en el metal central independiente del modelo de nanotubo y del defecto. Dicha distribución se evidenció en los híbridos con el modelo zigzag perfecto.

Previo a la simulación de la interacción de los nanotubos con las bisftalocianinas en los modelos de nanotubos silla y zigzag, se optimizaron las condiciones de cálculo para obtener una estructura de cada bisftalocianina más cercana a la estructura caracterizada por difracción de rayos X. En esta parte del proyecto se evaluó el efecto de los conjuntos base DN, DND y DNP en los sistemas con la bisftalocianina de itrio. Los híbridos de bisftalocianinas de lantano, gadolinio y lutecio fueron optimizados con el conjunto base DN. En comparación con las monoftalocianinas, los macrociclos constituidos por dos ligandos de ftalocianinas no son planos, sino que tienen una estructura abovedada y al interaccionar con los nanotubos sufren una distorsión adicional. La flexión es mayor cuando las bisftalocianinas interactuaron con el modelo de nanotubo de menor diámetro. La distribución HOMO-LUMO, diferencia de energía de la banda prohibida HOMO-LUMO y la densidad de spin dependen del átomo central de coordinación y la quiralidad del nanotubo. En el caso de los híbridos con la bisftalocianina de itrio, no hay influencia significativa del tamaño del conjunto base. Como tendencia general se observó que la energía de la banda prohibida HOMO-LUMO en los híbridos con nanotubos silla aumenta linealmente con el número de electrones del lantánido, mientras que con los nanotubos zigzag la tendencia es menos evidente. La densidad de espín se localizó en los ligandos cuando las moléculas están en la superficie del nanotubo silla. En el caso de la adsorción en un nanotubo en zigzag, la densidad de espín se encontró en ambos componentes, excepto en el híbrido de la bisftalocianina de lantano donde se localizó únicamente en el nanotubo.

Por último, se caracterizó un material carbonáceo obtenido en el proceso de purificación de la ftalocianina de base libre o sin metal H_2Pc a través del sistema de sublimación. El material carbonoso es identificado como nanofibras de carbono dopadas con nitrógeno producto de la pirolisis oxidativa del macrociclo. Las nanofibras son al menos tan estables térmicamente como el grafeno y los nanotubos sin defectos, presentando una temperatura final de descomposición de 827 °C en atmosfera de aire.

1

Chapter 1

Introduction

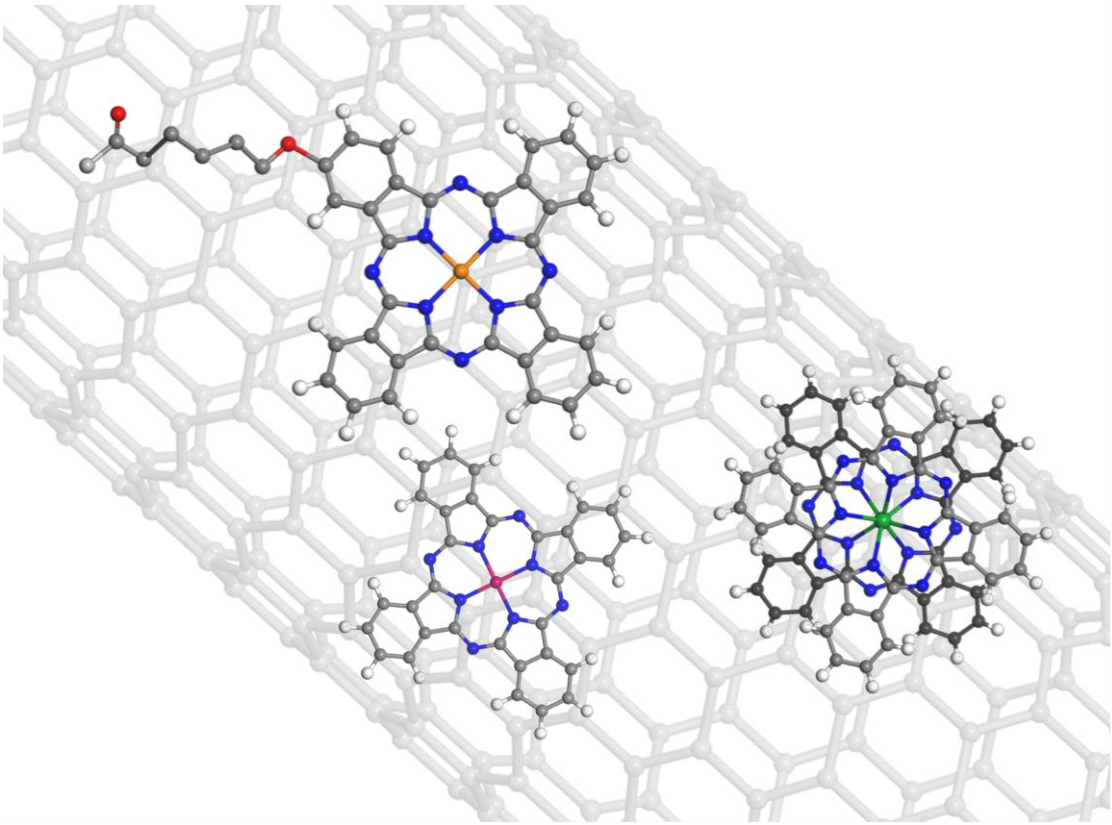

Phthalocyanines adsorbed on carbon nanotubes

General Introduction

Phthalocyanines (Pcs) are amongst the most thermally stable macrocyclic and aromatic compounds, with unique electronic properties and exhibiting rich redox chemistry. Their physical and chemical properties are determined by their molecular structure, such as the nature of the central atom and the presence of axial and peripheral substituents. The combination of exceptional thermal stability with other potentially useful properties makes Pcs very attractive for versatile applications, both as individual compounds and as components of complex systems. An outstanding example of the latter are hybrids of phthalocyanines with carbon nanotubes (CNTs). Thanks to the synergy between component parts, hybrid materials formed by covalent or non-covalent interactions offer a broad spectrum of potential applications. Hybrids are complex systems, and their characterisation is not an easy task, requiring molecular modelling methods such as density functional theory and to complement the information obtained by analytical techniques.

This thesis focuses on the deposition of single- and double-decker metal phthalocyanines on the surface of single-walled carbon nanotubes.

In this first chapter, the structure, properties, and applications of phthalocyanines and carbon nanotubes are described, followed by a brief review of the covalent and non-covalent functionalisation of carbon nanotubes with phthalocyanines, including molecular modelling by density functional theory. The chapter concludes with the goals of the research conducted towards this thesis and an outline of the resulting dissertation.

1.1. Phathalocyanines

Phthalocyanines, formally known as tetrabenzo [5,10,15,20]-tetraazaporphyrins, are arguably amongst the most important chromogens developed in the 20th century. They were accidentally discovered by A.V. Braun and J. Tcherniac in 1907 as a bluish insoluble by-product during the preparation of *o*-cyanobenzamide from phthalimide and acetic anhydride. Phthalocyanines were given their name in recognition of their origin and colour with the prefix *phthal,* derived from the Greek *naptha* (rock oil) and the Greek κυάνεος/κυανοῦς kyaneos/kyanous was chosen to emphasize the relationship with various phthalic acid-derived precursors. [1,2] The first molecules of this family were metal-free phthalocyanines (H_2Pc - $C_{32}H_{18}N_8$), shown in Fig.1. 1a. Twenty years after their discovery, Disbach and his coworker synthesised the first metal-phthalocyanine (MPc - $C_{32}H_{16}N_8M$; M=metal Fig.1. 1b) with copper in its centre (CuPc). [1,2]

1.1.2. Structure

Pcs are planar aromatic macrocycles and synthetic analogues of porphyrins; they consist of four isoindole units connected through nitrogen atoms known as azomethine nitrogen (γ-N; Fig.1. 1). Pcs present a π-electron aromatic cloud with 18 electrons delocalised over an arrangement of alternating carbon and nitrogen atoms. [3] The macrocycle (in which Pc^{-2} is the phthalocyaninate anion $C_{32}H_{16}N_8^{-2}$) has the capacity to coordinate with different cations. Interaction with two hydrogen atoms gives rise to the free-base phthalocyanine (H_2Pc; Fig.1. 1a) with symmetry D_{2h} and with metal ions, metal phthalocyanines are formed (MPcs; Fig.1. 1b). Depending on the oxidation state and size of the ionic radius of the metal (M), single-decker phthalocyanines (so-called monophthalocyanines, MPcs), double-decker (bisphthalocyanines; MPc_2; Fig.1. 1c), and triple-decker (M_2Pc_3) structures can be produced. [4–9] Additionally, a variety of substituents can be incorporated to fine-tune the physico-chemical properties, including at the periphery and non-periphery of the macrocycle as well as at axial positions (Fig.1. 1b). On the other hand, many modifications can be made on the phthalocyanine ring, resulting in so-called Pcs analogues. [10]

Conventional single-decker MPcs (Fig.1. 1b) are characterised by their interaction with various divalent transition metal cations (M^{+2}) such as manganese (Mn), iron (Fe), cobalt (Co), nickel (Ni), copper (Cu), and zinc (Zn), resulting in D_{4h} symmetry. Coordination of Pc^{-2} with large metal ions such as rare-earths elements, which comprise a group of fifteen lanthanides (Ln) plus yttrium (Y) and scandium (Sc), produces double-decker structures. The rare-earth ion is sandwiched between two phthalocyanines ligands with face to face stacking, forming a structure with (ideally) D_{4d} symmetry (Fig.1. 1c). The neutral form of these molecules is generally a radical complex (as confirmed by electron paramagnetic resonance studies, EPR). [11,12] Bisphthalocyanines are composed of a trivalent metal centre (M^{3+}), a dianionic macrocycle (Pc^{-2}), and a monoanionic radial ligand ($Pc^{\bullet -}$), that is [$M^{3+}(Pc^{-2})$ ($Pc^{\bullet -}$)]. [13–15] The first rare-earth Pcs were reported by Kirin and Moskalev in 1965.[5] These sandwich-type compounds are characterised by overlapping ligand π-orbitals depending on the lanthanide ionic radius. [6] To

avoid confusion in terminology, the following definitions will be used in this dissertation: $LnPc_2$ refers to lanthanide bisphthalocyanines and MPc_2 to the complete rare earth group.

Pcs show strong polymorphism, in other words, they crystallize into different structures, depending on the nature of the central metal ion, the substituents, and external conditions. Nine structures have been identified for phthalocyanines: α, β, γ, δ, ε, π, ρ, ξ, and σ. Most phthalocyanines crystallize into two phases: α and β (Fig.1. 2). [16,17] The main difference between these two polymorphs is the tilt angle of the molecular plane with respect to the stacking axis, the b-axis. In α-polymorphs, the tilt angle is 25-30° with respect to the normal to the molecular ring, whereas in the β-polymorphs the angle is 45-49°. [18] In the latter, in the case of single-decker phthalocyanine, the γ-N atoms (azomethine nitrogen; Fig.1. 1a) of one MPc molecule are located axially above and below the central metal ion of the neighbouring MPc molecule, as illustrated in Fig.1. 2. Since the β-polymorph is more thermodynamically stable than the α-polymorph (metastable), the latter can undergo a phase transition to the β-phase [16,17]. The phase transition alters the electronic structure as evident from a colour shift to a greener blue. Often this colour change goes hand in hand with a reduction in the intensity of the dye [1]

1.1.3. Properties and applications

Phthalocyanines are characterised by high thermal and chemical stability: many of them do not decompose up to 550° C and can sublimate, which can be an advantage for their purification. [19, 20] Pcs are not affected by strong acids or bases. Only very strong oxidizing agents, such as dichromate–$K_2Cr_2O_7$, can breakdown the molecules to phthalimide or phthalic acid.[21] Moreover, due to their stable electronic configuration, Pcs are chemically inert under a wide range of conditions. The macrocycle can only undergo oxidation-reduction and substitution reactions which do not alter the aromatic character of phthalocyanines and ring-opening reactions are unusual for Pcs because they require drastic conditions. [22]

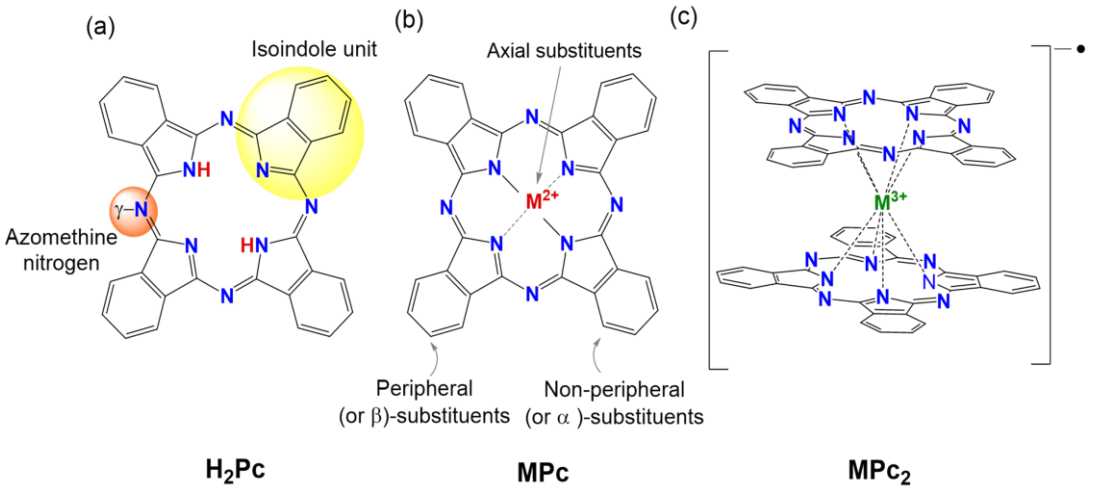

Fig.1. 1. Structure of (a) free-base phthalocyanine (b) single-decker phthalocyanine and (c) double-decker phthalocyanine. Hydrogen atoms are omitted for reasons of clarity.

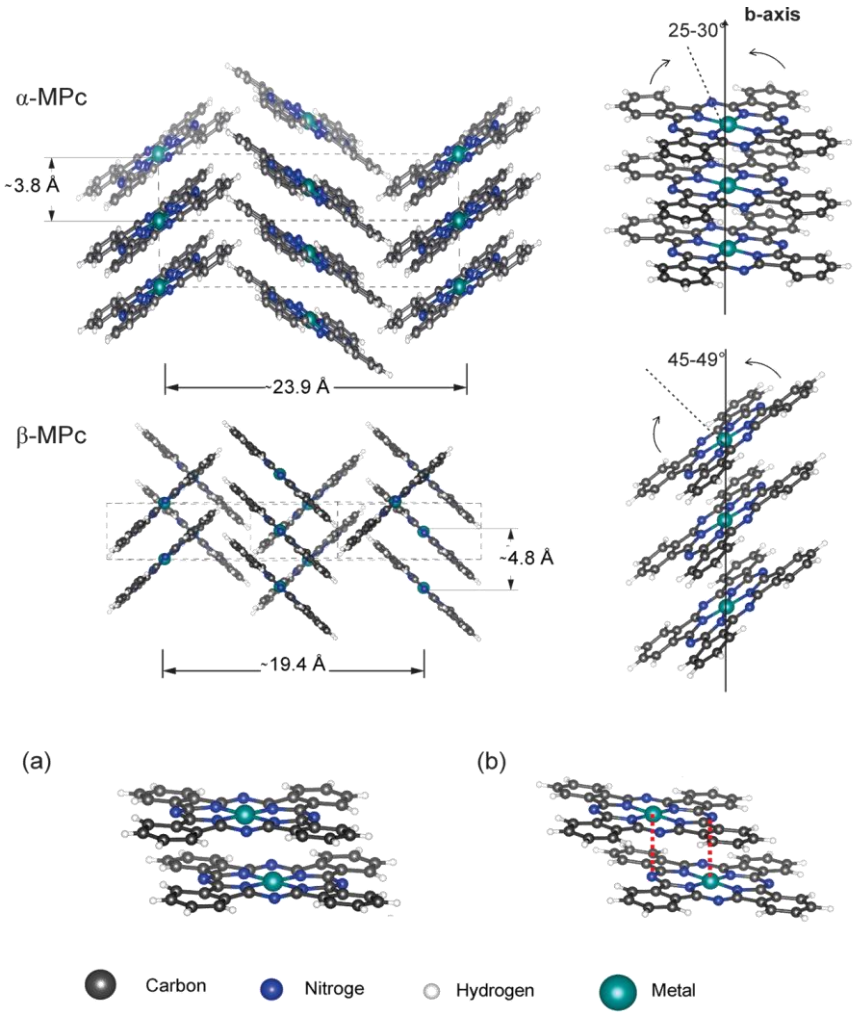

Fig.1. 2. Crystal structure of metal phthalocyanines: (a) α and (b) β —polymorphs. Modified from reference 16, Springer 2012.

The physical and chemical properties of phthalocyanines are determined by their molecular structure, for example, by the nature of the central metal atom and the presence of axial and peripheral substituents. Because they form aggregates as result of π-π stacking, unsubstituted Pcs have low solubility (approximately 10^{-4}–10^{-7} mol/kg) in water and conventional organic solvents with boiling points below 100°C. This limits their use in applications, so it is essential to design and synthesise soluble phthalocyanines derivates. [23–25] To increase the solubility a wide a diversity of substituents can be attached either axially or at the periphery or non-periphery of the macrocycle (Fig.1. 1b).[26] A variety of Pcs derivatives have been reported, incluiding sulfonated, cationic, zwitterionic, and carboxylated phthalocyanines. [26] Nevertheless, most substituted phthalocyanines are not as stable as the unsubstituted complex, and furthermore, their electronic properties are different. [23] For instance, polyethylene glycol (PEG)-substituted cobalt, nickel, copper and zinc phthalocyanines start to decompose in the range of 290-399 °C in an air atmosphere. In contrast, their unsubstituted counterparts do so at around 400 °C.[27] On the other hand, unsubstituted Pcs are usually soluble in solvents with high boiling points such as quinoline, chlorobenzene, nitrobenzene or strong acids, such as sulfuric acid. [23–25]

Phthalocyanines show outstanding optical properties. The conjugated aromatic system of the Pc generates two intense bands in visible region absorption spectrum (Fig.1. 3): B or also called the Soret-band at 300-450 nm and the Q-band at 600-750 nm. The broad B-band arises from transitions from deeper π-levels to the lowest unoccupied molecular orbital (LUMO), i.e., from to a_{2u} and b_{1u} to e_g. The strong Q-band derives from π-π* transitions from the highest occupied molecular orbital (HOMO) to the LUMO or a_{1u}.→ e_g transitions. [23,28,29] The position of the absorption bands of Pcs, specially the Q-band, is affected by the nature and position of ring substituents, the symmetry of the molecule determined by the nature of the central atom, but also aggregation and the molecular environment. [28,30,31] All phthalocyanines have similar optical properties, as in Fig.1. 3, indicating that the latter are determined more by the macrocycle structure rather than by the metal atom. [28,32,33]

Pcs tend to self-assemble and self-organise on different solid surfaces, due to strong attractive forces between their aromatic rings caused by π-π stacking interactions.[34–36] The adsorption and self-assembly of various Pcs on metal surfaces such as copper (Cu), [3738,39] silver (Ag), [8,40–43] gold (Au), [4,8,31,44–48], iridium (Ir), [49] lead (Pb), [50] bismuth (Bi), [51] on inert insulating surfaces such as NaCl [52], liquid crystals[34] and on the surface of carbon nanomaterials [9,53,54] such as carbon nanotubes,[55–57] fullerene, [58,59] graphene,[8,43,49,60] graphite, [61] graphene oxide [62] have been reported. Upon adsorption, the properties depend on the specific arrangement of the molecule as well as its interaction with the substrate including possible hybridisation. [49] MPcs are the most studied using scanning tunnelling microscopy (STM). Fig.1. 4 shows STM images of CuPc molecules assembled on a Bi(111) surface where each CuPc molecule exhibits a cross shape and four lobes [51] and the adsorption of yttrium and terbium bisphthalocyanines on Au(111) where for each molecule eight lobes can be distinguished. [4,63]

Since their discovery and identification, phthalocyanines have been widely used as dyes and pigments in the textile, paint, and printing industries.[1] More recently, they have attracted considerable attention in a variety of applications which rely on their unique electronic and optical properties together with their high chemical and thermal stability, such as chemical or electrochemical sensors, [64,65] photodynamic therapy (PDT), [66–68] solar cells,[35] optical storage data, [69] organic field-effect transistors (OFETs), [70] electrocatalysis, [71] organic light-emitting diodes (OLEDs), [72] spintronic devices, [73] and liquid crystal for displays. [74]

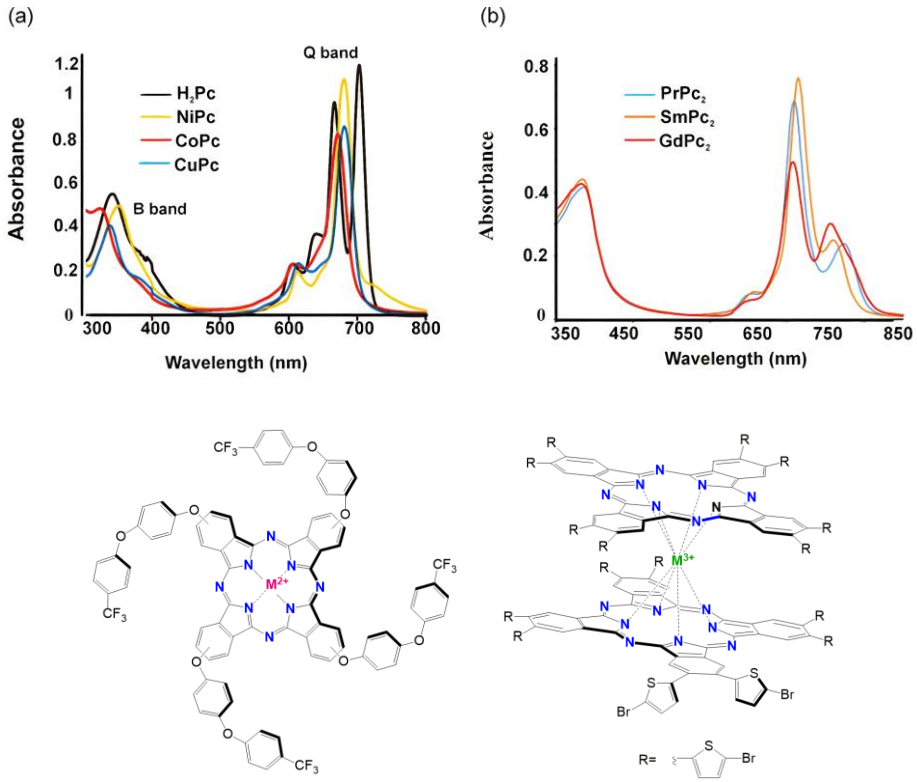

Fig.1. 3. UV-Vis spectra of different (a) substituted monophthalocyanines in chloroform [28] and (b) substituted bisphthalocyanines derivates in dimethylformamide (DMF). [3]

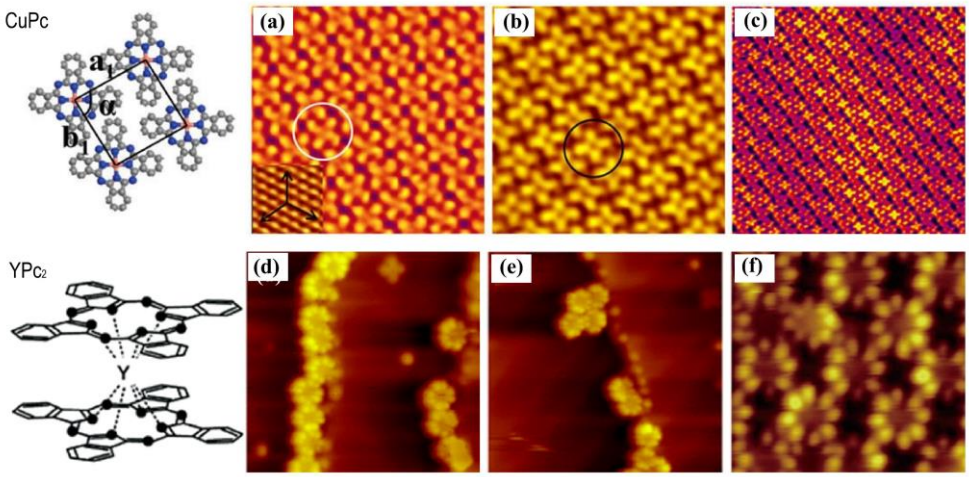

Fig.1. 4. STM images of (a-c) CuPc molecules on a Bi(111) surface . Reproduced with permission from reference 51, Copyright 2017,.MDPI. (d-f) double-decker bis(phthalocyaninato)yttrium and terbium (YPc_2 and $TbPc_2$) adsorbed on Au(111). Reproduced with permission from reference 63 and 4, Copyright 2009 and 2014, ACS Publications and ELSEVIER, respectively.

1.2. Carbon nanotubes

Carbon has an electronic configuration of $1s^2 2s^2 2p^2$ and it can hybridise in three forms sp^3, sp^2 and sp, giving rise to different allotropes namely graphite, graphene (single-layer graphite) and carbon nanotubes (tubular structure), where the carbon atoms form a hexagonal structure via sp^2 hybridisation; fullerenes, where hexagons alternate with pentagons to form spherical molecules; diamond a cubic structure with sp^3 hybridisation and lonsdaleite, that has a hexagonal lattice.[75]

Carbon nanotubes have become one of the most studied carbon materials and are credited with triggering the nanotechnology revolution. [76] Currently, their discovery is attributed to Sumio Ijima for his publications "Helical microtubules of graphitic carbon" in 1991, where he describes multi-walled carbon nanotubes and "Single-shell carbon nanotubes of 1-nm diameter" in 1993, where transmission electron microscopy (TEM) images of single-walled carbon nanotubes were first observed.[77,78] However, there are reports that precede the images of Ijima. The first is from 1889 and concerns the production of carbon filament, patented in the United States by Hughes and Chambers. [76] A second piece of evidence of carbon nanotubes dates back to the early 1950s when Radushkevich and Lukyanovich [76,79] published a report with clear images of hollow carbon fibres, a result that went unnoticed because it was published in the former Soviet Union in the Russian language in the middle of the Cold War. A third paper was published by Oberlin and Endo in 1976, who obtained carbon fibres from the decomposition of benzene. [76,80]

1.2.1. Structure

A carbon nanotube (CNT) is usually described as one or more graphene sheets rolled up to form a cylinder and can surprisingly enough also be obtained experimentally in that way.[81] Carbon nanotubes exhibit a one-dimensional (1-D) structure owing to their length to diameter ratio of about 1000 or more. Furthermore, they can have open ends or be closed with a fullerene-like structure at each end. [82] CNTs can be classified into two types (Fig.1. 5): single-walled (SWCNT) and multi-walled (MWCNT) depending on the number of graphene layers. [83,84] SWCNTs possess the simplest geometry, consisting of a single graphene sheet wrapped on itself in a tubular shape. They usually have a diameter of between 0.4 and 3 nm. MWCNTs are considered as an array of concentric SWCNTs, that is, they consist of multiple-sheets of graphene rolled in on themselves to form a tube leading to a diameter range of 5 to 100 nm. [76,83,85] Due to van der Waals interactions, the interlayer distance in MWCNTs is close to the distance between the atomic layers in graphite, approximately 3.3 Å. Since the length and diameter of MWCNTs differ a lot from those of SWCNTs their properties are of course also very different. [85]

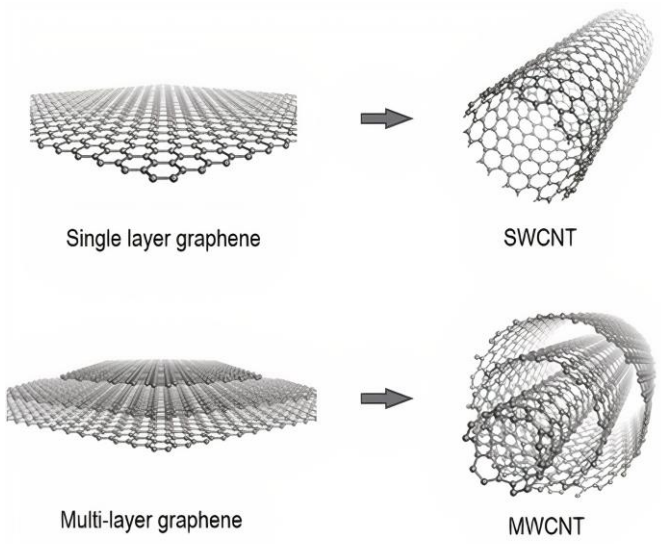

Fig.1. 5. Single-walled and multi-walled carbon nanotube structure.

SWCNTs are classified into three crystallographic configurations depending on how the graphene sheet is rolled up (Fig.1. 6). This is specified by the chiral vector $(\overrightarrow{C_h})$, which connects two equivalent carbon atoms on a graphene sheet and defines the circumference on the surface of the tube, $\overrightarrow{C_h} = n\hat{a}_1 + m\hat{a}_2$. The chiral vector is determined by $\hat{a}_1$ and $\hat{a}_2$, which are the unit cell vectors and n and m called indexes (integers $0 \leq m \leq n$) and determine the chiral angle (θ). The different values obtained for these two parameters determine the type of nanotube: achiral armchair (n = m, θ = 30°), achiral zigzag (m = 0, n > 0, θ = 0°) and chiral ($0< |m|< n$, $0 < \theta < 30°$). A nanotube is chiral when $n \neq m \neq 0$, otherwise it is achiral. The direction of the CNT axis is perpendicular (T) to the chiral vector. [82,86] Armchair and zigzag nanotubes structures have a high degree of symmetry, while the chiral tube structure can exist in two forms which are mirror images of one another. [76]

The curvature of the graphene sheet influences the reactivity of the CNTs because it determines the pyramidalisation angle θ and the π-orbital misalignment of the carbon atoms (Fig.1. 7). The chemical bonding of a CNT is composed entirely of sp^2 bonds, as in graphene. However, the curvature formed by rolling up the graphene sheet alters the orbital structure of the carbon atom, because the bond length between them decreases and the bond angle changes. Due to the surface bending, the σ and π orbitals are no longer perpendicular to each other. [87,88] Overlap of the π orbitals is introduced. Consequently, the parts of the π orbitals inside and outside of a nanotube rearrange, in a way that the outer contribution is larger than the inner one (Fig.1. 7). The curvature induces a mixed state of σ and π orbitals, called rehybridisation (h_π; σ-π), in other words, a mixture of sp^2 and sp^3 orbitals. [87,88] The curvature in CNTs also introduces a misalignment of π orbitals within the graphene sheet (Fig.1. 7). The π-orbitals of a CNT do not point directly toward the central axis of the nanotube, and adjacent carbon π-orbitals have a misalignment angle, φ, between them. [87,88]

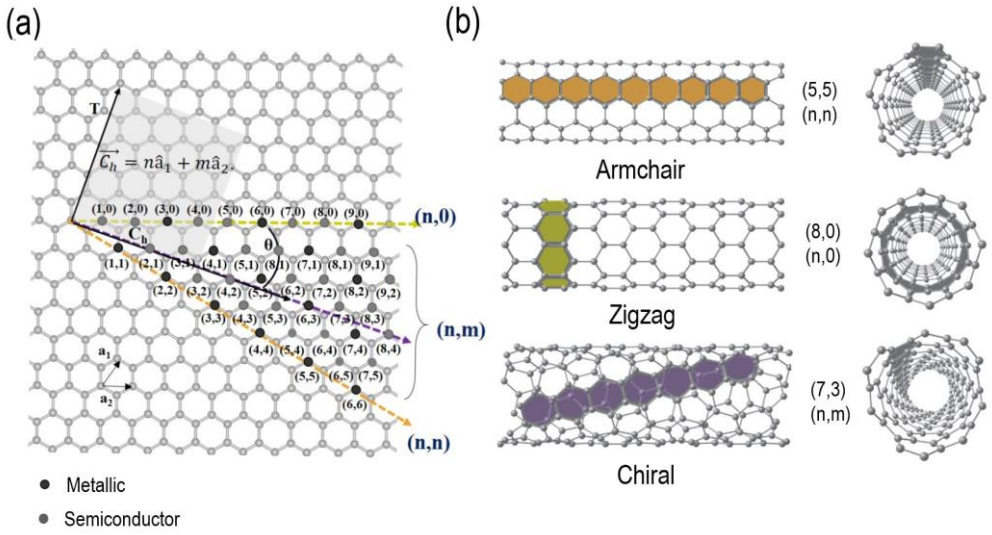

Fig.1. 6. (a) Schematic diagram showing how different CNT structures are obtained from a graphene sheet; Modified from reference 86, Copyright 2006, Taylor & Francis Group. (b) Structure of a CNT with different chirality: armchair, zigzag and chiral structure. Reproduced with permission from reference 75, Copyright 2016, CRC Press.

1.2.2. Properties and applications

CNTs are characterised by a tensile strength of over 100 GPa and a remarkable electronic response to strain and metal-insulator transition, a Young's modulus greater than 1 TPa due to the rehybridisation, excellent electrical capacity (1000 times higher than copper), high thermal conductivity (about twice as high as diamond), thermal stability (MWCNT start to decompose at around 400°C and SWCNT at 600°C in air atmosphere) and a high surface area (1315 m^2g^{-1}). Hence, CNTs can be considered for application in many fields, such as catalyst carrier, composite materials, supercapacitors, adsorbents for removing heavy metals ions (lead, copper, nickel, cadmium, and organic pollutants), batteries, fuel cells, hydrogen storage media, chemical and biological sensors, optical and optoelectronic devices, to mention but a few. [75,85,89] However, at present, no CNTs-based application makes use of the properties of individual nanotubes. (References 75,85,89 explain in detail SWCNT and MWCNT properties and their applications).

One of the limitations in the application of CNTs is the variation in their properties owing to a lack of structural homogeneity or uniformity. In any given sample, CNTs differ in length, diameter, chirality and the number of walls. Moreover, CNTs produced by different methods have multiple defects and impurities. To-date, synthesis methods are insufficient for the controlled production of CNTs with a uniform structure. [75,76]

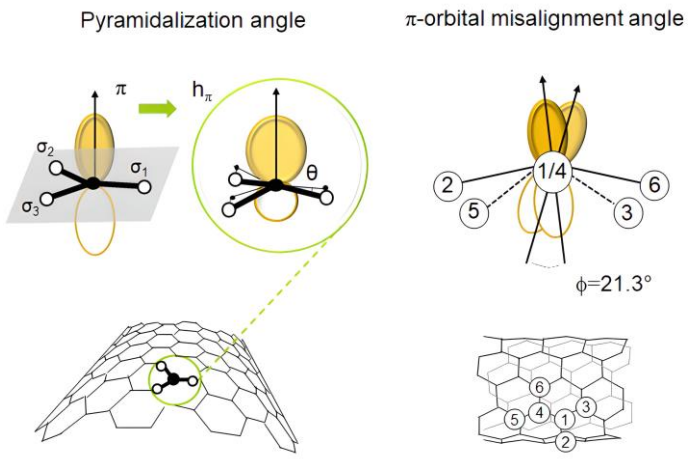

Fig.1. 7. Schematic representation of the π orbital in planar graphene and its change into h_π under bending together with the pyramidalization angle θ and the π-orbital misalignment angles along the C_1-C_4. Modified from reference 88, Royal Society of Chemistry.

Another intrinsic drawback of CNTs is their insolubility or extremely poor solubility which makes their dispersion difficult in water and organic solvents so that they tend to exist in the form of bundles. Individual nanotubes stick together due to strong hydrophobic interactions and are extremely difficult to separate from each other, their processability and hence their application. [90,91]

1.3. Functionalisation: Phthalocyanine + carbon nanotube hybrids

Dispersion of CNTs can be achieved by the chemical or physical modification of their nanotube surface, also called functionalisation. Of course this brings with it, changes in chemical, physical, electrical and mechanical properties, and is often utilised to improve interaction with other molecules and surfaces. [83,90–92]

Carbon nanotubes functionalisation methods are classified into covalent and non-covalent modification (Fig.1. 8). Covalent modification consists of the formation of covalent bonds between functional groups and the carbon atoms of the nanotube, either on its surface or at its ends. Covalent functionalisation can be direct or indirect. Direct covalent sidewall functionalisation involves a change in hybridisation from sp^2 to sp^3 and a simultaneous loss in conjugation by defect site creation (carboxylic acids and hydroxyl; -COOH, -OH, respectively; Fig.1. 8a). This can be accomplished using strong acids such as hydrochloric and nitric acid in an oxidation process, followed by functionalisation with the desired functional groups. [90–93] Indirect functionalisation is the chemical transformation of defects sites in the CNTs (Fig.1. 8b,c), that are originate in the synthesis and purification process as carboxylic acids and hydroxyl, pentagons, and heptagons (structural defects, they have greater reactivity than the perfect hexagonal lattice). Defects act as precursors for other reactions such as amidation, esterification, thiolation, silanisation, among others. [90–93] A detailed description of covalent modification can be found elsewhere. [83,90–97]

Non-covalent functionalisation or physical modification comprises the formation of supramolecular systems that are created from the interaction of CNTs with atoms/molecules through hydrogen bonding, π-π stacking and adsorption, and van der Waals, electrostatic forces (Fig.1. 8d,e,f,g). Non-covalent CNT functionalisation strategies can be classified into two groups: exohedral, involving interaction with outer surface of the nanotubes as shown in Fig.1. 8d,e and f, and endohedral where atoms/molecules inside the nanotube; Fig.1. 8g).[92,93,97] References 91–93 present a comprehensive summary of reported non-covalent hybrids.

Most research has focused on obtaining covalent hybrids of phthalocyanines and CNTs since substituted Pcs are more soluble than unsubstituted ones. [9,53,98–106] Direct and indirect covalent functionalisation of SWCNTs and oxidised multi-walled carbon nanotubes (*o*-MWCNT) *3d*(II) metal-substituted monophthalocyanines have been widely reported (R-MPc+CNT; Fig.1. 8a,b,c). [9,98–101,107] Regarding the formation of hybrids with rare earth double decker phthalocyanines, only octaamino substituted erbium bisphthalocyanine ($OAErPc_2$) covalently linked to oxidised SWCNTs ($OAErPc_2$+*o*-SWCNTs; Fig.1. 8c) has to our knowledge been published. [105] Usually, covalent functionalisation of CNT sidewalls involves the use of highly reactive species such as aryl radicals, aryl cations, nitrenes and carbenes.

Covalently functionalised CNTs are sufficiently dispersed to facilitate their manipulation, that is, the CNTs are less agglomerated or bundled (see Fig.1. 9a, covalent interaction between SWCNT and 2,3,9,10,16,17-Hexa-*tert*-butylphenoxy-23-(4-formylbenzoyloxymethyl) phthalocyaninate zinc, R-ZnPc, its structure is shown in Fig.1. 8b). [53,100] This approach is appealing because the stability of ensembles resulting from the covalent addition of functional molecules to the nanotube is much higher than physical interactions, which is desirable in terms of preparation of possible devices. [9,53,99]

Non-covalent interactions are particularly attractive, as the CNTs fully preserve their electronic network, hence, this approach is also important for the development of new materials. The immobilisation of Pc molecules onto the sidewalls of CNTs may give rise to novel nanodevices where the photophysical and conducting properties of the Pcs are coupled to the intrinsic electronic properties of the nanotubes (Fig.1. 8d.e,f).[53] The self-assembly of Pc cores onto CNTs results from π-π interactions between the conjugated surface of the CNTs and the aromatic Pc macrocycles. Substituted (*R*-Pc; Fig.1. 8d,e) [99,104,107–115] and unsubstituted (Fig.1. 8f)[19,116–126] phthalocyanines have been deposited on the surface of CNTs notably on *o*-MWCNT. As well as covalent interaction, transition metal monophthalocyanines are the most investigated systems. Only three supramolecular systems with substituted MPc_2 (M = Er, Tb and Lu) are known.[55,104,127–129] In the case of *R*-Pc, pyrene derivatives are frequently used as an anchor or bridge between the Pc and the nanotube (e.g., Fig.1. 8d).[99,104,127] On the other hand, the encapsulation or endohedral interaction of Pcs inside CNTs has been studied with H_2Pc,[130] CoPc[131] and $TbPc_2$[132] and there are few published examples of their characterisation (Fig.1. 8g).

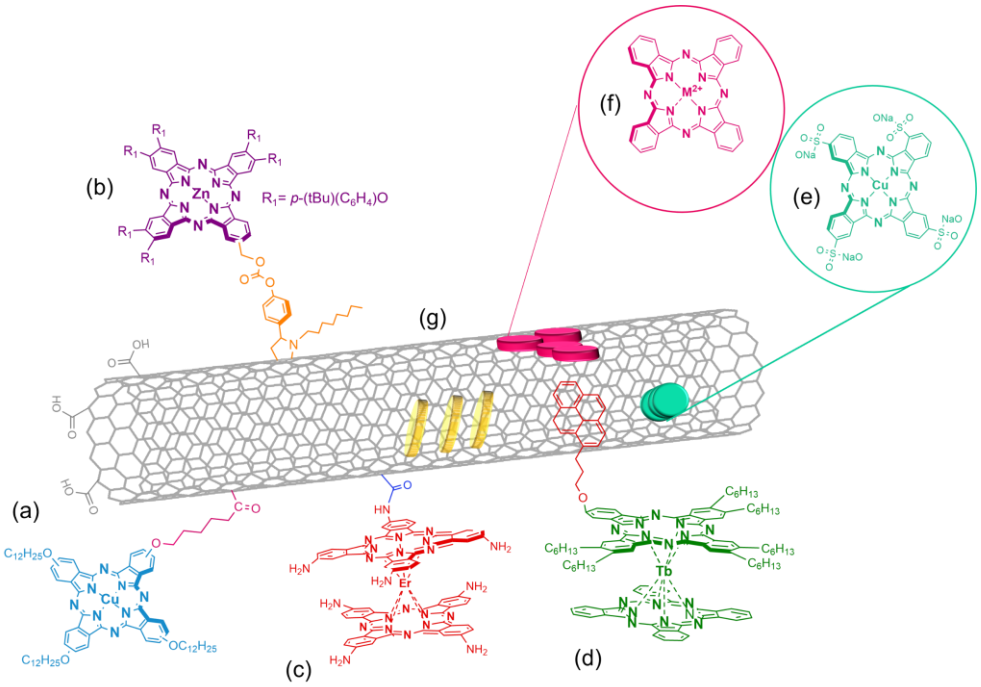

Fig.1. 8 General classification for the methods of CNT modification, based on different types of interactions and attachment sites employed with Pcs. (a) Direct [98] and (b) (c) indirect [100,105] covalent functionalization; (d) (e) (f) exohedral [104,113,129] and (g) endohedral noncovalent interactions [131,132].

The morphological differences between endohedral and exohendral interactions of CNTs can be clearly visualised by transmission electron microscopy (TEM; Fig.1. b,c). The roughness and increased thickness of the outer walls of the functionalised nanotubes reveal the presence of phthalocyanine molecules on the surface of the carbon nanomaterial. Fig.1. 9a shows the interaction of oxidised and functionalised multi-walled carbon nanotubes with 3,4,4,4-tetrasulfonic acid tetrasodium salt copper phthalocyanine (TS-CuPc; see structure in Fig.1. 8e). [113] The encapsulation of phthalocyanines in SWCNT and MWCNT is observed in Fig.1. b, where the nanotubes are filled with CoPc. [131]

1.3.1. Functionalisation methods

The production of Pc+CNTs hybrids has most often been performed in liquid phase, which includes the use of water and organic solvents such as DMF, tetrahydrofuran (THF) and alcohols (ethanol, methanol, isopropanol and pentanol). The methods that have been implemented are sonication, stirring, refluxing, centrifugation and solvothermal (hydrothermal treatment). [104,118,120,133–135] In contrast to the diversity of reported articles on functionalisation of CNTs in liquid phase, there are few studies describing solid phase processes. [118]

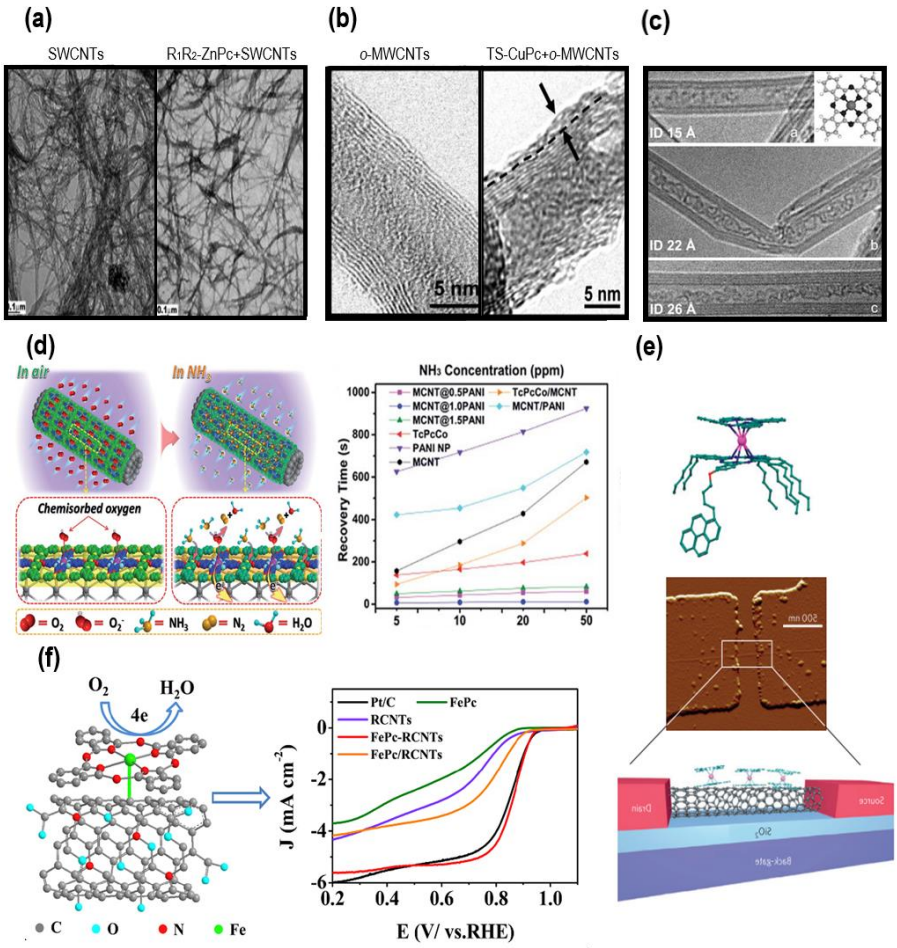

Fig.1. 9. (a) TEM images of pristine SWCNTs and R_1R_2-ZnPc+SWCNT. Reproduced with permission from reference 100, Copyright 2007, ACS Publications. (b) TEM image of ST-CuPc+*o*-MWCNT. Reproduced with permission from reference 113, Copyright 2007, ACS publications (c) TEM images of CoPc filled CNT, Reproduced from ref 131, Copyright 2007, Wiley-VCH. (d) A schematic of the gas-sensing mechanism of CoPc+MWCNT@PANI sensors upon interaction with NH_3. Reproduced with permission from reference 136, Copyright 2017, Royal Society of Chemistry. (e) FePc+*o*-MWCNT/N-doped realize the performance of similar single-atom catalysis for oxygen reduction reaction. Reproduced with permission from reference 133, Copyright 2018, Journal of Power Sources. (f) Spin valves. Top, Atomic Force Micrograph (AFM) of the supramolecular spin valve. The SWCNTs lies on a SiO_2 surface supported by a back gate and is connected to a palladium source and drain electrodes and bottom, scheme of the supramolecular spin-valve architecture (hexyl and pyrenyl groups are omitted for reasons of clarity). Reproduced from reference 129, Copyright 2011, Nature.

The functionalisation of CNTs in liquid and solid phase, whether covalent or non-covalent, requires the use of large amounts of organic solvents and subsequent purification processes (extraction, centrifugation, precipitation, filtration, solvent evaporation and drying) to remove excess reagent. In addition, they involve conventional multi-step techniques with extended reaction time, high energy consumption and the use of auxiliary reagents that can be toxic and corrosive. This leads to the search for alternative methodologies for obtaining Pc+CNTs hybrids. In this context, Basiuk et al. (2018) [19] proposes the functionalisation of nanotubes with transition metal phthalocyanines in gas phase and thus a solvent-free environment, this method requires a controlled thermal activation without need for subsequent purification processes.

1.3.2. Applications

Interactions of phthalocyanines and carbon nanotubes hybrids (Pc+CNTs) have drawn attention due to their synergic combination of electrical, optical, and mechanical properties. The individual features of Pcs and CNTs make them the molecular building blocks of donor-acceptor (D-A) systems, which has led to the use of Pc+CNTs hybrids in optoelectronic devices, [100,102,103] solar cells, [113] sensing devices (rutin, [121] isoniazid, [122] H_2O_2, [137] thiocyanate, [107] epinephrine, [138] glutathione, [124] acetone and hydrogen sulfide [139]), electroactivity toward oxygen reduction reaction (ORR), [118–120,125,133,140] gas sensors (dimethyl methylphosphonate-DMMP, [115] Cl_2 [111,114,116] and NH_3 [108,109,136]), oxidation of the asulam herbicide, [141] electrocatalytic CO_2 [126,134,135] and nitrate [123] reduction, removal of Cu(II), [112] and spintronic devices. [104,127,129] Various studies have shown these hybrids to present enhanced features compared to the individual CNTs or Pcs.

For example, the synthesis of non-covalent hybrids of MWCNTs and tetra-*b*-carboxyphthalocyanine cobalt (Tc-CoPc+MWCNT) for the detection of ammonia (NH_3) is presented in Fig.1. 9d. In this case, Tc-CoPc acts not only as a sensing promoter but also as an efficient mediator to couple MWCNTs with PANI (polyaniline). Fig.1. 9d shows an improvement in sensitivity and detection of NH_3 by the hybrid compared to its individual components. [136] Another example is illustrated in Fig.1. 9e the hybrid formed from FePc and *o*-MWCNTs/N-doped reaction, FePc+*o*-MWCNTs/N-doped exhibits superior catalytic activity for oxygen reduction than commercial platinum-carbon catalyst, with higher half-wave (0.86 V), lower Tafel slope (38 mV dec^{-1}) and excellent electrochemical stability. [133] Hybrids with double-decker phthalocyanines have been least explored. Their main applications tend towards the elaboration of spin devices with quantum properties, considering the behaviour of earth rare bisphthalocyanines as a single-molecule magnet (SMM). For this study, SWCNTs and R_1R_2-$TbPc_2$ (R_1 = pyrenyl and R_2 = hexyl; Fig.1. 9f) have been used. [129]

1.4. Molecular modelling

Molecular modelling is a set of computational techniques that represent molecular structures and simulate their behaviour using computer programmes. The data obtained include molecular geometries (bond lengths, bond angles, torsion angles), energies (formation, gap, and activation energy, etc.), electronic properties (electron affinity, HOMO-LUMO distribution, spin density and charges) and spectroscopic properties (vibrational modes and intensities). [142]

1.4.1. Molecular mechanics

Molecular mechanics (MM) is based on a mathematical model of a molecule as a collection of balls or spheres (atoms) held together by springs (bonds, see Fig.1. 10). It assumes that the relative positions of the nuclei of the atoms forming a structure are a function of operating attractive and repulsive forces, [143] thereby allowing the application of the laws of classical mechanics. MM does not consider electrons, therefore, it does not generate information on electronic properties such as charge distribution or nucleophilic or electrophilic behaviour. [143,144] Molecular mechanics is used when simulation of chemical reactions is not required. [143]

This modelling technique is suitable for predicting the potential energy of a system with a large number of atoms or molecules at a relatively low computational cost compared to quantum mechanics.[143]

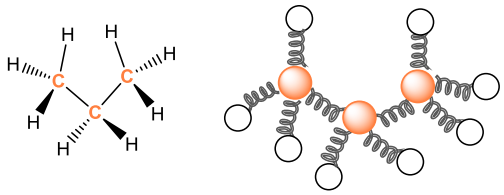

Fig.1. 10. Hypothetical mechanic model: spheres joined by mechanical springs, where the sphere and spring represent the atom and covalent bond, respectively.

The MM energy of a molecule is described in terms of a sum of contributions arising from bond stretching, angle bending, torsion angles, together with contributions due to "non-bonded" interactions: van der Waals and Coulombic (equation 1.1.) [144] The mathematical form of each contribution and the parameters in it, constitute a force field, and MM methods are sometimes called force field methods. Thus, the total potential energy of a molecule is expressed as the sum of all different attractive and repulsive forces between atoms in the structure. [143,144]

$$E_{total} = \sum E_{stretching} + \sum E_{\text{angles}} + \sum E_{torsion} + \sum E_{Coulombic} + \sum E_{van\ der\ Waals} \quad (1.1)$$

Numerous force fields have been developed within MM, such as AMBER, CHARMM, MM1, MM2, MM3 and MM4, which have been used to study different systems including biomolecules (proteins and nucleic acids), organic compounds and polymers, with the aim of achieving a geometry with the lowest energy conformation for the system. For systems with carbon nanotubes and phthalocyanines, only the self-assembly geometry of porphyrins in a nanotube and HOPG model has been previously reported using the MM^+ force field of the HyperChem software, [145–148] a variation of the MM2 force field. [144,149]

1.4.2. Density functional theory

Density functional theory has become the most popular and versatile modelling method for investigating electronic structure properties of many-body systems, such as atoms and molecules in physics, chemistry, and material science.[150] Density functional theory unlike *ab initio* and semiempirical methods is not based on the wavefunction, but is related to the electron probability density function or charge density, designated by $\rho(x, y, z)$. [142,151]Formally, this theory is based on the Hohenberg and Kohn theorems and computationally the Kohn-Sham (KS) method is applied using a mean-field approach. [152] This method represents the density functional $E_{KS\text{-}DFT}[\rho]$ as the kinetic energy contribution of the non-interacting electrons $T_s[\rho]$ (reference system), Coulomb repulsion $J[\rho]$ and the addition of $E_{XC}[\rho]$, a term containing the kinetic energy of the real system (interacting system $T[\rho]$), which is known as exchange and correlation energy (equation 1.2)[152]

$$E_{KS-DFT}[\rho] = T_s[\rho] + J[\rho] + E_{XC}[\rho] \quad (1.2)$$

$$E_{XC}[\rho] = (T[\rho] - T_s[\rho]) + (V_{ee}[\rho] - J[\rho]) \quad (1.3)$$

The first parenthesis in equation 1.3 may be considered as the kinetic correlation energy (T), while the last contains both potential correlation and exchange energy, where $V_{ee}[\rho]$ is the electron-electron interaction and is the sum of a classical (Coulomb repulsion) and a non-classical interaction. [152] However, the explicit expression of $E_{XC}[\rho]$ remains unknown. There are many approaches that have shown satisfactory results; such approaches have been grouped into generations that remember the Jacob's ladder rungs. [152] At the lowest rung of this ladder, the contribution to the energy from a volume element of 3-dimensional space is determined by the local density there. Higher rungs or levels incorporate increasingly complex ingredients constructed from the density or the Kohn-Sham orbitals in or around this volume element. The exchange-correlation functionals are: [153]

- **Local density approximation (LDA) approximation**: functionals assume that the density locally can be treated as a uniform electron gas, or equivalently that the density is a slowly varying function.
- **Generalised gradient approximation (GGA) approximation:** functionals that depend not only on the density at one point but also its gradient $\nabla[\rho]$.
- **Meta-GGA approximation**: functionals improve the GGA approximation by using the kinetic energy density and/or the Laplacian of the density.
- **Hybrid functionals**: functionals that mix the Hartree–Fock exchange integral with GGA exchange functionals at a constant ratio, based on the concept of the adiabatic connection
- **Functionals that consider virtual orbitals**

In relation to Pc+CNTs hybrids, the pure Perdew Burke Ernzerhof (PBE) functional in the frame of the GGA turns out to be the most frequently used one, due to its cost-efficiency and reliability.[19,57,125,134,139,154–160]

The parameters that have been evaluated for Pc+CNTs hybrids include the influence of the structural characteristics of the carbon nanotubes such as chirality, diameter, length and defects in the hexagonal lattice on the electronic and optical properties (e.g. HOMO, LUMO, and gap energies), as well as obtaining the most energetically stable geometry by evaluating the position of phthalocyanines on the carbon nanotubes surface. [19,57,125,134,139,154–160] Different DFT computational strategies and methodologies have started to be implemented to explain their behaviour in various applications especially for oxygen reduction reaction (ORR) and as sensors, determining the energy of the active centres and the geometry stability of each complex or systems formed.[57,125,134,139,155,160]

In particular, the Pc+CNTs hybrids formed by non-covalent interactions, two models of

nanotubes with chirality armchair and zigzag of closed-end and with free base phthalocyanines and transition metals (MPc; M=Fe, Co, Ni, Cu and Zn) have been studied. [19,157,158,161] The adsorption of MPc on nanotubes with perfect hexagonal lattice has been studied. However, H_2Pc has been deposited on the surface of nanotubes with and without Stone-Wales defects and the structural and electronic properties compared to determine the influence of defects on the electronic characteristics of the resulting H_2Pc+CNTs hybrids.[157,161] Additionally, the influence of different calculation conditions, such as the GGA functional type and basis set of the DMol^3 module from Materials Studio software, on the optimisation of the geometry of isolated or individual hybrid components and of the hybrid itself, and consequently of the electronic and structural features, has been evaluated.

In general, most experimental and computational research has focused on the functionalisation of carbon nanotubes with *3d* metal substituted phthalocyanines.

1.5. Challenges

Although the functionalisation of nanotubes with substituted metal phthalocyanines is proposed as an alternative to improve nanotube dispersion and other properties, obtaining non-covalent hybrids with unsubstituted phthalocyanines is a challenge. An essential feature for a homogeneous interaction between the phthalocyanines and the CNTs is that the phthalocyanines are soluble, however, both components tend to aggregate. In Chapter 3 of this thesis, an alternative solvent-free methodology is used to achieve the functionalisation of single-walled carbon nanotube with 3*d* metal phthalocyanines, taking advantage of their thermal stability. On the other hand, functionalisation with rare-earth double-decker phthalocyanines is even more complex, as they are not commercially available, and the yields of the different conventional experimental strategies are low (5 to 60%, only for unsubstituted double-decker),[5] high boiling point solvents (above 100 °C as mentioned in section 1.1.3.) are used, additional by-products are obtained, and their purification involves column chromatography. Chapter 5 explores this challenge further and proposes a new synthesis methodology using a solvothermal technique, followed by deposition on the SWCNTs by conventional methods such as a reflux system.

Unfortunately, experimental characterisation of Pc+CNTs hybrids is not an easy task and usually requires a range of analytic techniques (infrared, ultraviolet-visible, Raman, and X-ray photoelectron spectroscopy, thermogravimetric analysis, and different microscopies such scanning and transmission, among others). Even so, the information is often insufficient to provide detailed insight into the Pc-CNT hybrids. As a result, it is necessary to also use computational tools such as molecular modelling to complement experimental observations. [161]

Optimisation of the hybrids models is also complicated by the central coordination metal of the phthalocyanines, especially in DFT. The calculation of *d*-transition metal complexes (monophthalocyanines) does not involve large difficulties compared to lanthanide complexes (bisphthalocyanines). The quantum chemistry of lanthanides is more challenging, due to their non-A*ufbau* configuration and the characteristics of the *f* shell, [162] as discussed in Chapter 6.

1.6. The research aims of this thesis

As discussed in the previous sections, the π-π interactions between carbon nanotubes and phthalocyanines has the advantage of preserving the graphene lattice and possibly, its properties, as well as of the phthalocyanines. Additionally, the formed hybrids potential give rise to a wide spectrum of applications. Therefore, ***the main aim*** of this dissertation was to functionalise single-walled carbon nanotubes with unsubstituted phthalocyanines coordinated with transition (MPc; M= Mn, Fe, Co and Ni) and rare earth (MPc_2; M= Y, La, Gd, Tb and Lu) metals.

Non-covalent attachment is performed with pristine SWCNTs and unsubstituted *3d* transition metal phthalocyanines because they have higher thermal stability than their homologs phthalocyanines with substituents and MWCNTs. Furthermore, there has been no previous experimental and molecular modelling reports for unsubstituted bispthalocyanines with rare earth metals on the surface of carbon nanotubes, making this a novel system to study

The choice of pristine single-walled CNTs synthesised by Chemical Vapour Deposition (CVD) for functionalisation deserves a special explanation. In general, single-walled carbon nanotubes are preferable than multi-walled CNTs from a characterisation point of view: in the latter case, only the outer nanotube layer undergoes functionalisation, and therefore the contribution of functionalising molecules/moieties in spectra, microscopic images and thermal analysis data is 1 to 2 orders of magnitude lower than in the case of SWCNTs. Consequently, some techniques cannot detect functionalising molecules in multi-walled carbon nanotubes samples. When choosing between pristine and purified SWCNTs, there is a trade-off between two factors: purity (>95%) and cost ($200; especially important for large-scale applications).

The specific goals of this research were:

- To functionalise single-walled carbon nanotubes with unsubstituted transition metal phthalocyanines by sublimation and characterise each product obtained.

- To obtain rare earth double-decker phthalocyanines without substituents by solvothermal treatment as a new synthesis method and subsequently deposit them on single-walled carbon nanotubes surface.

- To analyse the self-assembly of phthalocyanines on the surface of single-walled carbon nanotubes by molecular mechanics and the electronic and structural characteristics of the hybrids by density functional theory.

1.7. Thesis outline

The research conducted has been organised into several chapters as follows

Chapter 2 explains each of the analytical techniques that were implemented for the characterisation of synthetised Pc+SWCNTs hybrids and the calculation methodology that was used for the geometry optimization of the hybrids and their individual components.

Chapter 3 describes the functionalisation of single-walled carbon nanotubes with *3d* metal monophthalocyanines (MPc; M= Mn, Fe, Co and Ni) by sublimation or gas phase as an alternative methodology to conventional ones that use organic solvents and long reaction times and the characterisation of each product. Additionally, the hybrids were tested as electrocatalysts for an oxygen evolution reaction in alkaline medium.

Chapter 4 presents the optimised geometries by DFT of the hybrids formed by cobalt and nickel monophthalocyanines and two models of carbon nanotubes (armchair and zigzag) with Stone-Wales defects incorporated in different orientations, with the aim of analysing the influence of the defects on the electronic properties such as formation and gap energy, HOMO-LUMO distribution, spin density and Mulliken population analysis of the hybrids and structural features such as closet distance between the transition monophthalocyanines and the CNT, bond angles and length. Results were compared from the same hybrids but with nanotubes with perfect graphitic lattice.

Chapter 5 is devoted to the solvothermal synthesis of rare-earth double-decker phthalocyanines (MPc_2; M= Y, La, Gd and Tb) as a new synthesis methodology and their adsorption on the surface of single-walled carbon nanotubes by reflux and the characterisation of the products obtained in each experimental process.

Chapter 6 provides a DFT study of the structural changes and electronic properties of rare-earth bispthalocyanines (MPc_2; M= Y, La, Gd and Lu) when they are absorbed on the surface of two models of carbon nanotubes (armchair and zigzag). Minimum energy geometries of individual components and of the MPc_2+SWCNT hybrids were obtained employing two calculation methods as a function of the central coordination metal. Core treatment semi-core pseudopotential (DSPP) with DN basis set was employed for lanthanide double-decker phthalocyanines ($LnPc_2$; Ln= La, Gd and Lu), whereas an all-electron treatment with three basis sets DN, DND and DNP was used for yttrium bispthalocyanines.

Finally, *Chapter 7* details the characterisation of a carbonaceous material obtained from the purification of free base phthalocyanines using a sublimation approach for the deposition of MPcs on the surface of nanotubes under the same functionalisation conditions (Chapter 3). The results obtained by analytical techniques and different tests indicate that the carbonaceous material corresponds to carbon fibres doped with nitrogen and the process of obtaining it is explained by DFT.

1.8. References

(1) Lomax, S. Q. Phthalocyanine and quinacridone pigments: their history, properties and use. *Stud. Conserv.* 2013, *50*, 19–29.

(2) Bekaroglu, Ö. History, development, and a new concept of phthalocyanines in turkey. *Turkish J. Chem.* 2014, *38* (6), 903–922.

(3) Armağanı, A.; Arslan, S. Phthalocyanines: structure, synthesis, purification and applications. *J. Life Sci.* 2016, *6* (2/2), 188–197.

(4) Komeda, T.; Katoh, K.; Yamashita, M. Double-decker phthalocyanine complex: scanning tunneling microscopy study of film formation and spin properties. *Prog. Surf. Sci.* 2014, *89* (2), 127–160.

(5) Pushkarev, V. E.; Tomilova, L. G.; Nemykin, V. N. Historic overview and new developments in synthetic methods for preparation of the rare-earth tetrapyrrolic complexes. *Coord. Chem. Rev.* 2016, *319*, 110–179.
(6) Pushkarev, V. E.; Tomilova, L. G.; Tomilov, Y. V. Synthetic approaches to lanthanide complexes with tetrapyrrole type ligands. *Russ. Chem. Rev.* 2008, *77* (10), 875–907.
(7) Luneau, D.; Liu, J.; del Barco, E.; Hill, S. *Molecular Magnets: A Microscopic and Spectroscopic View of Quantum Tunneling of Magnetization*; 2001; Vol. 5.
(8) Sk, R.; Deshpande, A. Unveiling the emergence of functional materials with STM: metal phthalocyanine on surface architectures. *Mol. Syst. Des. Eng.* 2019, *4* (3), 471–483.
(9) Şenocak, A.; Demirbaş, E.; Durmuş, M. *Phthalocyanine-Nanocarbon Materials and Their Composites: Preparation, Properties, and Applications*; 2019.
(10) De La Torre, G.; Claessens, C. G.; Torres, T. Phthalocyanines: old dyes, new materials. putting color in nanotechnology. *Chem. Commun.* 2007, No. 20, 2000–2015.
(11) Chen, X.; Chen, Y.; Bai, M.; Wang, C.; Qi, D.; Liu, Q.; Xu, M.; Jiang, J. Distribution of the unpaired electron in neutral bis(phthalocyaninato) yttrium double-deckers: an experimental and theoretical combinative investigation. *J. Porphyr. Phthalocyanines* 2018, *22* (1–3), 165–172.
(12) Kratochvílová, I.; Šebera, J.; Paruzel, B.; Pfleger, J.; Toman, P.; Marešová, E.; Havlová; Hubík, P.; Buryi, M.; Vrňata, M.; et al. Electronic functionality of gd-bisphthalocyanine: charge carrier concentration, charge mobility, and influence of local magnetic field. *Synth. Met.* 2018, *236*, 68–78.
(13) Bouvet, M.; Gaudillat, P.; Suisse, J. M. Lanthanide macrocyclic complexes: from molecules to materials and from materials to devices. *J. Porphyr. Phthalocyanines* 2013, *17* (8–9), 628–635.
(14) Sumimoto, M.; Kawashima, Y.; Hori, K.; Fujimoto, H. Theoretical study on the stability of double-decker type metal phthalocyanines, $M(Pc)_2$ and $M(Pc)_2^+$ (M = Ti, Sn and Sc): a critical assessment on the performance of density functionals. *Phys. Chem. Chem. Phys.* 2015, *17* (9), 6478–6483.
(15) Murdey, R.; Bouvet, M.; Sumimoto, M.; Sakaki, S.; Sato, N. Direct observation of the energy gap in lutetium bisphthalocyanine thin films. *Synth. Met.* 2009, *159* (15–16), 1677–1681.
(16) Lebedeva, N. S.; Mal, E. A.; V, A. I. *Polymorphism and Molecular Metal Phthalocyanine Complexes*; 2012; Vol. 2.
(17) E. Kuzmann, A. Nath, V. Chechersky, et al. *Industrial Applications of the Mössbauer Effect-Mossbauer Study of Oxygenated Iron-Phthalocyanines, a Precursor of Magnetic Storage Material*; 2002.
(18) Milev, A. S.; Tran, N.; Kannangara, G. S. K.; Wilson, M. A. Polymorphic transformation of iron-phthalocyanine and the effect on carbon nanotube synthesis. 2008, 5339–5347.
(19) Basiuk, V. A.; Flores-Sánchez, L. J.; Meza-Laguna, V.; Flores-Flores, J. O.; Bucio-Galindo, L.; Puente-Lee, I.; Basiuk, E. V. Noncovalent functionalization of pristine cvd single-walled carbon nanotubes with *3d* metal(II) phthalocyanines by adsorption from the gas phase. *Appl. Surf. Sci.* 2018, *436*, 1123–1133.
(20) Wagner, H. J.; Loutfy, R. O.; Hsiao, C. Purification and characterization of phthalocyanines. *J. Mater. Sci.* 1982, *17*, 2781–2791.
(21) Guillaud, G.; Simon, J.; Germain, J. P. Metallophthalocyanines. *Coord. Chem. Rev.* 1998, *178–180*, 1433–1484.
(22) Dini, D.; Hanack, M. *Physical Properties of Phthalocyanine-Based Materials*; 2012; Vol. 17.
(23) Ghani, F.; Kristen, J.; Riegler, H. Solubility properties of unsubstituted metal phthalocyanines in different types of solvents. *J. Chem. Eng. data* 2012, *57*, 439–449.
(24) Verdree, V. T.; Pakhomov, S.; Su, G.; Allen, M. W.; Countryman, A. C.; Hammer, R. P.; Soper, S. A. Water soluble metallo-phthalocyanines: the role of the functional groups on the spectral and photophysical properties.
(25) Nemykina, V. N.; Lukyanets, E. A. Synthesis of substituted phthalocyanines. *Arkivoc* 2010, *2010* (1), 136–208.
(26) Dumoulin, F.; Durmuş, M.; Ahsen, V.; Nyokong, T. Synthetic pathways to water-soluble phthalocyanines and close analogs. *Coordination Chemistry Reviews*. Elsevier December 1, 2010, pp 2792–2847.
(27) Şahin, S.; Ağar, E. Synthesis, spectroscopic properties, thermal properties and aggregation behaviors of macrogol-substituted phthalocyanines. *J. Mol. Struct.* 2019, *1187*, 121–131.
(28) Kalkan Burat, A.; Pınar, Z.; Altuntaş¸bayır, Z.; Altuntaş¸bayır, A. Synthesis and electronic absorption studies of novel (trifluoromethyl)phenoxy-substituted phthalocyanines. *Monatsh Chem* 2012, *143*, 437–442.
(29) Mack, J.; Stillman, M. J. Assignment of the optical spectra of metal phthalocyanines through spectral band deconvolution analysis and zindo calculations. *Coordination Chemistry Reviews*. Elsevier October 1, 2001, pp 993–1032.
(30) Dini, D.; Hanack, M. Phthalocyanines as materials for advanced technologies: some examples. In *Journal of Porphyrins and Phthalocyanines*; Society of Porphyrins and Phthalocyanines (SPP), 2004; Vol. 8, pp 915–933.
(31) Jiang, J. *Functional Phthalocyanine Molecular Materials*; 2015; Vol. 53.
(32) Černý, J.; Dokládalová, L.; Horáková, P.; Lyčka, A.; Mikysek, T.; Bureš, F. Preparation and characterization of novel double-decker rare-earth phthalocyanines substituted with 5-bromo-2-thienyl groups. *Chem. Cent. J.* 2017, *11*, 31.
(33) Davidson, A. T. The effect of the metal atom on the absorption spectra of phthalocyanine films. *J. Chem. Phys.* 1982, *77* (1), 168–172.
(34) Van Nostrum, C. F.; Nolte, R. J. M. Functional supramolecular materials: self-assembly of phthalocyanines and

porphyrazines. *Chem. Commun.* 1996, No. 21, 2385–2392.
(35) Urbani, M.; Ragoussi, M. E.; Nazeeruddin, M. K.; Torres, T. Phthalocyanines for dye-sensitized solar cells. *Coordination Chemistry Reviews*. Elsevier B.V. February 15, 2019, pp 1–64.
(36) Gottfried, J. M. Surface chemistry of porphyrins and phthalocyanines. *Surface Science Reports*. Elsevier B.V. June 27, 2015, pp 259–379.
(37) Wang, Y.; Wu, K.; Kröger, J.; Berndt, R.; KrögerKr, O. Review article: structures of phthalocyanine molecules on surfaces studied by stm. *Mg J. Chem. Phys.* 2012, *2*, 41402.
(38) Cuadrado, R.; Cerdá, J. I.; Wang, Y.; Xin, G.; Berndt, R.; Tang, H. CoPc adsorption on Cu(111): origin of the C4 to C2 symmetry reduction. *Mg J. Chem. Phys.* 2010, *133*, 154701.
(39) Heinrich, B. W.; Iacovita, C.; Brumme, T.; Choi, D. J.; Limot, L.; Rastei, M. V.; Hofer, W. A.; Kortus, J.; Bucher, J. P. Direct observation of the tunneling channels of a chemisorbed molecule. *J. Phys. Chem. Lett.* 2010, *1* (10), 1517–1523.
(40) Smykalla, L.; Shukrynau, P.; Zahn, D. R. T.; Hietschold, M. Self-metalation of phthalocyanine molecules with silver surface atoms by adsorption on Ag(110). *J. Phys. Chem. C* 2015, *119*, 17228–17234.
(41) Schmid, M.; Kaftan, A.; Steinrück, H. P.; Gottfried, J. M. The electronic structure of cobalt(II) phthalocyanine adsorbed on Ag(111). *Surf. Sci.* 2012, *606* (11–12), 945–949.
(42) Granet, J.; Sicot, M.; Gerber, I. C.; Kremer, G.; Pierron, T.; Kierren, B.; Moreau, L.; Fagot-Revurat, Y.; Lamare, S.; Chérioux, F.; et al. Adsorption-induced kondo effect in metal-free phthalocyanine on Ag(111). *J. Phys. Chem. C* 2020, *124* (19), 10441–10452.
(43) Kröger, J.; Néel, N.; Berndt, R.; Wang, Y. F.; Gopakumar, T. G. Exploring the organic-inorganic interface with a scanning tunneling microscope. In *Encyclopedia of Interfacial Chemistry: Surface Science and Electrochemistry*; Elsevier, 2018; pp 81–98.
(44) Komeda, T.; Isshiki, H.; Liu, J.; Zhang, Y. F.; Lorente, N.; Katoh, K.; Breedlove, B. K.; Yamashita, M. Observation and electric current control of a local spin in a single-molecule magnet. *Nat. Commun.* 2011, *2* (1).
(45) Cheng, Z. H.; Gao, L.; Deng, Z. T.; Jiang, N.; Liu, Q.; Shi, D. X.; Du, S. X.; Guo, H. M.; Gao, H.-J. Adsorption behavior of iron phthalocyanine on Au(111) surface at submonolayer coverage. *J.Phys.Chem.* 2007, *111*, 9240–9244.
(46) Zhang, Y.; Guan, P.; Isshiki, H.; Chen, M.; Yamashita, M.; Komeda, T. Bis(phthalocyaninato)yttrium grown on Au(111): electronic structure of a single molecule and the stability of two-dimensional films investigated by scanning tunneling microscopy/spectroscopy at 4.8 k. *Nano Res.* 2010, *3* (8), 604–611.
(47) Katoh, K.; Komeda, T.; Yamashita, M. Surface morphologies, electronic structures, and kondo effect of lanthanide(III)-phthalocyanine molecules on Au(111) by using stm, sts and fet properties for next generation devices. *Dalt. Trans.* 2010, *39* (20), 4693–4707.
(48) Robles, R.; Nicolás, †; Lorente, N.; Isshiki, H.; Liu, J.; Katoh, K.; Breedlove, B. K.; Yamashita, M.; Komeda, T. Spin doping of individual molecules by using single-atom manipulation. *NannoLetters* 2012, *12*, 3609–3612.
(49) Endlich, M.; Gozdzik, S.; Néel, N.; Da Rosa, A. L.; Frauenheim, T.; Wehling, T. O.; Kröger, J. Phthalocyanine adsorption to graphene on Ir(111): evidence for decoupling from vibrational spectroscopy. *J. Chem. Phys.* 2014, *141* (18), 184308.
(50) Jiang, Y. H.; Xiao, W. D.; Liu, L. W.; Zhang, L. Z.; Lian, J. C.; Yang, K.; Du, S. X.; Gao, H. J. Self-assembly of metal phthalocyanines on Pb(111) and Au(111) surfaces at submonolayer coverage. *J. Phys. Chem. C* 2011, *115* (44), 21750–21754.
(51) Sun, K.; Tao, M. L.; Tu, Y. B.; Wang, J. Z. Off-center rotation of cupc molecular rotor on a Bi(111) surface and the chiral feature. *Molecules* 2017, *22* (5).
(52) Miwa, K.; Imada, H.; Kawahara, S.; Kim, Y. Effects of molecule-insulator interaction on geometric property of a single phthalocyanine molecule adsorbed on an ultrathin nacl film. *Phys. Rev. B* 2016, *93*, 165419.
(53) Bottari, G.; Torre, G. De; Guldi, D. M.; Torres, T. Covalent and noncovalent phthalocyanine - carbon nanostructure systems : synthesis , photoinduced electron transfer , and application to molecular photovoltaics. *Chem. Rev.* 2010, *110*, 6768–6816.
(54) D'Souza, F.; Ito, O. Supramolecular donor-acceptor hybrids of porphyrins/phthalocyanines with fullerenes/carbon nanotubes: electron transfer, sensing, switching, and catalytic applications. *Chem. Commun.* 2009, No. 33, 4913–4928.
(55) Apetrei, C.; Nieto, M.; Rodríguez-Méndez, M. L.; De Saja, J. A. Development of lutetium bisphthalocyanine/carbon nanotube langmuir-blodgett films. sensing properties. *J. Porphyr. Phthalocyanines* 2011, *15* (9–10), 908–917.
(56) Abd El-Mageed, A. I. A.; Ogawa, T. Supramolecular structures of terbium(III) porphyrin double-decker complexes on a single-walled carbon nanotube surface. *RSC Adv.* 2019, *9* (48), 28135–28145.
(57) Basiuk, V. A.; Bolivar-Pineda, L. M.; Meza-Laguna, V.; Rybak-Akimova, E. V.; Basiuk, E. V. Carbon nanotubes and graphene promote pyrolysis of free-base phthalocyanine. *J. Phys. Chem. Lett.* 2018, *9* (15), 4420–4427.
(58) Konarev, D. V.; Khasanov, S. S.; Lyubovskaya, R. N. Fullerene complexes with coordination assemblies of metalloporphyrins and metal phthalocyanines. *Coordination Chemistry Reviews*. Elsevier March 1, 2014, pp 16–36.
(59) Basiuk, V. A.; Tahuilan-Anguiano, D. E. Complexation of free-base and 3*d* transition metal(II) phthalocyanines with

endohedral fullerene $Sc_3N@C_{80}$. *Chem. Phys. Lett.* 2019, *722*, 146–152.
(60) Oyedele, A. D.; Rouleau, C. M.; Geohegan, D. B.; Xiao, K. The growth and assembly of organic molecules and inorganic 2D materials on graphene for van der Waals heterostructures. *Carbon N. Y.* 2018, *131*, 246–257.
(61) Huang, Y. L.; Li, H.; Ma, J.; Huang, H.; Chen, W.; Wee, A. T. S. Scanning tunneling microscopy investigation of self-assembled cupc/f 16 cupc binary superstructures on graphite. *Langmuir* 2010, *26* (5), 3329–3334.
(62) Zhang, X.; Feng, Y.; Tang, S.; Feng, W. Preparation of a graphene oxide-phthalocyanine hybrid through strong π-π interactions. *Carbon N. Y.* 2010, *48* (1), 211–216.
(63) Zhang, Y. F.; Isshiki, H.; Katoh, K.; Yoshida, Y.; Yamashita, M.; Miyasaka, H.; Breedlove, B. K.; Kajiwara, T.; Takaishi, S.; Komeda, T. Low-temperature scanning tunneling microscopy investigation of bis(phthalocyaninato)yttrium growth on Au(111): from individual molecules to two-dimensional domains. *J. Phys. Chem. C* 2009, *113* (22), 9826–9830.
(64) De Saja, J. A.; Rodríguez-Méndez, M. L. Sensors based on double-decker rare earth phthalocyanines. *Advances in Colloid and Interface Science*. Elsevier November 30, 2005, pp 1–11.
(65) Abdullah, K.; Kong, X.; Imran, M.; Mustafa, G.; Chen, Y. Excellent ambipolar gas sensing response of $Eu[Pc(OC_4H_9)_8]_2$/acidified multiwalled carbon nanotubes hybrid at room temperature. *J. Porphyr. Phthalocyanines* 2019, *23* (11–12), 1455–1462.
(66) Pereira, G. F. M.; Tasso, T. T. From cuvette to cells: how the central metal ion modulates the properties of phthalocyanines and porphyrazines as photosensitizers. *Inorganica Chimica Acta*. Elsevier B.V. May 1, 2021, p 120271.
(67) Janas, K.; Boniewska-Bernacka, E.; Dyrda, G.; Słota, R. Porphyrin and phthalocyanine photosensitizers designed for targeted photodynamic therapy of colorectal cancer. *Bioorganic Med. Chem.* 2021, *30*, 115926.
(68) Roguin, L. P.; Chiarante, N.; García Vior, M. C.; Marino, J. Zinc(II) phthalocyanines as photosensitizers for antitumor photodynamic therapy. *International Journal of Biochemistry and Cell Biology*. Elsevier Ltd September 1, 2019, p 105575.
(69) Majumdar, H. S.; Bandyopadhyay, A.; Pal, A. J. Data-storage devices based on layer-by-layer self-assembled films of a phthalocyanine derivative. *Org. Electron.* 2003, *4* (1), 39–44.
(70) Rapp, L.; Nénon, S.; Alloncle, A. P.; Videlot-Ackermann, C.; Fages, F.; Delaporte, P. Multilayer laser printing for organic thin film transistors. In *Applied Surface Science*; Elsevier B.V., 2011; Vol. 257, pp 5152–5155.
(71) Wang, C.; Hou, B.; Yuan, S.; Zhang, Q.; Cui, X.; Wang, X. Highly active electrocatalysts of iron phthalocyanine by mofs for oxygen reduction reaction under alkaline solution. *RSC Adv.* 2020, *10* (45), 27014–27023.
(72) Choi, S. A.; Kim, K.; Lee, S. J.; Lee, H.; Babajanyan, A.; Friedman, B.; Lee, K. Effects of thermal preparation on copper phthalocyanine organic light emitting diodes. *J. Lumin.* 2016, *171*, 149–153.
(73) Gonidec, M.; Amabilino, D. B.; Veciana, J. Novel double-decker phthalocyaninato terbium(III) single molecule magnets with stabilised redox states. *Dalt. Trans.* 2012, *41*, 13632.
(74) Basova, T.; Hassan, A.; Durmuş, M.; Gürek, A. G.; Ahsen, V. Liquid crystalline metal phthalocyanines: structural organization on the substrate surface. *Coordination Chemistry Reviews*. Elsevier March 1, 2016, pp 131–153.
(75) Sattler, K. D. *Carbon Nanomaterials Sourcebook. Graphene, Fullerenes, Nanotubes and Nanodiamonds*; Group, T. & F., Ed.; 2016; Vol. I.
(76) Grobert, N. Carbon nanotubes – importance of clean. *Rev. Lit. Arts Am.* 2007, *10* (1), 28–35.
(77) Sumlo Iijima. Helical microtubules of graphitic carbon. *Nature* 1991, *354* (354), 56–58.
(78) Iijima, S.; Ichihashi, T. Single-shell carbon nanotubes of 1-nm diameter. *Nature* 1993, *363* (6430), 603–605.
(79) Sattler, K. D. *Handbook of Nanophysics Nanotubes and Nanowires*, 1 ed.; Group, T. and F., Ed.; 2011.
(80) Oberlin, A.; Endo, M.; Koyama, T. Filamentous growth of carbon through benzene decomposition. *J. Cryst. Growth* 1976, *32* (3), 335–349.
(81) Quintana, M.; Grzelczak, M.; Spyrou, K.; Calvaresi, M.; Bals, S.; Kooi, B.; Van Tendeloo, G.; Rudolf, P.; Zerbetto, F.; Prato, M. A simple road for the transformation of few-layer graphene into mwnts. *J. Am. Chem. Soc.* 2012, *134*, 13310–13315.
(82) Aqel, A.; El-Nour, K. M. M. A.; Ammar, R. A. A.; Al-Warthan, A. Carbon nanotubes, science and technology part (I) structure, synthesis and characterisation. *Arabian Journal of Chemistry*. Elsevier January 1, 2012, pp 1–23.
(83) Balasubramanian, K.; Burghard, M. Chemically functionalized carbon nanotubes. *Small* 2005, *1* (2), 180–192.
(84) Lavagna, L.; Nisticò, R.; Musso, S.; Pavese, M. Functionalization as a way to enhance dispersion of carbon nanotubes in matrices: a review. *Materials Today Chemistry*. Elsevier Ltd June 1, 2021, p 100477.
(85) Rathinavel, S.; Priyadharshini, K.; Panda, D. A review on carbon nanotube: an overview of synthesis, properties, functionalization, characterization, and the application. *Materials Science and Engineering B: Solid-State Materials for Advanced Technology*. Elsevier Ltd June 1, 2021, p 115095.
(86) O'Connell, M. J. *Carbon Nanotubes Properties and Applications*, 1 ed.; Group, T. & F., Ed.; 2006.
(87) Sadjadi, S. *Organic Nanoreactors*; 2016.
(88) Chris Hardacre. *Nanostructured Carbon Materials for Catalysis*; 2015.
(89) Meyyappan, M. *Carbon Nanotubes Science and Applications*; 2005.
(90) Basiuk, E. V.; Basiuk, V. A. Green chemistry of carbon nanomaterials. *Tech. Proc. NSTI-Nanotech 2014* 2014, *3* (1),

198–201.
(91) Ma, P.-C.; Kim, J.-K. *Carbon Nanotubes for Polymer Reinforcement*; 2011.
(92) Morelos-Gómez, A.; López, F. T.; Cruz-Silva, R.; Vega Díaz, S. M.; Terrones, M. Modified carbon nanotubes. *Springer Handb. Nanomater.* 2013, 189–232.
(93) Basiuk, Vladimir a. and Basiuk, E. v. *Chemistry of Carbon Nanotubes*; 2008; Vol. Volumen 1.
(94) Hirsch, A. Functionalization of single-walled carbon nanotubes. *Angew. Chemie - Int. Ed.* 2002, *41* (11), 1853–1859.
(95) Wang, C.; Zhou, G.; Liu, H.; Wu, J.; Qiu, Y.; Gu, B. L.; Duan, W. Chemical functionalization of carbon nanotubes by carboxyl groups on stone-wales defects: a density functional theory study. *J. Phys. Chem. B* 2006, *110* (21), 10266–10271.
(96) Qu, L.; Lee, K. M.; Dai, L. Chapter 8 functionalization and applications of carbon nanotubes; 2006; pp 191–234.
(97) Hirsch, A.; Vostrowsky, O. Functionalization of carbon nanotubes. *Top. Curr. Chem.* 2005, *245*, 193–237.
(98) Yang, Z.; Pu, H.; Yuan, J.; Wan, D.; Liu, Y. Phthalocyanines–mwcnt hybrid materials: fabrication, aggregation and photoconductivity properties improvement. *Chem. Phys. Lett.* 2008, *465* (1–3), 73–77.
(99) Bottari, G.; De La Torre, G.; Torres, T. Phthalocyanine-nanocarbon ensembles: from discrete molecular and supramolecular systems to hybrid nanomaterials. *Acc. Chem. Res.* 2015, *48* (4), 900–910.
(100) Ballesteros, B.; De La Torre, G.; Ehli, C.; Rahman, G. M. A.; Agulló-Rueda, F.; Guidi, D. M.; Torres, T. Single-wall carbon nanotubes bearing covalently linked phthalocyanines - photoinduced electron transfer. *J. Am. Chem. Soc.* 2007, *129* (16), 5061–5068.
(101) Yang, Z. L.; Chen, H. Z.; Cao, L.; Li, H. Y.; Wang, M. Synthesis and photoconductivity study of carbon nanotube bonded by tetrasubstituted amino manganese phthalocyanine. *Mater. Sci. Eng. B* 2004, *106* (1), 73–78.
(102) Ballesteros, B.; Campidelli, S.; De La Torre, G.; Ehli, C.; Guldi, D. M.; Prato, M.; Torres, T. Synthesis, characterization and photophysical properties of a swnt-phthalocyanine hybrid. *Chem. Commun.* 2007, No. 28, 2950–2952.
(103) Wang, Y.; Chen, H. Z.; Li, H. Y.; Wang, M. Fabrication of carbon nanotubes/copper phthalocyanine composites with improved compatibility. *Mater. Sci. Eng. B* 2005, *117* (3), 296–301.
(104) Kyatskaya, S.; Mascarós, J. R. G.; Bogani, L.; Hennrich, F.; Kappes, M.; Wernsdorfer, W.; Ruben, M. Anchoring of rare-earth-based single-molecule magnets on single-walled carbon nanotubes. *J. Am. Chem. Soc.* 2009, *131* (42), 15143–15151.
(105) Xu, H. B.; Chen, H. Z.; Shi, M. M.; Bai, R.; Wang, M. A novel donor–acceptor heterojunction from single-walled carbon nanotubes functionalized by erbium bisphthalocyanine. *Mater. Chem. Phys.* 2005, *94* (2–3), 342–346.
(106) D'Ambrosio, P.; Carchesio, M.; D'Alessandro, N.; De La Torre, G.; Torres, T. Linking Pd(II) and Ru(II) phthalocyanines to single-walled carbon nanotubes. *Dalt. Trans.* 2014, *43* (20), 7473–7479.
(107) Nkosi, D.; Ozoemena, K. I. Interrogating the electrocatalytic properties of coordination self-assembled nanostructures of single-walled carbon nanotube–octa(hydroxyethylthio)phthalocyaninatoiron(II) using thiocyanate as an analytical probe. *J. Electroanal. Chem.* 2008, *621* (2), 304–313.
(108) Wang, B.; Wu, Y.; Wang, X.; Chen, Z.; He, C. Copper phthalocyanine noncovalent functionalized single-walled carbon nanotube with enhanced nh3 sensing performance. *Sensors Actuators, B Chem.* 2014, *190*, 157–164.
(109) Wang, B.; Zhou, X.; Wu, Y.; Chen, Z.; He, C. Lead phthalocyanine modified carbon nanotubes with enhanced NH_3 sensing performance. *Sensors Actuators B Chem.* 2012, *171–172*, 398–404.
(110) Pu, Z.; Zhong, J.; Liu, X. Composites based on core–shell structured HBCuPc@CNTs-Fe_3O_4 and polyarylene ether nitriles with excellent dielectric and mechanical properties. *J. Electron. Mater.* 2017, *46* (10), 5519–5530.
(111) Sharma, A. K.; Mahajan, A.; Saini, R.; Bedi, R. K.; Kumar, S.; Debnath, A. K.; Aswal, D. K. Reversible and fast responding ppb level Cl_2 sensor based on noncovalent modified carbon nanotubes with hexadecafluorinated copper phthalocyanine. *Sensors Actuators, B Chem.* 2018, *255*, 87–99.
(112) Zhan, Y.; Hu, H.; He, Y.; Long, Z.; Wan, X.; Zeng, G. Novel amino-functionalized Fe_3O_4/carboxylic multi-walled carbon nanotubes: one-pot synthesis, characterization and removal for Cu(II). *Russ. J. Appl. Chem.* 2016, *89* (11), 1894–1902.
(113) Hatton, R. A.; Blanchard, N. P.; Stolojan, V.; Miller, A. J.; Silva, S. R. P. Nanostructured copper phthalocyanine-sensitized multiwall carbon nanotube films. *Langmuir* 2007, *23* (11), 6424–6430.
(114) Sharma, A. K.; Mahajan, A.; Bedi, R. K.; Kumar, S.; Debnath, A. K.; Aswal, D. K. CNTs based improved chlorine sensor from non-covalently anchored multi-walled carbon nanotubes with hexa-decafluorinated cobalt phthalocyanines. *RSC Adv.* 2017, *7* (78), 49675–49683.
(115) Wang, Y.; Hu, N.; Zhou, Z.; Xu, D.; Wang, Z.; Yang, Z.; Wei, H.; Kong, E. S. W.; Zhang, Y. Single-walled carbon nanotube/cobalt phthalocyanine derivative hybrid material: preparation, characterization and its gas sensing properties. *J. Mater. Chem.* 2011, *21*, 3779–3787.
(116) Sharma, A. K.; Mahajan, A.; Bedi, R. K.; Kumar, S.; Debnath, A. K.; Aswal, D. K. Non-covalently anchored multi-walled carbon nanotubes with hexa-decafluorinated zinc phthalocyanine as ppb level chemiresistive chlorine sensor. *Appl. Surf. Sci.* 2018, *427*, 202–209.
(117) Pérez-Cadenas, M.; Asedegbega-Nieto, E.; Carter, J.; Anderson, J. A.; Rodríguez-Ramos, I.; Guerrero-Ruiz, A. Study of the interaction of an iron phthalocyanine complex over surface modified carbon nanotubes. *Mater. 2021, Vol. 14,*

Page 4067 2021, *14* (15), 4067.
(118) Li, H.; Xu, Z.; Li, K.; Hou, X.; Cao, G.; Zhang, Q.; Cao, Z. Modification of multi-walled carbon nanotubes with cobalt phthalocyanine: effects of the templates on the assemblies. *J. Mater. Chem.* 2011, *21*, 1181–1186.
(119) González-Gaitán, C.; Ruiz-Rosas, R.; Morallón, E.; Cazorla-Amorós, D. Relevance of the interaction between the m-phthalocyanines and carbon nanotubes in the electroactivity toward orr. *Langmuir* 2017, *33* (43), 11945–11955.
(120) Türk, K.-K.; Kaare, K.; Kruusenberg, I.; Merisalu, M.; Joost, U.; Matisen, L.; Sammelselg, V.; Zagal, J. H.; Tammeveski, K. Oxygen electroreduction on zinc and dilithium phthalocyanine modified multiwalled carbon nanotubes in alkaline media. *J. Electrochem. Soc.* 2017, *164* (6), H338–H344.
(121) Xing, R.; Yang, H.; Li, S.; Yang, J.; Zhao, X.; Wang, Q.; Liu, S.; Liu, X. A sensitive and reliable rutin electrochemical sensor based on palladium phthalocyanine-MWCNTs-nafion nanocomposite. *J. Solid State Electrochem.* 2017, *21* (5), 1219–1228.
(122) Spindola, R. F.; Zanin, H.; Macena, C. S.; Contin, A.; de Cássia Silva Luz, R.; Damos, F. S. Evaluation of a novel composite based on functionalized multi-walled carbon nanotube and iron phthalocyanine for electroanalytical determination of isoniazid. *J. Solid State Electrochem.* 2017, *21* (4), 1089–1099.
(123) Rajmohan, K. S.; Chetty, R. Enhanced nitrate reduction with copper phthalocyanine-coated carbon nanotubes in a solid polymer electrolyte reactor. *J. Appl. Electrochem.* 2017, *47* (1), 63–74.
(124) Olmos Moya, P. M.; Martínez Alfaro, M.; Kazemi, R.; Alpuche-Avilés, M. A.; Griveau, S.; Bedioui, F.; Gutiérrez Granados, S. Simultaneous electrochemical speciation of oxidized and reduced glutathione. redox profiling of oxidative stress in biological fluids with a modified carbon electrode. *Anal. Chem.* 2017, *89* (20), 10726–10733.
(125) Yang, J.; Toshimitsu, F.; Yang, Z.; Fujigaya Abc, T.; Nakashima, N. Pristine carbon nanotube/iron phthalocyanine hybrids with a well-defined nanostructure show excellent efficiency and durability for the oxygen reduction reaction. 2017.
(126) Wu, Y.; Jiang, Z.; Lu, X.; Liang, Y.; Wang, H. Domino electroreduction of co2 to methanol on a molecular catalyst. *Nat. 2019 5757784* 2019, *575* (7784), 639–642.
(127) Krainov, I. V.; Klier, J.; Dmitriev, A. P.; Klyatskaya, S.; Ruben, M.; Wernsdorfer, W.; Gornyi, I. V. Giant magnetoresistance in carbon nanotubes with single-molecule magnets tbpc2. *ACS Nano* 2017, *11* (7), 6868–6880.
(128) Cao, L.; Chen, H. Z.; Zhou, H. B.; Zhu, L.; Sun, J. Z.; Zhang, X. Bin; Xu, J. M.; Wang, M. Carbon-nanotube-templated assembly of rare-earth phthalocyanine nanowires. *Adv. Mater.* 2003, *15* (11), 909–913.
(129) Urdampilleta, M.; Klyatskaya, S.; Cleuziou, J. P.; Ruben, M.; Wernsdorfer, W. Supramolecular spin valves. *Nat. Mater.* 2011, *10* (7), 502–506.
(130) Alvarez, L.; Fall, F.; Belhboub, A.; Le Parc, R.; Almadori, Y.; Arenal, R.; Aznar, R.; Dieudonné-George, P.; Hermet, P.; Rahmani, A.; et al. One-dimensional molecular crystal of phthalocyanine confined into single-walled carbon nanotubes. *J. Phys. Chem. C* 2015, *119* (9), 5203–5210.
(131) Schulte, K.; Swarbrick, J. C.; Smith, N. A.; Bondino, F.; Magnano, E.; Khlobystov, A. N. Assembly of cobalt phthalocyanine stacks inside carbon nanotubes. *Adv. Mater.* 2007, *19*, 3312–3316.
(132) Katoh, K.; Sato, J.; Nakanishi, R.; Ara, F.; Komeda, T.; Kuwahara, Y.; Saito, T.; Breedlove, B. K.; Yamashita, M. Terbium(III) bis-phthalocyaninato single-molecule magnet encapsulated in a single-walled carbon nanotube. 2021, *9* (33).
(133) Yan, X.; Xu, X.; Liu, Q.; Guo, J.; Kang, L.; Yao, J. Functionalization of multi-walled carbon nanotubes with iron phthalocyanine via a liquid chemical reaction for oxygen reduction in alkaline media. *J. Power Sources* 2018, *389*, 260–266.
(134) Han, N.; Wang, Y.; Ma, L.; Wen, J.; Li, J.; Zheng, H.; Nie, K.; Wang, X.; Zhao, F.; Li, Y.; et al. Supported cobalt polyphthalocyanine for high-performance electrocatalytic co2 reduction. *Chem* 2017, *3* (4), 652–664.
(135) Karapinar, D.; Zitolo, A.; Huan, T. N.; Zanna, S.; Taverna, D.; Galvão Tizei, L. H.; Giaume, D.; Marcus, P.; Mougel, V.; Fontecave, M. Carbon-nanotube-supported copper polyphthalocyanine for efficient and selective electrocatalytic CO_2 reduction to co. *ChemSusChem* 2020, *13* (1), 173–179.
(136) Wu, H.; Chen, Z.; Zhang, J.; Wu, F.; He, C.; Wu, Y.; Ren, Z. Phthalocyanine-mediated non-covalent coupling of carbon nanotubes with polyaniline for ultrafast NH_3 gas sensors †. *J. Mater. Chem. A* 2017, *5*, 24493–24501 |.
(137) Ye, J. S.; Wen, Y.; De Zhang, W.; Cui, H. F.; Xu, G. Q.; Sheu, F. S. Electrochemical biosensing platforms using phthalocyanine-functionalized carbon nanotube electrode. *Electroanalysis* 2005, *17* (1), 89–96.
(138) Moraes, F. C.; Golinelli, D. L. C.; Mascaro, L. H.; MacHado, S. A. S. Determination of epinephrine in urine using multi-walled carbon nanotube modified with cobalt phthalocyanine in a paraffin composite electrode. *Sensors Actuators B Chem.* 2010, *148* (2), 492–497.
(139) Prasongkit, J.; Tangsukworakhun, S.; Jaisutti, R.; Osotchan, T. Highly sensitive and selective sensing of acetone and hydrogen sulfide using metal phthalocyanine – carbon nanotube hybrids. *Appl. Surf. Sci.* 2020, *532*.
(140) Son, H.; Yang, M. H.; Mutyala, A. K.; Chang, D. W.; Park, J. S. Superior electrocatalytic performance of polyisobutylene-substituted metallophthalocyanines supported on single-walled carbon nanotubes for an oxygen reduction reaction. *Dye. Pigment.* 2019, *162*, 662–670.
(141) Siswana, M. P.; Ozoemena, K. I.; Nyokong, T. Electrocatalysis of asulam on cobalt phthalocyanine modified multi-

walled carbon nanotubes immobilized on a basal plane pyrolytic graphite electrode. *Electrochim. Acta* 2006, *52* (1), 114–122.
(142) Errol, L. Computational chemistry. introduction to the theory and applications of molecular and quantum mechanics. *Kluwer Acad. Publ.* 2004.
(143) Errol, L. *Computational Chemistry*; 2003; Vol. 5.
(144) Hypercube. *HyperChem: Tools for Molecular Modeling, Hypercube Incorporation*; 2002.
(145) Bassiouk, M.; Álvarez-zauco, E.; Basiuk, V. A. Self-assemblies of *meso* -tetraphenylporphine ligand on surfaces of highly oriented pyrolytic graphite and single-walled carbon nanotubes : insights from scanning tunneling microscopy and molecular modeling. 2011, *11* (6), 5457–5468.
(146) Bassiouk, M.; Basiuk, V. A.; Basiuk, E. V.; Álvarez-Zauco, E.; Martínez-Herrera, M.; Rojas-Aguilar, A.; Puente-Lee, I. Noncovalent functionalization of single-walled carbon nanotubes with porphyrins. *Appl. Surf. Sci.* 2013, *275*, 168–177.
(147) Basiuk, V. A.; Bassiouk, M. Nanoassembly of *meso*-tetraphenylporphines on surfaces of carbon materials: initial steps as studied by molecular mechanics and scanning tunneling microscopy. *J. Nanosci. Nanotechnol.* 2008, *8*, 259–267.
(148) Bassiouk, M.; Álvarez-Zauco, E.; Basiuk, V. A. Adsorption of meso-tetraphenylporphines on thin films of C_{60} fullerene. *Appl. Surf. Sci.* 2013, *275*, 374–383.
(149) Hocquet, A.; Langgård, M. An evaluation of the MM+ force field. *J. Mol. Model.* 1998, *4* (3), 94–112.
(150) Argaman, N.; Makov, G.; Argaman, N. Density functional theory : an introduction. *Am. Journal Phys.* 2000, *1*, 68–79.
(151) Obot, I. B.; Macdonald, D. D.; Gasem, Z. M. Density functional theory (DFT) as a powerful tool for designing. *Corros. Sci.* 2015.
(152) Contreras-torres, F. F.; Basiuk, E. V; Basiuk, V. A.; Meza-laguna, V.; Gromovoy, T. Y. Nanostructured diamine − fullerene derivatives : computational density functional theory study and experimental evidence for their formation via gas-phase functionalization. *J. Phys. Chem. A* 2012, *116*, 1663–1676.
(153) Tsuneda, T. *Density Functional Theory in Quantum Chemistry*, 1st ed.; Springer, Ed.; 2014.
(154) Correa, J. D.; Orellana, W. Optical response of carbon nanotubes functionalized with (free-base , Zn) porphyrins , and phthalocyanines : a DFT study. *Phys. Rev. B* 2012, *86*, 125417/1-6.
(155) Orellana, W. Metal-phthalocyanine functionalized carbon nanotubes as catalyst for the oxygen reduction reaction : a theoretical study. *Chem. Phys. Lett.* 2012, *541*, 81–84.
(156) Krasnov, P. O.; Basova, T. V.; Hassan, A. Interaction of metal phthalocyanines with carbon zigzag and armchair nanotubes with different diameters. *Appl. Surf. Sci.* 2018, *457*, 235–240.
(157) Basiuk, V. A.; Chávez-colorado, E. Adsorption of free-base phthalocyanine on stone-wales defect-containing carbon nanotubes : a DFT study. *Diam. Relat. Mater.* 2019, *97* (March), 107443.
(158) Basiuk, E. V.; Huerta, L.; Basiuk, V. A. Noncovalent bonding of *3d* metal(II) phthalocyanines with single-walled carbon nanotubes: a combined DFT and XPS study. *Appl. Surf. Sci.* 2019, *470*, 622–630.
(159) Wang, Y.; Zhang, Z.; Zhang, X.; Yuan, Y.; Jiang, Z.; Zheng, H.; Wang, Y. G.; Zhou, H.; Liang, Y. Theory-driven design of electrocatalysts for the two-electron oxygen reduction reaction based on dispersed metal phthalocyanines. *CCS Chem.* 2022, *4* (1), 228–236.
(160) Cao, R.; Thapa, R.; Kim, H.; Xu, X.; Kim, M. G.; Li, Q.; Park, N.; Liu, M.; Cho, J. Promotion of oxygen reduction by a bio-inspired tethered iron phthalocyanine carbon nanotube-based catalyst. *Nat. Commun.* 2013.
(161) Chávez-Colorado, E.; Basiuk, V. A. Noncovalent interactions of free-base phthalocyanine with elongated fullerenes as carbon nanotube models. *Struct. Chem.* 2017, *28*, 1765–1773.
(162) Ferbinteanu, M.; Stroppa, A.; Scarrozza, M.; Humelnicu, I.; Maftei, D.; Frecus, B.; Cimpoesu, F. On the density functional theory treatment of lanthanide coordination compounds: a comparative study in a series of Cu−Ln (Ln =Gd, Tb,Lu) binuclear complexes. 2017.

2

Chapter 2

Experimental & computational techniques

2.1. Introduction

This chapter details the analytical techniques that were used to characterise the synthesized materials. Most experiments were carried out at facilities of the National Autonomous University of Mexico (UNAM) and the University of Groningen (RUG). Some of them, which were performed in collaboration with external universities, are also mentioned in this section. If a specific measurement was not performed by the author, this is specified herein as well.

2.2. Characterisation techniques

2.2.1. Fourier transform infrared spectroscopy

Fourier-transform infrared (FTIR) spectroscopy is a non-destructive technique to identify the functional groups in materials (gas, liquid and solid) using a beam of infrared radiations. [1] An infrared spectrum is commonly obtained by passing infrared radiation through a sample and determining what fraction of the incident radiation is absorbed at a particular energy. [2] The energy at which a peak appears in an absorption spectrum corresponds to the frequency of a vibration of a part of a sample molecule. [2] For a molecule to absorb infrared light, the electric dipole moment of the molecule must change during the vibration. This is the selection rule for infrared spectroscopy. [1,2]

FITR is often used with an attenuated total reflection (ATR) accessory, a crystal placed horizontally in contact the sample. An infrared beam is directed onto this optically dense crystal with a high refractive index at a certain angle. This internal reflectance creates an evanescent wave that extends beyond the surface of the crystal into the sample. The evanescent wave is attenuated in the regions of the infrared spectrum where the sample absorbs energy. The attenuated beam returns to the crystal, then exits the opposite end of the crystal and is directed to the detector in the spectrometer. The detector records the attenuated infrared beam as an interferogram signal, which can then be used to generate an FTIR spectrum (see Fig.2. 1). [1,3]

ATR-FTIR spectroscopy has dramatically improved the quality of infrared spectra and minimized the time required for data acquisition.[2] ATR-FTIR spectroscopy is most widely used for the qualitative analysis of organic compounds. Each compound has a unique spectral fingerprint that depends on its molecular structure. [1] On the projects described in this dissertation, ATR-FTIR was employed to identify the typical features of commercial and synthesized phthalocyanines and their presence on the functionalised single-walled carbon nanotubes.

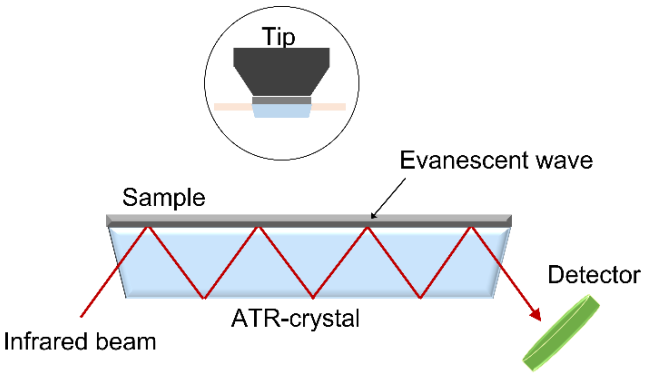

Fig.2. 1.Schematic if a typical attenuated total reflectance. Modified from reference 2, Copyright 2006, Wiley.

The FTIR spectra reported in Chapters 3 and 7 were acquired at room temperature and under atmospheric pressure, using a Spectrum 100 FTIR PerkinElmer spectrophotometer, complemented with a universal attenuated total reflection sampling accessory (UNAM).

The FTIR spectra shown in Chapter 5 were collected on a Bruker Vertex 70 spectrometer, complemented with ATR sampling accessory. Each spectrum was the sum of 40 scans acquired in the range 500-4000 cm^{-1} with a resolution of 4 cm^{-1} at room temperature and under atmospheric pressure (RUG). All the samples were analysed in powder form and placed without any treatment on the ATR crystal.

2.2.2. Raman spectroscopy

Raman spectroscopy is a technique that exploits light scattering to measure the vibrational energy modes of a sample. Raman spectroscopy, like ATR-FTIR spectroscopy, is a non-destructive technique that provides chemical and structural information and allows the identification of substances, even different forms of carbon. [1,4]

When monochromatic light is scattered, the oscillating electromagnetic field of a photon induces a polarisation (deformability) of the electron cloud, which leaves the molecule in a virtual higher energetic state (energy of the photon transferred to the molecule) which is not stable and the photon is reemitted almost immediately, as scattered light. [4,5] This scattering phenomenon occurs in different ways (Fig.2. 2a). [4,5] If the energy of the molecules does not change after their interaction with the photon, in other words, if the molecules relax back to the initial ground state (energy of scattering particle is conserved), this is known as elastic or Rayleigh scattering. Rayleigh scattering is by far the dominant process in light scattering. Nevertheless, the relaxation can also be inelastic, when the molecules release a different quantity of energy to that of the incident photon, this phenomenon is Raman scattering.

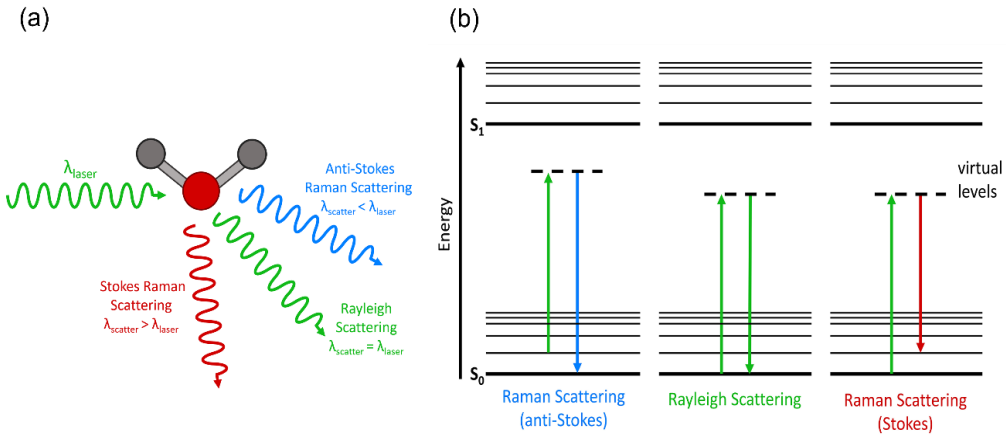

Fig.2. 2. Three types of scattering processes that can occur when light interacts with a molecule and (b) Jacoblonski diagram showing the origin of Rayleigh, as well as Stokes and Anti-Stokes Raman Scattering.

There are two types of Raman scattering: Stokes and anti-Stokes Raman scattering. [4,5] In the case of Stokes scattering, the molecules initially in the ground vibrational state, gain energy from the photon during the scattering (excitation to a higher vibrational level) and then the wavelength of the scattered light is higher that of the incident light. [4,5] Conversely, in anti-Stokes scattering, the molecules initially in a vibrational excited state, lose energy by relaxing to a lower vibrational level and the wavelength of the scattered light is lower than the incident light. [4,5] Fig.2. 2b displays the Jablonski diagram of the energetic transitions involved in light scattering. In the Raman spectrum the Stokes bands are much more intense than anti-Stokes since at ambient temperature most molecules are in the ground state. [4]

Raman spectra shown in Chapter 3 served to evaluate the structural characteristics of the single-walled carbon nanotube after functionalisation; those depicted in Chapter 5 to determine the typical features of the rare-earth bisphthalocyanines; and the ones in Chapter 7 to identify the carbonaceous material obtained after pyrolysis of the metal-free phthalocyanine.

The Raman spectra reported in Chapter 3 were acquired using a Thermo Fisher Scientific micro-Raman spectrometer with a laser wavelength of λ =532 nm was used and normalised in origin pro 2017 software on a scale from 0 to 1. The Raman spectra were collected by Cristina Zorrilla Cangas from the Laboratory of Advanced Materials of the Institute of Physics of UNAM.

The Raman spectra displayed in Chapter 5 were recorded at an excitation wavelength of 785 nm on using a 50x long working distance objective on a BX-51 microscope. Excitation was provided by an ONDAX LM-785 laser (75 mW at source), which was passed through a laser line clean up filter (Semrock LL01-785), a $\frac{1}{2}\lambda$ retarder and polarising beamsplitter to control power and then through a second $\frac{1}{2}\lambda$ retarder to control polarisation. The spectra were the sum of 60 scans acquired with typical acquisition of 0.5 to 1 s. The measurements were carried out by Dr Wesley Browne from the Molecular Inorganic Chemistry Department of the Stratingh Institute of Chemistry of RUG.

A Thermo-Nicolet Almega Dispersive Raman spectrometer operating with a laser wavelength of λ =532 nm was employed for the spectra obtained in Chapter 7. Each spectrum was the sum of the 5 scans and silicon was used as reference and calibration. The spectra were acquired by the author of the research at Spectroscopic Characterization University Laboratory of Institute of Applied Sciences and Technology (ICAT by its acronym in Spanish) of UNAM.

All samples were measured in powder form, placed on glass microscope slides.

2.2.3. UV-visible spectroscopy

UV-Vis spectroscopy can be used to measure which wavelengths of ultra violet or visible light that are absorbed by or transmitted through a sample in comparison to a reference or blank sample. [6] The technique can be used both quantitatively and qualitatively. Since the electronic excitations giving rise to absorption depend on the sample's composition, UV-Vis spectroscopy

can potentially provide information on what is in the sample and in what concentration.[6] In this PhD project, UV-vis spectroscopy was used to identify the bands characteristic of commercial phthalocyanines, of phthalocyanines synthesised in this research and of those found in the functionalised carbon nanotube samples. It is known that phthalocyanines and their complexes absorb light in the blue-green region of the visible spectrum (see Chapter 1).

UV-vis spectra shown in Chapter 3 and 5 were measured in two aprotic polar solvents with high boiling points, 153°C for N, N-dimethylformamide (DMF, 99.8% purity) and 189 °C for dimethyl sulfoxide (DMSO, 99.9%) in the range of λ=300-800 nm using a Cary 60 UV-vis spectrophotometer. Solutions were prepared with 1 mg of the product in 2 mL of the solvent. Since these were saturated solutions, a dilution was prepared from aliquots of 1 mL in 1 mL of each solvent. For the spectra shown in Chapter 3 only DMF was employed.

2.2.4. X-ray photoelectron spectroscopy

X-ray photoelectron spectroscopy (XPS) is a surface sensitive analytical technique, in which X-rays bombard the surface of a material and the kinetic energy of the emitted electrons is measured. The two major characteristics of this technique that make it powerful as an analytical method are its surface sensitivity and its ability to reveal chemical state information for the elements in the probed volume. XPS can detect all elements except for hydrogen and helium, whose X-ray absorption cross sections are too small. Only the kinetic energy of photoelectrons, which have not suffered inelastic scattering more than once on their way from the photoemitting atom to the detector, can be used to deduce their binding energy. This implies that XPS probes to a depth of at most 10 nm.[7]

X-ray photoelectron spectroscopy analysis detailed in Chapter 3 was performed using a Surface Science SSX-100 ESCA instrument with a monochromatic Al Kα X-ray source (hν= 1486.6 eV). The pressure in the measurement chamber was maintained at $1x10^{-9}$ mbar during data acquisition. The electron take-off angle with respect to the surface normal was 37°. The samples were dispersed in isopropanol by sonication for 10 min, and two small drops of the suspension were deposited on a homemade 150 nm thick gold film supported on mica [8] and left to dry in air. All XPS spectra were analysed using a least-squares curve-fitting program Winspec (developed at LISE laboratory of the University of Namur, Belgium). Spectral analysis included a Shirley background subtraction and fitting with peak profiles taken as a convolution of Gaussian and Lorentzian functions. All bindings energies derived from deconvolution are reported ±0.1 eV.

The XPS measurements reported in Chapter 7 were performed using a Thermo K-Alpha XPS system using monochromated Al K-α X-rays (energy of 1486.6 eV). The X-ray source was operated at 12 kV accelerating voltage and 6 mA emission. An electron flood gun was employed for charge compensation. Peak fitting was performed using the Thermo Scientific Avantage XPS software package; it included a Shirley background subtraction and fitting with Gaussian-Lorentzian peaks profiles. The measurements were realised by Dr. Billy J. Murdoch from the RMIT Microscopy & Microanalysis Facility, College of Science, Engineering & Health, RMIT

University, Melbourne 3001, Victoria, Australia.

2.2.5. Electron paramagnetic resonance spectroscopy

Electron paramagnetic resonance (EPR), which is also called electron spin resonance (ESR), is a technique based on the absorption of electromagnetic radiation, in the microwave frequency region, by a paramagnetic sample placed in a magnetic field. The absorption takes place only for definite frequencies and magnetic field combinations that depend on the sample characteristics, which means that the absorption process is resonant. [9] The basic concepts of the technique are analogous to those of nuclear magnetic resonance spectroscopy, but it is the unpaired electron spins that are excited instead of the spins of atomic nuclei. ESR is particularly useful for studying metal complexes or organic radicals. [10]

The EPR spectra reported in Chapter 5 were recorded at room temperature on a Bruker EMXNano X-band spectrometer with optical access to the cavity operating at 9.65 GHz with a power of 50 dB, a gain 40 dB, a sweep width of 200 G, a sweep time 60 s and a modulation amplitude of 1.0 G. The free radical detection of the synthesised rare-earth double-decker phthalocyanines was carried out with approximately 2 mg, that were placed inside a glass EPR tube. The carbon nanotubes fictionalised with bisphthalocyanines were measured in a barium sulphate mixture at a ratio of 1:2 (CNT:$BaSO_4$). The measurements were carried out by Dr Wesley Browne from the Molecular Inorganic Chemistry Department of the Stratingh Institute of Chemistry of RUG.

2.2.6. Thermal analysis

Thermal analysis refers to a set of techniques in which the weight change of a sample is measured as a function of temperature or time in an atmosphere of nitrogen, helium, air, other gas, or in a vacuum. [11] Weight loss or gain can be due to decomposition, oxidation, or dehydration. [11] Among the most common methods are thermogravimetric analysis (TGA) and differential thermal analysis (DTA). [11] DTA relies upon the temperature difference between the sample and the reference material, to determine the presence of endothermic and exothermic processes. [11] For the projects described in this dissertation, thermal analysis was employed to determine the composition of materials and to explore their thermal stability at temperatures up to 1200° C. [11] DTA relies on the temperature difference between the sample and the reference material, to determine the presence of endothermic and exothermic processes. [11]

Thermogravimetric analysis and differential thermal analysis reported in Chapters 3 and 7 were performed using a NETZSCH STA 449C Jupiter instrument, under air flow of 30 $mLmin^{-1}$ and with a heating ramp of 10°C min^{-1} to 1000°C (Faculty of Science of UNAM).

The TGA/DTA curves displayed in Chapter 5 were acquired on a TA Instruments SDT 2960 setup. Samples of approximately 5 mg were heated in an air flow of 100 $mLmin^{-1}$ from 10 °C min^{-1} to 1000 °C (Zernike Institute for Advanced Materials of RUG).

2.2.7. Scanning electron microscopy

Scanning electron microscopy (SEM) is an electron microscopy technique capable of imaging the morphology of a sample surface with higher resolution than that of an optical microscope. [12] In SEM a highly energetic focused electron beam is scanned over the surface of the sample and the reflected electrons are collected (Fig.2. 3a). [13] The most common collected signals are secondary electrons (SE) from excited atoms. The amount of electrons collected depends on the presence of asperities at the surface and hence provides a morphological image.[12] Since the impinging electrons can also lose energy to core electrons of surface atoms and hence cause the emission of X-rays, scanning electron microscopes are frequently equipped with energy-dispersive X-ray (EDS or EDX) analysis to also perform elemental analysis of the scanned materials. [1]

For the samples described in Chapters 3 and 7, SEM was performed using a JEOL JSM-6510LV microscope operating at 20 kV, coupled to an EDS INCA Energy 250 Energy Dispersive X-ray Microanalysis System from Oxford Instruments. The measurements were performed by Dr. Victor Meza-Laguna from the Nuclear Science Institute of UNAM.

A FEI Nova NanoSEM 650 equipped with an Ametek EDAX-TLS EBSD system has been used operating at 20kV for the imaging and analysis of the samples of the study detailed in Chapter 5. Elemental analysis and phase mapping were also conducted using this microscope.

The samples were analysed in powder form, attached to carbon tape.

2.2.8. Transmission electron microscopy

Transmission electron microscopy (TEM) imaging is analogous to SEM in that both use an electron beam. However, in TEM the electron beam is incident onto a defined area of the specimen (Fig.2. 3b) and the electrons transmitted through the specimen are focused by lenses and collected by a parallel detector to form an image. TEM is used for higher magnification than SEM [1,13] and allows the analysis of morphology, size and size distribution of nanomaterials. [1]

Many new types of microscopic modes have been introduced, for example, high-resolution transmission electron microscopy (HRTEM), scanning transmission electron microscopy (STEM); moreover the signals caused by inelastically scattered electrons can be analysed in electron energy-loss spectroscopy (EELS) and energy-dispersive X-ray spectroscopy (EDX). [1]

For the HR-TEM analysis reported in Chapter 3, pristine and functionalised single-walled carbon nanotubes with cobalt and nickel phthalocyanine were suspended in isopropanol (99.5% purity) and subjected to 1-minute ultrasonic bath. Subsequently, the suspensions were placed in a glass capillary and dropwise deposited on Formvar/Carbon coated copper grids (Ted Pella, Inc). The grids were left to dry in air and analysed by a JEOL 4000EX microscope operating at 200 kV. The TEM images were collected by Iván Puente-Lee from the Faculty of Chemistry of UNAM.

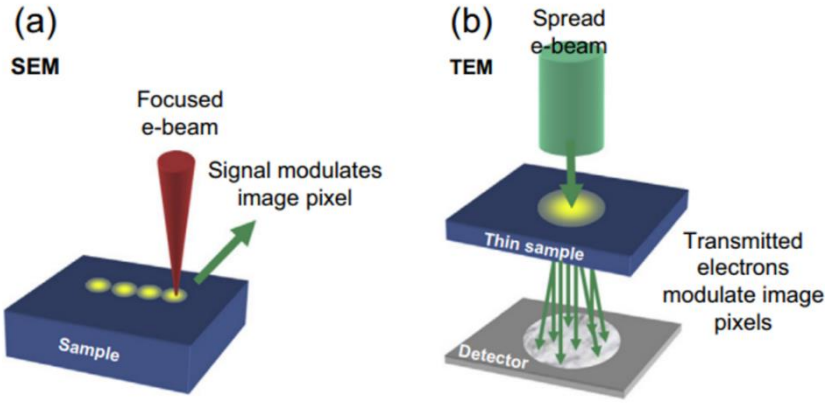

Fig.2. 3. Schematic of **(a)** scanning electron and **(b)** transmission electron microscopy imaging methodology. Reproduced with permission from reference 13, Copyright 2016, Elsevier.

Transmission electron microscopy imaging described in Chapter 5 was conducted on a Philips CM120 microscope equipped with a lanthanum hexaboride cathode and operated at an accelerating voltage of 120 kV. Images were acquired using a Gatan 4k CCD camera. Samples were prepared by depositing 5 μL of the SWCNT dispersion (either pristine or modified, ~ 1 mg in 1.5 mL HPLC-grade iPrOH) onto a 400-mesh copper grid with a carbon support film and adsorption for 30 seconds before blotting. The TEM images were analysed with Image J software's, using the software brightness and contrast correction tools to enhance the general quality of the snapshots. The images were obtained with the help of Dr. Théophile Pelras from Macromolecular Chemistry & New Polymereic Materials department of the Zernike Institute for Advanced Materials (RUG).

For HRTEM of the samples, the subject of Chapter 7, a JEOL JEM 2100F was employed at 200 kV voltage. The samples were deposited onto Formvar-covered copper grids from ultrasonicated ethanol suspensions. Images were collected at the Microscopy Australia facility at the Advanced Imaging Precinct, Australian National University. Scientific and technical assistance was provided by Dr. Billy J. Murdoch.

2.2.9. Elemental analysis

Elemental analysis, also known as carbon hydrogen nitrogen sulphur (CHNS) analysis, is a classical, destructive method to obtain information about the elemental composition of an unknown substance. A known amount of unknown substance is heated very quickly to a sufficiently high temperature to induce the instant and complete oxidation of samples in a process called "flash combustion", where every organic and inorganic substance is converted into a combustion product and the resulting combustion gas is then passed through the analyzer where a detector quantifies the elements present. [10,12]

The elemental analysis measurements illustrated in Chapter 5 were performed with a CHNS analyser vario MICRO cube elemental. About 10 mg of each sample was used, corresponding to the synthesised bisphthalocyanines. The data were obtained by Ing Hans van der Velde from the Stratingh Institute for Chemistry of RUG.

2.2.10. Dispersion test

Dispersion tests in water, isopropanol (99.5% purity), ethanol (99.5%) and toluene (99.8%) described in Chapters 3 and 5 were performed in order to observe physical changes of the material before and after functionalisation or deposition of phthalocyanines on the carbon nanotubes. Each test was carried out with 1 mg powders in 2 mL of solvent. To favour the dispersion process, the samples were subjected to ultrasound for 10 minutes and then the dispersion was evaluated with the help of photographs. The solvents were anhydrous and were purchased from Sigma-Aldrich.

2.3. Electrochemical measurements

2.3.1. Cell set up

Electrochemical measurements shown in Chapter 3 were carried out at room temperature using a three-electrode electrochemical cell made of Teflon. Platinum and Hg/HgO (Koslow Scientific) electrodes were used as counter and reference electrodes, respectively. Glassy carbon (GC) electrodes (Ø=5mm, Pine Research Instrumentation) were used as a working electrode after deposition of electrocatalysts. Before each measurement, the GC surface was polished with 30-micron alumina (Al_2O_3, Carveth Metallurgical Limited) and 3-micron alumina (Al_2O_3, Buehler) and washed in deionized water.

The catalyst ink was prepared by adding 3 mg of the single-walled carbon nanotubes functionalised with four 3*d* metal phthalocyanines (MnPc, FePc, CoPc and ZnPc in powder form) to 500 µL of deionized water, 50 µL of 5wt% Nafion® (Sigma-Aldrich) and 100 µL of isopropanol (99.9% purity, Fisher Scientific). The ink was sonicated in an ultrasonic bath (40 kHz Ultrasonic Bath, Fischer Scientific) for 10 min. Thereafter, aliquots of 10 µL of the dispersion were deposited onto the glassy carbon electrode surface and dried in an oven at 60 °C for 10 min. The electrolytes were aqueous solutions of 1M and 0.1M KOH (potassium hydroxide, ≥85%, Sigma-Aldrich). The presented current was normalized per geometric area.

2.3.2. Electrochemical testing

A BioLogic VSP potentiostat/galvanostat equipped with EC Lab software (BioLogic Science Instruments SAS) was used to conduct all electrochemical measurements (cyclic voltammetry (CV) and chronoamperometry (CA) experiments). Cyclic voltammograms were measured at a scan rate of 20 mV/s in the potential range of 0.8 and 0.1 V *vs* Hg/HgO. Chronoamperometric experiments were performed for 10 h at 0.74 V and 0.7 V *vs* Hg/HgO. All the potentials were measured with respect to a Hg/HgO reference electrode, but they were converted and reported *vs* the reversible hydrogen electrode (RHE) using equation 2.1 and 2.2 for data in 1 and 0.1 M KOH solutions, respectively. These calculations are further explained in reference 14.

$$E_{RHE} = E_{Hg/HgO} + 0.925 \quad (2.1)$$

$$E_{RHE} = E_{Hg/HgO} + 0.866 \quad (2.2)$$

Electrochemical measurements were performed at the Department of Chemical and Biological Engineering, Centre for Catalysis Research and Innovation (CCRI), University of Ottawa, Canada by Dr Natalia Alzate-Carvajal.

2.4. Computational methods

2.4.1. Molecular Mechanics: Hyperchem

Optimisation of the geometry of a single-walled carbon nanotube model, a free-base phthalocyanine (H_2Pc) and the hybrids with several H_2Pc molecules assembled on the nanotube surface (H_2Pc+SWCNT) was performed using HyperChem version 7.0 software (Hypercube Inc). The force field employed was MM+ with the Polak-Ribiere gradient algorithm and a RMS (root mean square) gradient of 0.001 kcal/Åmol.[15,16] The formation energies $\Delta E_{\mathrm{Pc+SWCNT}}$ (hereafter, simply ΔE) for the adsorption of the phthalocyanines molecules on the surface of a carbon nanotube is the difference between the absolute energy of the hybrids and the sum of the absolute energies of each component molecular species, see equation 2.3:

$$\Delta E_{\mathrm{Pc+SWCNT}} = E_{\mathrm{Pc+SWCNT}} - (E_{\mathrm{SWCNT}} + nE_{\mathrm{Pc}}) \quad (2.3)$$

where E_{i} is the corresponding absolute energy, E_{SWCNT} carbon nanotube energy, E_{Pc} ligand energy and n the number of phthalocyanines molecule participating in the adsorption or self-assembly model.

2.4.2. Density functional theory: Material Studio DMol³ software

All density functional theory calculations were carried out with the numerical-based module DMol³ within the Materials Studio 6.0 and 8.0 software package from Accelrys Inc. [17–20] The computational technique chosen was the general gradient approximation functional PBE in combination with a long-range dispersion correction developed by Grimme (PBE- D; also referred to as PBE-D2), due the need to account for dispersion interactions, which is very important in noncovalently bonded molecular systems. [21,22] Three double numerical basis sets were used (first of all, for the optimised geometry): DN, without polarization functions included (equivalent to 6–31G); DND, which adds a polarization *d*-function on all non-hydrogen atoms only (equivalent to 6–31G(d)); and DNP, which has a polarization *d*-function added on all non-H atoms, as well as a polarization *p*-function added on all hydrogen atoms (equivalent to 6–31G(d, p)). The convergence criteria for full geometry optimisation and calculations of the electronic parameters were an energy gradient of 10^{-4}, 20^{-5} and 10^{-5} Ha for DN, DND and DNP, respectively; a maximum force of 0.02, 0.004 and 0.002 Ha/Å correspondingly; a maximum displacement of 0.05 (DN) and 0.005 Å (DND and DNP), and a self-consistent field (SCF)

tolerance of 10^{-4} for DN, 10^{-5} for DND and 10^{-6} for DNP. The choice of the basis set depended on the system analysed.

Chapter 4 reports on the DFT calculations on hybrid systems of a MPc (M=Co and Ni) and a single-walled carbon nanotubes with a Stone Wales defect in different orientations, abbreviated as MPc+SWCNT_SW. Two nanotube models were examined, namely, armchair (ANT) and zigzag (ZNT). The same computational methodology was applied as in the previously reported analysis of MPc adsorbed on defect-free SWCNT models (MPc+SWCNT).[23] Therefore, the numerical DNP basis set was used. The calculations employed the 'all-electron' core treatment with Fermi orbital occupation (no thermal smearing). A global orbital cutoff was set to 4.7 and for open-shell systems containing cobalt, the calculations were spin unrestricted with maximum step size of 0.1 Å. In contrast, for closed-shell systems with nickel the latter was set to 0.02 Å and the calculations were spin-restricted.

The formation energies for SW defects were calculated as

$$\Delta E_{\mathrm{SW}} = E_{\mathrm{def}} - E_{\mathrm{Perf}} \tag{2.4}$$

where E_{def} and E_{Perf} are the total energies of nanotube with and without defect, respectively.[10,11]

The approach taken has been successfully applied to describe different types of bonding (covalent and noncovalent) between tetraazamacrocyclic (including porphyrins and Pcs) and many other compounds with fullerene, graphene, graphene oxide, nanodiamond and carbon nanotube models. [16,26–31] Consequently, in the study detailed in Chapter 7, this calculation method was applied to suggest possible initial steps of the oxidative pyrolysis H_2Pc leading to the formation of nanofibers. The results described in Chapter 4 and 7 were obtained in Material Studio 6.0.

For the calculations described in Chapter 6, changes were made to the calculation method used for the study detailed in Chapter 4. The optimisation of the hybrid with yttrium double-decker phthalocyanine was performed with the same ANT and ZNT nanotube models used for the hybrid modelling with *3d* metal phthalocyanines and in Material Studio 6.0. Three basis sets (DN, DND and DNP) were implemented to analyse the influence of the basis size on the structural and electronic characteristics of both the hybrid and each isolated component. Another important adjustable parameter was the global orbital cut-off (or real space cutoff). The global orbital cutoff was applied to the generation of the numerical basis sets to limit the range of the numerical integrations and reduce the computational cost. It is justified by the fact that the charge density decreases quickly as the distance from an atomic nucleus increases. [32] The real space cutoff values used in this study were 4.2, 4.8 and 5.6 Å for DN, DND and DNP basis sets, respectively, as defined by the presence of Y atom (electron configuration $[Kr]4d^{1}5s^{2}$). The calculation quality corresponding to the use of DN, DND and DNP basis set is referred to as 'coarse', 'medium' and 'fine'. All the calculations were spin-unrestricted, the core treatment was all-electron with Fermi orbital occupation and the maximum step size allowed was 0.3 Å.

The modelling of the hybrids of lanthanum, gadolinium, and lutetium bispthalocyanines and carbon nanotubes, was carried out using Material Studio 8.0 software. Considering a recently published study by our group on the optimization of the geometry of lanthanide bispthalocyanines [33] and the possible self-consistent field convergence problems due to the presence of *4f*-electrons, DFT semi-core pseudopotentials (DSPP; especially designed to use within the DMol^3 module) were used in all calculations. This approach includes relativistic effects, spin-orbit coupling and the double numerical basis set DN, without polarization functions included (equivalent to 6-31G). A global orbital cutoff set to 4.3 Å (defined by the presence of a heavy Ln atom-default), 'coarse' quality and maximum step size of 0.1 Å were the settings employed for full geometry optimization and for the calculations of electronic parameters. As a tool to avoid (SCF) convergence drawbacks, thermal smearing was used with a value of 0.0001Ha.

The formation energies $\Delta E_{\mathrm{Pc+SWCNT}}$ were calculated with equation 2.3.

2.5. References

(1) Sharma, S. K. *Handbook of Materials Characterization*; 2018.
(2) Stuart, B. H. *Infrared Spectroscopy: Fundamentals and Applications*; 2005.
(3) Scientific, T. F. Introduction to ft-ir sample handling how does it work? 2013.
(4) Larkin, P. J. *IR and Raman Spectroscopy: Principles and Spectral Interpretation*; 2018; Vol. 2.
(5) Ember, K. J. I.; Hoeve, M. A.; Mcaughtrie, S. L.; Bergholt, M. S.; Dwyer, B. J.; Stevens, M. M.; Faulds, K.; Forbes, S. J.; Campbell, C. J. Raman spectroscopy and regenerative medicine: a review.
(6) Edwards, A. A.; Alexander, B. D. *UV-Visible Absorption Spectroscopy, Organic Applications*, 3rd ed.; Elsevier Ltd., 2016.
(7) Stevie, F. A.; Donley, C. L. Introduction to X-ray photoelectron spectroscopy. *J. Vac. Sci. Technol. A* 2020, *38* (6), 063204.
(8) Ivashenko, O.; Logtenberg, H.; Areephong, J.; Coleman, A. C.; Wesenhagen, P. V; Geertsema, E. M.; Heureux, N.; Feringa, B. L.; Rudolf, P.; Browne, W. R. Remarkable stability of high energy conformers in self-assembled monolayers of a bistable electro-and photoswitchable overcrowded alkene. *J. Phys. Chem. C* 2011, *115*, 22965–22975.
(9) Brustolon, M.; Giamello, E. *Electron Paramagnetic Resonance : A Practitioner's Toolkit*; 2009.
(10) Speight, J. G. Sources and types of inorganic pollutants. In *Environmental Inorganic Chemistry for Engineers*; 2017; pp 231–282.
(11) Abraham, J.; Mohammed, A. P.; Kumar, M. P. A.; George, S. C.; Thomas, S. Thermoanalytical techniques of nanomaterials. In *Characterization of Nanomaterials: Advances and Key Technologies*; Elsevier Ltd., 2018; pp 213–236.
(12) Bagheri, H.; Rezvani, O.; Zeinali, S.; Asgari, S.; Aqda, T. G.; Manshaei, F. Electrospun nanofibers. In *Solid-Phase Extraction*; 2019; pp 311–339.
(13) Inkson, B. J. Scanning electron microscopy (SEM) and transmission electron microscopy (TEM) for materials characterization. In *Materials Characterization Using Nondestructive Evaluation (NDE) Methods*; Elsevier Ltd, 2016; pp 17–43.
(14) Cossar, E.; Oyarce Barnett, A.; Seland, F.; Baranova, E. A. The performance of nickel and nickel-iron catalysts evaluated as anodes in anion exchange membrane water electrolysis.
(15) Bassiouk, M.; Álvarez-Zauco, E.; Basiuk, V. A. Self-assemblies of meso -tetraphenylporphine ligand on surfaces of highly oriented pyrolytic graphite and single-walled carbon nanotubes : insights from scanning tunneling microscopy and molecular modeling. 2011, *11* (6), 5457–5468.
(16) Basiuk, V. A.; Bassiouk, M. Nanoassembly of meso-tetraphenylporphines on surfaces of carbon materials: initial steps as studied by molecular mechanics and scanning tunneling microscopy. *J. Nanosci. Nanotechnol.* 2008, *8*, 259–267.
(17) Delley, B. An all-electron numerical method for solving the local density functional for polyatomic molecules. 1990, *92*, 508–517.
(18) Delley, B. Fast calculation of electrostatics in crystals and large molecules. *J. Phys. Chem.* 1996, *100* (15),

6107–6110.
(19) Delley, B. From molecules to solids with the DMOL^3 approach. *J. Chem. Phys.* 2000, *113* (18), 7756–7764.
(20) Delley, B.; Ellis, D. E.; Freeman, A. J.; Baerends, E. J.; Post, D. Binding energy and electronic structure of small copper particles. *Phys. Rev. B* 1983, *27* (4), 2132–2144.
(21) Perdew, J. P.; Burke, K.; Ernzerhof, M. Generalized gradient approximation made simple. *Phys. Rev. Lett.* 1996, *77*, 3865–3868.
(22) Grimme, S. Semiempirical gga - type density functional constructed with a long-range dispersion correction. *J. Comput. Chem.* 2006, *27*, 1787–1799.
(23) Basiuk, E. V.; Huerta, L.; Basiuk, V. A. Noncovalent bonding of *3d* metal(II) phthalocyanines with single-walled carbon nanotubes: a combined DFT and XPS study. *Appl. Surf. Sci.* 2019, *470*, 622–630.
(24) Kabir, M.; Van Vliet, K. J. Kinetics of topological Stone-Wales defect formation in single-walled carbon nanotubes. *J. Phys. Chem. C* 2016, *120* (3), 1989–1993.
(25) You, A.; Be, M. A. Y.; In, I. Formation energy of Stone – Wales defects in carbon nanotubes. 2004, *1222* (August 2003), 1–4.
(26) Bassiouk, M.; Álvarez-Zauco, E.; Basiuk, V. A. Adsorption of *meso*-tetraphenylporphines on thin films of C_{60} fullerene. *Appl. Surf. Sci.* 2013, *275*, 374–383.
(27) Basiuk, V. A.; Rybak-Akimova, E. V.; Basiuk, E. V. Graphene oxide and nanodiamond: same carboxylic groups, different complexation properties. *RSC Adv.* 2017, *7* (28), 17442–17450.
(28) Matsuda, Y.; Tahir-Kheli, J.; Goddard, W. A. Definitive band gaps for single-wall carbon nanotubes. *J. Phys. Chem. Lett.* 2010, *1* (19), 2946–2950.
(29) Basiuk, V. A.; Basiuk, E. V. Complexation of free-base and 3*d* transition metal (II) phthalocyanines with fullerene C_{60} : a dispersion-corrected dft study. *Fullerenes, Nanotub. Carbon Nanostructures* 2017, *25* (7), 410–416.
(30) Basiuk, V. A.; Tahuilan-Anguiano, D. E. Complexation of free-base and *3d* transition metal(II) phthalocyanines with endohedral fullerene$Sc_3N@C_{80}$. *Chem. Phys. Lett.* 2019, *722* (March), 146–152.
(31) Chávez-Colorado, E.; Basiuk, V. A. Noncovalent interactions of free-base phthalocyanine with elongated fullerenes as carbon nanotube models. *Struct. Chem.* 2017, *28*, 1765–1773.
(32) Luo, Y.; Yin, S.; Lai, W.; Wang, Y. Effects of global orbital cutoff value and numerical basis set size on accuracies of theoretical atomization energies. *Theor. Chem. Acc.* 2014, *133* (11).
(33) Martínez-Flores, C.; Bolívar-Pineda, L. M.; Basiuk, V. A. Lanthanide bisphthalocyanine single-molecule magnets : a DFT survey of their geometries and electronic properties from lanthanum to lutetium. *Mater. Chem. Phys.* 2022, *287*, 126271.

3

Chapter 3

Carbon nanotubes and monophthalocyanines hybrids as electrocatalysts of the oxygen evolution reaction

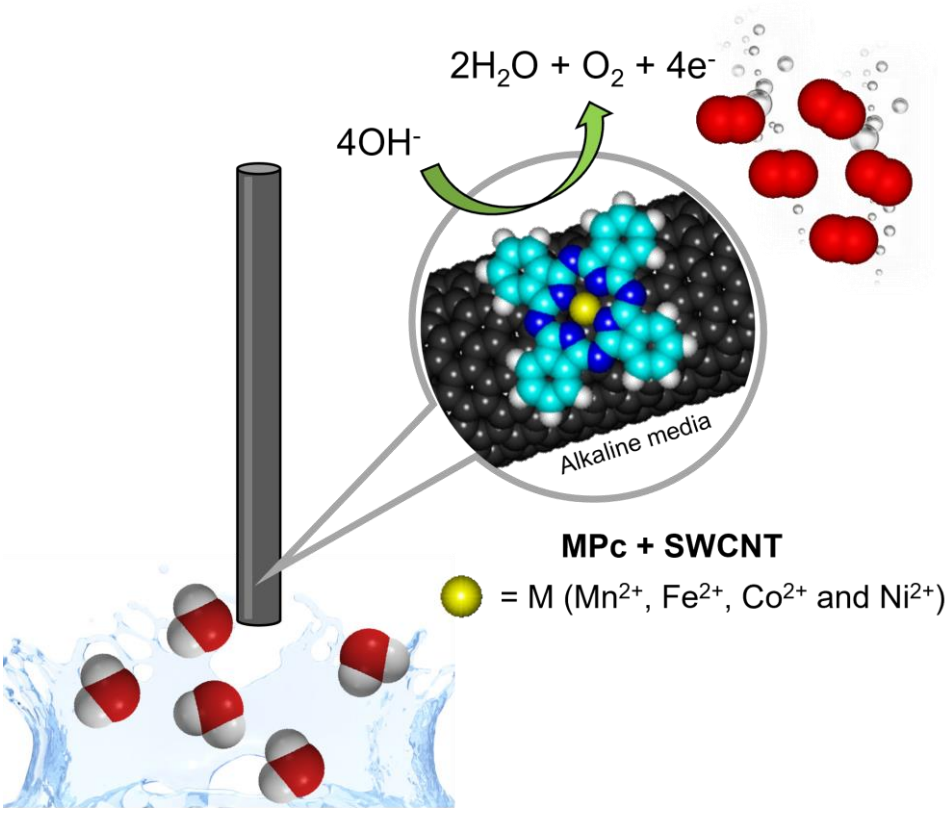

Published as
Natalia Alzate-Carvajal, Lina M. Bolivar-Pineda, Victor Meza-Laguna, Vladimir A. Basiuk, Elena V. Basiuk, and Elena A. Baranova. ChemElectroChem. 2020, 7, 428-436

Abstract

Non-covalent functionalisation of carbon nanotubes with phthalocyanines is usually carried out with substituted phthalocyanines as they have better solubility in conventional solvents than unsubstituted phthalocyanines, the latter having better thermal stability. Taking advantage of this feature, here, we report the formation of non-covalent hybrids with three unsubstituted transition metal phthalocyanines (iron, cobalt and nickel) by sublimation at 450°C. The adsorption of the manganese phthalocyanines was realised by refluxing in butanol. Dispersion tests and scanning electronic microscopy images suggest that the functionalisation generates higher agglomeration compared to pristine nanotubes due to the additional π-π interaction between neighbouring nanotubes and the adsorbed macrocycle. Electrochemical evaluation of modified nanotubes in the oxygen evolution reaction in alkaline medium show better performance than pristine nanotubes. The excellent electrocatalytic activity of hybrids, especially with nickel and cobalt phthalocyanines, and the straightforward method of their synthesis opens the possibility of exploring these materials for applications in anion exchange membranes for water electrolysis.

3.1. Introduction

One of the desirable characteristics of covalent or non-covalent Pc+CNTs hybrids is a homogeneous distribution of Pcs molecules on the nanotube surface. However, unsubstituted Pcs have a low solubility (approximately 10^{-4}–10^{-7} mol/kg). [1,2] This challenge has mainly been addressed using more soluble substituted phthalocyanines. The disadvantage of this approach is the high economic cost and consequently their availability is limited compared to their unsubstituted counterparts, and their thermal stability depends on the nature of the substituent. [3] Another option is *the in-situ* synthesis of Pcs in the presence of nanotubes and although an interaction between the macrocycle and the nanotube does occur, a separate Pcs phase is also formed. [4,5] Both strategies involve conventional routes that are usually carried out using organic solvents as the medium, followed by additional procedures such as ultrasonication, centrifugation, washing and drying. Such multi-step processes increases the cost of catalysis and produce a large amount of chemical waste, which is not favourable from an environmental point of view (green chemistry principles)

One alternative that has been explored by Basiuk *et al* (2018), [6] which was developed in this chapter for the non-covalent functionalisation of single-walled carbon nanotubes with iron, cobalt and nickel monophthalocyanines is by sublimation or gas-phase under moderate vacuum conditions. It is a one-step method that is solvent free and has a short adsorption time of the Pcs over the nanomaterial. This process takes advantage of the ability of unsubstituted Pcs to sublimate without decomposition at high temperatures (450 °C) and moderate vacuum (roughly of 10^{-2} Torr). [7]

On the other hand, electrochemical water splitting has become one of the sustainable methodologies for obtaining hydrogen and oxygen. Water splitting (equation 3.1) is constituted of two half reactions, hydrogen evolution reaction (HER), which takes place at the cathode and oxygen evolution reaction (OER) at the anode, and it can be carried out in acidic and alkaline media (equations 3.2 and 3.3). [8,9] Although the alkaline water electrolysis is a well-established technology and it has been performed at an industrial scale for many years, the recent, tremendous progress in the development of anion exchange membrane (AEM) opened up the possibility of developing water electrolysers. [10,11] However, OER has a major bottleneck in the water electrolysis process. [10,11] The evolution of O_2 requires the transfer of four electrons, and the favourable kinetics takes place in multi-step reactions with single electron transfer at each step (see equations from 3.4 to 3.7). [9,12] The accumulation of energy in each step triggers a slowing of the OER kinetics, resulting in a large overpotential. Therefore, a highly active OER electrocatalyst is required to overcome the energy barrier. [9,12]

$$2H_2O + Energy \rightarrow O_2 + 2H_2 \quad (3.1)$$

Alkaline conditions

Cathode reaction $$4H_2O + 4e^- \rightarrow 2H_2 + 4OH^- \quad (3.2)$$

Anode reaction $$4OH^- \rightarrow O_2 + 4e^- + 2H_2O \quad (3.3)$$

The proposed OER mechanism is the following

$$OH + * \rightarrow OH* + e^- \quad (3.4)$$
$$OH* + OH^- \rightarrow O* + H_2O + e^- \quad (3.5)$$
$$O* + OH^- \rightarrow OOH* + e^- \quad (3.6)$$
$$OOH* + OH^- \rightarrow * + O_2 + H_2O + e^- \quad (3.7)$$

where * stands for an active site on the surface and *O, *OH and *OOH are adsorbed intermediates. [9–12]

Precious metal catalysts such as iridium and ruthenium and their respective oxides (IrO_2, and RuO_2) are widely used in the OER process to reduce energy consumption and improve energy conversion efficiency. [13,14] Nevertheless, these catalysts are scarce, expensive and lack durability, which makes them impractical for large-scale applications. Alkaline media opens the possibility to apply catalysts that are based on abundant materials that do not compromise their activity towards OER. Compounds containing $3d$ transition metals such as oxides and phosphides of Co, Ni, Mn and Fe have been widely studied as alternative catalysts.[8,15–17] In this sense, MPc+SWCNT hybrids obtained by sublimation of the MPcs were proposed as electrocatalysts for oxygen evolution reaction considering that: metal monophthalocyanines are cheaper than precious metal catalysts; commercially available; that their self-assembly on high surface area carbon nanotubes can decrease MPc aggregation and consequently increase the active sites for catalytic processes; and finally that π-π interactions facilitate electron transfer and enhances system stability.[18,19]

The work described in this section focuses on the characterisation of the material obtained in sublimation experiments by a combination of analytical techniques, followed by electrochemical evaluation towards OER in alkaline medium using two concentrations of the electrolyte 0.1 M and 1 M KOH. The catalytic behaviour was compared with bulk Ni and Ir black electrodes.

3.2. Experimental section

3.2.1. Materials

Pristine SWCNT (>95% purity) synthesized by CVD process were purchased from NanoLab, Inc. According to the company's specifications, the nanotubes are approximately 1.5 nm in diameter and 1–5 μm in length. The metallophthalocyanines MnPc (95 %), NiPc (85%), FePc (90%) and CoPc (97%) were obtained from Sigma-Aldrich. NiPc was additionally purified by sublimation.

3.2.2. Functionalization

The non-covalent functionalization of SWCNT with MPc (M= Fe^{2+}, Co^{2+} and Ni^{2+}) by sublimation deposition was carried out using a tubular reactor made of quartz for all the experiments, its dimensions were 25 mm in diameter and 60 cm in length. A Barnstead

Thermolyne 21100 tube furnace capable of providing stable controllable temperatures of up to 1200°C was employed as a heating device. Fig.3. 1 shows the experimental setup, which was described previously for the sublimation of free-base phthalocyanine and its metal complexes with $Co^{2+,}$ Ni^{2+}, Zn^{2+} and Cu^{2+} in the presence of single-walled carbon nanotubes. [6,20]

Usually, single-walled CNTs storage for a long time results in the accumulation of a considerable amount of impurities adsorbed from the environment. In order to remove them, prior to the functionalization experiments, SWCNT were outgassed in vacuum of ca. 10^{-2} Torr for 1 hour at 450°C using the same experimental setup above. The conditions employed were the same for all sublimation deposition experiments. As the weight loss due to the outgassing can be of the order of 10–12%, the purified single-walled CNTs were immediately weighted and thoroughly mixed with phthalocyanines at a weight ratio of 2:1 (for example, 200 mg of SWCNT and 100 mg of 3*d* metal phthalocyanine). In the case of cobalt, nickel and iron phthalocyanines, the resulting mixture was slightly compressed into pellets using a hydraulic press, and the gas-phase deposition experiments were performed by heating the phthalocyanines and nanotubes mixture under constant evacuation at about 10^{-2} Torr at 450°C for 2 hours (counted from the moment once the temperature stabilized). This temperature was found as optimal from our previous experiments of non-covalent functionalisation of the single-walled carbon nanotube with different metal phthalocyanines. [6] The increase in weight of the SWCNT after deposition of the phthalocyanines, served as the most direct estimation of MPc content in the resulting hybrids with 20.2% of FePc, 26.3% of CoPc and 28.4% of NiPc in the single-walled CNTs mixture. The hybrids synthesised in this way are referred to as: FePc+SWCNT, CoPc+SWCNT and NiPc+SWCNT, respectively.

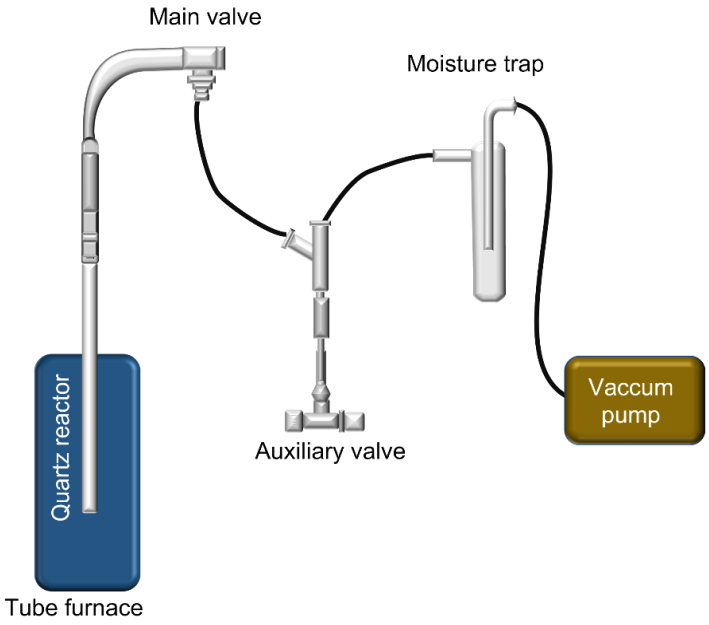

Fig.3. 1. Vacumm system used for gas-phase functionalization experiments of MnPc, FePc and NiPc on the surface of single-walled carbon nanotubes.

The nanotubes were also functionalised with manganese phthalocyanines. Due to the lower thermal stability of manganese phthalocyanine (245°C in nitrogen atmosphere) [21] and the impossibility to use a sublimation procedure for its deposition, the preparation of MnPc+SWCNT was accomplished by reflux in butanol (10 mL) of 200 mg of SWCNT and 100 mg of MnPc for 7 hours at 117°C. The resulting solid was filtered and dried in vacuum at 100°C. A MnPc content of 27.3%. was estimated from an increase in weight of the nanotubes after phthalocyanine deposition.

3.3. Results and discussion

3.3.1. Characterization of MPc+SWCNT hybrids

Comparison of the infrared spectra for phthalocyanine complexes with divalent cations (Mn^{2+}, Fe^{2+}, Co^{+2} and Ni^{2+}), pristine single-walled CNTs and MPc+SWCNT hybrids is presented Fig.3. 2a. One should note that, as is usually observed,[6] the overall quality of FTIR spectra for CNT-based samples is rather low due to a low signal-to-noise ratio, resulting from the heterogeneity of bundled nanotube samples and a strong absorption of infrared radiation. An evident exception is the spectrum of the carbon nanotubes with manganese phthalocyanines hybrids, which can be attributed to some single-walled carbon nanotubes reordering during liquid-phase deposition of MnPc.

The spectral features common for neat metal monophthalocyanines complexes [21–24] comprise the bands at 719 and 773 cm^{-1} due to C-H out-of plane deformation vibrations, at 871 cm^{-1}due to ligand in-plane vibrations, at 902 cm^{-1}due to metal-ligand vibrations, at 1076 cm^{-1} due to C-H in-plane deformation, at 1118 cm^{-1} due to C-H in-plane bending, at 1160 cm^{-1} due to C-N in-plane bending, at 1288 cm^{-1} due to C-N stretching in isoindole moieties, at 1330 and 1417 cm^{-1} due to C-C stretching in isoindole, at 1463 cm^{-1} due to C-H in-plane bending, at 1500 cm^{-1} due to C-N stretching, and at 1604 cm^{-1} due to C-C macrocyclic ring deformation. [21–24] Most of these features are clearly seen in the spectrum of MnPc+SWCNT, and some of them in particular, the bands at 719, 1076, 1118, 1160, 1288 and 1330 cm^{-1}, can be distinguished in the case of NiPc+SWCNT.

The Raman spectra obtained for pristine single-walled CNTs and MPc+SWCNT hybrids are shown in Fig.3. 2b. The characteristic features of the single-walled CNTs can be identified in each spectrum: the radial breathing mode (RBM), disorder-induced D band, as well as graphene- related G and G' bands.[25] The presence of D band reveals the presence of defects (sp^3-hybridized carbon atoms) in the nanotube sidewalls, which is common for both the single-walled CNTs and multi-walled CNTs fabricated by CVD. Its frequency is rather constant, being 1351 cm^{-1} in the spectrum of the pristine SWCNT and 1350–1352 cm^{-1} in the case of the MPc+SWCNT samples. At the same time, the D band intensity, and correspondingly the ID/IG ratio, as a measure of the amount of disorder induced by defects in the CNTs, notably (in some cases dramatically) decreases after phthalocyanine deposition. In particular, while the ID/IG ratio for pristine single-walled CNTs is 0.21, it drops to 0.09 for MnPc+SWCNT, 0.12 for FePc+SWCNT, 0.08 for CoPc+SWCNT and 0.13 for NiPc+SWCNT. This observation suggests

that the high-temperature sublimation deposition of phthalocyanine complexes produces some (catalytic) effect, which helps to reduce single-walled CNTs defects by means of rearrangement of sp^3 hybridized carbon atoms into graphene-derived hexagonal lattice.[26, 27]

The G band (tangential mode) is located at 1590 $cm^{-1}$for the pristine single-walled CNTs and at 1586–1591 cm^{-1} for the MPc+SWCNT hybrids, thus exhibiting slightly broader variability. The composite nature of RBM signals can be attributed to the presence of SWCNTs of different diameters in the pristine material employed. [28] The manufacturer-specified diameter of ca. 1.5 nm is just an average value. The radial breathing frequency range observed for all samples is observed at 162–275 cm^{-1}. One more graphene-related G' band is found in the range of 2663–2672 cm^{-1}.

In contrast to the hybrids of metal phthalocyanines with single-walled nanotubes and pure MPcs spectra, some of the pure macrocycle vibrations are only visible at low intensity only for the NiPc+SWCNT hybrid (Fig.3. 3). The dominance of the nanotube signals in the hybrid spectra can be attributed to the low concentration of the MPcs on the nanomaterial or by the nature of the macrocycle. Fig.3. 3 displays the comparison of NiPc+SWCNT and pure NiPc, where the intensity of the phthalocyanines (from 0 to 80 arb.units) is much lower than that of the functionalised nanotubes (from 0 to 3500 arb.units).

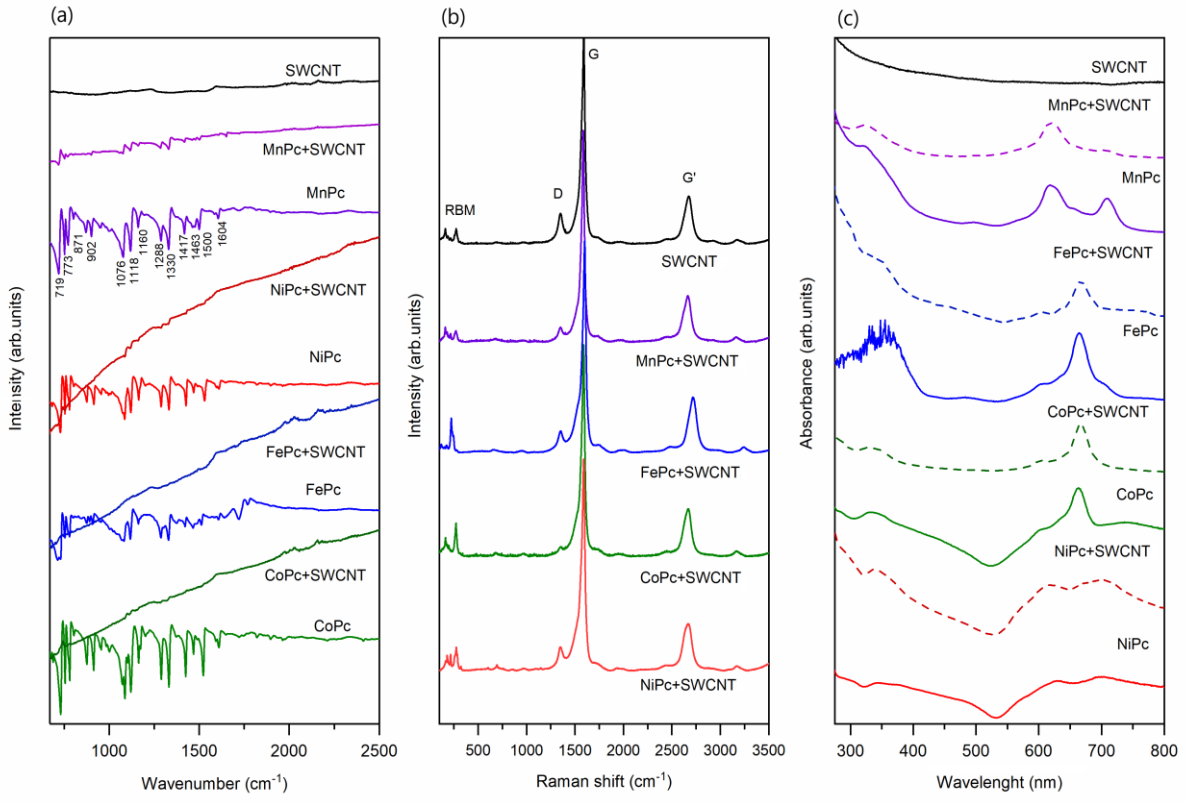

Fig.3. 2. (a) Infrared (b) Raman and (c) UV–vis spectra of MPc+SWCNT hybrids obtained in comparison with the spectra of pristinel single-walled carbon nanotubes and metal phthalocyanines acquired under the same conditions. The UV-visible spectra were measured in dimetilformamide.

In the spectra obtained from the dispersions in dimethylformamide, the electronic absorption spectra of the four hybrids of metallic phthalocyanines and single-walled carbon nanotubes (Fig.3. 2) are also dominated by a strong background due to the carbon nanotubes. Despite this, the spectra of the hybrids show two characteristic signals typical of phthalocyanines, the Soret or Q-band at about 330 nm and the B-band, which presents the maximum absorption in the visible region between 600 and 700 nm. [29–31] Even though the UV-vis spectra were recorded for pure crystalline phthalocyanines under the same conditions as the hybrids, a detailed comparison cannot be made because the electronic absorption is not an intrinsic property, that is, it is highly dependent on the particular state in which the phthalocyanine molecules are found (gas phase, film thickness, different crystals, polymorphs, etc.) and their chemical environment.[6,32]

The comparative results of the dispersion test in water, isopropanol and toluene of the pristine and functionalised carbon nanotubes are shown in Fig.3. 4. The pristine nanotubes in water have low dispersibility, the aggregates have precipitated after 1 hour, while the hybrids with FePc, CoPc and NiPc, no change was observed although they were subjected to ultrasound for 10 minutes. In contrast, the nanotubes with manganese phthalocyanine displayed higher dispersibility, as evidenced by the suspension of the solid being for more than 24 hours.

A slightly polar solvent such as isopropanol improved dispersion substantially in all samples tested, which indicates a slight change in polarity of the nanotubes. Nevertheless, the MPc+SWCNT hybrids show better dispersion than the pristine carbon nanotubes and they also acquire a bluish-green colour depending on the metal monophthalocyanine. After 1 hour, the samples have mostly precipitated.

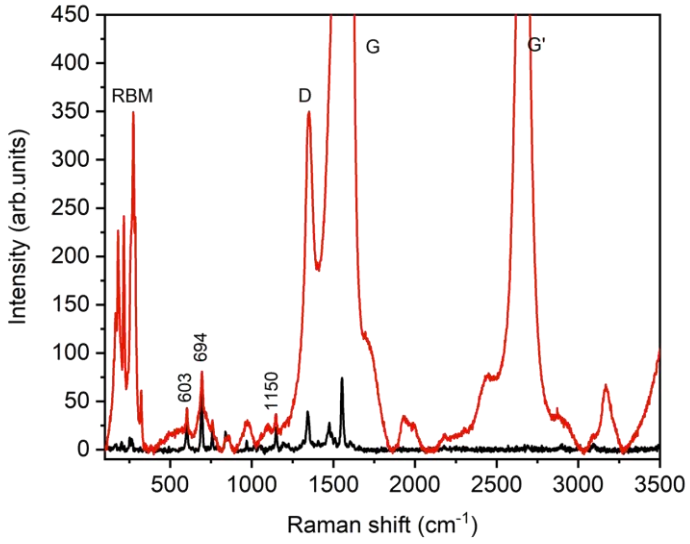

Fig.3. 3. Raman spectra of pristine nickel phthalocyanine (black line) and of the single-walled carbon nanotube after NiPc sublimation (NiPc+SWCNT hybrid; red line).

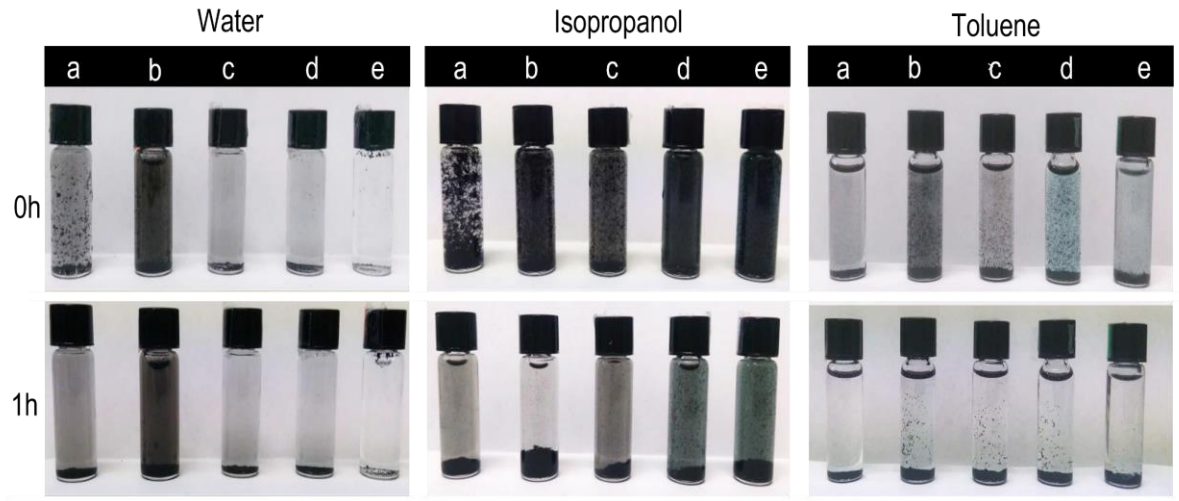

Fig.3. 4. Comparative dispersibility test (1 mg of each sample per 2 mL of solvent) in water and isopropanol for (a) single-walled carbon nanotubes before and after functionalization with (b) MnPc, (c) FePc, (d) CoPc and (e) NiPc. Images were taken at elapsed time of 0, 1 and 12 h after ultrasonic bath treatment for 10 min.

To evaluate the influence of solvent polarity on pristine nanotubes and hybrids, a dispersion test in toluene, a non-polar, high boiling point (110 °C) solvent, was proposed, which showed a slight increase in hybrid dispersion, and like isopropanol, the solid started to precipitate after ultrasound treatment. However, the hybrids disperse better in isopropanol.

As a whole, no dramatic changes in the nanotube morphology after phthalocyanine deposition were observed by SEM. In all cases (Fig.3. 5), we observed the single-walled carbon nanotubes as typical bundles. The fact that no evident presence of metal phthalocyanines crystallites can be detected by SEM in any of the samples suggests the formation of a relatively homogeneous layer (probably a monolayer) of adsorbed phthalocyanine molecules on nanotube sidewalls. A similar behaviour was observed previously for both free-base phthalocyanine H_2Pc [22] and its transition metal phthalocyanines. [6] The morphology and size of the MPc crystals are different from those of nanotubes and can be distinguished in the SEM images from pristine metal phthalocyanines (Fig.3. 5). On the other hand, in all of the MPc+SWCNT hybrids, nanotube bundles look more 'glued' together as compared to pristine nanotubes, that is, non-covalent functionalisation with MPc does not produces a debundling effect (at least in the solid phase). This is caused by the additional agglomeration of the metal monophthalocyanines, due to π-π interaction between neighbouring phthalocyanines molecules and nanotubes. The presence of other materials in the samples was not detected.

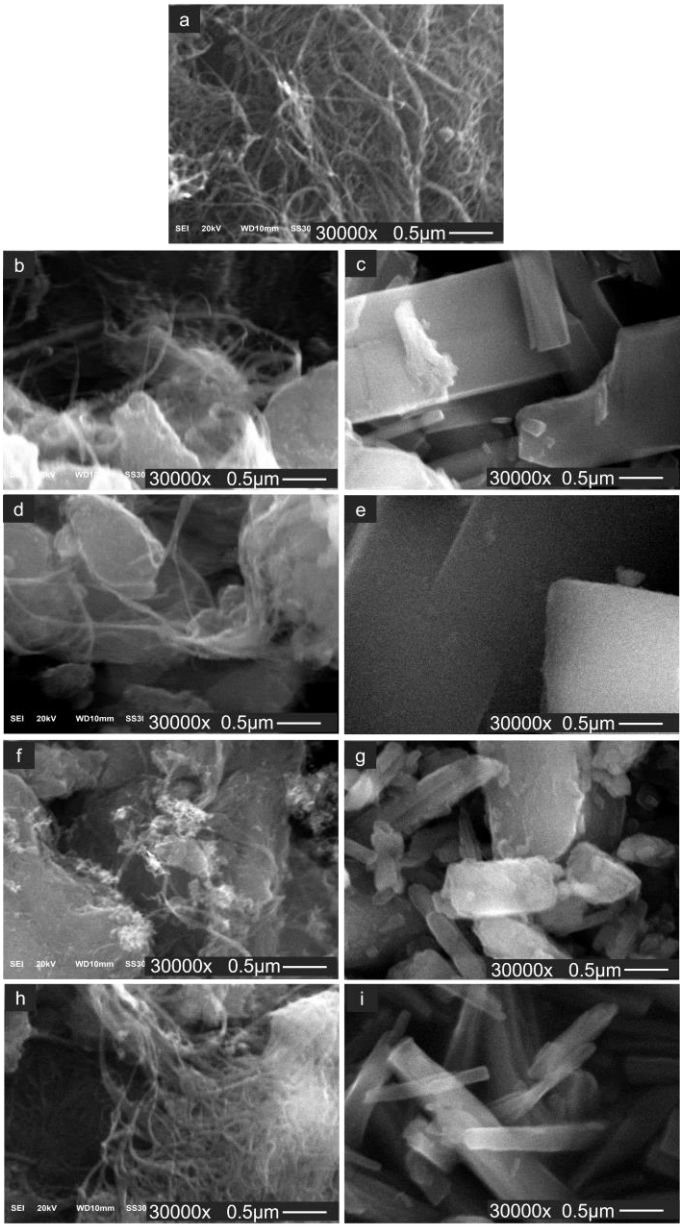

Fig.3. 5. SEM images of (a) pristine and (b,d,f,h) non-covalently functionalised: MnPc+SWCNT, FePc+SWCNT, CoPc+SWCNT and NiPc+SWCNT and (c, e, g, i) crystals of the metal phthalocyanines.

The results of TEM observations confirm the general homogeneous nature of the single-walled CNTs functionalised with the metal phthalocyanines. One can see that even though pristine single-walled carbon nanotube have numerous defects throughout their sidewalls (which is common for carbon nanotubes obtained by the CVD process), the tubular morphology is easily discernible (Fig.3. 6a). However, after metal phthalocyanines deposition onto the SWCNT, the latter becomes totally or almost totally obscured, and instead, nanotube bundles appear as amorphous structures (exemplified for CoPc+SWCNT and NiPc+SWCNT in Fig.3. 6b,c). This is a typical effect in both noncovalent and covalent nanotube functionalization with organic molecules. As in the case of SEM imaging, micro and/or nanocrystals of starting MPcs materials was not detected by TEM.

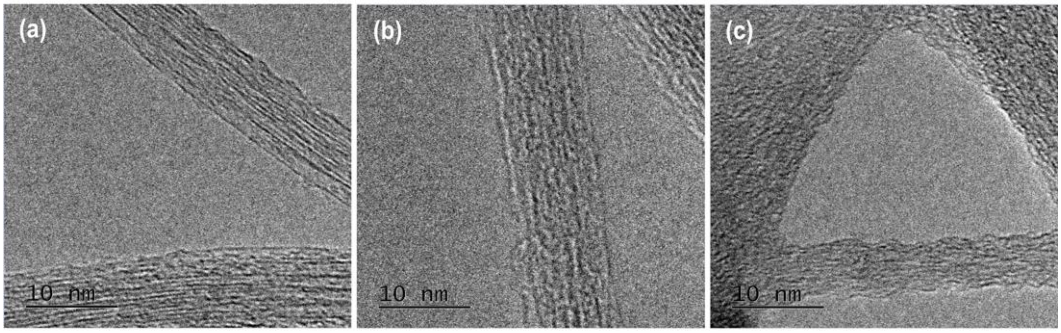

Fig.3. 6. Representative TEM images of (a) single-walled carbon nanotube before and after non-covalent functionalisartion with (b) cobalt and (c) nickel phthalocyanine

Thermogravimetric analysis and differential thermal analysis were carried out simultaneously. Thr results are presented in Fig.3. 7a. TGA curves show two events of mass loss in most of the samples. An initial loss attributed to moisture and other minor volatile impurities is observed in the range of about 50–328°C, within which pristine single-walled CNTs and MPc+SWCNT hybrids are thermally stable. In the case of carbon nanotubes treated with MnPc, a continuous further mass loss is observed in TGA Fig.3. 7a, with two steps observed for other hybrids. The corresponding DTA curves demonstrate clearly that the thermal decomposition process consists of three steps as suggested by three DTA exothermic peaks in thermogram of pristine SWCNT and modified nanotubes with the iron, cobalt, and nickel phthalocyanines, and two peaks for MnPc+SWCNT (Fig.3. 7a).

For pristine SWCNTs (Fig.3. 7a), the first event between 499 and 621°C is associated with the oxidation of amorphous carbon impurities, structural defects in SWCNT sidewalls and multi-walled carbon nanotubes (always present in the SWCNTs samples synthesized by CVD), all of them exhibiting similar thermal behavior.[33–37] The further mass loss at 621–839°C is associated with the decomposition of SWCNTs and double-walled carbon nanotubes (DWCNTs) also present in the SWCNT from CVD proces. [38,39] As regards MPc+SWCNT hybrids, the first and second peak were attributed to the pyrolysis of the metal phthalocyanines, which starts at roughly 247, 273, 335 and 328°C for MnPc+SWCNT, FePc+SWCNT, CoPc+SWCNT and NiPc+SWCNT, and ends at about 634, 709, 664 and 613°C, respectively.[21,40–42] According to DTA curves, the most dramatic mass loss occurs at 444°C for MnPc+SWCNT, at 409°C for FePc+SWCNT, at 443°C for CoPc+SWCNT, and at 462°C for NiPc+SWCNT.

Estimating the MPcs content from TGA curves suggests that it reaches 51.7%, 47% and 35.2% for FePc, CoPc and NiPc, respectively, since the shape of DTA curves of the hybrids in the first and second mass loss steps is similar to that observed for pure MPcs.[40] Nevertheless, it is impossible to correctly account for the interference of mass losses due to double and multi-walled CNTs. One can see that the above values strongly disagree with the most direct estimates of metal phthalocyanine content from the increase in weight of SWCNT material after phthalocyanine deposition, that is 20.2%, 26.3% and 28.4% for FePc, CoPc and NiPc, respectively.

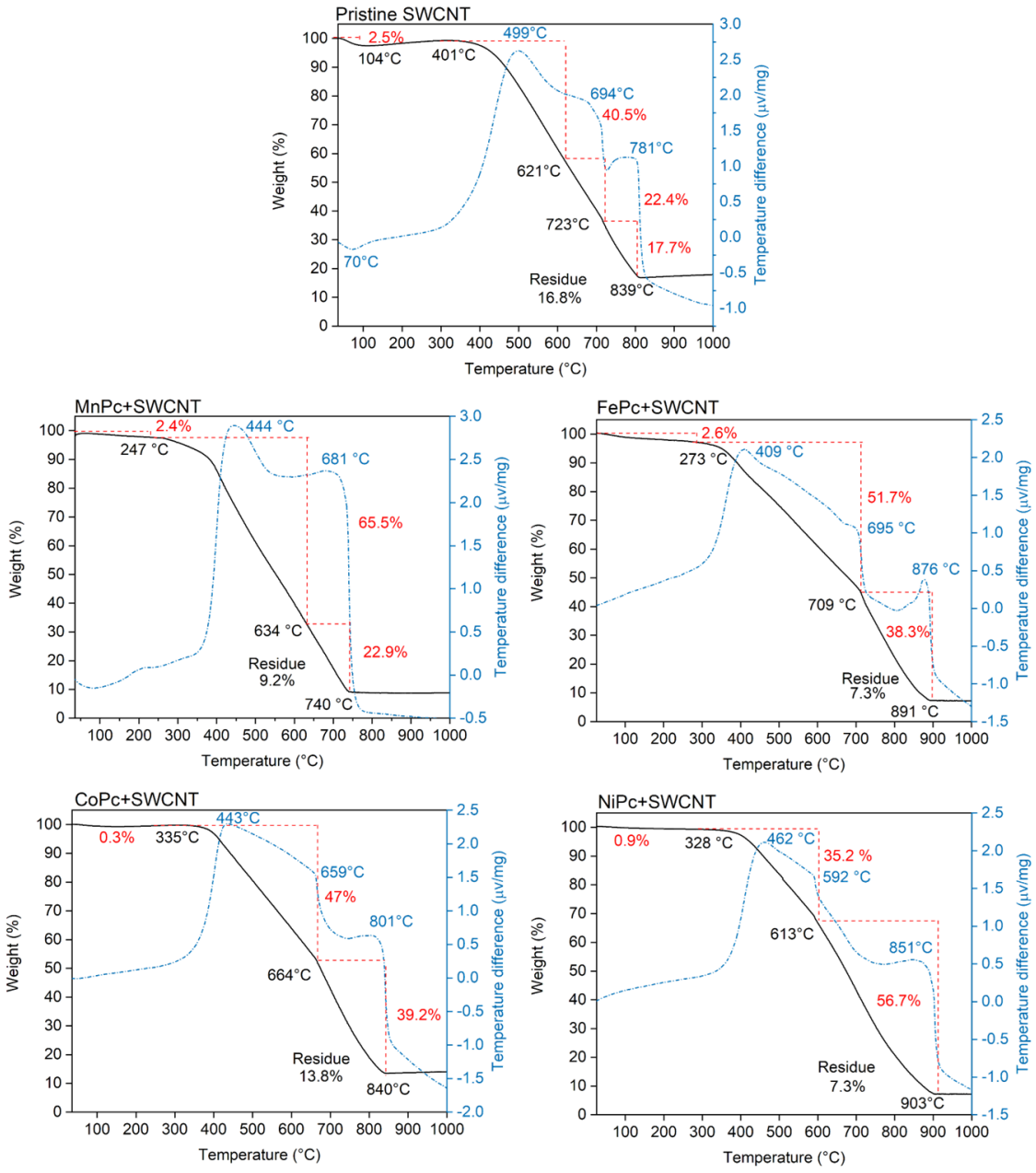

Fig.3. 7. TGA (black) and DTA (blue) curves of pristine SWCNT and MPc+SWCNT hybrids obtained: MnPc+SWCNT, FePc+SWCNT, CoPc+SWCNT and NiPc+SWCNT. Air flow 30 mLmin^{-1} with a heating ramp of 10°C min^{-1} to 1000°C.

The most conflicting estimation are observed in the case of the manganese phthalocyanine, for which TGA mass loss gives 65.5%, whereas only 27.3% phthalocyanine was directly deposited from the liquid phase. One of the reasons is the aforementioned interference of mass losses due to double and multi-walled CNTs. Another possible reason can be the formation of manganese oxides MnO_2, Mn_2O_3 and Mn_3O_4 as the products of MnPc decomposition, which catalyse the combustion of carbon nanotubes, effectively decreasing their oxidation temperature by up to several hundred degrees Celsius. [43–45] In other words, the steady mass loss between

380 and 740°C observed for MnPc+SWCNT is due to continuous catalytic oxidation of the nanotubes, and not only owing to MnPc decomposition. Such catalytic processes can be explained by the Mars and Van Krevelen (MvK) mechanism of oxidation (see Chapter 5). [43,46] In the three remaining cases, FePc, CoPc and NiPc, the thermal stability of the corresponding hybrids is higher than that of pristine SWCNT, suggesting possible a stabilizing action of phthalocyanine complexes due to their strong π-π interactions with nanotube sidewalls. [40,47]

Another way to estimate phthalocyanine content in the MPc+SWCNT hybrids obtained was by measuring their EDS spectra. In Fig.3. 8, both weight and atomic % content range for manganese, iron, cobalt and nickel is specified, as measured at six different sites of each functionalized sample. Pristine SWCNTs exhibit the presence of impurities of Fe used as the catalyst during CVD nanotube synthesis. The range of values is rather wide due to the small size (10×10 μm) of the measuring spot. The weight ranges obtained for elemental Mn, Fe, Co and Ni are 0.9–4.1%, 1.9–5.9%, 3.4–5.7% and 2.3–7.6%, respectively. The corresponding values recalculated for the total molecular weight of metal phthalocyanines are 9–42%, 20– 60%, 33–55% and 22–74%. These values are less precise, but generally consistent with the weight content of phthalocyanine in the MPc+SWCNT hybrids estimated from SWCNT weight differences before and after deposition of the metal phthalocyanines (27.3%, 20.2%, 26.3% and 28.4% of MnPc, FePc, CoPc and NiPc, respectively).

XPS analysis was performed to study the surface composition and chemical state of the single walled carbon nanotubes before and after functionalisation with 3*d* metal phthalocyanines. Fig.3. 9 displays the wide survey scan for pristine single-walled CNTs, which have the expected characteristic peaks, C 1*s* and O 1*s*. The Au peaks observed in the survey arise from the Au/silicon substrate on the samples was deposited. Therefore, all the spectra were calibrated to the Au $4f_{7/2}$ peak at a binding energy (BE) of 84 eV. The C 1*s* core level peak consists of five components. The main peak at 284.7 eV is attributed to C-C/C=C bonding. The sp^2 hybridisation of the carbon is assigned to the graphite lattice and the sp^3 hybridisation to species that indicate amorphous carbon or structural defects, which is visualised by the presence of the D band in the Raman spectrum (Fig.3. 2). The peaks at 285.9, 287.3 and 289.1 eV are due to the existence of oxygen bonded to the carbon atoms of the nanotubes -CO, -C=O and -COO, respectively (carbonyl and carboxylic groups), which are formed due to the presence of edge and defect sites in the nanotube structure which provide suitable anchoring sites for functionalities, possibly during synthesis. Oxygen is also evident in the corresponding EDS spectrum (Fig.3. 8). Finally, the fifth peak located at 290.9 eV is associated with a π–π* shake-up shake-up feature typical of aromatic structures. [48,49]

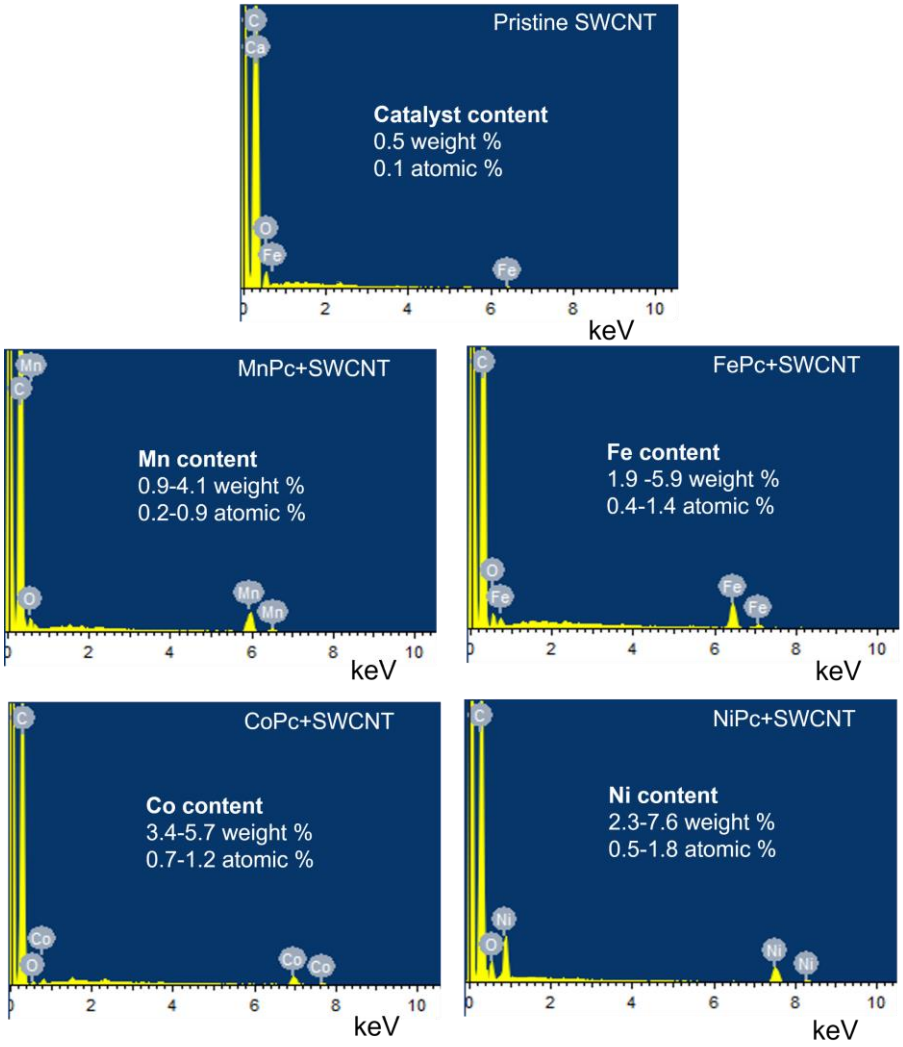

Fig.3. 8. EDS spectra of pristine single-*walled* carbon nanotube and non-covalent hybrids obtained: MnPc+SWCNT, FePc+SWCNT, CoPc+SWCNT and NiPc+SWCNT. For EDS the metal content was estimated from measurements at six different sites for each functionalized material.

The XPS spectra of pristine 3*d* metal phthalocyanines are characterised by the core level region of C 1*s*, N 1*s* and the corresponding transition metal (Fig.3. 10a presents the metal monophthalocyanine structure). In Fig.3. 11, at the top, the C 1*s* spectra show four contributions. The highest peak located at low binding energy between 284.4 and 284.9 eV corresponds to the 24 carbon atoms of the benzene ring, namely carbon sp^2. The second peak between 285.2 and 286.0 eV arises from the carbon-nitrogen bond, which can be attributed to the 8 pyrrole carbon atoms in the structure (N-C=N). At high energy and low intensity, the third and fourth contributions are observed, assigned to shake-up satellites of the main peaks respectively, shake-up$_{C=C}$ at binding energy between 287.2 and 287.5 eV and shake-up$_{N-C=N}$ around 288.4 to 290.0 (Table 3. 2).[50,51]

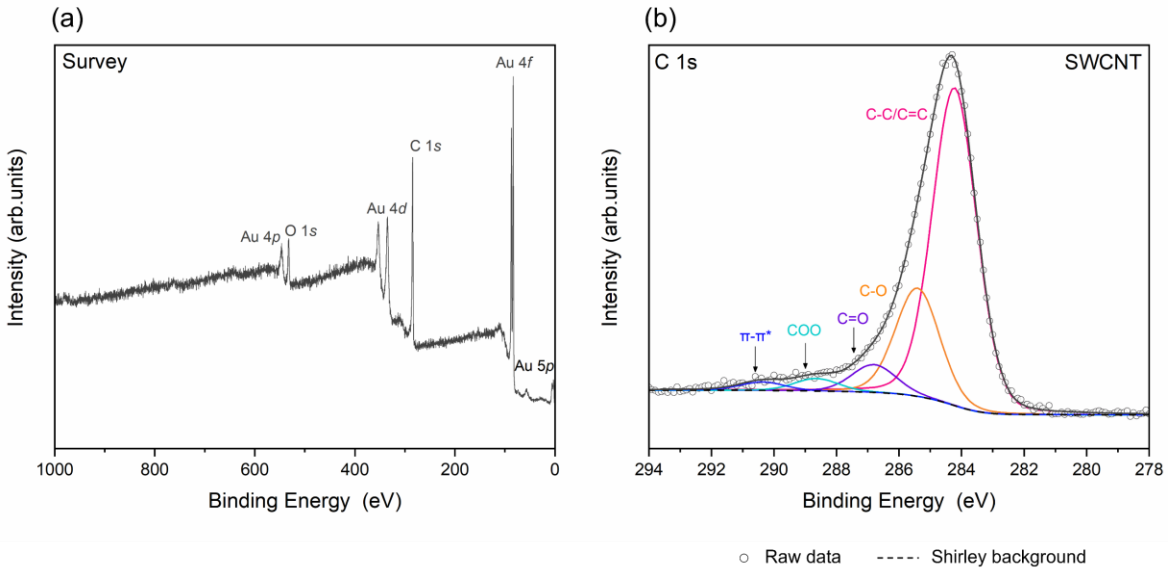

Fig.3. 9. XPS spectra of pristine single walled carbon nanotube: (a) survey scan and (b) detailed spectrum of the C 1*s* core level region with corresponding fit.

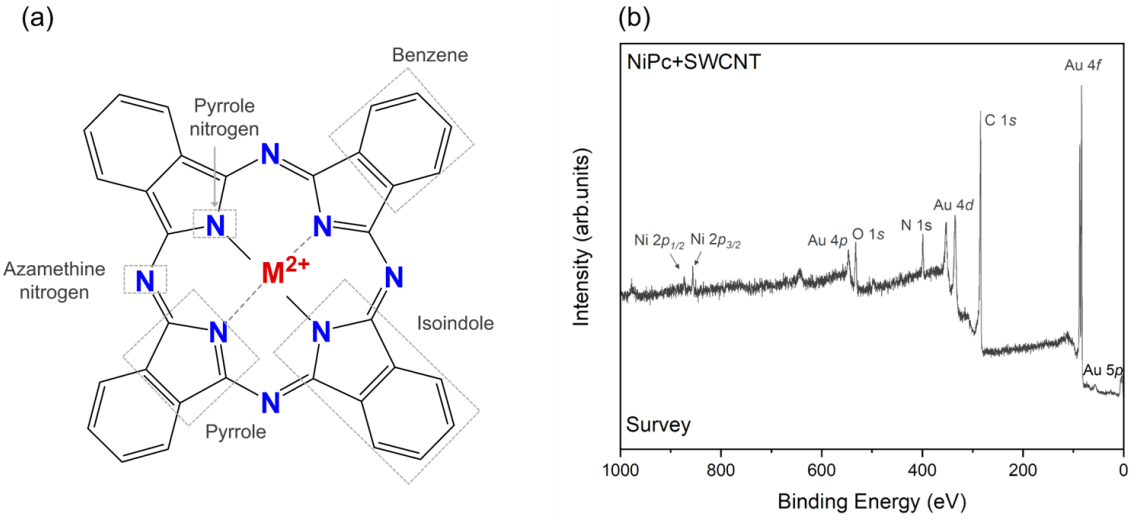

Fig.3. 10. (a) Phthalocyanine structure and (b) survey scan XPS spectrum of the single-walled carbon nanotubes functionalised with nickel phthalocyanines.

Fig.3. 12 presents the N 1*s* core level spectra for all pristine phthalocyanines, where three contributions can be assigned. Nitrogen atoms of the isoindole units coordinated to the metal ion (M-N$_{iso}$, where M= Mn, Fe, Co and Ni and N$_{iso}$ = nitrogen atom of isoindole or unit) at a BE between 398.0 and 398.3 eV; azomethine nitrogen (γ-N) bonded with carbon atoms C-N=C at a BE from 398.8.0 to 399.3 eV and shake-up features around 400.0 and 400.5 eV. [52] Table 3. 3 reports the binding energies of the different components identified in the fits and their percentage contribution.

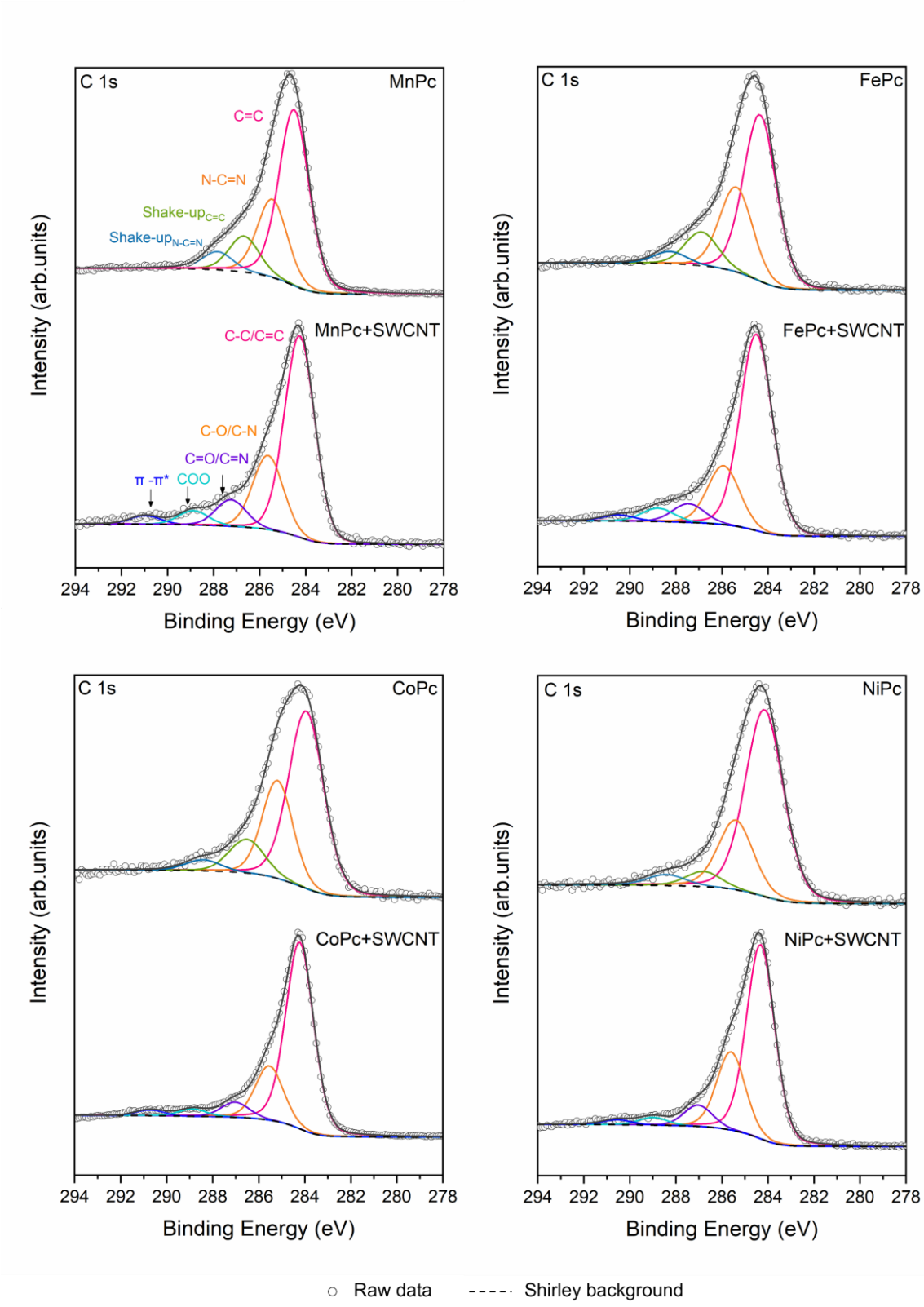

Fig.3. 11. XPS spectra of the C 1*s* core level region of the single-walled carbon nanotubes functionalised non-covalently with manganese, iron, cobalt, and nickel phthalocyanines with corresponding fits. The C 1s core level region spectra for the pristine (commercial) metal phthalocyanines are also reported for comparison.

Table 3. 1. Binding energies (BE in eV) and percentages (in parenthesis) indicating how much the component contributes to the total C 1*s* core level region for single-walled carbon nanotubes before and after the deposition of phthalocyanines.

	C 1*s* (eV)				
Sample	C-C/C=C (%)	C-O (%)	C=O (%)	COO (%)	π–π* shake-up (%)
Pristine SWCNT	284.7 (60.9)	285.9 (22.8)	287.3 (5.9)	289.1 (2.6)	290.9 (1.8)
	C-C/C=C (%)	C-O/C-N (%)	C=O/C=N (%)	COO (%)	π–π* shake-up (%)
MnPc+SWCNT	284.5 (62.0)	285.8 (22.8)	287.2 (8.2)	288.8 (4.4)	290.8 (2.7)
FePc+SWCNT	284.6 (66.9)	285.9 (20.0)	287.5 (6.4)	289.0 (4.6)	290.0 (2.1)
CoPc+SWCNT	284.4 (69.9)	285.7 (20.3)	287.0 (5.6)	288.9 (2.7)	290.7 (1.5)
NiPc+SWCNT	284.7 (63.3)	286.0 (25.5)	287.4 (6.9)	289.3 (2.6)	290.0 (1.6)

Table 3. 2. Binding energies (BE in eV) and percentages (in parenthesis) indicating how much the component contributes to the total C 1*s* core level region for commercial 3*d* metal monophthalocyanines.

	C 1*s* (eV)			
Sample	C=C (%)	N-C=N (%)	Shake-up$_{C=C}$ (%)	Shake-up$_{N-C=N}$ (%)
MnPc	284.9 (57.1)	285.9 (25.3)	287.2 (11.7)	288.4 (5.9)
FePc	284.9 (56.0)	286.0 (28.6)	287.5 (11.4)	288.8 (4.1)
CoPc	284.4 (56.4)	285.6 (33.3)	287.2 (7.7)	289.0 (2.7)
NiPc	284.6 (64.2)	285.9 (25.4)	287.3 (7.2)	288.9 (3.2)

Further confirmation of the formation of the coordination bond (M-N) of the transition metal phthalocyanines comes from the M 2*p* core level region. The metal (Mn, Fe, Co and Ni) species yield two 2 $p_{3/2}$ and 2 $p_{1/2}$ ionization peaks with some additional intensity at higher binding energies causing asymmetry in the band shape. The core ionization process (M 2 $p_{3/2}$ $\rightarrow\infty$) is quite simple, there are many possible final states due to the multiplet structure of transition metal ions. [53] The M 2 $p_{3/2}$ photoemission spectrum of each phthalocyanine used for the functionalisation of the single-walled carbon nanotubes is displayed in Fig.3. 13 and the binding energy values are reported in Table 3. 3.

As for the nanotubes functionalised with manganese, iron, cobalt, and nickel metal phthalocyanines, they present similar XPS spectral characteristics as the phthalocyanines described above. Fig.3. 10b illustrates the survey scan of the carbon nanotubes functionalised with nickel phthalocyanine, as an example of the sample set.

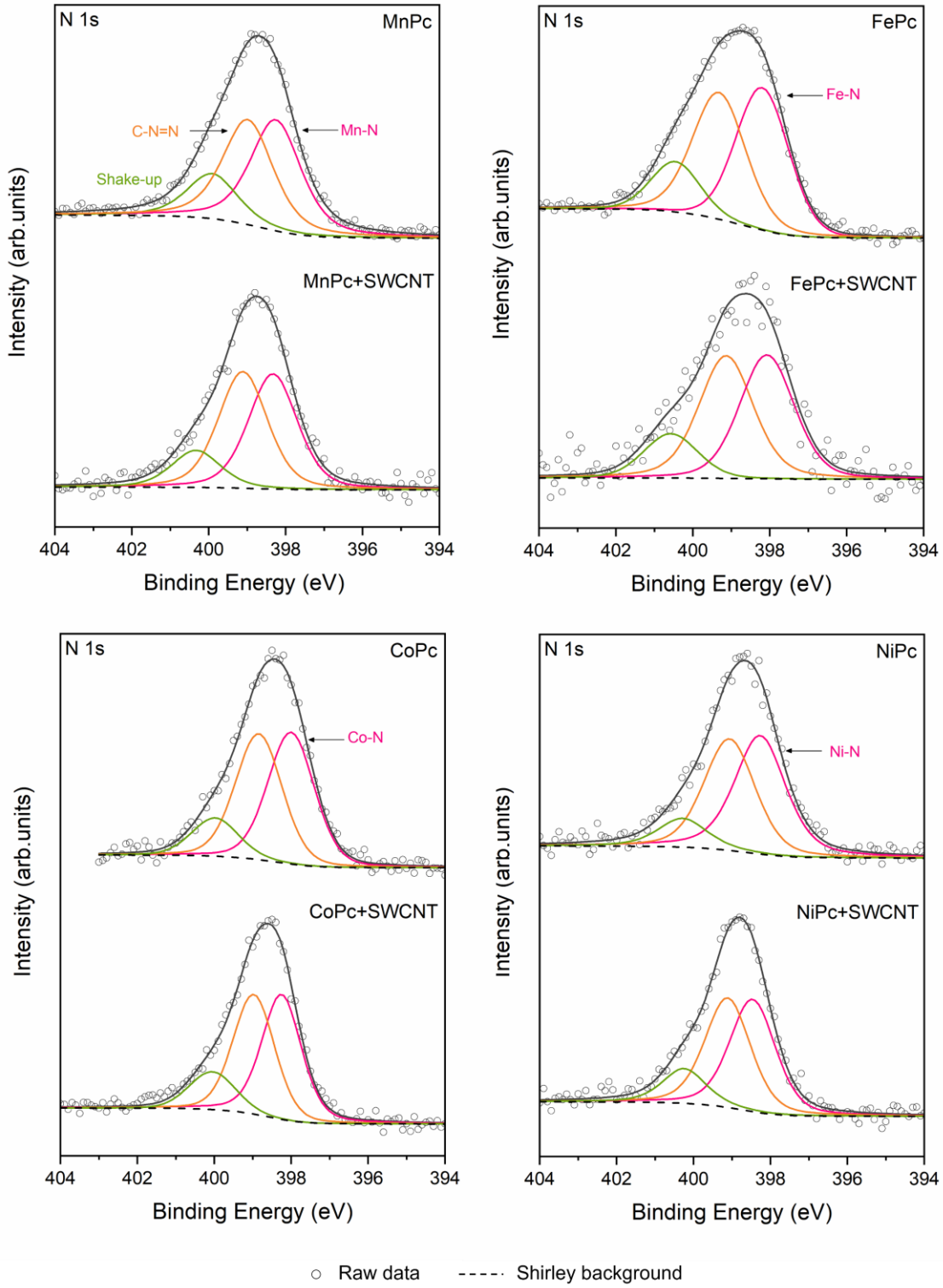

Fig.3. 12. XPS spectra of the N 1*s* core level region of the single-walled carbon nanotubes functionalised non-covalently with manganese, iron, cobalt and nickel phthalocyanines with the corresponding fits. The N 1*s* core level region spectra for the pristine (commercial) metal phthalocyanines are also reported for comparison.

Table 3. 3. Binding energies (BE in eV) and percentages (in parenthesis) indicating how much the component contributes to the total N 1*s* and M $2p_{3/2}$ core level region for each pristine metal monophthalocyanine and single-walled carbon nanotubes after the deposition of phthalocyanines.

	N 1s (eV)				M $2p_{3/2}$ (eV)
Sample	M-N	C=N-C	FWHM[a]	Shake-up	
MnPc	398.3 (42.6)	399.2 (40.2)	1.5	400.0 (17.3)	642.4
FePc	398.2 (43.4)	399.3 (41.8)	1.7	400.5 (14.7)	710.8
CoPc	398.0 (44.5)	398.8 (42.6)	1.4	400.0 (12.9)	780.6
NiPc	398.3 (45.3)	399.1 (42.3)	1.6	400.3 (12.4)	855.6
MnPc+SWCNT	398.3 (43.5)	399.4(44.0)	1.5	400.3(14.4)	642.3
FePc+SWCNT	398.1 (42.2)	399.1 (43.4)	1.6	400.6 (14.2)	710.8
CoPc+SWCNT	398.3 (44.1)	399.0 (41.8)	1.2	400.1 (14.1)	780.7
NiPc+SWCNT	398.5 (43.8)	399.1 (42.6)	1.4	400.2 (13.7)	855.7

[a] value of FWHM for the peak of the M-N and C-N=C bond contributions.

Fig.3. 11 at the bottom of each set of images shows the C 1*s* region of the nanotubes functionalised with the respective phthalocyanines. This signal was fitted into five components as well as the pristine nanotubes (Fig.3. 11). The first contribution was mainly assigned to the sp^2 carbon bonds of the aromatic lattice of the nanotube and the MPcs with a BE around 284.4 and 284.7 eV. The second component can be assigned to two bond types, the C-O present in the nanotubes and C-N of the phthalocyanines, whose binding energy in the range of 285.8 and 286.0 eV, is too close to resolve the deconvolution. The same case for the third component assigned to C=O and C=N at BE from 287.0 to 287.5 eV. [54] The last two correspond to COO and $\pi-\pi^*$ shake-up (Table 3. 1).

N 1*s* for the four MPc+SWCNT samples is shown in the lower part of Fig. 3. 12. Each spectrum shows the three contributions of the metallic phthalocyanines: coordination bonding with the respective M-N metal, C-N=C bonding and stirring. However, comparing the pristine macrocycles reveals some changes. There is a BE shift of the M-N bond contribution of 0.2 and 0.3 eV to higher binding energy for the nanotubes with cobalt and nickel phthalocyanines, respectively, and the C-N=C bond shifts 0.2 eV to lower binding energy for iron and cobalt phthalocyanines. For manganese, the latter shifts to higher energy. The ratio between the spectral intensity of the M-N bond and that of the C-N=C bond is about 1, suggesting that the 4 N_{iso} atoms of MnPc, FePc, CoPc and NiPc are coordinated with the metal atom and the four nitrogen atoms (azamethine N) are not. This confirms the presence of phthalocyanines on the surface of the nanotubes.

The most notable change relates to the full width at half maximum (FWHM) of the N 1*s* peak of the MPc+SWCNT hybrids, which are less broad than the peak of the pristine phthalocyanines (Table 3. 3). This factor may indicate a possible formation of a phthalocyanine monolayer on the nanotube surface or on the agglomerates and corroborates by TEM images since one of the parameters that can influence the FWHM is the thickness of the organic film deposited on the gold substrate (see Chapter 2 the pristine phthalocyanines were prepared in bulk).[52,55] The modification in the shape indicates a stronger interaction between the nitrogen atoms of the MPcs molecules.[53,56]

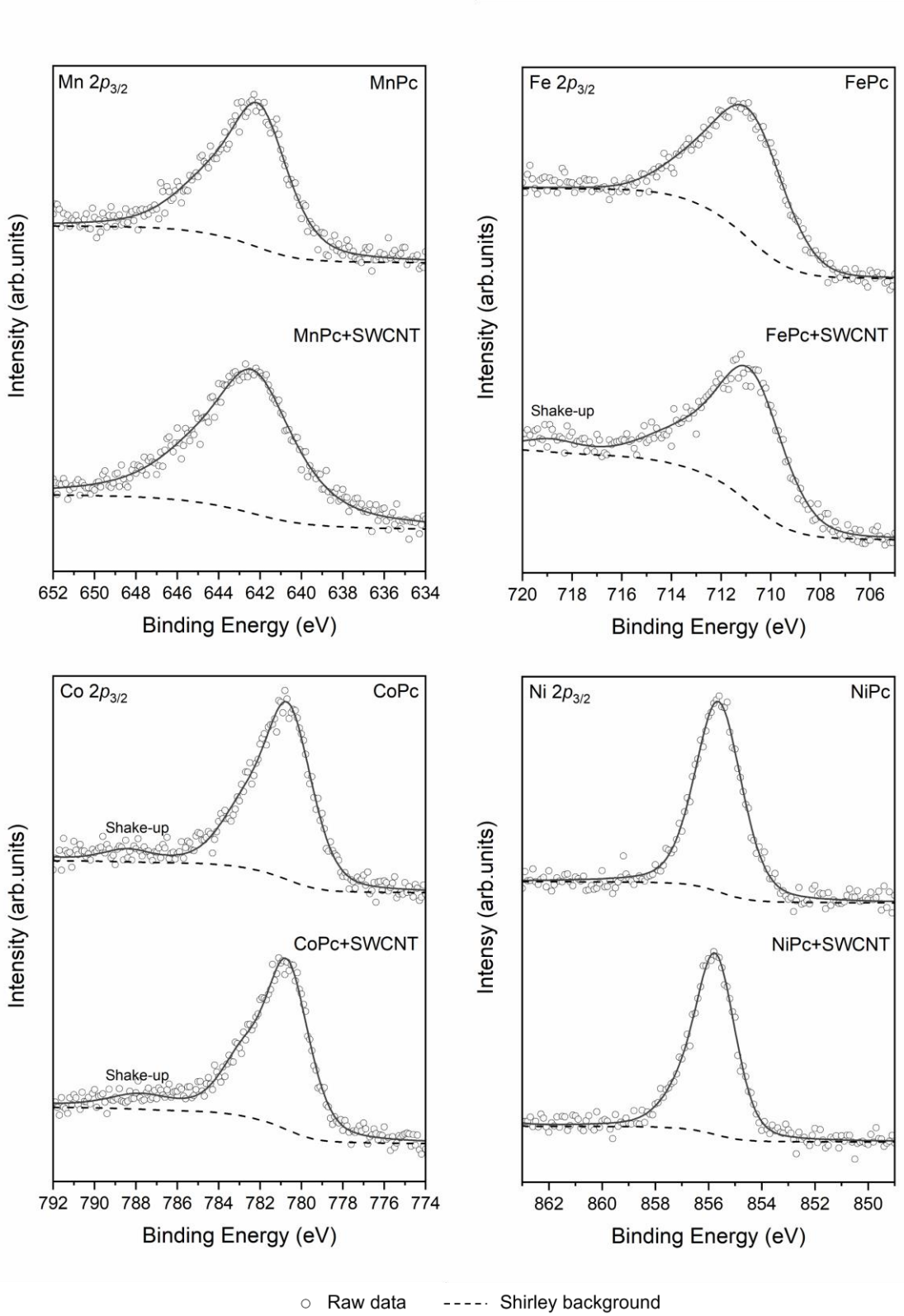

Fig.3. 13. XPS spectra of the M $2p_{3/2}$ (where M = Mn^{2+}, Fe^{2+} Co^{2+} and Ni^{2+}) core level region of the single-walled carbon nanotubes functionalised non-covalently with manganese, iron, cobalt, and nickel phthalocyanines with the corresponding fits. The M $2p_{3/2}$ core level region spectra for the pristine (commercial) metal phthalocyanines are also reported for comparison.

Fig.3. 13 illustrates the M $2p_{3/2}$ core level region for single-walled CNTs functionalised with the four phthalocyanines. The parallel binding energy is not significantly shifted in most of the MPc+SWCNT hybrids. The slight changes in peak shape can be attributed to the presence of carbon nanotubes.

Similar to the EDS and infrared spectra, the photoemission spectra do not indicate any additional components to the elements of each metal macrocycle.

3.3.2. Self-assembly: from molecular mechanics

Molecular modelling by molecular mechanics was implemented to determine and analyse the self-assembly geometry or adsorption arrangement of the phthalocyanines on the nanotube surface using the most energetically stable hybrid model. Unfortunately, no detailed STM characterisation of the self-assembled arrays on CNTs has been reported, only of porphyrins.[57,58]

For the analysis of the simulation of the self-assembly, the structure of free-base phthalocyanine was used as a model molecule to represent the transition metal monophthalocyanines, since mechanic molecular disregards the electron density, the four transition complexes would have the same geometry and behaviour in the non-covalent interactions with the nanotubes. For this purpose, a single-walled carbon nanotube model of choice was a closed-end with C_{180} fullerene and zigzag nanotube (15,0) with 1.16 nm diameter and 8.21 nm long (optimised geometry) was utilised (Fig.3. 14).

The patterns of phthalocyanine self-assembly or adsorption on a carbon nanotube (H_2Pc+SWCNT) were made from one and two free base phthalocyanine molecules placed in different positions on the nanotube surface (Fig.3. 15 to Fig.3. 15). From the most energetically stable template, models with up to eight molecules on the nanotube surface were constructed.

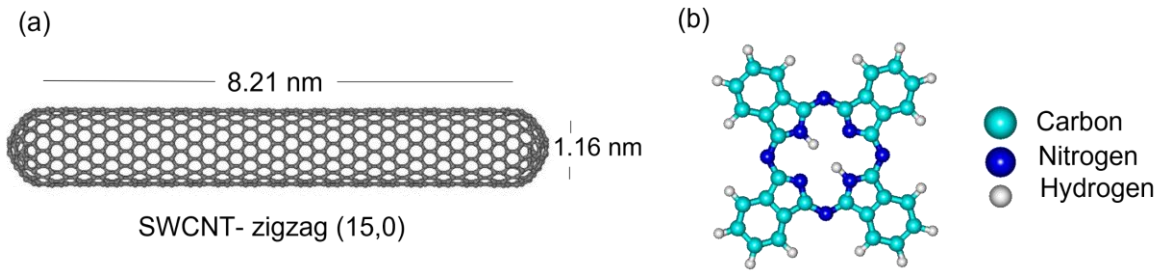

Fig.3. 14. Model of a single-walled carbon nanotube and a molecule of the free-base phthalocyanine optimized by molecular mechanics.

Simulation of the non-covalent interactions of a H_2Pc molecule with a single-walled CNT by MM can occur on the sidewall or on the tips of the nanotube (Fig.3. 15). The adsorption of a H_2Pc molecule on the tip has a formation energy of -27.8 kcal/mol, while macrocycle adsorption on the sidewall can take placed in three different positions depending on the orientation of the hydrogen atom of the pyrrole unit (-NH) with respect to the nanotube axis: diagonal (Fig.3. 15b), vertical (Fig.3. 15c) or parallel position (Fig.3. 15d) with formation energies of -47.4, 46.8 and 47.0 kcal/mol respectively. Thus, the interaction of a H_2Pc molecule on the sidewall with the amine groups diagonal (Fig.3. 15b) to the nanotube axis is the most energetically favourable option. The vertical (Fig.3. 15c) and horizontal (Fig.3. 15d) orientation of the hydrogen atoms on the nanotube surface can be considered as tautomers of the free-base phthalocyanine because these atoms migrate from one pair of nitrogen atoms to the other. [59,60] For the metal monophthalocyanines, the arrangements are equivalent.

The aforementioned lower energy orientation has been reported from DFT studies for the adsorption of free-base, cobalt, copper and zinc phthalocyanines on open nanotubes of different diameters and chiralities (armchair and zigzag). [60,61]

Starting from arrangement b of Fig.3. 15, two molecules of H_2Pc can be accommodated on the surface of a single-walled CNT in seven ways: molecules separated in the different planes (Fig.3. 16a), interacting with the benzene rings (C_6H_4) of the isoindole, which come into contact side by side with the other molecule face to face (Fig.3. 16b), separated in alignment with the benzene rings (Fig.3. 16c), stacked staggered (Fig.3. 16d) and eclipsed (Fig.3. 16e) and interacting with the benzene rings with a slight displacement, where, if the addition of more H_2Pc is continued, a long (Fig.3. 16f) or short (Fig.3. 16g) periodicity helix would be generated. The least energetically stable adsorption arrangement are alternated and eclipsed stacking, followed by the hybrid with the separated macrocycles (opposite planes and aligned), with formation energies of -78.4, -78.9, -94.6 and -94.6 kcal/mol respectively. This suggests that the adsorption of the phthalocyanines occurs in a monolayer, which is in agreement with TEM, SEM and XPS results. These four models were not used to determine the self-assembly pattern with more than three molecules of phthalocyanines.

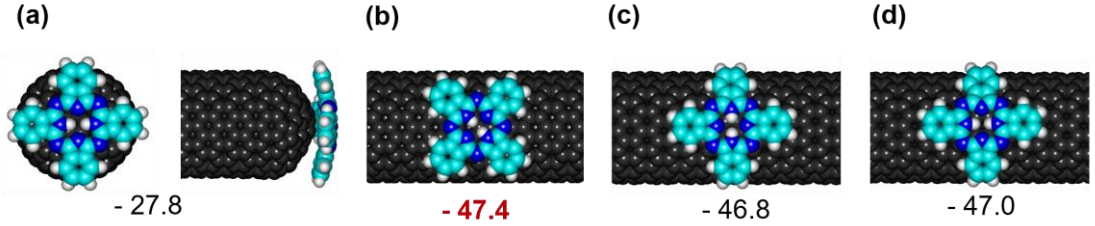

Fig.3. 15. Four positions of adsorption of a H_2Pc molecule on the surface of a single-walled carbon nanotube: (a) on the tip and according to the position hydrogen atoms of pyrrole unit in (b) diagonal, (c) vertical and (d) parallel direction of the nanotube axis. Energy of formation in kcal/mol.

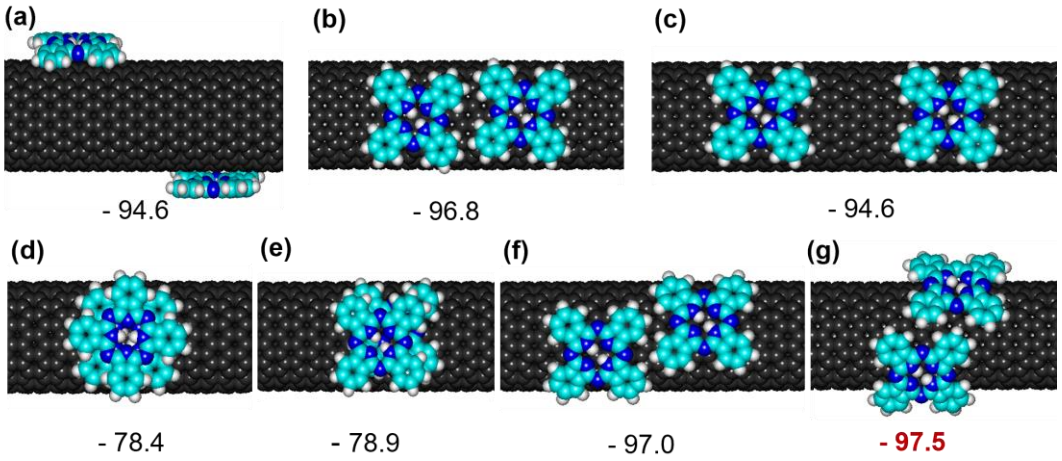

Fig.3. 16. Optimised geometry of seven possibilities of self-assembly arrangements of two H_2Pc molecules on a carbon nanotube: molecules (a) separated in different planes but on the same surface, (b) interacting with the benzene rings of each macrocycle facing each other, (c) separated in alignment with the benzene rings, (d) stacked alternating (e) eclipsed, (f) long and (g) short periodicity helixes. Energy of formation in kcal/mol.

A third H_2Pc molecule was added to the most energetically favourable hybrids so that a monolayer of three interacting molecules is obtained. As a result, four possible arrangements were achieved. The molecules can be arranged in a short (Fig.3. 17a) or long helix (Fig.3. 17b), forming a right angle (Fig.3. 17c) or an obtuse angle (Fig.3. 17d). The short helix arrangement is the most energetically favourable option with a formation energy of -147.7 kcal/mol.

The inclusion of a fourth phthalocyanine in the two helical architectures results in a formation energy of -197.9 kcal/mol for the short periodicity (Fig.3. 18a) and -196.6 kcal/mol for the long period (Fig.3. 14b). The fourth molecule can also be added to the right-angle (Fig.3. 18c) and obtuse angle (Fig.3. 18d) arrangement, with a formation energy of -199.8 and 196.6 kcal/mol, respectively. Thus, the least energetically favourable adsorption arrangements are the long periodicity helix and the obtuse angle, resulting to be isoenergetic. While the lowest potential energy was obtained for the right angle (or square) arrangement followed by the short helix. An interesting observation is that the right-angle arrangement of four H_2Pc molecules can be seen as a combination of two helices of short or long periodicity. This type of self-assembly ensures the interaction of each free-base phthalocyanine with as many neighbouring molecules as possible, due to the dense packing between molecules. [62]

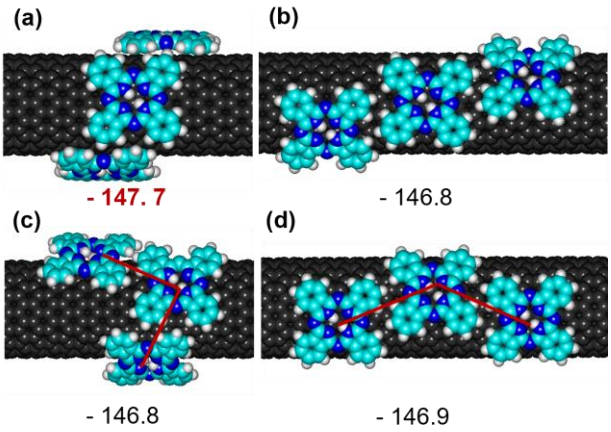

Fig.3. 17. Four possibilities of array for three free-base phthalocyanine molecules on the sidewall CNT: (a) short and (b) long periodicity helixes, forming (c) a right-angle and (d) an open-angle or obtuse angle. Energy of formation in kcal/mol.

The accommodation of eight phthalocyanines molecules on the surface of a single-walled nanotube model was performed using the lowest energy patterns of the hybrids obtained with six H_2Pc molecules (results equal to four adsorbed molecules): formation of a short-periodicity (Fig.3. 19a), right-angle helix (Fig.3. 19b). Two separated (Fig.3. 19c) and nearby (Fig.3. 19d) long-periodicity helices and two associated short-periodicity helices of four free-base phthalocyanines (Fig.3. 19e) were also modelled. The most thermodynamically stable geometry, once again, was the right-angle hybrid with -404.5 kcal/mol, followed by the two associated short-periodicity helices with -404.1 kcal/mol. These results confirm the energetic preference of the free base phthalocyanines towards the formation of short and long helix architectures intercalated forming right angles between every three macrocycles adsorbed on a SWCNT surface (Fig.3. 19b). The trend becomes more pronounced as the number of molecules increases on the nanotube. The reason for obtaining lower formation energy for these arrangements is attributed to the compact periodicity produced, resulting in an optimal interaction of each free-base phthalocyanine with every possible neighbouring molecule.

Overall, the results obtained overall show that the helical geometries (short and long periodicity) in the case of adsorption of two, three and four molecules if they continue to grow with the same self-assembly pattern could lead to the same architecture, an arrangement of eight molecules located at right angles (Fig.3. 19b). The energy differences between the complexes with the same molecule number suggest a possible sequence of events for the self-assembly of Pcs on a SWCNT surface. An example can be visualised with a set of three H_2Pc molecules, especially with the short helix and right-angle architecture hybrids in which the most thermodynamically stable eight-molecule arrangement can be achieved. However, the difference in formation energy suggests that the helix self-assembly is an intermediate stage to produce the lowest energy geometry through the helical association generated by π-π interactions and thus obtain complete H_2Pc coverage of the nanotube surface. The behaviour of the free base phthalocyanine is similar to that of H_2TPP molecules on the surface of the same SWCNT model and under the same computational conditions (MM+ force field). [62]

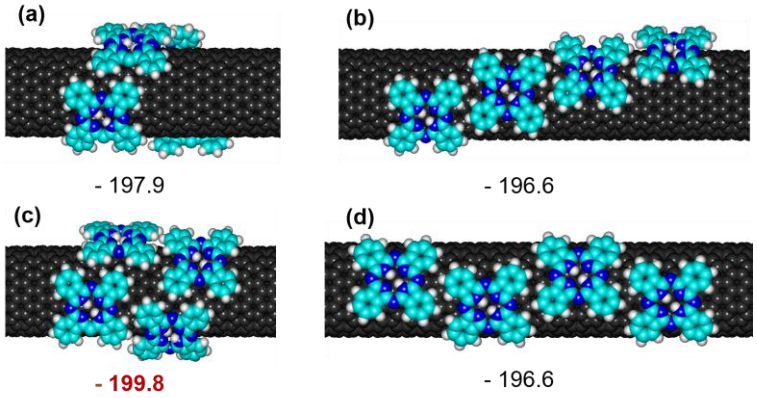

Fig.3. 18.Optimised geometry of different arrangement of four H_2Pc molecules adsorbed on a single-walled carbon nanotube: a) short and (b) long periodicity helixes, forming (c) a right-angle (square) and (d) an obtuse angle. Energy of formation in kcal/mol.

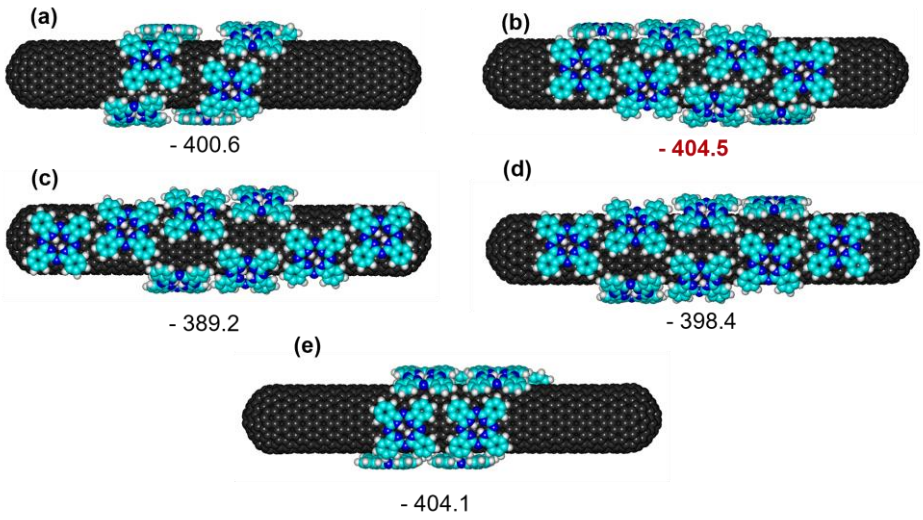

Fig.3. 19. Molecular modelling of eight H_2Pc molecules self-assembled on a single-walled carbon nanotube. Energy of formation in kcal/mol.

Assuming the hypothesis that the deposition of the macrocycles did not only occur on individual nanotubes but also on the surface of nanotube agglomerates, due to the strong π-π interactions of each conjugated component and visualised by SEM and TEM images together with dispersion tests, an agglomerate of three nanotubes each with six H_2Pc molecules was modelled following the lower energy self-assembly model, (see Fig.3. 20). The agglomerate has an energy of -1651.4 kcal/mol, indicating that the adsorption is energetically favourable.

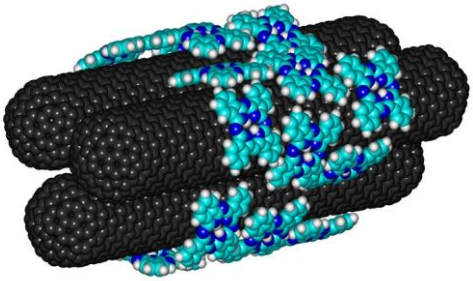

Fig.3. 20. Molecular model of an agglomerate of carbon nanotubes each with six self-assembled H_2Pc molecules forming a rectangle as the most energetically arrangement.

3.3.3. Electrochemical behaviour

To investigate the electrocatalytic activity of the synthesized hybrids for oxygen evolution reaction (OER), cyclic voltammetry was performed in 0.1M KOH and 1M KOH solutions in a three-electrode cell. Fig.3. 21a, b. depicts cyclic voltammograms (CV) of the hybrids of the four metal phthalocyanines with single-walled CNTs and bulk nickel electrode. In both concentrations the pristine SWCNTs showed the lowest current density for OER compared to functionalized single-walled CNTs. In 0.1 M KOH, the best performing catalyst was the nanotubes with the CoPc following by NiPc, FePc and then MnPc+SWCNT. At low KOH concentration bulk Ni activity was very low, and all hybrids outperformed Ni for OER. Contrary to lower KOH concentration, bulk Ni showed a lower onset potential by 20 mV compared to all the MPc+SWCNT hybrids. For 1M KOH, a more negative onset potential located at about 1.50 V was found for NiPc+SWCNT in comparison with 1.51, 1.53, 1.56 and 1.57 for CoPc, FePc, MnPc, Ni wire and single-walled carbon nanotubes, respectively. The onset potentials for both electrolyte concentrations are summarized in Table 3. 4.

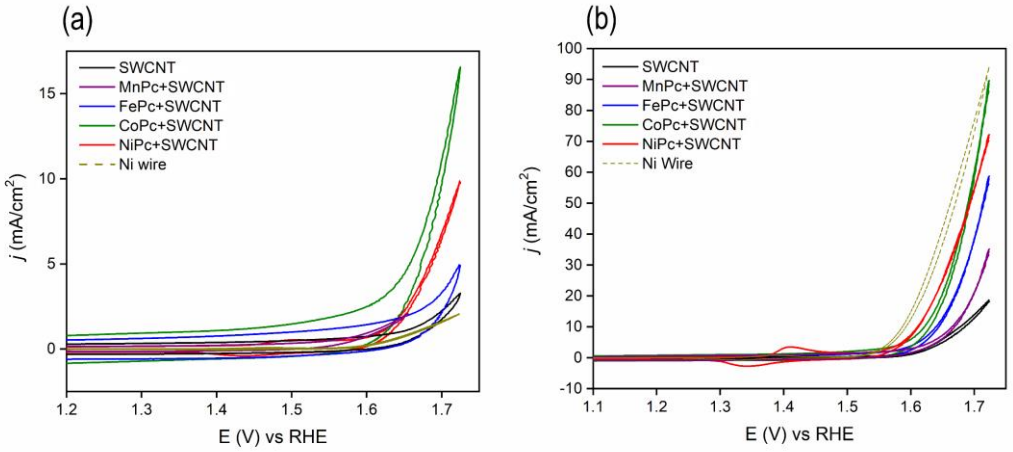

Fig.3. 21. Cyclic voltammograms of the hybrids of the manganese, iron, cobalt, and nickel phthalocyanines with single-walled carbon nanotube in (a) 0.1 M KOH and (b) 1 M KOH solution at scan rate of $20mVs^{-1}$

Table 3. 4. Onset potentials and Tafel slopes for two different concentrations of MPc+SWCNT hybrids in comparison with Ir black and Ni wire catalysts

Catalyst	Onset V vs RHE (0.1M KOH)	Onset V vs RHE (1M KOH)	Tafel slope mV/dec (0.1MKOH)	Tafel slope mV/dec (1MKOH)
SWCNT	1.60	1.60	103.25	106.66
NiPc+SWCNT	1.50	1.50	64.02	56.05
CoPc+SWCNT	1.55	1.51	80.45	75.36
FePc+SWCNT	1.56	1.53	86.63	85.48
MnPc+SWCNT	1.55	1.56	95.84	99.20
Ir Black	1.42	1.48	57.66	43.08
Ni wire	1.50	1.50	56.31	53.89

The OER activity found for the pristine single-walled CNTs can be attributed to Fe impurities present in single-walled CNTs (as corroborated by EDS) due to the CVD technique employed for their synthesis, thus affecting the catalytic response. For the nickel phthalocyanine an oxidation and reduction peak at ~1.4 V was observed for both concentrations corresponding to $\beta NiOOH/Ni(OH)_2$ redox processes.[63] The results for 0.1M and 1M KOH (Fig.3. 21a and b) determined the pH dependence of the activity of the MPc+SWCNT hybrids, showing that the activity increases with increasing pH. However, hybrids show higher current densities for OER at lower pH than Ni bulk. Nevertheless, for CoPc+SWCNT, the onset potential is shifted to more negative potentials for lower pH values.

The activity of catalysts for OER is commonly determined by the overpotential needed for achieving 10 mA cm^{-2}.[64] For NiPc+SWCNT, a potential obtained was of 1.6 V, followed by 1.62 V for CoPc+SWCNT, 1.64 V for FePc+SWCNT, 1.66 V for MnPc+SWCNT and 1.68 V for pristine single-walled CNT. The lowest overpotential of 370 mV was obtained for NiPc+SWCNT, in comparison to other synthesized hybrids. This confirms that the most active hybrid is NiPc+SWCNT, showing the best activity with the lowest overpotential among the other hybrids and pristine nanotubes as well.

Liner sweep voltammetry (LSV) of electrocatalyst in 1M KOH (Fig.3. 22) agrees with cyclic voltammetry showing that NiPc+SWCNT and CoPc+SWCNT show high current densities with a sharp onset potential located at about 1.5 V vs. RHE. To obtain more insights into the catalytic activity of functionalized nanotube samples, Tafel plots were evaluated, as illustrated in Fig.3. 22. The Tafel slopes obtained are similar for both concentrations and are summarized in Table 3. 4. The smallest Tafel slope was found for NiPc+SWCNT at about 56 mV dec^{-1} in 0.1M KOH and 64 mV dec^{-1} in 1M KOH. The Tafel slopes of the functionalized samples are comparable to the values obtained for Ni bulk and Ir black electrodes in the same electrolyte (Table 3. 4). However, in comparison with other catalysts based on phthalocyanines, the Tafel slopes found for MPc+SWCNT are lower (Table 3. 5). This can be explained by the fact that single-walled carbon nanotubes are a conductive material with high surface area. In addition, the non-covalent

π–π bond between the carbon nanotubes and the phthalocyanines, provides the materials with a stable and active structure.

The stability of MPc+SWCNT hybrids was evaluated in 0.1M and 1M KOH. Long term chronoamperometry (CA) was carried out at 1.56 and 1.59 V vs. RHE in 0.1M and 1M KOH respectively and the results are summarized in Fig.3. 23.

Table 3. 5. Tafel slopes of 3*d* transition metal phthalocyanine based electrocatalysts.

Catalyst	Substrate	Electrolyte	Tafel slope (mv dec-1)	Reference
NiPc	SWCNT	1M KOH	64.02	**Present work**
CoPc	SWCNT	1M KOH	80.45	**Present work**
CoPc	FTO	0.1M NaPO3	120.00	65
FePc	MWCNT	0.1M KOH	108.5	18
NiPc	MWCNT	0.1M KOH	132.9	18
NiPc	MOF	1M KOH	74.00	66
MnPc	ITO/PANI	4-azidoaniline	300.0	67
FePc	Hollow carbon spheres	0.1 M KOH	83.0	68

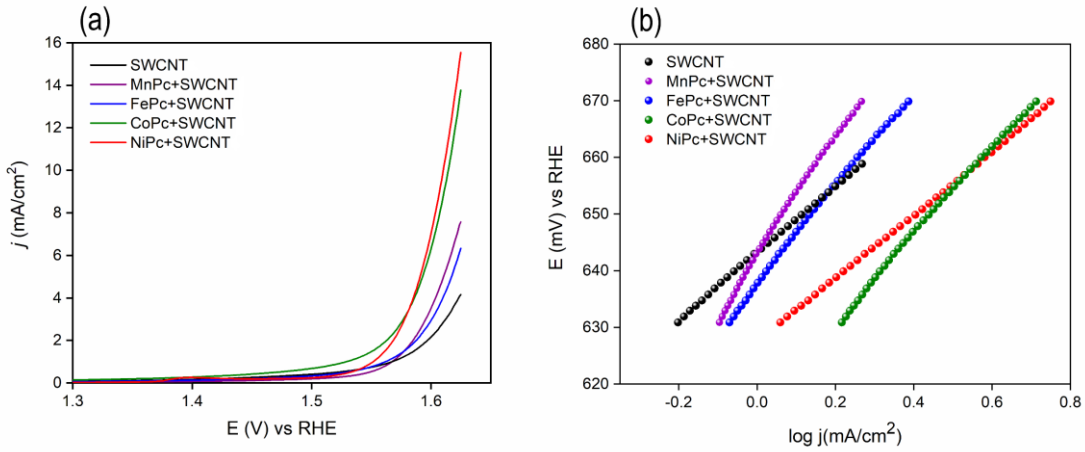

Fig.3. 22. (a) Linear sweep voltammetry curves at 1mVs^{-1} and (b) Tafel plots of the MPc+SWCNT hybrids in 1 M KOH.

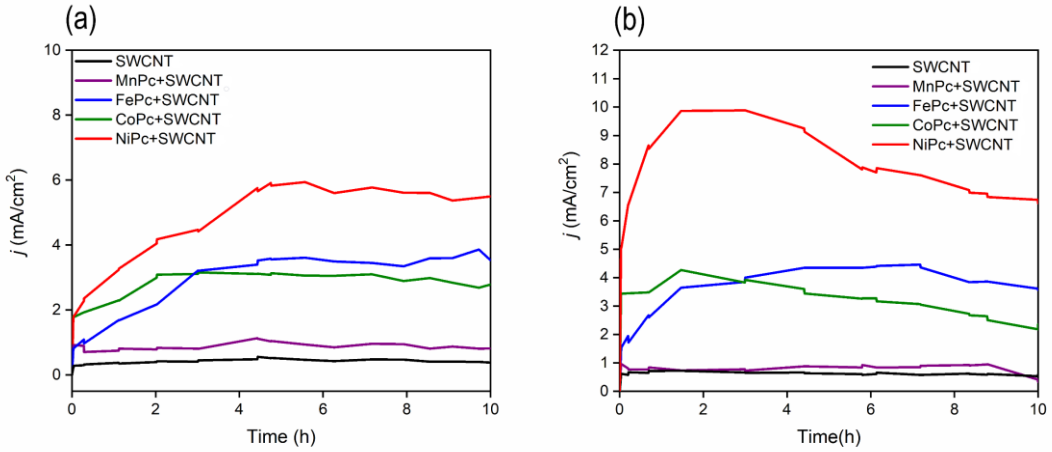

Fig.3. 23. Chronoamperometric curves in (a) 0.1 M KOH at 1.56 V and (b) 1M KOH at 1.59 V on MPc+SWCNT

An increase in the current density was observed (Fig.3. 23) for NiPc, CoPc and FePc-based catalysts within the first 4 h of the experiment. In 1M KOH, NiPc+SWCNT displayed an important increase in the current density. After four hours, the activity decreased and remained stable for the rest of the experiment. A similar behaviour was observed for CoPc+SWCNT. However, after 10 hours of experiment, the activity decreased considerably. For FePc+SWCNT an interesting behaviour was observed, where the current density kept increasing for 6 h and then started to decrease gradually. The increase in current density at the beginning of experiment was possibly caused by surface activation of the catalyst and formation of $Ni(OH)_2$ and $Co(OH)_2$ sites.

The current density for NiPc+SWCNT and FePc+SWCNT increased over time in 0.1M KOH, with no further decrease observed after 10 h. Even though the activity of FePc+SWCNT is not as high as that of other catalysts, the behaviour was found to be more stable over time. Furthermore, the stability of the catalysts was evaluated by acquiring cyclic voltammograms immediately after finishing the chronoamperometry experiments (Fig.3. 24).

The mechanism for the OER with single-walled carbon nanotubes noncovalently functionalized with metal phthalocyanines in general follows a similar path to metal catalysts. In this case, the metal phthalocyanine of the MPc+SWCNT hybrid, acts as the active site. In Fig.3. 25 it is noted that there are two different approaches for O_2 formation. The first, consists of the direct coupling of two O-MPc+SWCNT intermediaries (pink line) and in the second route, the OO-MPc+SWCNT intermediaries are formed initially by the reaction of O-MPc+SWCNT with OH and then the combination with OH to produce O_2 (black route).[14,19,69]

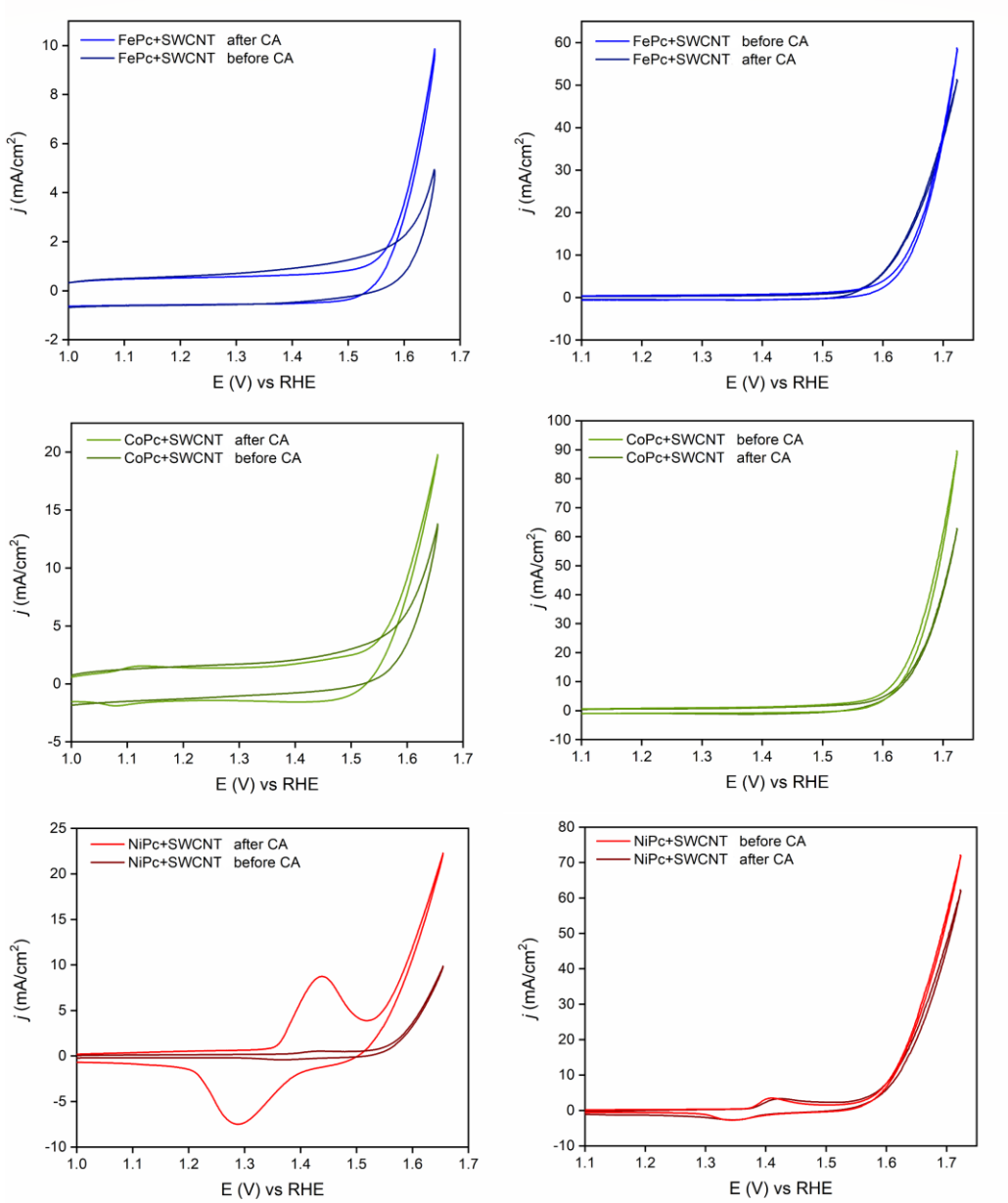

Fig.3. 24. Cyclic voltammograms responses of electrocatalysts immediately after finishing CA experiments in a, c, e) 0.1 M KOH and b, d, f) 1 M KOH. Scan rate 20 mVs^{-1}.

The OER mechanism for nickel-based catalysts is still under study, however, it has been reported that the formation of catalytically active species for the OER occur through a deprotonation of hydrated nickel oxyhydroxide towards the formation of oxide ($NiO-$) or superoxide ($NiOO^-$) species. [70,71] These mechanisms propose the formation of O_2 through the decomposition of negatively charged surface species (O_2^-) which differs from the "classical" OH^-/e^-transfer mechanism (Fig.3. 25).

The oxidative deprotonation process to generate the catalytic species for the OER is not

particular for nickel. It has been reported that catalysts based on cobalt, iron and manganese are also deprotonated before the oxygen evolution, in processes that are pH depend. [63,70]

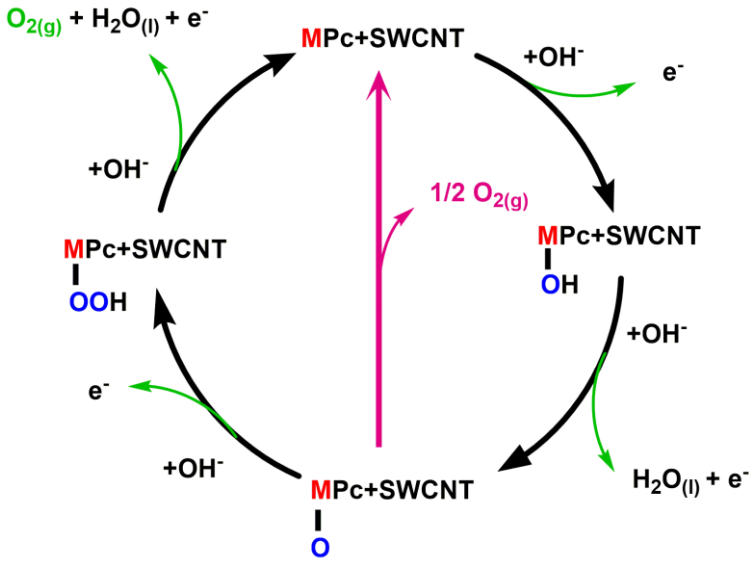

Fig.3. 25. Mechanism of OER for alkaline conditions (green line). The black line indicates that the evolution of oxygen involves the formation of a peroxide intermediate (M-OOH), while another route is also possible for the direct reaction of two adjacent oxo (M-O) intermediates (pink) to produce oxygen.

3.4. Conclusions

Single-walled carbon nanotube-supported metal phthalocyanines hybrids, NiPc+SWCNT, CoPc+SWCNT, FePc+SWCNT, were synthesized through an ecologically friendly gas-phase deposition method and studied as electrocatalysts for oxygen evolution reaction. The preparation of the functionalisation of the nanotubes with manganese phthalocyanines was carried out in liquid phase, by reflux in butanol, due to the to lower thermal stability of the MnPc. TEM and SEM micrographs showed the uniform deposition of MPc. The amount of phthalocyanine calculated from the weight difference before and after functionalization of the CNTs as 20.2%, 26.3%, 28.4% and 27.3% for FePc, CoPc, NiPc and MnPc, respectively.

The results of molecular mechanic calculations suggest that H_2Pc molecules self-assemble on the surface of a SWCNT with a combined geometry of short and long periodicity helices interacting at a right angle, as the most thermodynamically stable arrangement.

All the hybrids synthesized showed an increase in electrochemical activity in comparison with pristine single-walled carbon nanotubes and much higher current densities in 0.1M KOH than bulk Ni and Ir black electrodes. The effect of repetitive cycling was investigated. It was found that the activity increases with the cycling, for both electrolyte concentrations, and to a large extent for the NiPc+SWCNT sample. This is consistent with chronoamperometry results were an increase over time was observed. These results can be attributed to the activation of Ni centres due to the formation of NiOOH. The higher electrocatalytic activity of the synthesized hybrids can be associated with the contribution of high surface area and porosity of the SWCNT

supports together with non-covalent interactions between the monophthalocyanines and the carbon nanotubes.

The electrochemical results suggest that the performance of the hybrids of monophthalocyanines and single-walled CNTs is related to the contribution of phthalocyanine and CNT structure due to synergistic effects between them, which enhances the active catalytic sites and conductivity of these materials. The synthesized MPc+SWCNT hybrid materials could offer a potential alternative to existing conventional precious metal catalyst and extends the applications of non-covalent functionalised carbon nanotubes towards the development of materials for energy applications

3.5. References

(1) Ghani, F.; Kristen, J.; Riegler, H. Solubility properties of unsubstituted metal phthalocyanines in different types of solvents. *J. Chem. Eng. data* 2012, *57*, 439–449.

(2) Kumar, A.; Srivastava, K. Electronic absortion spectra of copper phthalocyanine dye. *Asian J. Chem.* 2000, *3*, 723–731.

(3) Bottari, G.; Torre, G. De; Guldi, D. M.; Torres, T. Covalent and noncovalent phthalocyanine - carbon nanostructure systems : synthesis , photoinduced electron transfer , and application to molecular photovoltaics. *Chem. Rev.* 2010, *110*, 6768–6816.

(4) Xu, Z.; Li, H.; Sun, H.; Zhang, Q.; Li, K. Carbon nanotubes with phthalocyanine-decorated surface produced by NH_3-assisted microwave reaction and their catalytic performance in Li/$SOCl_2$ battery. *Chinese J. Chem.* 2010, *28*, 2059–2066.

(5) Li, H.; Xu, Z.; Li, K.; Hou, X.; Cao, G.; Zhang, Q.; Cao, Z. Modification of multi-walled carbon nanotubes with cobalt phthalocyanine: effects of the templates on the assemblies. *J. Mater. Chem.* 2011, *21*, 1181–1186.

(6) Basiuk, V. A.; Flores-Sánchez, L. J.; Meza-Laguna, V.; Flores-Flores, J. O.; Bucio-Galindo, L.; Puente-Lee, I.; Basiuk, E. V. Noncovalent functionalization of pristine CVD single-walled carbon nanotubes with *3d* metal(II) phthalocyanines by adsorption from the gas phase. *Appl. Surf. Sci.* 2018, *436*, 1123–1133.

(7) Wagner, H.; Loutfy, R.; Hsiao, C.-K. *Purification and Characterization of Phthalocyanines*; 1982; Vol. 17.

(8) Hu, C.; Zhang, L.; Gong, J. Recent progress made in the mechanism comprehension and design of electrocatalysts for alkaline water splitting. *Energy Environ. Sci.* 2019, *12* (9), 2620–2645.

(9) Calle-Vallejo, F.; Koper, M. T. M. First-principles computational electrochemistry: achievements and challenges. *Electrochim. Acta* 2012, *84*, 3–11.

(10) Varcoe, J. R.; Atanassov, P.; Dekel, D. R.; Herring, A. M.; Hickner, M. A.; Kohl, P. A.; Kucernak, A. R.; Mustain, W. E.; Nijmeijer, K.; Scott, K.; et al. Anion-exchange membranes in electrochemical energy systems. 2014.

(11) Park, J. E.; Kang, S. Y.; Oh, S. H.; Kim, J. K.; Lim, M. S.; Ahn, C. Y.; Cho, Y. H.; Sung, Y. E. High-performance anion-exchange membrane water electrolysis. *Electrochim. Acta* 2019, *295*, 99–106.

(12) Bajdich, M.; Mónica García-Mota, M.; Vojvodic, A.; Nørskov, J. K.; Bell, A. T. Theoretical investigation of the activity of cobalt oxides for the electrochemical oxidation of water. 2013.

(13) Gim, S.; Bisquert, J.; Principles, F. B.; Devices, A. *Photoelectrochemical Solar Fuel Production*; 2016.

(14) Li, X.; Hao, X.; Abudula, A.; Guan, G. Nanostructured catalysts for electrochemical water splitting: current state and prospects. *J. Mater. Chem. A* 2016, *4* (31), 11973–12000.

(15) Surendranath, Y.; Kanan, M. W.; Nocera, D. G. Mechanistic studies of the oxygen evolution reaction by a cobalt-phosphate catalyst at neutral ph. *J. Am. Chem. Soc.* 2010, *132* (46), 16501–16509.

(16) Wu, L.; Li, Q.; Cheng, §; Wu, H.; Zhu, H.; Mendoza-Garcia, A.; Shen, B.; Guo, J.; Sun, S. Stable cobalt nanoparticles and their monolayer array as an efficient electrocatalyst for oxygen evolution reaction. 2015.

(17) Han, L.; Dong, S.; Wang, E. Transition-metal (Co, Ni, and Fe)-based electrocatalysts for the water oxidation reaction. *Adv. Mater.* 2016, *28* (42), 9266–9291.

(18) Abbaspour, A.; Mirahmadi, E. Electrocatalytic activity of iron and nickel phthalocyanines supported on multi-walled carbon nanotubes towards oxygen evolution reaction. *Electrochim. Acta* 2013, *105*, 92–98.

(19) Cheng, Y.; Jiang, S. P. Advances in electrocatalysts for oxygen evolution reaction of water electrolysis-from metal oxides to carbon nanotubes. *Prog. Nat. Sci. Mater. Int.* 2015, *25* (6), 545–553.

(20) Alzate-Carvajal, N.; Bolivar-Pineda, L. M.; Meza-Laguna, V.; Basiuk, V. A.; Basiuk, E. V.; Baranova, E. A. Oxygen evolution reaction on single-walled carbon nanotubes noncovalently functionalized with metal phthalocyanines. *ChemElectroChem* 2020, *7*, 428–436.

(21) Seoudi, R.; El-Bahy, G. S.; El Sayed, Z. A. FTIR, tga and dc electrical conductivity studies of phthalocyanine and its complexes. *J. Mol. Struct.* 2005, *753* (1–3), 119–126.

(22) Basiuk, V. A.; Bolivar-Pineda, L. M.; Meza-Laguna, V.; Rybak-Akimova, E. V.; Basiuk, E. V. Carbon nanotubes and graphene promote pyrolysis of free-base phthalocyanine. *J. Phys. Chem. Lett.* 2018, *9* (15), 4420–4427.

(23) Verma, D.; Dash, R.; Katti, K. S.; Schulz, D. L.; Caruso, A. N. Role of coordinated metal ions on the orientation of phthalocyanine based coatings. *Spectrochim. Acta - Part A Mol. Biomol. Spectrosc.* 2008, *70*, 1180–1186.

(24) Ridhi, R.; Singh, S.; Saini, G. S. S.; Tripathi, S. K. Comparison of interaction mechanisms of copper phthalocyanine and

nickel phthalocyanine thin films with chemical vapours. *J. Phys. Chem. Solids* 2018, *115* (December 2017), 119–126.
(25) Dresselhaus, M. S.; Dresselhaus, G.; Saito, R.; Jorio, A. Raman spectroscopy of carbon nanotubes. *Phys. Rep.* 2005, *409*, 47–99.
(26) Liu, Y.; Wang, Y.; Liu, Y.; Li, W.; Zhou, W.; Wei, F. Purifying double-walled carbon nanotubes by vacuum high temperature treatment. *Nanotechnology* 2007, *18* (17).
(27) Tsai, J. T. H.; Tseng, A. A. Defect reduction of multi-walled carbon nanotubes by rapid vacuum arc annealing. *J. Exp. Nanosci.* 2009, *4* (1), 87–93.
(28) Wang, Y.; Hu, N.; Zhou, Z.; Xu, D.; Wang, Z.; Yang, Z.; Wei, H.; Kong, E. S. W.; Zhang, Y. Single-walled carbon nanotube/cobalt phthalocyanine derivative hybrid material: preparation, characterization and its gas sensing properties. *J. Mater. Chem.* 2011, *21*, 3779–3787.
(29) Pereira, G. F. M.; Tasso, T. T. From cuvette to cells: how the central metal ion modulates the properties of phthalocyanines and porphyrazines as photosensitizers. *Inorganica Chimica Acta*., p 120271.
(30) Dini, D.; Hanack, M. Phthalocyanines as materials for advanced technologies: some examples. In *Journal of Porphyrins and Phthalocyanines*; Society of Porphyrins and Phthalocyanines (SPP), 2004; Vol. 8, pp 915–933.
(31) Jiang, J. *Functional Phthalocyanine Molecular Materials*; 2015; Vol. 53.
(32) Kadish, K. M.; Smith, K. M. *The Porphyrin Handbook Properties*; Vol. 11.
(33) Shah, K. A.; Najar, F. A.; Sharda, T.; Sreenivas, K. Synthesis of multi-walled carbon nanotubes by thermal CVD technique on pt–w–mgo catalyst. *J. Taibah Univ. Sci.* 2018, *12* (2), 230–234.
(34) Palacio, R.; Gallego, J.; Gabelica, Z.; Batiot-Dupeyrat, C.; Barrault, J.; Valange, S. Decomposition of ethanol into h_2-rich gas and carbon nanotubes over Ni, Co and Fe supported on SBA-15 and aerosil. *Appl. Catal. A Gen.* 2015.
(35) Gallego, J.; Sierra, G.; Mondragon, F.; Barrault, J.; Batiot-Dupeyrat, C. Synthesis of MWCNTs and hydrogen from ethanol catalytic decomposition over a Ni/La_2O_3 catalyst produced by the reduction of lanio$_3$. *Appl. Catal. A Gen.* 2011, *397* (1–2), 73–81.
(36) Zeng, G.; Zhang, H.; Huang, H.; Xie, Z.; Jie, X.; Chen, Y. The thermal properties of controllable diameter carbon nanotubes synthesized by using AB_5 alloy of micrometer magnitude as catalyst. *Mater. Sci. Eng. A* 2007, *464* (1–2), 17–22.
(37) San-José-Alonso, D.; Juan-Juan, J.; Illán-Gómez, M. J.; Román-Martínez, M. C. Ni, Co and bimetallic Ni-Co catalysts for the dry reforming of methane. *Appl. Catal. A Gen.* 2009, *371* (1–2), 54–59.
(38) Inoue, S.; Maruyama, T.; Wang, H.; Ghosh, K.; Li, Z.; Ando, Y. Synthesis of double-walled carbon nanotube films and their field emission properties. *Carbon N. Y.* 2010, *48* (10), 2882–2889.
(39) Chen, Z.-G.; Liu, C.; Li, F.; Lu, G. Q.; Cong, H.; Cheng, H.-M.; Ren, W.-C. Double-walled carbon nanotubes synthesized using carbon black as the dot carbon source. *Nanotechnology* 2006, *17* (13), 3100–3104.
(40) Zhang, Z.; Yang, S.; Dou, M.; Liu, H.; Gu, L.; Wang, F. Systematic study of transition-metal (fe, co, ni, cu) phthalocyanines as electrocatalysts for oxygen reduction and their evaluation by dft. *RSC Adv.* 2016, *6* (71), 67049–67056.
(41) Zhang, L.; Yu, H.; Liu, L.; Wang, L. Study on the preparation of multi-walled carbon nanotube/phthalocyanine composites and their optical limiting effects. *J. Compos. Mater.* 2014, *48* (8), 959–967.
(42) Hsieh, T. C.; Tsou, Y. H.; Chen, J. S. Iron phthalocyanine supported on 3*d* nitrogen-doped graphene aerogel as an electrocatalyst for non-aqueous Li−O_2 batteries. *Electrochim. Acta* 2019, *295*, 490–497.
(43) Aksel, S.; Eder, D. Catalytic effect of metal oxides on the oxidation resistance in carbon nanotube-inorganic hybrids. *J. Mater. Chem.* 2010, *20* (41), 9149–9154.
(44) Neeft, J. P. A.; Makkee, M.; Moulijn, J. A. Metal oxides as catalysts for the oxidation of graphite. *Carbon N. Y.* 1970, *8* (5), 295–302.
(45) Stobbe, E. R.; De Boer, B. A.; Geus, J. W. The reduction and oxidation behaviour of manganese oxides. *Int. J. Hydrogen Energy* 2013, *148–149* (3), 1557–1566.
(46) Stobbe, E. R.; De Boer, B. A.; Geus, J. W. The reduction and oxidation behaviour of manganese oxides. *Int. J. Hydrogen Energy* 2013, *148–149* (3), 1557–1566.
(47) Li, H.; Xu, Z.; Li, K.; Hou, X.; Cao, G.; Zhang, Q.; Cao, Z. Modification of multi-walled carbon nanotubes with cobalt phthalocyanine: effects of the templates on the assemblies. *J. Mater. Chem.* 2011, *21* (4), 1181–1186.
(48) Okpalugo, T. I. T.; Papakonstantinou, P.; Murphy, H.; McLaughlin, J.; Brown, N. M. D. High resolution XPS characterization of chemical functionalised MWCNTs and SWCNTs. *Carbon N. Y.* 2005, *43* (1), 153–161.
(49) Chen, X.; Wang, X.; Fang, D. A review on C1s XPS-spectra for some kinds of carbon materials. *Fullerenes Nanotub. Carbon Nanostructures* 2020, *28* (12), 1048–1058.
(50) Åhlund, J.; Nilson, K.; Schiessling, J. The electronic structure of iron phthalocyanine probed by photoelectron and X-ray absorption spectroscopies and density functional theory calculations. *Mg J. Chem. Phys.* 2006, *125*, 9780.
(51) Brena, B.; Luo, Y.; Nyberg, M.; Carniato, S.; Nilson, K.; Alfredsson, Y.; Åhlund, J.; Mårtensson, N.; Siegbahn, H.; Puglia, C. Equivalent core-hole time-dependent density functional theory calculations of carbon 1s shake-up states of phthalocyanine. *Phys. Rev. B* 2004, *70*, 195214.
(52) Watanabe, S. FePc and fepcf16 on rutile TiO_2(110) and (100): influence of the substrate preparation on the interaction strength. *Molecules* 2019, *24* (110), 1–20.
(53) Basiuk, E. V.; Huerta, L.; Basiuk, V. A. Noncovalent bonding of *3d* metal(II) phthalocyanines with single-walled carbon nanotubes: a combined dft and XPS study. *Appl. Surf. Sci.* 2019, *470*, 622–630.
(54) Briggs, D. X-ray photoelectron spectroscopy (XPS). *Handb. Adhes. Second Ed.* 2005, 621–622.
(55) Petraki, F.; Papaefthimiou, V.; Kennou, S. The electronic structure of ni-phthalocyanine/metal interfaces studied by X-ray and ultraviolet photoelectron spectroscopy. 2007.
(56) Yang, J.; Toshimitsu, F.; Yang, Z.; Fujigaya Abc, T.; Nakashima, N. Pristine carbon nanotube/iron phthalocyanine hybrids with a well-defined nanostructure show excellent efficiency and durability for the oxygen reduction reaction. *J. Mater. Chem.*

A 2017, *5*, 1184–1191.
(57) Bassiouk, M.; Alvarez-Zauco, E.; Basiuk, V. A. -Tetraphenylporphine ligand on surfaces of highly oriented pyrolytic graphite and single-walled carbon nanotubes: insights from scanning tunneling microscopy. *J. Nanosci.* 2011, *11* (6), 5457–5468.
(58) Basiuk, V. A.; Bassiouk, M. Nanoassembly of meso-tetraphenylporphines on surfaces of carbon materials: initial steps as studied by molecular mechanics and scanning tunneling microscopy. *J. Nanosci. Nanotechnol.* 2008, *8*, 259–267.
(59) Braun, J.; Limbach, H. H.; Schlabach, M.; Wehrle, B.; Kocher, M.; Vogel, E. NMR study of the tautomerism of porphyrin including the kinetic HH/HD/DD isotope effects in the liquid and the solid state. *J. Am. Chem. Soc.* 1994, *116* (15), 6593–6604.
(60) Krasnov, P. O.; Basova, T. V.; Hassan, A. Interaction of metal phthalocyanines with carbon zigzag and armchair nanotubes with different diameters. *Appl. Surf. Sci.* 2018, *457*, 235–240.
(61) Correa, J. D.; Orellana, W. Optical response of carbon nanotubes functionalized with (free-base , Zn) porphyrins , and phthalocyanines : a DFT study. *Phys. Rev. B* 2012, *86*, 125417/1-6.
(62) Bassiouk, M.; Álvarez-Zauco, E.; Basiuk, V. A. Self-assemblies of meso -tetraphenylporphine ligand on surfaces of highly oriented pyrolytic graphite and single-walled carbon nanotubes : insights from scanning tunneling microscopy and molecular modeling. 2011, *11* (6), 5457–5468.
(63) Trotochaud, L.; Young, S. L.; Ranney, J. K.; Boettcher, S. W. Nickel-iron oxyhydroxide oxygen-evolution electrocatalysts: the role of intentional and incidental iron incorporation. *J. Am. Chem. Soc.* 2014, *136* (18), 6744–6753.
(64) Liu, Y.; Jiang, H.; Zhu, Y.; Yang, X.; Li, C. Transition metals (Fe, Co, and Ni) encapsulated in nitrogen-doped carbon nanotubes as bi-functional catalysts for oxygen electrode reactions. *J. Mater. Chem. A* 2016, *4* (5), 1694–1701.
(65) Morlanés, N.; Joya, K. S.; Takanabe, K.; Rodionov, V. Perfluorinated cobalt phthalocyanine effectively catalyzes water electrooxidation. *Eur. J. Inorg. Chem.* 2015, *2015* (1), 49–52.
(66) Jia, H.; Yao, Y.; Zhao, J.; Gao, Y.; Luo, Z.; Du, P. A novel two-dimensional nickel phthalocyanine-based metal-organic framework for highly efficient water oxidation catalysis. *J. Mater. Chem. A* 2018, *6* (3), 1188–1195.
(67) O ¨ Ztas -, B.; Akyü Z, D.; Koca, A. Immobilization of alkynyl functionalized manganese phthalocyanine via click electrochemistry for electrocatalytic oxygen evolution reaction. *Phys. Chem. Chem. Phys* 2017, *19*, 26121.
(68) Song, M. Y.; Yang, D. S.; Singh, K. P.; Yuan, J.; Yu, J. S. Nitrogen-doped hollow carbon spheres with highly graphitized mesoporous shell: role of Fe for oxygen evolution reaction. *Appl. Catal. B Environ.* 2016, *191*, 202–208.
(69) Suen, N. T.; Hung, S. F.; Quan, Q.; Zhang, N.; Xu, Y. J.; Chen, H. M. Electrocatalysis for the oxygen evolution reaction: recent development and future perspectives. *Chem. Soc. Rev.* 2017, *46* (2), 337–365.
(70) Diaz-Morales, O.; Ferrus-Suspedra, D.; Koper, M. T. M. The importance of nickel oxyhydroxide deprotonation on its activity towards electrochemical water oxidation. *Chem. Sci.* 2016, *7* (4), 2639–2645.
(71) Bediako, D. K.; Surendranath, Y.; Nocera, D. G. Mechanistic studies of the oxygen evolution reaction mediated by a nickel-borate thin film electrocatalyst. *J. Am. Chem. Soc.* 2013, *135* (9), 3662–3674.

4

Chapter 4

Interactions of *3d*-metal (II) phthalocyanines with a Stone-Wales defect on single-walled carbon nanotubes: A theoretical study

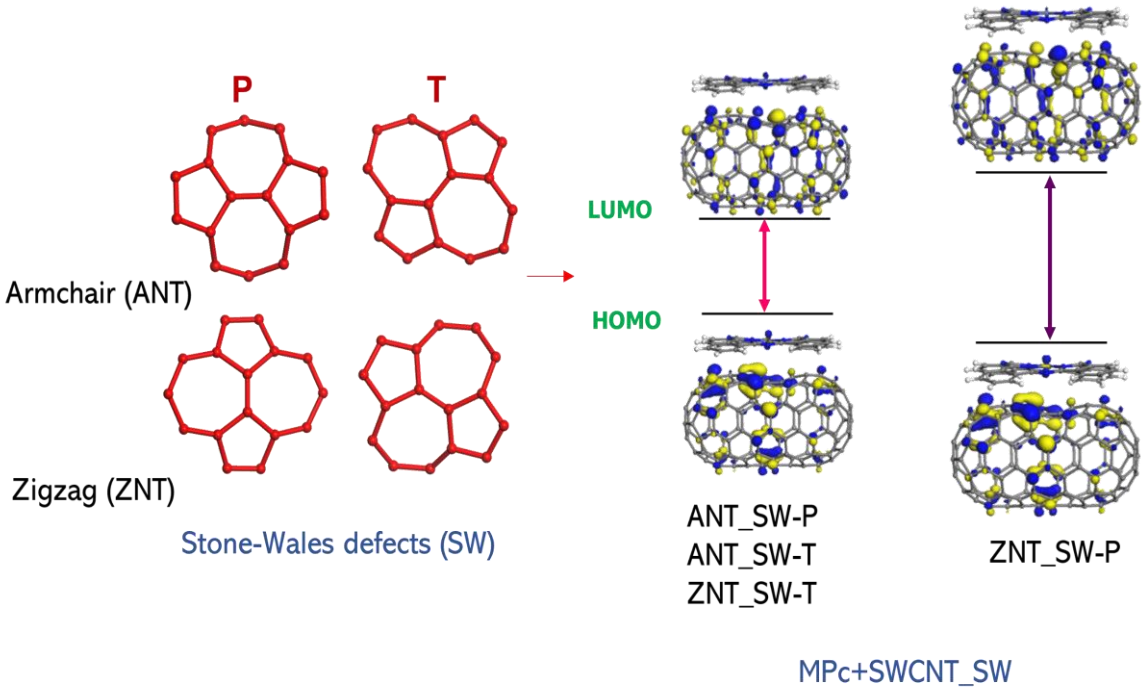

Published as
Lina M. Bolivar-Pineda and Vladimir A. Basiuk. J. Appl. Phys. 2020, 127 (2), 025302

Abstract

The presence of structural defects alters the properties of a material. Among the various defects in carbon nanotubes, single vacancies and Stone-Wales (SW) defects are the simplest and most common. In this chapter, a density functional theory analysis of the influence of a Stone-Wales defect incorporated into armchair and zigzag single-walled carbon nanotube models functionalised noncovalently with unsubstituted nickel(II) and cobalt(II) phthalocyanines as representative metal phthalocyanines, was performed at the PBE-D/DNP level of theory. The data obtained (bonding and frontier orbital energies, geometries, charge and spin distribution) were compared with the results for similar systems based on defect-free nanotube models. The Stone-Wales defect was incorporated into each nanotube model in different orientations with respect to the nanotube axis, namely with the (7,7) junction tilted, parallel in armchair nanotube or perpendicular in zigzag nanotube with respect to the axis. The formation energy of Stone-Wales defect-containing single-walled carbon nanotubes depends on the defect orientation and nanotube chirality. It is lowest for the armchair tube where the (7,7) junction is tilted to the tube axis and highest for a zigzag tube with the same defect orientation. In almost all cases, HOMO-LUMO gap narrowing was observed.

4.1. Introduction

The covalent and noncovalent functionalisation of carbon nanotubes of both multi-walled and single-walled, with macrocyclic compounds such as phthalocyanines, has been addressed in numerous studies due to the broad spectrum of applications that such nanohybrid materials can offer (see Chapter 1). [1,2,11,12,3–10] The performance of functional materials and devices relies upon the particular distribution and position of Pcs molecules on CNTs sidewalls (especially in the case of non-covalent functionalisation, when π- π stacking interactions between the aromatic rings are explored), but also the nature of central metal atom of the Pc. CNTs size and chirality also play a role. [13] In this context, it is necessary to consider that carbon nanotubes (as any graphene-derived materials) cannot be produced with a perfect structure, they usually contain different types of topological defects incorporated during their growth (synthesis) or purification, irradiation or chemical preparation. The most important ones are vacancies, Stone-Wales (SW) defects, octagon-pentagon pairs as well as adatoms, all of which can significantly change the electrical, chemical, and mechanical properties of carbon nanomaterials. [14–18]

The formation of a SW defect consists of the 90° rotation of only two carbon atoms (C-C) in the plane of the hexagonal lattice, creating two pairs of five-membered and seven-membered rings (5775). This is the only mechanism of defect generation that does not alter the nature of the sp^2 backbone. [15,18–20] The abundance of SW defects might be desirable for many novel chemical and electronic applications employing interlinked CNTs. The defect formation and its effects on the structural and electronic properties of nanotubes have been examined theoretically by a number of researchers,[14,16,20–27] who have demonstrated that incorporation of SW defects can reduce or close the band gap in wide band gap CNTs and therefore increase their metallic character.[16,23,28] Alternatively, it has been shown to induce band gap opening in narrow band gap carbon nanotubes. Naturally, the number of SW defects and their orientation in the tube structure can further enhance the change from a semiconductor nanotube to a conductor, as well as modify chirality and diameter.[14,24] Previous related studies have shown that the nanotube stability increases as the defects are found closer to the open end of the SWCNT,[15] and that C–C bonds associated with SW defects are more reactive compared to those in a perfect hexagon,[20,27] thus enhancing the adsorption of ozone [26], Ni [27] atoms and alkanethiol molecules,[29] as well as in covalent bond formation when interacting with carboxyl groups,[30] methylene CH_2 [20] and amine groups.[31,32]

Despite the importance of the phenomena mentioned above, the relevant information on the influence of SW defects on the structural, chemical and physical properties for a wide variety of hybrid systems on CNTs systems is relatively scarce or at least controversial. This is especially true for nanotubes noncovalently functionalised with Pcs. For example, a few studies (including our own reports) addressed the adsorption of Pcs on defect-free carbon nanotubes, [13,33–36] but only one was focused on the adsorption of free-base phthalocyanine on Stone-Wales defect-containing single-walled CNTs models.[19] One should especially emphasise that the experimental characterisation of carbon nanohybrids non-covalently functionalised with organic compounds is not an easy task, and the data provided is often insufficient to make well-grounded conclusions on the mechanisms of interaction between organic functionalising species

with a carbon nanomaterial.[35] Under such circumstances, it is necessary to employ theoretical tools, in particular density functional theory (DFT) calculations, which are capable of providing valuable information on the geometry, stability and electronic characteristics of Pc–carbon materials such as carbon nanotubes [34–36] and fullerenes [37–39].

The goal of the studies reported in the present chapter was to carry out a DFT analysis of the influence of a Stone-Wales defect incorporated into armchair and zigzag single-walled CNTs models functionalised noncovalently with unsubstituted nickel(II) and cobalt(II) phthalocyanines (MPc, where M = Ni^{2+}, Co^{2+}) as representative Pc, since these showed better catalytic performance in Chapter 3. The data obtained are compared with our previous DFT results reported for similar the hybrids of metal monophthalocyanines with defect-free nanotube models. [34]

4.2. Results and discussion

4.2.1. A Stone-Wales defect in single walled carbon nanotubes models

The carbon nanotube models employed to study the influence of a SW defect on the non-covalent interactions of single-walled CNTs with CoPc and NiPc were derived from the armchair (5,5) and zigzag (10,0) nanotubes (ANT and ZNT, respectively), which are composed of 120 and 140 carbon atoms, and whose ends are capped with C_{60} and C_{80} (spherical with I_h symmetry) fullerene hemispheres, respectively. [34–36,40,41] The incorporation of a SW defect in a nanotube is possible in two different ways resulting in four different models depending on the defect orientation with respect to the nanotube axis (Fig.4. 1). When the (7,7) junction is tilted with respect to the nanotube axis as in the Fig.4. 1e and Fig.4. 1f, the defects are referred to as SW-T, and the nanotube models as ANT_SW-T and ZNT_SW-T. In the other two alternative models the SW defect is oriented with the (7,7) junction parallel in ANT (Fig.4. 1c) and perpendicular in ZNT (Fig.4. 1d) with respect to the nanotube axis (SW-P notation in both cases; ANT_SW-P and ZNT_SW-P models). These models were used in the recent analysis of adsorption of base-free phthalocyanine on single-walled CNTs with SW defects.[19]

In the present study, the structures of four isolated models of defective nanotubes were fully optimised, and their computed properties were compared to those of defect-free ANT and ZNT nanotubes. We examined the geometry parameters (bond lengths, bond angles and dihedral angles), formation energies, HOMO, LUMO, LUMO-HOMO gap energies and Mulliken charge distribution. The calculated energy of SW defect formation for any particular CNT with diameter d increases monotonically with the angle θ that the C-C bond common to the two heptagons forms with the tube axis. Their values were calculated by considering the total energies presented in Table 4. 1 and those published previously for defect-free ANT and ZNT. [34] The formation energy of 71.02 kcal/mol is highest for ANT_SW-P with $\theta = \pi/2$) and 20% lower for ANT_SW_T with $\theta = \pi/6$ (49.39kcal/mol). For the zigzag tubes the difference is even larger since ZNT_SW-T with $\theta = \pi/3$ has a formation energy of 63.84 kcal/mol, while ZNT_SW-P with $\theta = 0$ necessitates 33.93 kcal/mol. When considering a series of periodic nanotube models

with chiralities (*n*,0) and (*n*,*n*), Pan et al.,[24] as well as Kabir and Van Vliet[42] reported a similar dependence on the orientation of SW dislocation dipole θ and diameter. In particular, they indicated that the greater the diameter the greater the formation energy for any particular θ or orientation of SW defect, converging toward the value calculated for graphene (114.38 kcal/mol). [42]

One of the first visible changes due to the incorporation of pentagons and heptagons as imperfections in the sp^2 hexagonal lattice, is the distortion of curvature of the nanotubes [43,44] after geometry optimisation, as can be seen in Fig.4. 1. The presence of these defect generates an increase and/or decrease in the diameter of nanotube in different points along the tube axis within the same structure.[45,46] Where precisely the diameter changes and by how much depends on a particular orientation of [7,7] C–C bond, whereas in a defect-free closed-end nanotube, the diameter is a function of the size of the fullerene cap only. The correlation between the angle θ of the central [6,6] C–C bond and ΔE_{SW} value can be explained qualitatively in terms of the curvature-induced rehybridisation upon defect formation. The Coulomb repulsion inside the nanotube increases with increasing curvature, leading to significant rehybridisation of σ and π orbitals. The real hybridisation in CNTs is intermediate between sp^2 and sp^3, that is, $sp^{2+\tau}$. [42] For a particular CNT with diameter *d*, the rehybridisation τ decreases with increasing θ. For the defect-containing structure (SWCNT_SW), the local curvature at the site of the [7,7] C–C bond increases for higher θ, and correspondingly τ decreases, which in turn increases ΔE_{SW} [42] (Table 4. 2). Also, when comparing the C-C bond length for nanotubes with and without the defect, we find it to be shorter in the former case (Table 4. 2).

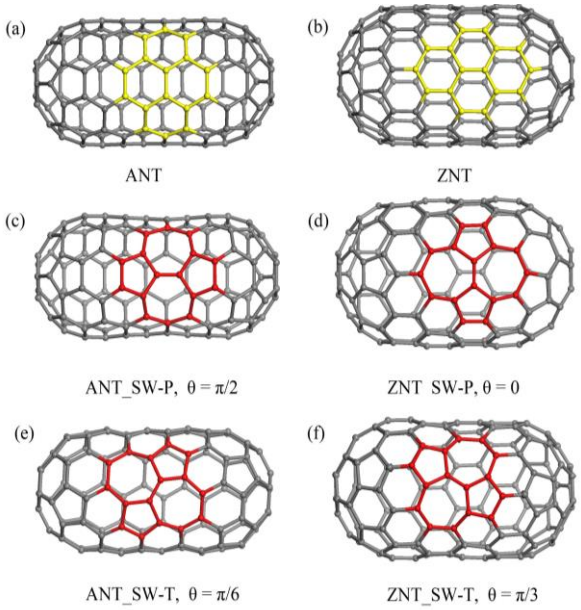

Fig.4. 1. Optimised geometries for armchair (ANT) and zigzag (ZNT) nanotube models, incorporating SW defects in parallel (in ANT) or perpendicular (in ZNT) and tilted orientation (SW-P and SW-T, respectively) of the (7,7) junction with respect to nanotube axis. Two pentagonal and two heptagonal rings forming SW defect (sixteen carbon atoms) are highlighted in red. θ is the angle between the rotating C–C bond in the pristine SWCNT and the nanotube axis.

Table 4. 1 Total energies (in Ha) for separated components and noncovalent hybrids MPc+SWCNT_SW, formation energies ΔE (in kcal/mol) for the hybrids, HOMO, LUMO and HOMO-LUMO gap energies (in eV), calculated using the PBE GGA functional with Grimme's dispersion correction in conjunction with DNP basis set.

System	E_{total} (Ha)	ΔE (kcal/mol)	E_{HOMO} (eV)	E_{LUMO} (eV)	E_{gap} (eV)
ANT_SW-P	-4569.0963321		-5.105	-4.789	0.316 (0.648) [a]
ANT_SW-T	-4569.1308181		-5.333	-4.757	0.576 (0.648)
ZNT_SW-P	-5330.8183555		-5.652	-5.563	0.089 (0.388)
ZNT_SW-T	-5330.7706864		-5.571	-5.443	0.128 (0.388)
CoPc	-3048.5589861		-5.043	-4.021	1.023
NiPc	-3174.1081023		-5.064	-3.601	1.463
CoPc+ANT_SW-P	-7617.7136811	-36.62 (-35.73) [a]	-4.923	-4.647	0.276 (0.609)
CoPc+ANT_SW-T	-7617.7501554	-37.87 (-35.73)	-5.134	-4.604	0.530 (0.609)
CoPc+ZNT_SW-P	-8379.4405070	-39.64 (-40.03)	-5.370	-5.291	0.079 (0.065)
CoPc+ZNT_SW-T	-8379.3901180	-37.93 (-40.03)	-5.308	-5.268	0.039 (0.065)
NiPc+ANT_SW-P	-7743.2559499	-32.33 (-33.07)	-4.877	-4.599	0.278 (0.610)
NiPc+ANT_SW-T	-7743.2915988	-33.06 (-33.07)	-5.118	-4.570	0.547 (0.610)
NiPc+ZNT_SW-P	-8504.9829471	-38.00 (-37.61)	-5.375	-5.289	0.086 (0.070)
NiPc+ZNT_SW-T	-8504.9343370	-37.41 (-37.61)	-5.325	-5.263	0.062 (0.070)

[a] For comparison, ΔE and E_{gap} values obtained previously for the defect-free structures [34] are presented in parenthesis.

The length difference ($\Delta b = b_{perf} - b_{def}$) is larger for larger θ values: ANT_SW-P (θ = π/2) > ANT_SW-T (θ = π/6), and ZNT_SW-T (θ = π/3) > ZNT_SW-P (θ = 0). Thus, the structures ANT_SW-T and ZNT_SW-P are lower in energy than ANT_SW-P and ZNT_SW-T models due to comparatively higher rehybridisation. This phenomenon was observed for periodic nanotube models (with no closed ends). [42]

Table 4. 2. Carbon-carbon bond lengths before (SWCNT) and after rotation (SWCNT_SW) for zigzag and armchair nanotubes studied here. Bond lengths for different defect orientations are shown. The difference between bond lengths for pristine and defected structures is calculated as $(\Delta b = b_{perf} - b_{def})$

SWCNT	ΔE_{SW} (kcal/mol)	[6,6] C-C bond (Å)	SWCNT_SW	[7,7] C-C bond (Å)	$\Delta b = b_{perf} - b_{def}$
ANT-P	71.02	1.4400	ANT_SW-P	1.3620	0.0780
ANT-T	49.39	1.4200	ANT_SW-T	1.3980	0.0220
ZNT-P	33.93	1.4150	ZNT_SW-P	1.3780	0.0370
ZNT-T	63.84	1.4280	ZNT_SW-T	1.3470	0.0810

4.2.1.1. Torsion angles

Another geometric parameter convenient for the characterisation of structural changes due to SW defect is dihedral or torsion angle (ϕ). Fig.4. 2 shows the fragments (sixteen carbon atoms) of geometries optimised for defect-free ANT and ZNT and those incorporating Stone-Wales defects in different orientations, along with the set of values of dihedral angles for each fragment. One can see that in the defect-free ANT, the angles perpendicular to the nanotube axis (ϕ_p; for example, C(1)-C(2)-C(3)-C(15) in ANT-P) have zero values, whereas the 'horizontal' angles (ϕ_h; exemplified by C(14)-C(1)-C(2)-C(3) in ANT-P) parallel to nanotube axis vary between -21°.9 and 21.9°, for both perpendicular (ANT-P) and tilted orientation (ANT-T) of the[7,7] C-C bond. In the case of zigzag chirality (ZNT-P and ZNT-T), ϕ_p vary between -20.7° and 20.9° and, ϕ_h between -5.6° and 6.8°. The introduction of a SW defect generally results in a strong distortion of the dihedral angles, as illustrated by the following ranges for each particular single-walled CNT model: for ANT_SW-P, ϕ_p between -48.5° and 48.8°, and ϕ_h between -26.6° and 26.7°; for ANT_SW-T, ϕ_p between -13.1° and 14.8°, and ϕ_h between -29.8° and 30.6°; for ZNT_SW-P, ϕ_p between -24.0° and 24.1°, and ϕ_h between -16.7° and 15.0°; for ZNT_SW-P, ϕ_p between -40.5° and 26.2°, and ϕ_h between -32.1° and 20.1°. At the same time, the corresponding bond angle distortion turns out to be relatively small in all cases.

4.2.1.2. HOMO-LUMO gap energies

The difference between HOMO and LUMO levels represents the band gap energy.[45,47] Since the band gap is one of the critical parameters in the design of CNTs-based systems for electronics applications, its behaviour upon Stone-Wales defect formation is of special interest.[48] Table 4. 1 compares band gap values for ANT and ZNT models with and without a SW defect. Regardless of the nanotube chirality and defect orientation, gap narrowing is always observed. For SW-P models, the gap energy decreases from 0.648 (defect-free ANT) and 0.388 eV (defect-free ZNT) to 0.316 and 0.089 eV, respectively; for the corresponding SW-T models, the decrease is less significant, to 0.576 and 0.128 eV. In other words, the smallest effect is found for ANT_SW-T. Besides that, armchair (5,5) nanotube models studied exhibit a wider band gap than zigzag (10,0) models, which can be attributed not only to chirality, but to diameter and consequently sidewall curvature.[46] One can add that in chemical terms, a smaller HOMO-LOMO gap implies higher reactivity and correspondingly lower stability. [14]

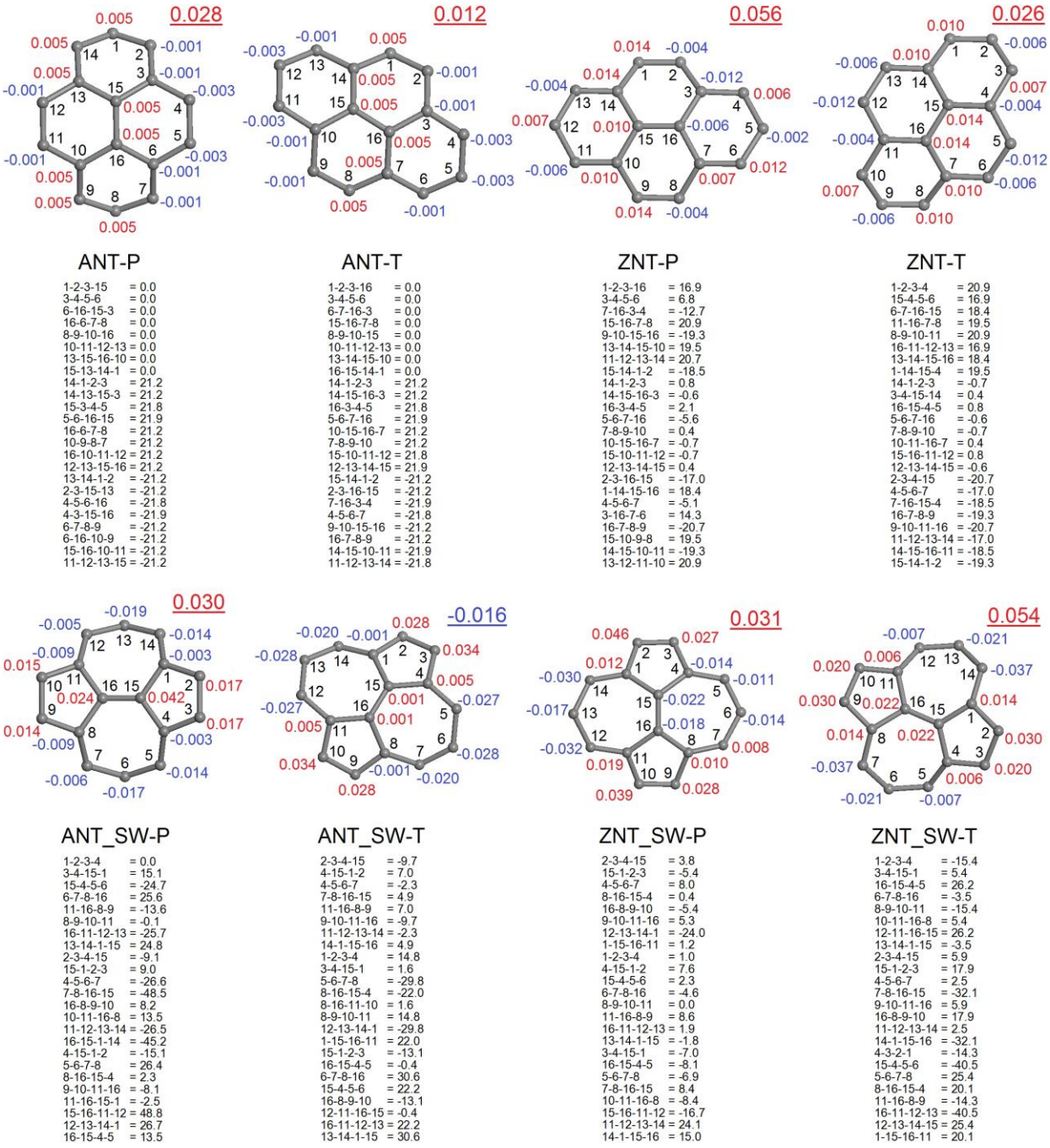

Fig.4. 2. Fragments (16 carbon atoms; other atoms are omitted for clarity) of geometries optimised for defect-free ANT and ZNT (top structures) and those incorporating Stone-Wales defects in different orientations (bottom structures), along with the values of the dihedral angles (in degrees; only atom numbers without "C" symbols are shown for simplicity) and the Mulliken population charges. The numbers in blue denote negative charges, and those in red positive charges of carbon atoms. The underlined values (upper right corner of each fragment) specify the total charge on the 16 atoms.

4.2.1.3. Mulliken population analysis

One more aspect is the atomic charge redistribution caused by the defect incorporation, which we addressed using a Mulliken population analysis. The results are presented in Fig.4. 2 and include both individual charges on the 16 carbon atoms participating in the SW defect formation, and the total charge on this structural unit. The latter are positive in all cases before C-C bond rotation, from 0.012 to 0.056 e. They remain positive for three of the four defect-containing structures, with the largest changes found for ZNT_SW-T (from 0.026 to 0.054 e) and the smallest one, for ANT_SW-P (from 0.028 to 0.030 e). In other words, in the above two transformations electron acceptor properties increase. In the remaining two cases of ANT_SW-T and ZNT_SW-P a gain in electrons is observed, from 0.012 to -0.016 e and from 0.056 to 0.031 e, respectively; that is, with a SW defect in ZNT_SW-P this structure remains an electron acceptor, contrary to its counterpart ANT_SW-T, whose total charge becomes negative (like it was found elsewhere [49] for 585 defect).It is noteworthy,that the C atoms of [7,7] junction in most SW defect units keep the positive sign of charge of [6,6] bond atoms in defect-free nanotubes, the only exception being ZNT_SW-P. In the case of ANT_SW_P and ZNT_SW-T the positive charge increased, whereas for ANT_SW-T it decreased. It is also interesting to note that heptagon ring atoms tend to gain electrons, whereas pentagon atoms generally lose charge. Such a charge redistribution influences the reactivity and explains the mechanisms of covalent and non-covalent interactions with various chemical species. [50,51]

4.2.1.4. Distribution of frontier orbital HOMO and LUMO

The incorporation of a SW defect results in a frontier orbital redistribution, which is illustrated by HOMO-LUMO plots in Fig.4. 3. The extent of this redistribution depends on the particular nanotube model. The most pronounced changes as compared to the lobe shape in parent defect-free model were found for the HOMO of ANT_SW-P and the LUMO of ANT_SW-T where large lobes localised on the SW defect can be clearly observed. As for the distribution in the isolated phthalocyanines, the HOMO is located on the isoindole units of CoPc and NiPc, exclusively from the carbon atoms, while the contribution of the LUMO in CoPc is given only by the metal and in NiPc, the LUMO comes from two isoindole units and two pyrrole units. There is also a contribution from the azomethine nitrogen atoms (γ-N).

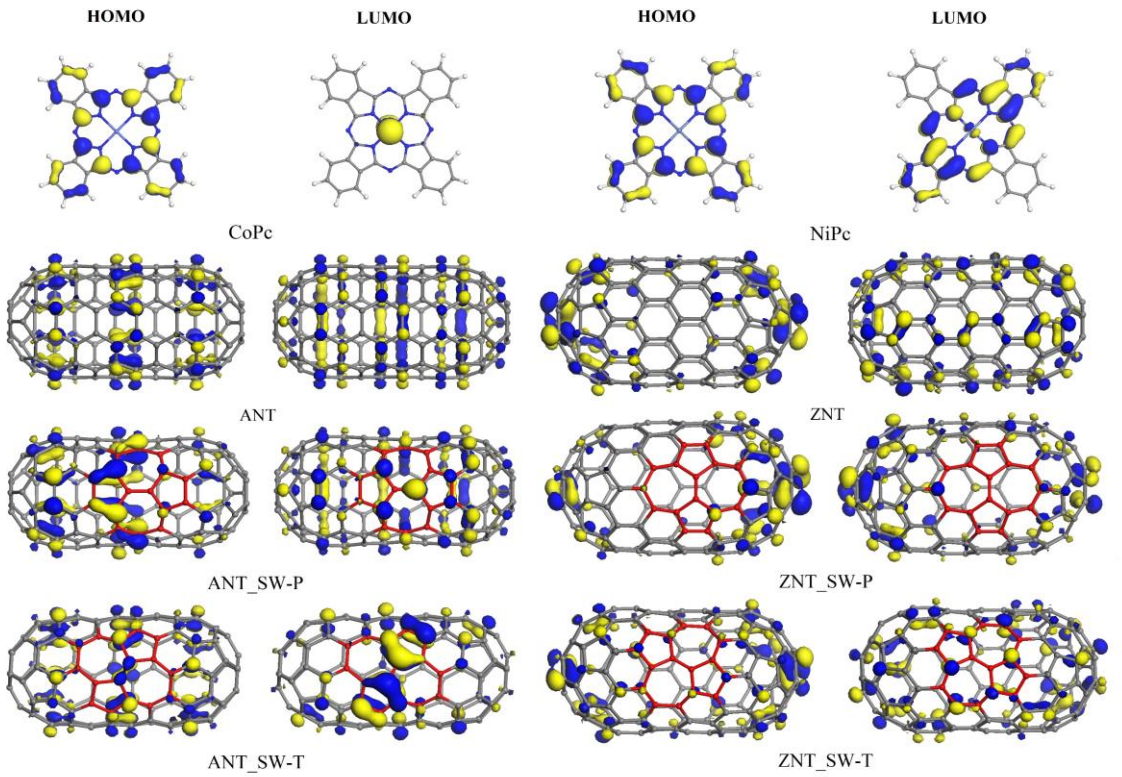

Fig.4. 3. HOMO and LUMO plots (isosurfaces at 0.03 arb.units.) for phtalocyanines (CoPc and NiPc) and Stone-Wales defect-containing armchair (ANT) and zigzag (ZNT) nanotube models. The two pentagonal and two heptagonal rings forming the SW defect (16 carbon atoms) are highlighted in red.

4.2.2. Hybrids of metal phthalocyanine and single-walled carbon nanotube with a Stone-Wales defect

The length of nanotube models with a SW defect employed in our calculations is barely enough to accommodate one MPc molecule, with its overwhelming part contacting the tubular part. We made attempts to use longer models, however this dramatically increased the computational cost and, most importantly, caused serious convergence problems, especially in the case of open-shell systems. The choice of spin-restricted *versus* unrestricted calculations on MPc+SWCNT_SW hybrids was based on the spin state of the central metal atom in the MPc component, that is, for Ni-containing systems closed-shell calculations were performed, whereas those including Co atoms were treated as open-shell systems.

To analyse the influence of SW defect on different parameters characterising the non-covalent interactions of a SWCNT with CoPc and NiPc, a comparison was made with the results of previous DFT computations on the adsorption of the same phthalocyanines on defect-free ANT and ZNT.[34] The data obtained are summarised in Table 4. 1, which shows the total energies for the separate components and non-covalent hybrids MPc+SWCNT_SW, the formation energies ΔE for the hybrids, HOMO, LUMO and HOMO-LUMO gap energies, and the Table 4. 3 which lists the shortest M···C_{SWCNT}, N···C_{SWCNT} and C_{MPc}···C_{SWCNT} distances between MPc and SWCNT, as well as N-M-N angles in the metal phthalocyanine molecules.

4.2.2.1. Nitrogen-Metal-Nitrogen angles

The optimised geometries of all of the MPc+SWCNT_SW hybrids considered here exhibit the important feature typical for non-covalent hybrids of phthalocyanines with a variety of nanotubes, including both cluster[19,35] and periodic models[13,33,52] of different diameters and chirality, studied at different levels of DFT. It consists of strong bending distortion of a usually planar macrocyclic ring system occurs in order to increase the area of contact with the nanotube sidewall, as illustrated Fig.4. 4. The degree of distortion can be quantitatively interpreted by comparing the values of N-M-N angles (diagonally opposite nitrogen atoms of the coordination sphere MN4, nitrogen atoms of the isoindole units; Fig.4. 5) in isolated monophthalocyanine, which are approximately 179-180°, with those when the macrocycle is adsorbed on single-walled CNT (Fig.4. 4). One can see that the strongest distortion occurs for both hybrids with ZNT_SW-P, where N-M-N angle decreases to 175.6° in CoPc and to 174.2° in NiPc. The strong non-covalent interactions between nanotube and the phthalocyanine make the central metal atom move slightly towards the nanotube sidewall and out of the macrocyclic plane. This behaviour is similar to the one observed for MPc hybrids with defect-free SWCNT models, [34] including the fact that the distortion is generally greater on a zigzag nanotube.

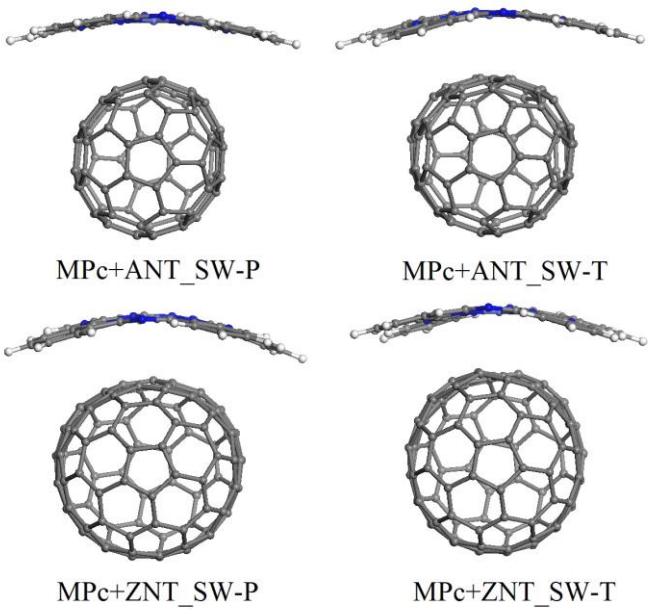

Fig.4. 4. Optimised geometries for non-covalently hybrids of MPc and single-walled carbon nanotubes with a Stone-Wales defect, illustrating bending distortion of the macrocycle ring plane.

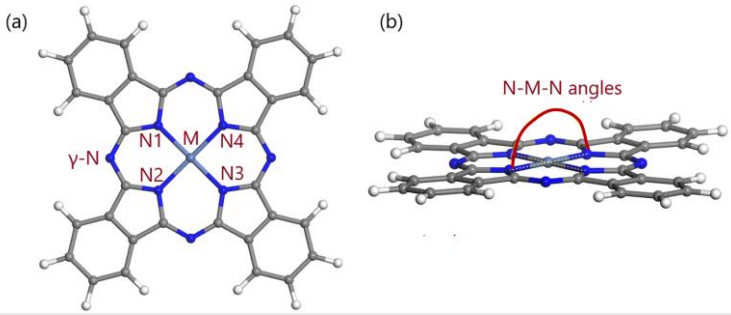

Fig.4. 5.(a) Structure of an isolated MPc, highlighting the nitrogen atoms of the coordination sphere (MN4) and the nitrogen azamethine and **(b)** representation of the N-M-N angles analysed both in the isolated MPc molecule and on the nanotube surface, where N are the diagonally opposite nitrogen atoms (N1-M-N3, N2-M-N4)

4.2.2.2. Closest contact

The shortest distance between the metal and carbon atoms of the nanotube defect (M···C$_{SWCNT}$;Table 4. 3) spans from 2.899 Å in CoPc+ANT_SW_T to 3.150 Å in NiPc+ZNT_SW-T. Compared to the corresponding distances in hybrids with defect-free nanotubes, they tend to increase slightly for ANT_SW-P and ZNT_SW-T (roughly by 0.05-0.10 Å) and to decrease in the case of ANT_SW-T and ZNT_SW-P (by 0.07-0.12 Å). The longest M···C$_{SWCNT}$ distances were found in the hybrids of zigzag model with SW-T defects, namely 3.137 Å for CoPc and 3.150 Å for NiPc. The nitrogen atoms forming shortest N···C$_{SWCNT}$ distances are those belonging to the MN$_4$ coordination sphere or γ-N atoms (the latter situation being more frequent), with separations of 3.035-3.186 and 3.034-3.110 Å, respectively. The closest contact between heteroatoms in MPc and single-walled CNT is not always M···C$_{SWCNT}$: in three hybrids (CoPc+ZNT_SW-T, NiPc+ANT_SW-P and NiPc+ZNT_SW-T) of eight, it is N···C$_{SWCNT}$. Furthermore, in half of the hybrids C$_{MPc}$···C$_{SWCNT}$ turns out to be the shortest separation: namely, for CoPc+ANT_SW-P (2.951 Å), CoPc+ZNT_SW-T (2.941 Å), NiPc+ANT_SW-P (2.982 Å) and NiPc+ZNT_SW-T (3.007 Å).

4.2.2.3. Formation energies

The most important issue we intended to address is how Stone-Wales defect incorporation influences the strength of MPc bonding to single-walled CNT. Compared to MPc hybrids with defect-free nanotubes,[34] ΔE values decrease (that is, bonding strength increases) for three hybrids, namely by 0.89kcal/mol for CoPc+ANT_SW-P, by 2.14 kcal/mol for CoPc+ANT_SW-T and by 0.39 kcal/mol for NiPc+ZNT_SW-P, (Table 4. 1). An opposite effect was found for four hybrids CoPc+ZNT_SW-T, CoPc+ZNT_SW-P, NiPc+ANT_SW-P and NiPc+ZNT_SW-T, where ΔE increases by 0.39, 2.1, 0.74 and 0.2 kcal/mol. In the case of NiPc+ANT_SW-T the variation is negligible (an increase by 0.01 kcal/mol). In general, the binding energy for armchair models is stronger (by 1.25 kcal/mol for CoPc and 0.73 kcal/mol for NiPc) with a SW_T defect than with a SW-P defect, in contrast to zigzag nanotubes where the interaction with SW-P is stronger (by 1.71 kcal/mol for CoPc and 0.59 kcal/mol for NiPc) than with SW_T, similar to the adsorption of metal-free H$_2$Pc on the same nanotube models.[19] In other words, the interaction strength depends on both the single-walled CNT chirality and the orientation of the Stone-Wales defect, matching the order of defect formation energies of

ANT_SW-P > ANT_SW_T and ZNT_SW-T > ZNT_SW-P (see Sec.4.2.1).

4.2.2.4. HOMO-LUMO gap energies

We also analysed the HOMO, LUMO and HOMO-LUMO gap energies (Table 4. 1) as well as the corresponding orbital plots (Fig.4. 6). Compared to the gap width calculated for CoPc and NiPc with defect-free SWCNT,[34] SW defect-containing hybrids exhibit variable behaviour. For most (six of eight) hybrids, gap narrowing can be observed, which is the least for NiPc+ZNT_SW-T (by 0.008 eV) and the most for CoPc+ANT_SW-P (by 0.333 eV). The two exceptions are the hybrids with ZNT_SW-P, where E_{gap} insignificantly increased by 0.014 (CoPc) and 0.016 eV (NiPc). In terms of the magnitude of the change, the strongest one is found for both hybrids with ANT_SW-P, for which the gap energy reduces more than by half: by 0.333 (CoPc) and 0.332 eV (NiPc). When comparing gap energies for MPc+SCWNT_SW hybrids with those of the respective isolated nanotube models, one can see that non-covalent bonding with phthalocyanines tends to narrow the HOMO-LUMO gap. The exception is NiPc+ANT_SW-T, where E_{gap} increases insignificantly, by 0.001 eV. Regardless of the presence of defect, the gap is considerably broader for all hybrids with ANT compared with ZNT, matching E_{gap} of the corresponding isolated nanotube models. Further differences between them depend more on SW defect orientation, rather than on the central metal atom.

Table 4. 3. The shortest M···C_{SWCNT}, N···C_{SWCNT} and C_{MPc}···C_{SWCNT} distances (in Å) between MPc and single-walled CNT models, as well as N-M-N angles in MPc components, calculated using the PBE GGA functional with Grimme's dispersion correction in conjunction with DNP basis set.

System	M···C $_{SWCNT}$ (Å)	N···C_{SWCNT} (Å)	C_{MPc}···C_{SWCNT} (Å)	N-M-N (°)
CoPc				179.2, 179.3
NiPc				179.4, 179.8
CoPc+ANT_SW-P	3.020 (2.969) [a]	3.050 (3.106) [b]	2.951	178.4, 179.2
CoPc+ANT_SW-T	2.899 (2.969)	3.035 [c]	3.018	179.1, 179.4
CoPc+ZNT_SW-P	2.951 (3.069)	3.070 (3.091) [b]	3.042	175.6, 179.4
CoPc+ZNT_SW-T	3.137 (3.069)	3.034 (3.091) [b]	2.941	178.1, 178.5
NiPc+ANT_SW-P	3.141 (3.043)	3.085 (3.186) [b]	2.982	176.4, 179.8
NiPc+ANT_SW-T	3.004 (3.043)	3.095 [c]	3.085	177.2, 177.3
NiPc+ZNT_SW-P	3.004 (3.106)	3.110 (3.133) [b]	3.051	174.2, 179.3
NiPc+ZNT_SW-T	3.150 (3.106)	3.129 [c]	3.007	177.3, 178.2

[a] For comparison M···C_{SWCNT} values obtained previously for the defect-free structures [34] are presented in parenthesis.
[b] The shortest distance N···C_{SWCNT} is formed with one of the γ-N atoms, with the shortest distance N···C_{SWCNT} for the N atom of the MN4 coordination sphere is given in parenthesis.
[c] The shortest distance N···C_{SWCNT} is formed with the N atom of the MN4 coordination sphere.

4.2.2.5. Distribution of frontier orbital HOMO and LUMO

A closely related aspect is the frontier orbital distribution. In CoPc and NiPc hybrids with defect-free ANT and ZNT, both HOMO and LUMO are localised mainly on the carbon nanotube.[34] The presence of the SW defect gives rise to variation in the HOMO-LUMO distribution in all hybrids (Fig.4. 6), but to a different degree, depending on the particular system. For most of them, the above pattern with HOMO and LUMO mainly localised on single-walled CNT remains. Additionally, a variable minor fraction of both orbitals can be found on MPc, an effect that is most evident for the HOMO of CoPc+ANT_SW-T. Only the two hybrids with ZNT_SW-T exhibit a different behaviour. Here, the HOMO is shifted almost completely to the MPc, and the LUMO is localised exclusively (for the given isosurface value of 0.03 arb.units.) on the nanotube, which corresponds to the most common pattern for non-covalent hybrids of porphyrins and phthalocyanines with carbon nanoclusters (nanotubes and fullerenes), thus being indicative of weak charge transfer.[35,39]

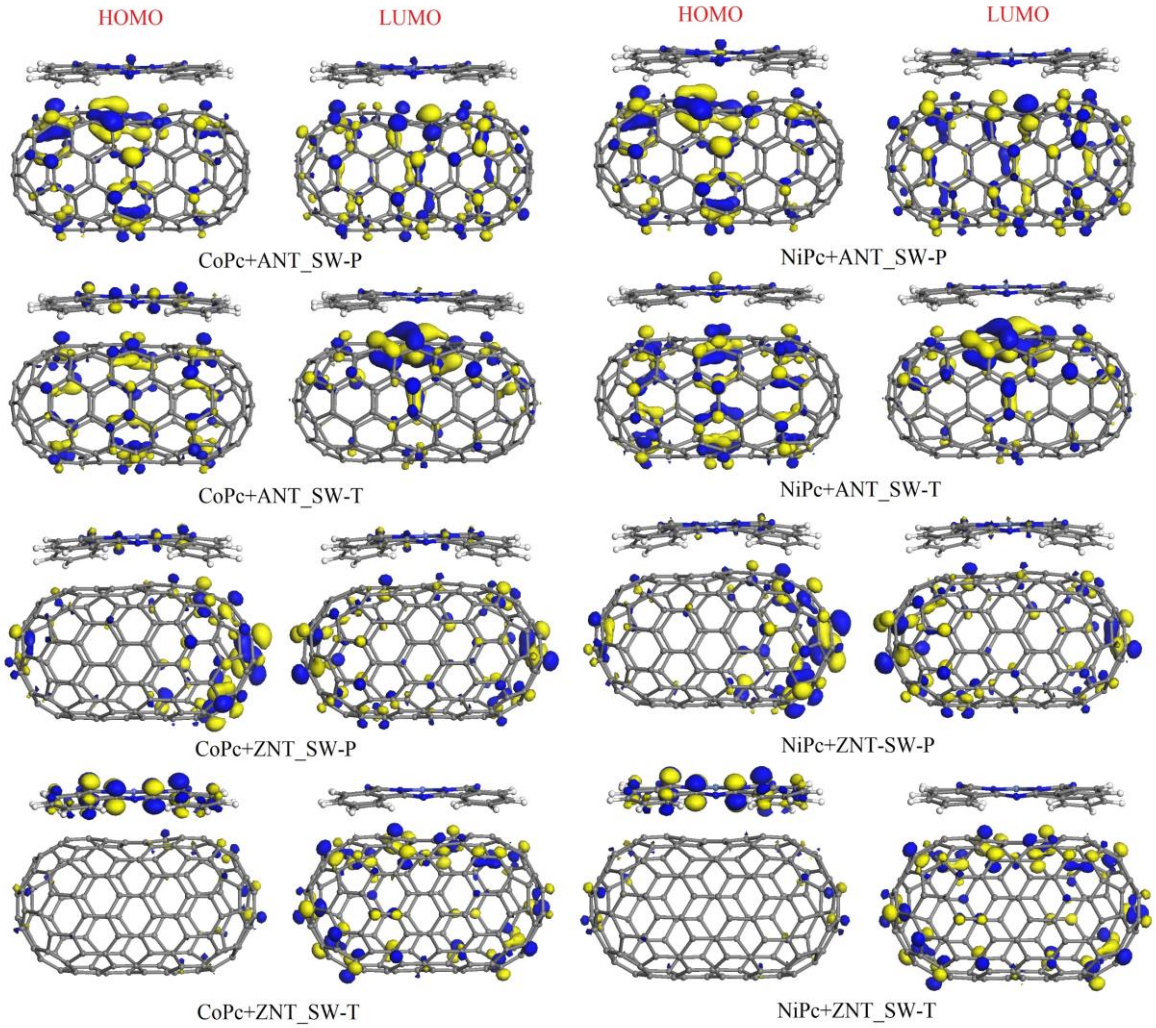

Fig.4. 6. HOMO and LUMO plots (isosurfaces at 0.03 arb.units.) for the non-covalent hybrids of CoPc and NiPc with Stone-Wales defect-containing armchair (ANT) and zigzag (ZNT) nanotube models.

4.2.2.6. Spin density

Finally, for open-shell systems containing paramagnetic CoPc we analysed the spin density plots (Fig.4. 7). The parent defect-free hybrids CoPc+ANT and CoPc+ZNT [34] had two very different patterns of spin distribution. The 'typical' one, in which the unpaired electron density is localised exclusively on the central Co atom, was found only on the zigzag nanotube, whereas in the armchair nanotube the spin density was totally shifted to the donor nitrogen atoms. In the present study, all the hybrids (including ANT-based ones) match the 'typical' pattern of CoPc+ZNT.[34] An additional feature found in CoPc+ANT_SW-P, CoPc+ANT_SW-T and CoPc+ZNT_SW-P is the appearance of minor spin lobes on carbon atoms of single-walled CNT model, at the site of contact between the interacting units (CoPc+ANT_SW-P and CoPc+ANT_SW-T) or even as far from it as at closed nanotube cap (CoPc+ZNT_SW-P). The spin density comparison is performed exclusively with the 'spin-up' lobes.

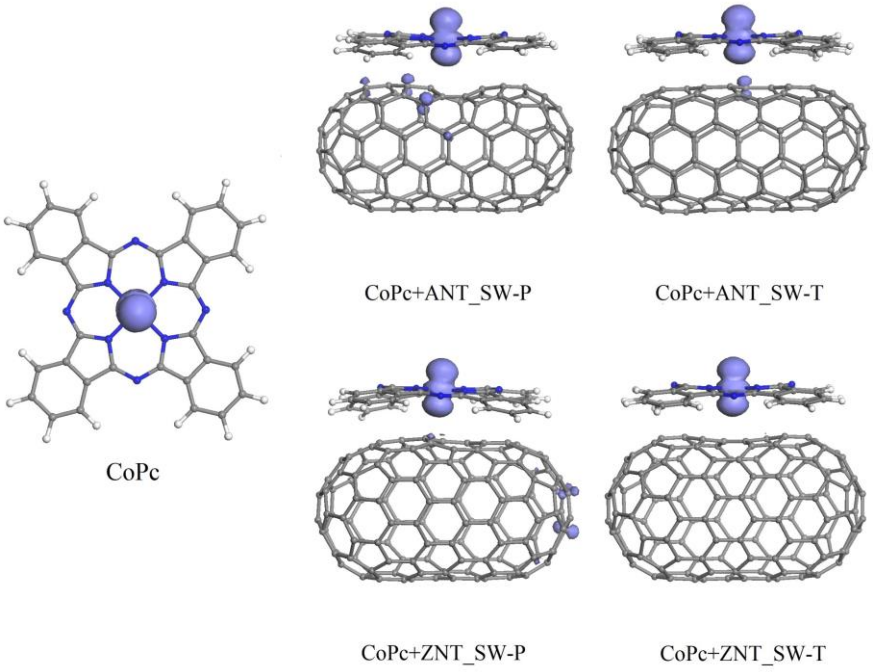

Fig.4. 7. Spin density plots (isosurfaces at 0.01 arb.units) for open-shell non-covalently hybrids of CoPc with Stone-Wales defect-containing armchair (ANT) and zigzag (ZNT) nanotube models.

4.3. Conclusions

The main results of this study can be summarised as follows:

The formation energy of Stone-Wales defect-containing single-walled CNTs depends on the defect orientation and the nanotube chirality, decreasing in the order ANT_SW-P (71.02 kcal/mol) > ZNT_SW-T (63.84 kcal/mol) > ANT_SW_T (49.39 kcal/mol) > ZNT_SW-P (33.93 kcal/mol).

In all cases HOMO-LUMO gap narrowing is observed for nanotube with the Stone-Wales defects. For the nanotubes models with the SW-P defect, the gap energy decreases from 0.648 (defect-free ANT) and 0.388 eV (defect-free ZNT) to 0.316 and 0.089 eV, respectively; for the corresponding nanotubes with SW-T, the decrease is less significant, namely to 0.576 and 0.128 eV.

Phthalocyanine molecules on the single-walled carbon nanotubes with Stone-Wales undergo strong bending distortion in order to increase the area of their contact with nanotube sidewall, like in the case of similar hybrids with defect-free nanotubes.

Compared to NiPc and CoPc hybrids with defect-free nanotubes, the formation energy ΔE decreases (that is, the bonding strength increases) for three hybrids CoPc+ANT_SW-P, CoPc+ANT_SW-T and NiPc+ZNT_SW-P, by 0.89, 2.14 and 0.39 kcal/mol. For four hybrids CoPc+ZNT_SW-T, CoPc+ZNT_SW-P, NiPc+ANT_SW-P and NiPc+ZNT_SW-T an opposite effect was found, where ΔE increases by 0.39, 2.1, 0.74 and 0.2 kcal/mol. In the case of NiPc+ANT_SW-T the variation is negligible (an increase by 0.01 kcal/mol).

For most hybrids, gap narrowing can be observed, which is the smallest for NiPc+ZNT_SW-T (by 0.008 eV) and the largest for CoPc+ANT_SW-P (by 0.333 eV), with respect to the defect-free systems. For the hybrids with ZNT_SW-P, E_{gap} insignificantly increased by 0.014 (CoPc) and 0.016 eV (NiPc). As compared with gap energies of the respective isolated nanotube models, non-covalent bonding with phthalocyanines also tends to narrow the HOMO-LUMO gap.

4.4. References

(1) Xu, Z.; Li, H.; Sun, H.; Zhang, Q.; Li, K. Carbon nanotubes with phthalocyanine-decorated surface produced by NH_3-assisted microwave reaction and their catalytic performance in Li/$SoCl_2$ battery. *Chinese J. Chem.* 2010, *28*, 2059–2066.

(2) Zhang, L.; Yu, H.; Liu, L.; Wang, L. Study on the preparation of multi-walled carbon nanotube/phthalocyanine composites and their optical limiting effects. *J. Compos. Mater.* 2014, *48* (8), 959–967.

(3) Zhang, X.; Wu, Z.; Zhang, X.; Li, L.; Li, Y.; Xu, H.; Li, X.; Yu, X.; Zhang, Z.; Liang, Y.; et al. Highly selective and active CO_2 reduction electrocatalysts based on cobalt phthalocyanine/carbon nanotube hybrid structures. *Nat. Commun.* 2017, *8*, 1–8.

(4) Li, H.; Xu, Z.; Li, K.; Hou, X.; Cao, G.; Zhang, Q.; Cao, Z. Modification of multi-walled carbon nanotubes with cobalt phthalocyanine: effects of the templates on the assemblies. *J. Mater. Chem.* 2011, *21*, 1181–1186.

(5) Yan, X.; Xu, X.; Liu, Q.; Guo, J.; Kang, L.; Yao, J. Functionalization of multi-walled carbon nanotubes with iron phthalocyanine via a liquid chemical reaction for oxygen reduction in alkaline media. *J. Power Sources* 2018, *389*, 260–266.

(6) Cao, L.; Chen, H. Z.; Zhou, H. B.; Zhu, L.; Sun, J. Z.; Zhang, X. Bin; Xu, J. M.; Wang, M. Carbon-nanotube-templated assembly of rare-earth phthalocyanine nanowires. *Adv. Mater.* 2003, *15* (11), 909–913.

(7) Ballesteros, B.; Filoramo, A.; Rahman, A.; Ehli, C.; Kiessling, D.; Werner, F.; Sgobba, V.; Guldi, D. M.; Ciof, C.; Prato, M.; et al. Facile decoration of functionalized single-wall carbon nanotubes with phthalocyanines via “click chemistry.” *J. Am. Chem. Soc.* 2008, *130*, 11503–11509.

(8) Bottari, G.; Torre, G. De; Guldi, D. M.; Torres, T. Covalent and noncovalent phthalocyanine - carbon nanostructure systems : synthesis , photoinduced electron transfer , and application to molecular photovoltaics. *Chem. Rev.* 2010, *110*, 6768–6816.

(9) Bottari, G.; de la Torre, G.; Guldi, D. M.; Torres, T. Phthalocyanine-pyrene conjugates: a powerful approach toward carbon nanotubes solar cells. *Chem. Rev.* 2010, *110* (11), 6768–6816.

(10) Urdampilleta, M.; Klyatskaya, S.; Cleuziou, J. P.; Ruben, M.; Wernsdorfer, W. Supramolecular spin valves. *Nat. Mater.* 2011, *10* (7), 502–506.

(11) Jha, P.; Sharma, M.; Chouksey, A.; Chaturvedi, P.; Kumar, D.; Upadhyaya, G.; Rawat, J. S. B. S.; Chaudhury, P. K. Functionalization of carbon nanotubes with metal phthalocyanine for selective gas sensing application. *Synth. React. Inorganic, Met. Nano-Metal Chem.* 2014, *44* (10), 1551–1557.
(12) Wang, Y.; Hu, N.; Zhou, Z.; Xu, D.; Wang, Z.; Yang, Z.; Wei, H.; Kong, E. S. W.; Zhang, Y. Single-walled carbon nanotube/cobalt phthalocyanine derivative hybrid material: preparation, characterization and its gas sensing properties. *J. Mater. Chem.* 2011, *21*, 3779–3787.
(13) Krasnov, P. O.; Basova, T. V.; Hassan, A. Interaction of metal phthalocyanines with carbon zigzag and armchair nanotubes with different diameters. *Appl. Surf. Sci.* 2018, *457*, 235–240.
(14) Zhou, Q. X.; Wang, C. Y.; Fu, Z. B.; Tang, Y. J.; Zhang, H. Effects of various defects on the electronic properties of single-walled carbon nanotubes: a first principle study. *Front. Phys.* 2014, *9* (2), 200–209.
(15) Ding, F. Theoretical study of the stability of defects in single-walled carbon nanotubes as a function of their distance from the nanotube end. *Phys. Rev. B - Condens. Matter Mater. Phys.* 2005, *72*, 245409-1-245409–7.
(16) Charlier, J.-C. Defects in carbon nanotubes. *Acc. Chem. Res.* 2002, *35*, 1063–1069.
(17) Qin, X.; Meng, Q.; Zhao, W. Effects of stone-wales defect upon adsorption of formaldehyde on graphene sheet with or without al dopant: a first principle study. *Surf. Sci.* 2011, *605* (9–10), 930–933.
(18) Johll, H. A.; Low, R. Density functional theory study of metal adatoms at or near a Stone-Wales defect in graphene. *Procedia Eng.* 2014, *93*, 2–7.
(19) Basiuk, V. A.; Chávez-Colorado, E. Adsorption of free-base phthalocyanine on Stone-Wales defect-containing carbon nanotubes : a dft study. *Diam. Relat. Mater.* 2019, *97*, 107443.
(20) Bettinger, H. F. The reactivity of defects at the sidewalls of single-walled carbon nanotubes: the Stone-Wales defect. *J. Phys. Chem. B* 2005, *109*, 6922–6924.
(21) Miyamoto, Y.; Rubio, A.; Berber, S.; Yoon, M.; Tomànek, D. Spectroscopic characterization of Stone-Wales defects in nanotubes. *Phys. Rev. B - Condens. Matter Mater. Phys.* 2004, *69* (12), 1–4.
(22) Zhou, L. G.; Shi, S.-Q. Formation energy of Stone–Wales defects in carbon nanotubes. *Appl. Phys. Lett.* 2003, *83*, 1222–1224.
(23) Choi, H. J.; Ihm, J.; Louie, S. G.; Cohen, M. L. Defects, quasibound states, and quantum conductance in metallic carbon nanotubes. *Phys. Rev. Lett.* 2000, *84*, 2917–2920.
(24) Pan B. C.; Yang W. S.; Yang J. Formation energies of topological defects in carbon nanotubes. *Phys. Rev. B - Condens. Matter Mater. Phys.* 2000, *62*, 12652–12655.
(25) Charlier, J.; Ebbesen, T.; Lambin, P. Structural and electronic properties of pentagon-heptagon pair defects in carbon nanotubes. *Phys. Rev. B* 1996, *53*, 11108–11113.
(26) Picozzi, S.; Santucci, S.; Lozzi, L.; Valentini, L.; Delley, B. Ozone adsorption on carbon nanotubes: the role of stone-wales defects. *J. Chem. Phys.* 2004, *120* (15), 7147–7152.
(27) Yang, S. H.; Shin, W. H.; Kang, J. K. Ni adsorption on stone-wales defect sites in single-wall carbon nanotubes. *J. Chem. Phys.* 2006, *125*.
(28) Azadi, S.; Moradian, R.; Shafaee, A. M. The effect of stone-wales defect orientations on the electronic properties of single-walled carbon nanotubes. *Comput. Mater. Sci.* 2010, *49* (3), 699–703.
(29) Roh, S.; Oh, J.; Choi, Y.; Sohn, D.; Kim, W.; Cho, C.; Yi, W.; Yoo, J.; Lee, C.; Kim, J. Adsorption of alkanethiol molecules onto carbon nanotube surface. *J. Vac. Sci. Technol. B Microelectron. Nanom. Struct.* 2004, *22* (3), 1411.
(30) Wang, C.; Zhou, G.; Liu, H.; Wu, J.; Qiu, Y.; Gu, B. L.; Duan, W. Chemical functionalization of carbon nanotubes by carboxyl groups on stone-wales defects: a density functional theory study. *J. Phys. Chem. B* 2006, *110* (21), 10266–10271.
(31) Turabekova, M. A.; Dinadayalane, T. C.; Leszczynska, D.; Leszczynski, J. Comprehensive study on the dissociative chemisorption of NH_3 on the sidewalls of stone-wales defective armchair (5,5) single-walled carbon nanotubes. *J. Phys. Chem. C* 2012, *116* (10), 6012–6021.
(32) Ben Doudou, B.; Chen, J.; Vivet, A.; Poîlane, C.; Ayachi, M. Role of stone-wales defects on the functionalization of (8,0) single wall carbon nanotubes by the amine group: *ab* initio study. *Phys. E Low-Dimensional Syst. Nanostructures* 2011, *44* (1), 120–123.
(33) Correa, J. D.; Orellana, W. Optical response of carbon nanotubes functionalized with (free-base , Zn) porphyrins , and phthalocyanines : a DFT study. *Phys. Rev. B* 2012, *86*, 125417/1-6.
(34) Basiuk, E. V.; Huerta, L.; Basiuk, V. A. Noncovalent bonding of *3d* metal(II) phthalocyanines with single-walled carbon nanotubes: a combined DFT and XPS study. *Appl. Surf. Sci.* 2019, *470*, 622–630.
(35) Chávez-Colorado, E.; Basiuk, V. A. Noncovalent interactions of free-base phthalocyanine with elongated fullerenes as carbon nanotube models. *Struct. Chem.* 2017, *28*, 1765–1773.
(36) Basiuk, V. A.; Flores-Sánchez, L. J.; Meza-Laguna, V.; Flores-Flores, J. O.; Bucio-Galindo, L.; Puente-Lee, I.; Basiuk, E. V. Noncovalent functionalization of pristine cvd single-walled carbon nanotubes with *3d* metal(II) phthalocyanines by adsorption from the gas phase. *Appl. Surf. Sci.* 2018, *436*, 1123–1133.
(37) Basiuk, V. A.; Basiuk, E. V. Complexation of free-base and 3*d* transition metal (II) phthalocyanines with fullerene c_{60} : a dispersion-corrected dft study. *Fullerenes, Nanotub. Carbon Nanostructures* 2017, *25* (7), 410–416.

(38) Basiuk, V. A.; Tahuilan-Anguiano, D. E. Complexation of free-base and *3d* transition metal(II) phthalocyanines with endohedral fullerene $Sc_3N@C_{80}$. *Chem. Phys. Lett.* 2019, *722*, 146–152.
(39) Basiuk, V. A.; Basiuk, E. V. Noncovalent complexes of $i_h - C_{80}$ fullerene with phthalocyanines. *Fullerenes , Nanotub. Carbon Nanostructures* 2018, *26*, 69–75.
(40) Basiuk, V. A. Electron smearing DFT calculations: a case study ofo doxorubicin interaction with single-walled carbon nanotubes. *Int. J. Quantum Chem.* 2011, *111*, 4197–4205.
(41) Basiuk, V. A.; Bolivar-Pineda, L. M.; Meza-Laguna, V.; Rybak-Akimova, E. V.; Basiuk, E. V. Carbon nanotubes and graphene promote pyrolysis of free-base phthalocyanine. *J. Phys. Chem. Lett.* 2018, *9* (15), 4420–4427.
(42) Kabir, M.; Van Vliet, K. J. Kinetics of topological Stone-Wales defect formation in single-walled carbon nanotubes. *J. Phys. Chem. C* 2016, *120* (3), 1989–1993.
(43) Lehman, J. H.; Terrones, M.; Mansfield, E.; Hurst, K. E.; Meunier, V. Evaluating the characteristics of multiwall carbon nanotubes. *Carbon.* 2011, *49* (8), 2581–2602.
(44) Zsoldos, I. Effect of topological defects on graphene geometry and stability. *Nanotechnol. Sci. Appl.* 2010, *3*, 101.
(45) Talla, J. A. Electronic properties of silicon carbide nanotube with Stone Wales defects under uniaxial pressure: a computational study. *Comput. Condens. Matter* 2019, *19*, e00378.
(46) Partovi-Azar, P.; Namiranian, A. Stone-Wales defects can cause a metal-semiconductor transition in carbon nanotubes depending on their orientation. *J. Phys. Condens. Matter* 2012, *24* (3).
(47) Cui, H.; Li, Q.; Qiu, G.; Wang, J. Carbon-chain inserting effect on electronic behavior of single-walled carbon nanotubes: a density functional theory study. *MRS Commun.* 2018, *8* (1), 189–193.
(48) Matsuda, Y.; Tahir-Kheli, J.; Goddard, W. A. Definitive band gaps for single-wall carbon nanotubes. *J. Phys. Chem. Lett.* 2010, *1* (19), 2946–2950.
(49) Li, J.-W.; Liu, Y.-Y.; Xie, L.-H.; Shang, J.-Z.; Qian, Y.; Yi, M.-D.; Yu, T.; Huang, W. Revealing the interactions between pentagon–octagon–pentagon defect graphene and organic donor/acceptor molecules: a theoretical study. *Phys. Chem. Chem. Phys.* 2015, *17* (7), 4919–4925.
(50) Zhang, W.; Lu, W. C.; Zhang, H. X.; Ho, K. M.; Wang, C. Z. Lattice distortion and electron charge redistribution induced by defects in graphene. *Carbon N. Y.* 2016, *110*, 330–335.
(51) He, C. N.; Huang, W. Q.; Xu, L.; Yang, Y. C.; Zhou, B. X.; Huang, G. F.; Peng, P.; Liu, W. M. Tuning near-gap electronic structure, interface charge transfer and visible light response of hybrid doped graphene and Ag_3PO_4 composite: dopant effects. *Sci. Rep.* 2016, *6* (October 2015), 1–12.
(52) Alvarez, L.; Fall, F.; Belhboub, A.; Le Parc, R.; Almadori, Y.; Arenal, R.; Aznar, R.; Dieudonné-George, P.; Hermet, P.; Rahmani, A.; et al. One-dimensional molecular crystal of phthalocyanine confined into single-walled carbon nanotubes. *J. Phys. Chem. C* 2015, *119* (9), 5203–5210.

5

Chapter 5

Synthesis of rare-earth double-decker phthalocyanines and non-covalent functionalisation of carbon nanotubes

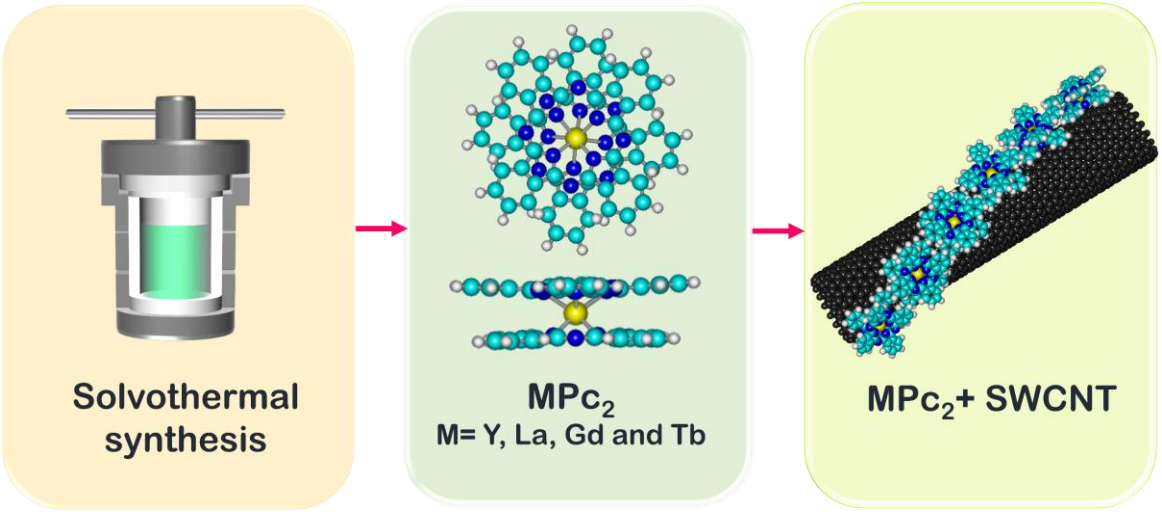

Manuscript in preparation

L. M. Bolívar-Pineda, Carlos. U. Mendoza-Domínguez, P. Rudolf, Elena. V. Basiuk and Vladimir. A. Basiuk

Abstract

Rare earth double-decker phthalocyanines on the surface of carbon nanotubes have attracted significant attention for their magnetic properties. The synthesis of bisphthalocyanines is classified into two routes depending on the precursor: synthesis from phthalonitrile and metalation of the free or dilithium phthalocyanine. In both options, side products such as free base phthalocyanine and in the first route additional PN oligomers are generate. In this chapter, four unsubstituted bisphthalocyanines with different rare-earth metals (Y, La, Gd and Tb) were synthesised using the solvothermal as a new method. The complexes were purified by sublimation yielding 68% for YPc_2, 43% for $LaPc_2$, 63% for $GdPc_2$ and 62% for $TbPc_2$. No evidence of free-base phthalocyanine was observed after purification by sublimation. Electron paramagnetic resonance results show that the phthalocyanines contain a free radical. The bisphthalocyanines were adsorbed on single-walled carbon nanotubes by refluxing. Dispersion testing, scanning and transmission electron microscopy images suggest that functionalisation of carbon nanotubes not only occurs on individual nanotubes but also in agglomerates as well as non-covalent functionalisation with transition metal phthalocyanines.

5.1. Introduction

The main synthetic approaches for the preparation of bisphtalocyanines with and without substituents can be classified according to the type of precursors involved in their preparation. Among the best know are the tetramerization reactions of phthalic acid derivatives, mainly phthalonitrile (PN) in the presence of the respective rare earth ions (also called template synthesis) and metal insertion reactions into pre-formed macrocyclic systems such as free-base phthalocyanine and/or lithium phthalocyanine (Li_2Pc). [1–3]

Template synthesis is a simple method, however, its selectivity is very sensitive to reaction conditions (see review of the reference 1,2) due to rare earth ions forming stable single, double and triple-decker complexes. The most significant reaction parameters are the temperature, time, the type of rare earth salt precursor, the type of phthalic acid derivate, and the ratio of reactants. Three methods of preparations for this approach have been reported. The first one consists in the heating of a mixture of rare earth acetates and phthalonitrile at 250 to 350 °C (thermal fusion), the second microwave radiation and the third, condensation reaction by reflux of the above mixture in the presence of DBU (1,8-Diazabicyclo[5.4.0]undec-7-ene) as a strong organic base and alcohol with a long chain (pentanol and hexanol). [1,2]

The preparation of double-decker phthalocyanines using free-base and lithium phthalocyanines with rare earth acetates or acetylacetonates in quinoline, trichlorobenzene and/or *n*-octanol (basic medium) also by reflux and microwave irradiation. This approach has the advantage of not forming by-products such as oligomers from phthalonitrile. Both synthesis strategies generate free-base phthalocyanine as an impurity and column chromatography and sublimation have been implemented as purification alternatives. [1,2]

The selection of a suitable method for the preparation of phthalocyanines is important for their properties and the cost of production. [4] In this context, the solvothermal method has been used for the synthesis of single-decker phthalocyanines, since it is an easily operable and environmentally friendly method, results in direct transformation into products from reactants, and give rise to crystalline structures with particular shapes, and the morphologies of the products can be regulated, largely due to the high reactivity of the reagents and the limited solubility of the products in the reaction media under high pressure conditions. [4,5] Despite the above, there are few single-decker phthalocyanines structures obtained by such a method [4–8] and none of rare earth bisphthalocyanines.

All things considered and emphasising that unsubstituted MPc_2 (in this section M denotes Y, La, Gd and Tb.) are not commercially available, it was proposed to synthesise rare earth bisphthalocyanines of yttrium, lanthanum, gadolinium, and terbium by the solvothermal method using acetylacetonates and dilithium phthalocyanine as precursor in toluene (Scheme 5. 1) as a new synthesis strategy.

The complexes were deposited on the surface of single-walled carbon nanotubes by refluxing. The hybrids were characterised by a set of analytical techniques, which are described below. The interest in hybrid formation (MPc_2+SWCNT) is explained in the Chapters 1 and 6.

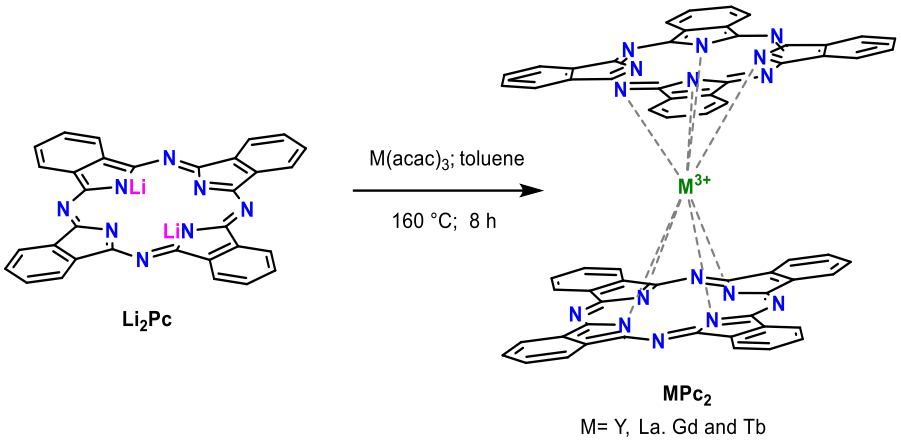

Scheme 5. 1. Synthesis route of rare-earth bisphthalocyanines (MPc_2= YPc_2, LPc_2, $TbPc_2$ and $GdPc_2$)

5.2. Experimental section

5.2.1. Materials

Dilithium phthalocyanines with 70% purity and the rare earth (III) acetylacetonates hydrate $M(C_5H_7O_2)_3\ xH_2O$ (M= Y, La, Gd and Tb) such as yttrium, lanthanum, and gadolinium acetylacetonate and terbium with 99.9% purity were obtained from Sigma-Aldrich.

Pristine single-walled carbon nanotubes (>95% purity) synthesized by CVD process were purchased from NanoLab, Inc. According to the company's specifications, the nanotubes are approximately 1.5 nm in diameter and 1–5 μm in length.

5.2.2. Solvothermal synthesis of rare earth double-decker phthalocyanines

All rare earth double-decker phthalocyanines were synthesized by the solvothermal method. For this purpose, a stainless-steel reactor with a polytetrafluoroethylene (PTFE-Teflon) was used. Dilithium phthalocyanine (200 mg) and rare earth acetylacetates (600 mg) were used as precursors, mixed in a molar ratio of 1:3 respectively in 60 mL of toluene and brought to a temperature of 160 °C in oven for a time of 8 h. The reactor was then allowed to cool down to room temperature. The colour of the solution after the reaction turned dark green and as the solvent evaporated at room temperature the solid began to precipitate and the solution turned light green. The solid crude product had a dark blue green to green coloration, depending on the metal used. The crude product was washed successively with methanol to eliminate the acetylacetates that did not react; every washing included ultrasonic waves, the

product acquired a mixture of colour between dark green and purple, which corresponds to the presence of free-base phthalocyanines H_2Pc. The purification of the different earth rare bisphthalocyanines was carried out in a train sublimation system under nitrogen atmosphere at 350°C during two and three hours to remove the free-base phthalocyanine, which is a by-product.

5.2.3. Functionalisation

The non-covalent functionalisation of single-walled carbon nanotubes with the four synthesized bisphthalocyanines was carried out by refluxing in butanol (50 mL) for 24 hours at 117 °C with constant stirring. A weigh ratio of 3:4 was used, for example 45 mg of bisphthalocyanine and 60 mg of single-walled CNTs. The final product was filtered and dried in vacuum at 100°C.

5.3. Results and discussion

5.3.1. Characterisation of the bisphthalocyanines

Synthesis of rare earth double-decker phthalocyanines such as yttrium, lanthanide, gadolinium, and terbium using metalation of the lithium phthalocyanine has the advantage of avoiding unwanted by-products, especially the formation of linear oligomers of phthalonitrile.[1] However, the presence of free-base phthalocyanine as a contaminant is unavoidable.[9] The removal of H_2Pc from the crude product was carried out by sublimation at constant temperature of 350°C for two or three hours, depending on the central metal of the MPc_2. Table 5. 1 shows the yields obtained for each of the bisphthalocyanines: 68% for YPc_2, 43% for $LaPc_2$, 63% for $GdPc_2$ and 62% for $TbPc_2$, these percentages were calculated based on dilithium phthalocyanine which is the limiting reactant. In addition, Table 5. 1 displays the content of H_2Pc in the washed end product.

Infrared spectroscopy has been used to analyses the purity of the unsubstituted MPc_2, especially to detect the free base phthalocyanine and to study its intrinsic features. [9–11] According to the reported literature,[9,10,12–19] Fig.5. 1a exhibits the characteristic vibrational modes of phthalocyanine ligands in the four rare-earth double-decker phthalocyanines in the region of 500-1800 cm^{-1}. In this range, five main IR absorptions with strong and medium intensity are observed in all four spectra. Fig.3. 10a depicts the detailed structure of the MPc_2, for a better understanding of the vibrational modes present in the infrared and Raman spectra.

The highest intensity band at 731 cm^{-1} is attributed to C-H out of plane bending, the absorption at 1001cm^{-1} is assigned to pyrrole N- in plane bending of phthalocyanine ligand, vibrational frequency at 1066 cm^{-1} is due to coupling of isoindole deformation and aza group stretching (C=N), the pyrrole and isoindole stretching at 1311 and 1443 cm^{-1}, respectively.[12,13,19] Another band typical of these complexes and which has weak intensity appears at 1117 cm^{-1} that corresponds to a isoindole breathing mode with small contributions from C-H in plane bending. [12,13] Among this group of vibrations, it is noteworthy the absorption

of pyrrole stretching at 1311 cm^{-1} indicates the presence of phthalocyanine monoanion-radical, $Pc^{\bullet-}$, that is, the spectra show that these double-decker phthalocyanines have one unpaired electron in one of the tetrapyrrole rings. [10,12,13] A band around 1329 cm^{-1} is related to the presence of dianionic phthalocyanine ligands, ($[MPc_2]^-$), the absence of this band in the spectra of the rare earth bisphthalocyanines (Fig.5. 1a) is also an argument in favour of the delocalization of the unpaired electron over both phthalocyanine rings.[18] On the other hand, the vibrational mode of isoindole, pyrrole deformation and aza stretching contribution are also reflected with the weak bands at 874 and 1500 cm^{-1}. The other weak bands that appear from 500 to 1000 cm^{-1} represent Pc ligand breathing and the vibration of C-H out of the plane, whereas the C-H in plane bending is found from 1000 to 1300 cm^{-1}.[12,13] The vibrations in the region from 1344 to 1479 cm^{-1} are attributed to isoindole stretching and from 1537 to 1599 cm^{-1} are assigned to benzene stretching. [12,13] A set of bands at 3022-3271 cm^{-1} is due to aromatic C-H stretching in the phthalocyanine rings. [12,13]

Comparing the infrared spectrum of each of the bisphthalocyanines with the infrared spectrum of the free base phthalocyanine, it can be deduced that its presence is minimal as an impurity since significant differences are observed in the region from 1000 to 1600 cm^{-1}, especially the presence of the band 1311 cm^{-1} typical of the neutral rare-earth bispthalocyanines. [10,12,13] The slight differences of the FITR spectra analysed from bisphthalocyanines powder form and the reported spectra are due to several random factors such as sample preparation, most of the spectra were obtained from MPc_2 in thin films [14,16] and KBr pellets [11,12,15,16], molecular orientation and the direction of the incident light.[16] Despite this, the results showed that the synthesized compounds were consistent with the expected target products. This was also verified by the elemental analysis of each product (Table 5. 1), which indicated that the mass percentages correspond satisfactorily to the four earth-rare bispthalocyanines: YPc_2, $LaPc_2$, $GdPc_2$ and $TbPc_2$.

Table 5. 1. Yield, elemental analysis of the rare earth double-decker phthalocyanine and amount of free-base phthalocyanine present in the end product and elemental analysis.

MPc_2 complexes	Yield (%) [a]	H_2Pc (%) [b]	Elemental analysis (%)			
			C	H	N	M
YPc_2	68.1	5.0	69.37	2.92	20.17	7.54
			(69.00) [c]	(2.89)	(20.12)	(7.98)
$LaPc_2$	43.0	33.6	66.09	2.69	19.28	12.04
			(66.04)	(2.65)	(19.25)	(11.93)
$GdPc_2$	63.1	16.7	65.08	2.80	19.53	12.64
			(65.04)	(2.73)	(18.96)	(13.3)
$TbPc_2$	61.8	18.3	65.44	2.98	18.96	12.63
			(64.92)	(2.72)	(18.93)	(13.4)

[a] calculated from the Li_2Pc (limiting reactant)
[b] calculated from the washed end product.
[c] theoretical percentage

As can be expected, the Raman spectra of the bisphthalocyanines at room temperature show characteristic Raman shifts for typical rare-earth double-decker phthalocyanines (Fig.5. 1b). For MPc_2, the weak medium and strong intensity bands at 476-807 cm^{-1} are assigned to phthalocyanine breathing, except for the medium band at 736-740 cm^{-1}, that is due to aromatic phthalocyanine C-H wagging. There are several bands with different intensity in the range of 900 to 1300 cm^{-1}, which are attributed to aromatic C-H bending. The band around 1141-1145 cm^{-1} and 1536-1544 cm^{-1} represent the pyrrole breathing. Raman bands in the range of 1350-1600 cm^{-1} originate from isoindole ring stretching vibrations and the aza group stretching. The bands between 1420-1425 cm^{-1} and 1448-1453 cm^{-1} are typical of isoindole stretching.[12,13,20–22]

The electronic absorption spectra of the four bisphthalocyanines were recorded in DMF and DMSO. The spectra exhibit two main characteristic bands of the phthalocyanines compounds, the Q and B or Soret bands of Pcs. [18,23,24] The absorption of the Q band resulting from $\pi(a_{1u})$-$\pi^*(e_g)$ HOMO-LUMO transition that originates from electronic charge transfer from the pyrrole skeleton to the condensed benzene rings of Pc ligands [18,23] was observed between 662 nm ($LaPc_2$. $GdPc_2$ and $TbPc_2$ in DMF) and 667 nm ($GdPc_2$ in DMSO) in both solvents (see Table 5. 2). This band is identified in the spectra as the maximum absorption (λ_{max}) as displayed in the Fig.5. 2 . Differences in absorption wavelength are negligible between polar aprotic solvents and the small hypochromic shift of the Q-band is due to the decrease in the ionic radii of the rare earth cations in the case of dimethylformamide solvent.[18,24]

Table 5. 2. Position of the B (Soret) and Q bands (λmax, nm) in the UV-Vis spectra of double-decker phthalocyanines, MPc_2 (M = Y, La, Gd and Tb) in N, N-dimethylformamide (DMF) and dimethyl sulfoxide (DMSO)

Phthalocyanines	Solvent	Absorption (nm)			
		Q band		B-band	Radical
YPc_2	DMF	665	603	333	--
	DMSO	665	--	333	448
$LaPc_2$	DMF	662	599	328	--
	DMSO	665	602	328	448
$GdPc_2$	DMF	662	599	329	--
	DMSO	667	602	328	446
$TbPc_2$	DMF	662	599	328	--
	DMSO	665	601	326	--

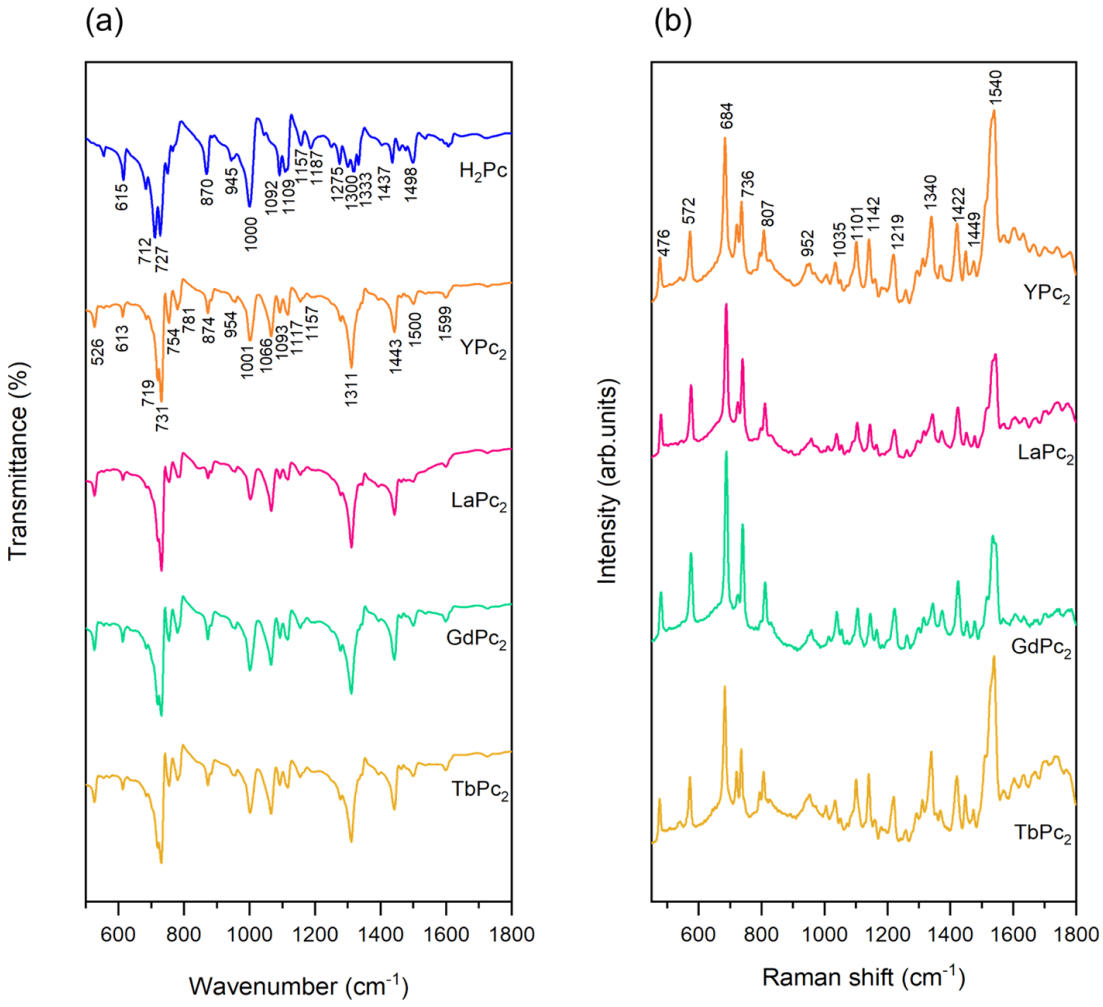

Fig.5. 1.(a) Infrared and (b) Raman spectra of free-base and rare earth double-decker phthalocyanines.

On the other hand, the Q-band of phthalocyanines presents a small shoulder peak near 599 nm for the lanthanide bispthalocyanines ($LnPc_2$) and 603 nm for YPc_2 in DMF. In dimethyl sulfoxide this band is only observed for $LnPc_2$ at 601-602 nm. It has been reported that the Q-band splitting indicates that these compounds have a strong tendency to aggregate between the phthalocyanines rings. [18,24] The B band that corresponds to an additional π (a_{2u})-π^*(e_g) transition is produced by a redistribution of the electronic density. It provokes an increase in electron density in correspondence with the bridging atoms of the azamethine group [18,23] and is localized between at 333 nm (YPc_2 in DMF and DMSO) and 329 nm for ($GdPc_2$ in DMF) in DMF and DMSO (Table 5. 2).

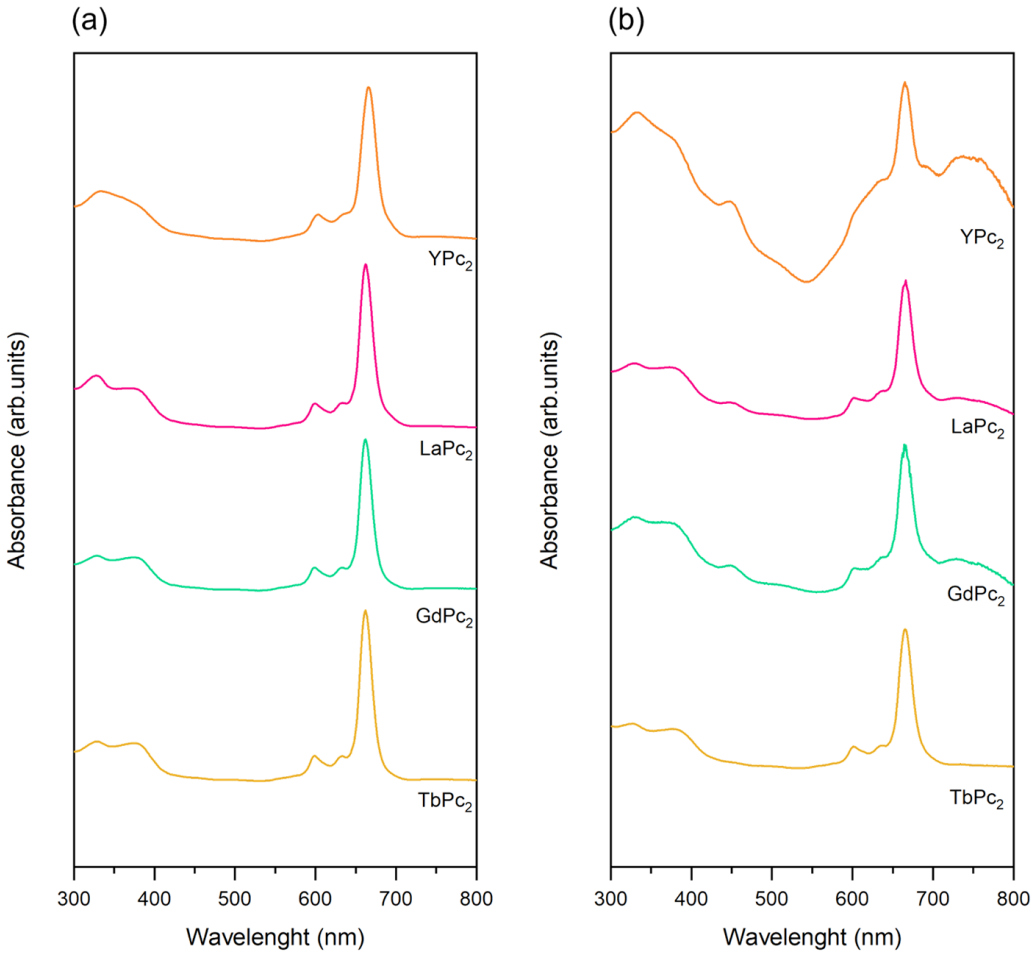

Fig.5. 2. UV-visible spectra of rare earth of bisphthalocyanines in (a) dimetylformamide and (b) dimethyl sulfoxide

One of the additional features in the spectrum of the double-decker phthalocyanines is the band around 450 nm, which appears as a result of electron delocalisation between two aromatic systems in the neutral-radical form of the metal complex. [23,25,26] This band can be visualised in the spectra of yttrium, gadolinium, and terbium bisphthalocyanines from the dimethyl sulfoxide solutions (Fig.5. 2b and Table 5. 2). The absence of this band in the spectra obtained from the dimethylformamide solutions can be attributed to a possible reduction of the $[MPc_2]^{\bullet-}$ complex to $[MPc_2]^{-}$ by the amine impurities that are often present in reagent grade DMF.[18] This would explain the colour difference between DMSO and DMF with the four double-decker phthalocyanines solutions. Fig.5. 3 illustrates that the DMF solutions acquired a blue-green colour corresponding to a mixture of the anionic and the neutral form of bisphthalocyanines. The dimethyl sulfoxide solutions have a dark and light green colour typical of a neutral form.[18,23,27,28] Therefore, it can be deduced, together with the infrared spectra, that the bisphthalocyanines obtained by the solvothermal method are monoanionic neutral radical ($[MPc_2]^{\bullet-}$).

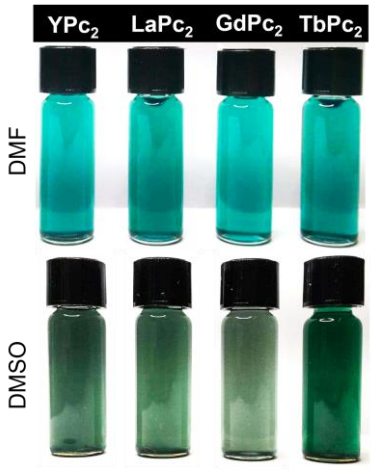

Fig.5. 3. Colorations of the solutions of rare earth of bisphthalocyanine in dimetylformamide (DMF) and dimethyl sulfoxide (DMSO).

It is important to mention that the optical properties of phthalocyanines are not considered an intrinsic property, because they depend on the chemical environment such as the type of solvent and its interaction with rare-earth metal complexes. Hence, some discrepancies can be found between spectra of MPc_2 complexes reported from thin films, solution, and solid pellets.[14-19,23-27,29,30]

The presence of an unpaired electron (free radical) in one of Pc ligands of the bisphthalocyanines is confirmed by EPR (Fig.5. 4). The spectra of all the powder complexes studied here show a strong and sharp isotropic Landé signal around *g*-factor of 2.0 with a peak-to peak linewidth of 0.2 mT, which is attributed to the 1/2 spin radical. This result showed the formation and the paramagnetic nature of the rare earth sandwich structures. [14,19,31]

The thermal stability of the four bisphthalocyanines was determined simultaneously by thermogravimetric analysis and differential thermal analysis. Fig.5. 5 displays that all the MPc_2 reveal similar behaviour upon heating and that the TGA curves were in good agreement with the DTA. The first weight loss is attributed to moisture and the second loss is attributed to the oxidative pyrolysis of the double decker which is generated in two main exothermic events. The initial decomposition temperature of YPc_2, $LaPc_2$, $GdPc_2$ and $TbPc_2$ is at 355, 353, 359 and 356 °C, respectively. The second event coincides with the maximum temperature of the DTA curves and the final temperature is between 505 and 517 °C, illustrating that it is the strong conjugation within the macrocyclic ligand itself that governs the stability phthalocyanine compounds, that determines that of the the transition metal phthalocyanines and H_2Pc. [32]

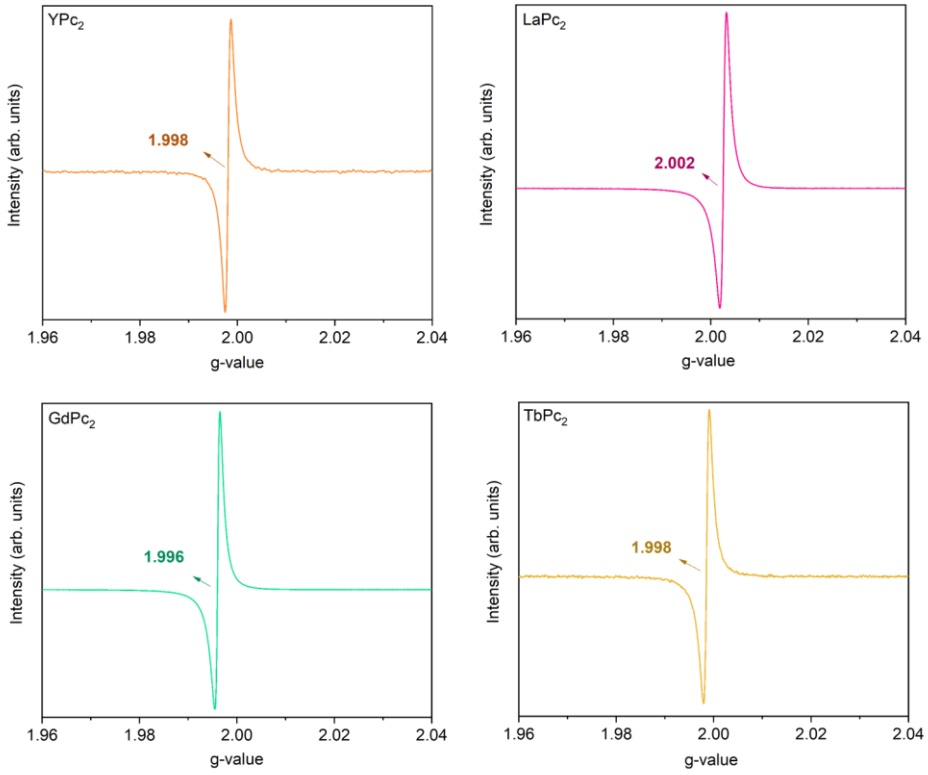

Fig.5. 4. EPR spectra of the four rare earth double-decker phthalocyanines: YPc_2, $LaPc_2$, $GdPc_2$ and $TbPc_2$ at room temperature.

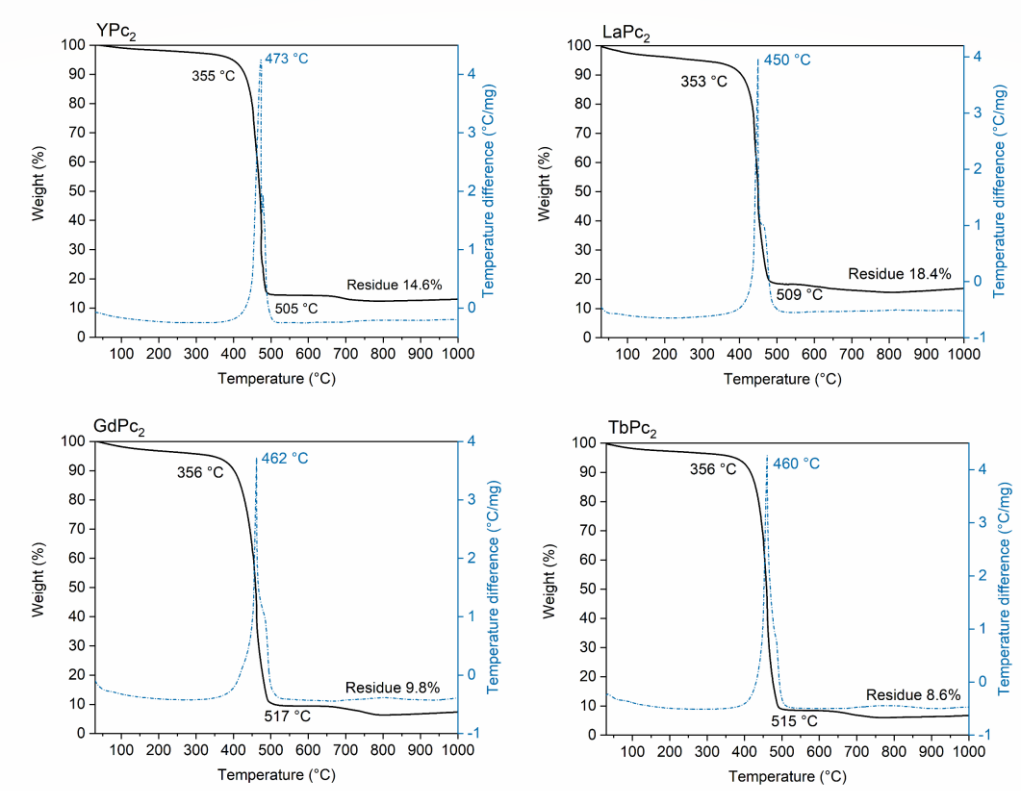

Fig.5. 5. TGA (Black) and DTA (blue) curves of rare-earth double-decker phthalocyanines: YPc_2, $LaPc_2$, $GdPc_2$ and $TbPc_2$. Air flow100 $mLmin^{-1}$

Fig.5. 6 exhibits the SEM images at different magnifications of the bisphthalocyanines (Fig.5. 6 a-c for YPc_2, Fig.5. 6d-f for $LaPc_2$, Fig.5. 6g-i for $GdPc_2$ and Fig.5. 6j-l for $TbPc_2$). The images reveal agglomerated and stacked crystallites with a microstructure in laminar shape (sheet) with rectangular and/or square geometry (Fig.5. 6e,f,i,l). The images also confirm the absence of free-base phthalocyanines, needle-shaped crystals (Fig.5. 6m-o; SEM image for commercial H_2Pc).

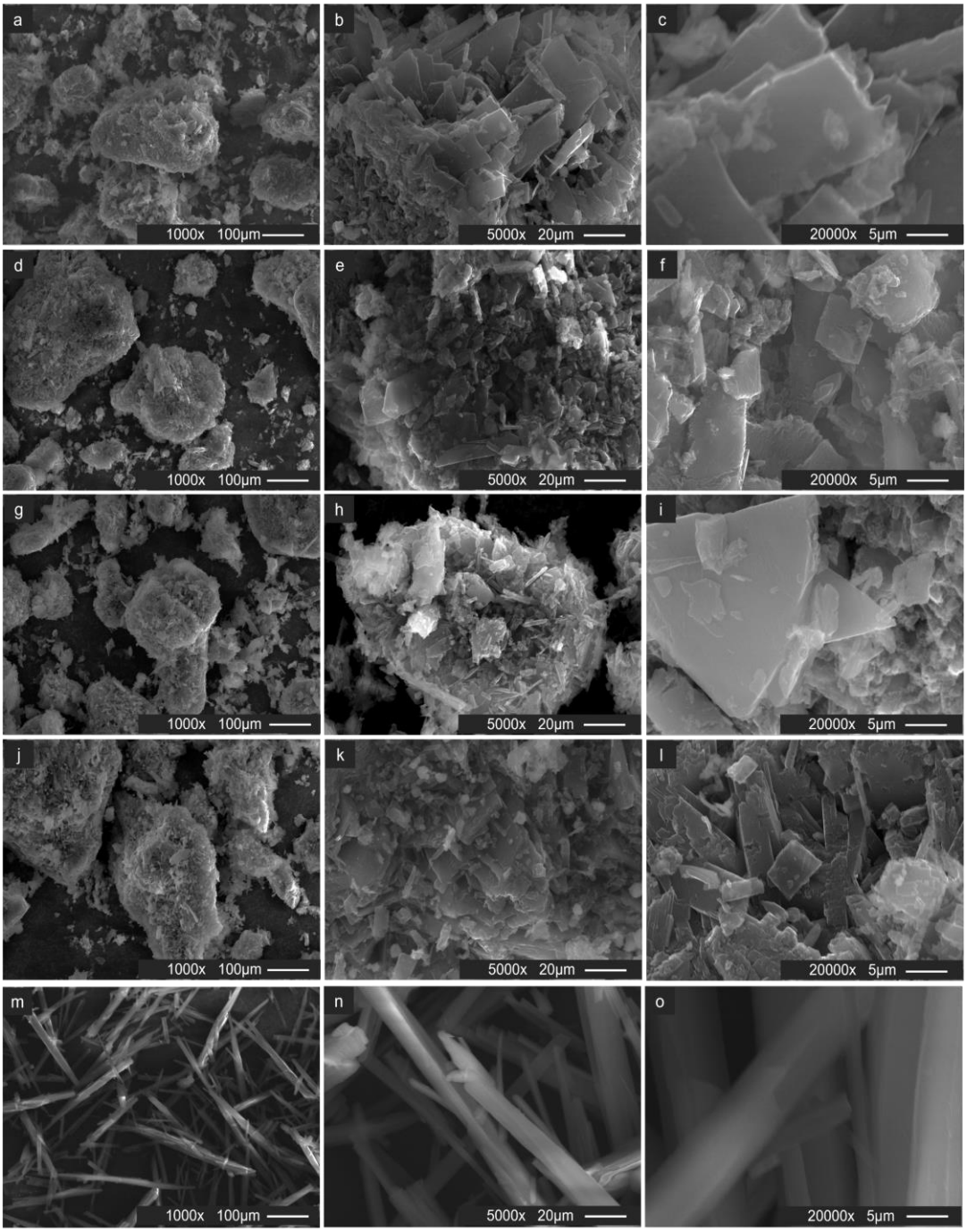

Fig.5. 6. Representative SEM images at different magnificationfor for (a-c) YPc_2, (d-f) $LaPc_2$, (g-i) $GdPc_2$, (j-l) and $TbPc_2$ and (m-o) commercial free-base phthalocyanine. Scale bars: (a,d,g,j,m) 100 µm, (b,e,h,k,n) 20 µm and (c,f,i,l,o) 5 µm.

5.3.2. Deposition of MPc_2 on the surface of single-walled carbon nanotubes

The percentage content of rare earth double-decker phthalocyanines on functionalised carbon nanotubes was estimated from the weight difference before and after reflux treatment of SWCNTs, as a direct method. It was calculated as 28.7% for YPc_2, 26.4% for $LaPc_2$, 30.6% for $GdPc_2$ and 25.9% for $TbPc_2$.

The dispersion test of the pristine and functionalised nanotubes with the four rare earth bisphthalocyanines was performed in two solvents: ethanol and isopropanol (see Fig.5. 7). The dispersibility test was used as simple evidence of changes in the chemical nature of the pristine nanotube surface. Fig.5. 7 displays that the pristine nanotubes have higher dispersibility in isopropanol. After one hour of being treated in an ultrasonic bath, the nanotubes precipitate indicating that their stability in both solvents is low.

The functionalised nanotubes show different behaviour depending on the polarity of the solvent and the coordination metal of the bisphthalocyanines. In polar solvents such as ethanol, the hybrid with terbium bisphthalocyanine dispersion is homogeneous and higher in contrast to its analogues and pristine CNTs. The dispersion of the pristine and modified nanotubes is in spongy agglomerates, except for the nanotubes with $LaPc_2$ which has fine "particles". As for the dispersion in isopropanol, a slightly polar solvent, it is observed that the dispersion decreases for hybrids with yttrium bisphthalocyanine, while those with $LaPc_2$, $GdPc_2$ and $TbPc_2$ maintain a similar performance. Additionally, the size of the agglomerates decreases, making them less spongy.

The stability of the functionalised dispersions is the same in both solvents, immediately after the ultrasound treatment, the MPc_2+SWCNT hybrids start to precipitate and after one hour most of the product is at the bottom of the vial, nonetheless the stability is better than that of the pristine nanotubes. The instability is related to the presence of conjugated aromatic systems such as phthalocyanines that enable π-π interaction with other neighbouring nanotubes, causing them to "stick" to each other and form agglomerates of larger particles that eventually precipitate.[33]

Infrared and UV-visible spectroscopy were carried out to verify the presence of the double-decker phthalocyanines on the functionalised nanotubes. The spectra of the carbon nanotubes do not show any signal. The infrared spectra of the nanotubes treated in reflux with the four bisphthalocyanines and each of the individual components are compared in Fig.5. 8a. The presence of five signals can be identified at low intensity that are located at 727-728 (C-H out of plane bending), 999 (N-pyrrole in plane bending of phthalocyanine ligand), 1065 (coupling of isoindole deformation and aza stretching), 1310 (pyrrole stretching) and 1441 cm^{-1} (isoindole stretching). These correspond to signals typical of bisphthalocyanines (see section 5.3.1). The absence of other signals indicates that no new bonds are formed after the functionalisation process.

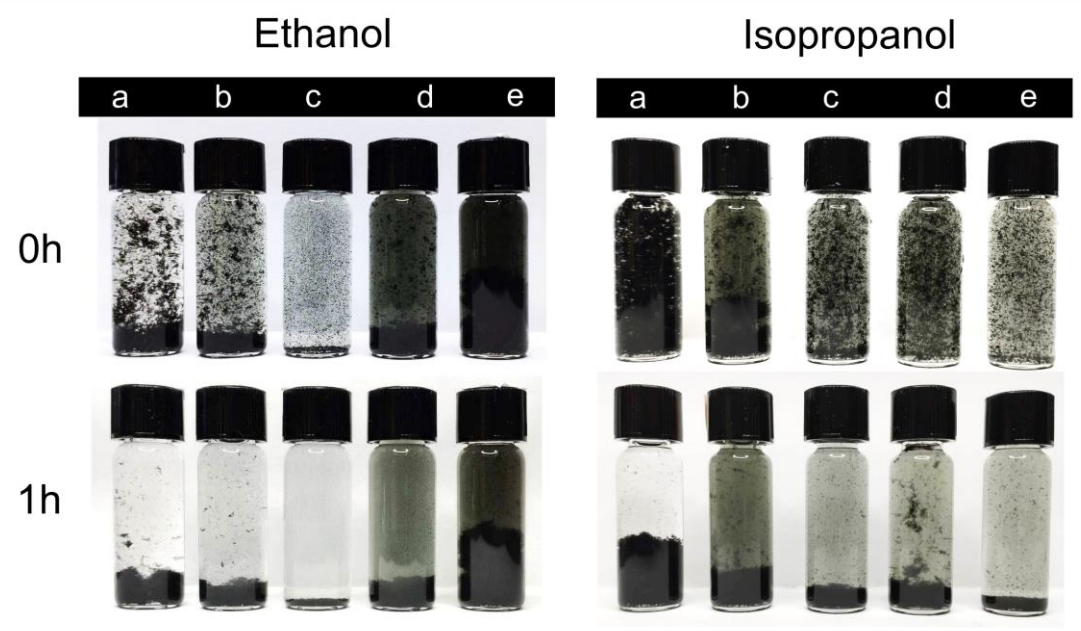

Fig.5. 7. Comparative dispersibility test (1 mg of each sample per 2 mL of solvent) in ethanol and isopropanol for (a) pristine single-walled carbon nanotubes and after functionalization with (b) YPc_2, (c) $LaPc_2$, (d) $GdPc_2$ and (e) $TbPc_2$. Images were taken at elapsed time of 0 and 1 h after ultrasonic bath treatment for 10 min.

The absorption spectra of the MPc_2+SWCNT hybrids (Fig.5. 8b) in DMF show the Q-band located at 668, 663, 665 and 662 nm for the nanotubes with YPc_2, $LaPc_2$, $GdPc_2$ and $TbPc_2$, respectively. The negligible shift compared to bisphthalocyanines could be attributed to the new chemical environment involving the π- π interaction with the nanotubes. As in the *3d* metal phthalocyanines with the SWCNT spectra (Chapter 3), the IR and Uv-Visible spectra are dominated by the nanomaterial background.

The characterisation of the morphology of the pristine nanotubes and the MPc_2+SWCNT hybrids was studied at high magnification by SEM. Fig.5. 9a illustrates that the pristine carbon nanotubes are found in dense bundles (visible as wide entangled fibres) and aggregates, a typical characteristic of this material, due to their nature (π-π interaction between the graphitic lattice of the nanotubes). As for the nanotubes with the bisphthalocyanines (Fig.5. 9b-e), there are no drastic changes in morphology, but more aggregation of the bundles is observed. On the other hand, in the SEM images of the functionalised nanotubes with the MPc_2 there is no evidence of bisphthalocyanine crystals, which may confirm their adsorption on the surface of the nanotubes. This can be attributed to two phenomena: (i) stacking interactions between the adsorbed bisphthalocyanines on neighbouring bundles and (ii) interaction of the sandwiched structures with the nanotubes is not strong enough to break the sidewall interactions that hold the nanotubes together in aggregates or agglomerates. This give rise to the possibility that the adsorption of the double-decker phthalocyanines is on the outer surface of the aggregates rather than individual nanotubes, which is in agreement with the results of the dispersion tests. This behaviour was reported for the hybridisation of transition metals phthalocyanines (Chapter 3) and with metal porphyrins.[34,35]

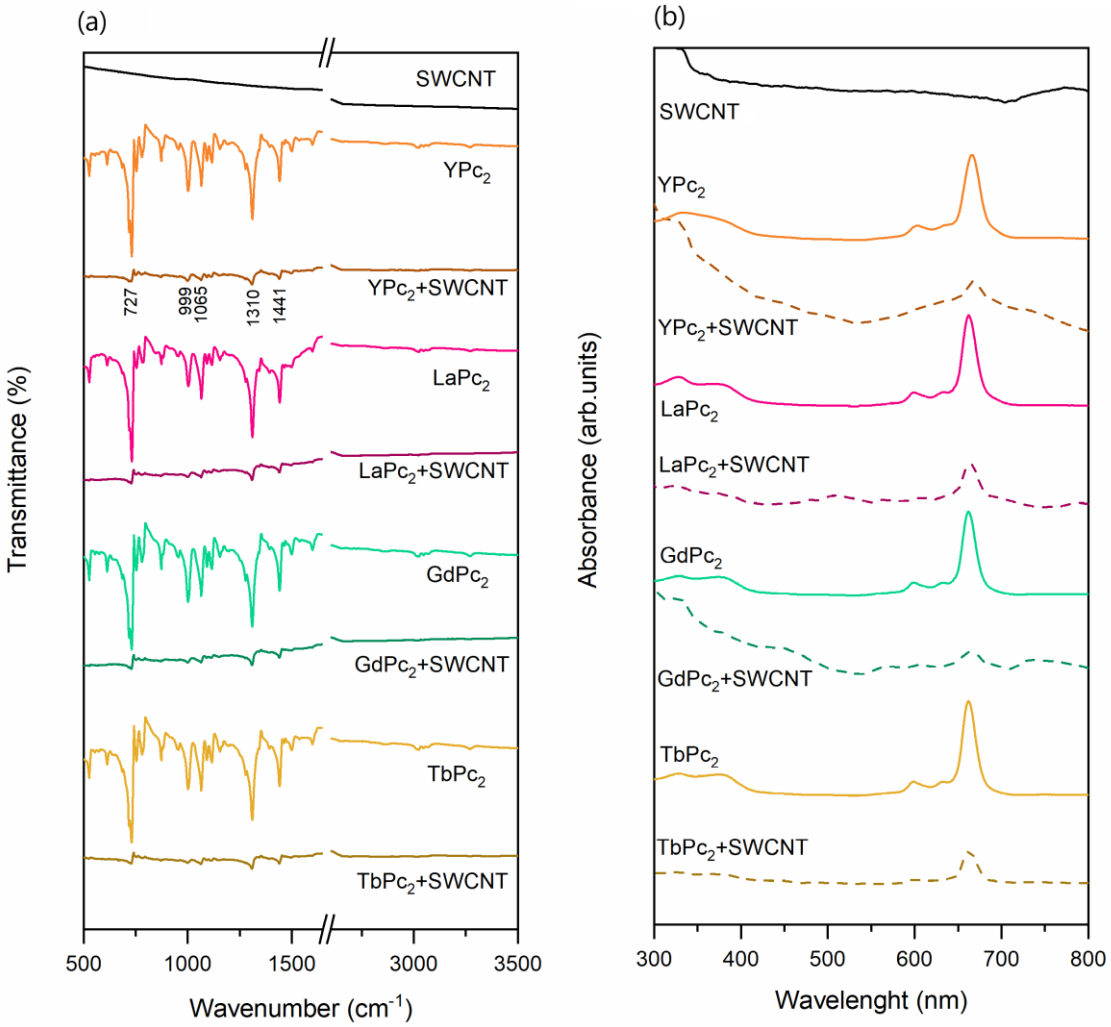

Fig.5. 8. (a) Infrared and (b) UV-visible spectra of rare earth bisphthalocyanines with single-walled carbon nanotubes (MPc_2+SWCNT) in comparison with the spectra of pristine single-walled CNT and bisphthalocyanines acquired under the same conditions. The UV-vis spectra were measured in dimetilformamide. The infrared spectra were of pure powder samples.

Fig.5. 10 presents the elemental analysis obtained by EDS. The spectra of the pristine single-walled CNTs exhibit the peak of carbon as the main component and oxygen as a possible component from functional groups attached to the nanotube. In the spectra of the functionalised nanotubes, additional nitrogen and metal signals are observed for each complex of YPc_2, $LaPc_2$, $GdPc_2$ and $TbPc_2$. In each EDS spectrum, the range of content, in weight and atomic percentage of the metal corresponding to the bisphthalocyanine (yttrium, lanthanum, gadolinium and terbium) obtained from 7 different sites of each sample is specified. The recalculated values for the total molecular weight of the metal phthalocyanines from the weight percentages are 5-60%, 2- 60%, 4-41% and 5-36% for YPc_2+SWCNT, $LaPc_2$+SWCNT, $GdPc_2$+SWCNT and $TbPc_2$+SWCNT, respectively. These values are less precise (measurement spot size is 3x3μm), but generally agree with the weight content of the phthalocyanine in the MPc_2+SWCNT hybrids estimated from the weight differences of the single-walled CNTs before and after of MPc_2

deposition. Furthermore, Fig.5. 9 reveals the elemental mapping specifically of the metal for each hybrid formed, indicating that there is a homogeneous distribution.

The morphology of the nanotubes before and after reflux treatment can be seen in detail in the TEM images. In Fig.5. 11a, as well as the SEM images, the pristine single-walled carbon nanotubes are in bundles and their surface appears to be smooth and uniform. While thesurface of the bundle of the functionalised nanotubes is coated with an amorphous structure (Fig.5. 11b-e), which generates a rough surface. Such morphology indicates that the rare earth bisphthalocyanines were deposited on the surface of the nanotubes.

Free radical (Pc^{-}) neutral rare earth bisphthalocyanines [$M^{3+}(Pc^{-2})$ ($Pc^{\bullet-}$)] are ideal candidates for applications in spintronic devices, because they possess large magnetic anisotropies, which generate high activation barriers for the reversal of magnetization (420 cm^{-1} to 652 cm^{-1}), depending on the substituents and the metal).[17,36] However, this property can be influenced by oxidation or reduction of the Pc ligands ($MPc_2^{+/-/}$; oxidation states also have been shown to possess SMM properties at low bulk temperatures). [36–38] Possible changes can be evaluated by EPR, e.g., lutetium fluorinated bisphthalocaynines (fluorine instead of hydrogen atoms) with oxidation states +1 and -1(($M^{3+}(Pc^{\bullet-})$ ($Pc^{\bullet-}$) and $M^{3+}(Pc^{-2})$ (Pc^{-2}), respectively) are EPR-silent species. [36] Usually the radical neutral bisphthalocyanines have a non-reducing metal centre and their first reduction is the most common and is influenced by the type of solvent used (reducing agent, see Fig.5. 3).[17] In view of the above, electron paramagnetic resonance experiments were performed to confirm that the deposition process on the nanotubes and/or bundle by butanol reflux does not affect the radical neutral electronic structure of the double-decker. Fig.5. 12 shows the first derivative of the characteristic magnetic absorption of the radical species with an approximate *g*-factor of 2 and an approximate linewidth of 0.2 mT. The experiments were performed on powder in a mixture of $BaSO_4$.

According to the TGA/DTA results (Fig.5. 13), the thermal decomposition of pristine single-walled carbon nanotubes occurs in three steps. The first loss between 30 and 102°C corresponds to water molecules physisorbed onto the material. The second change around 391°C is due to multi-walled carbon nanotubes that are present as impurities that form during the single walled synthesis process, whose thermal behaviour is represented in the last event at 544°C and ends at 709°C.[39,40] The multi-walled were detected by TEM imaging (Fig.5. 11a). The 7.9 % residue is assigned to the metal catalyst particles used in the manufacturing process. The percentage provided by TGA of multi-walled nanotubes (around 48%) present in the commercial single samples (42%) does not indicate that they are in the same proportion, as the molecular weight of the multi-walled nanotubes is much higher than the single-walled carbon nanotubes. DTA curves indicate that the oxidative decomposition is an exothermic process.

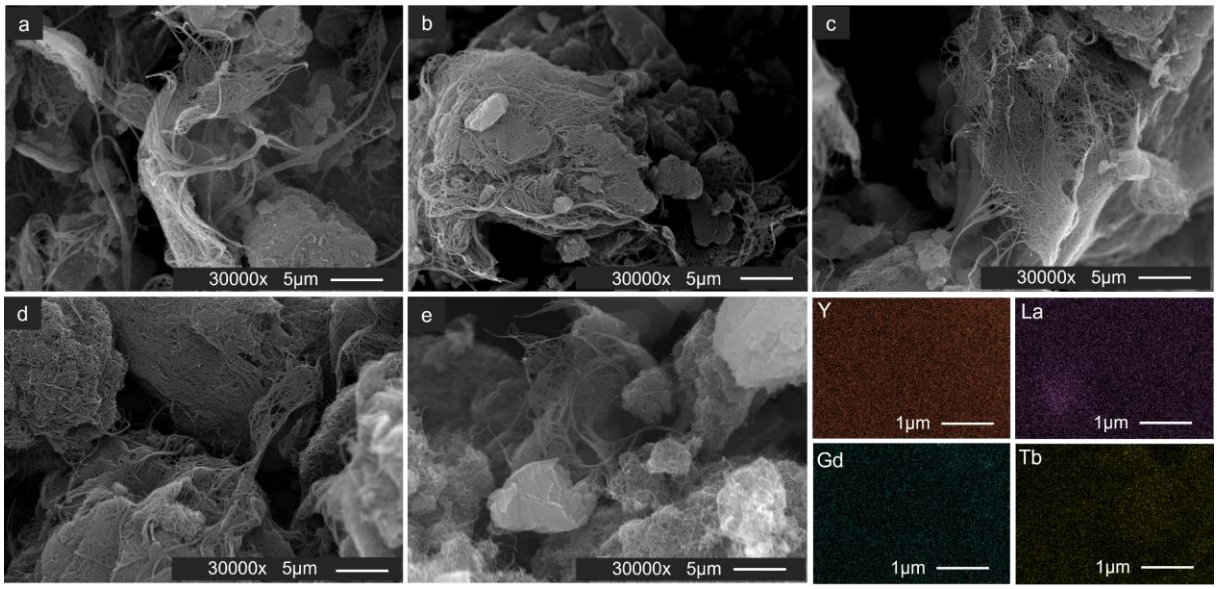

Fig.5. 9. SEM images of (a) pristine single-walled CNTs and with the four rare earth double-decker phthalocyanines (b) YPc_2, (c) $LaPc_2$ (d) $GdPc_2$ and (*e*) $TbPc_2$. Bottom row elemental mapping of the MPc_2+SWCNT hybrids.

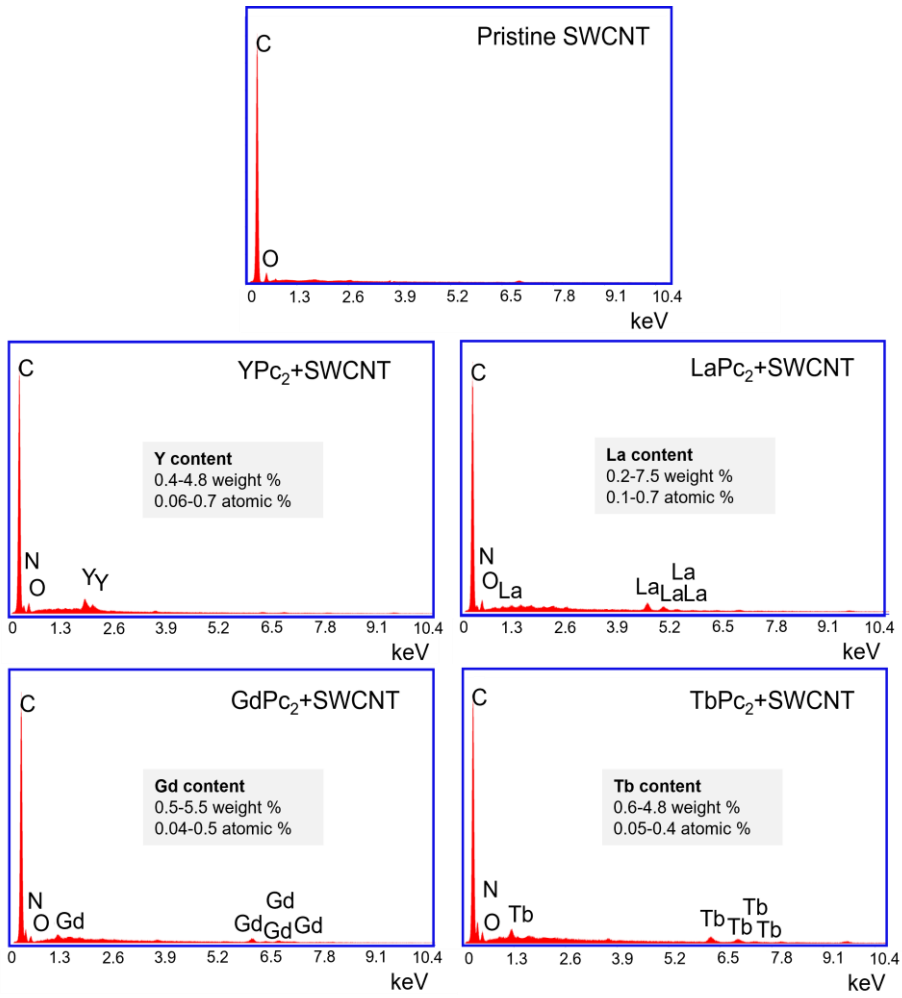

Fig.5. 10. EDS spectra of (a) pristine single-walled CNTs and with the four rare earth double-decker phthalocyanines (b) YPc_2, (c) $LaPc_2$ (d) $GdPc_2$ and (e) $TbPc_2$. Bottom row elemental mapping of the MPc_2+SWCNT hybrids

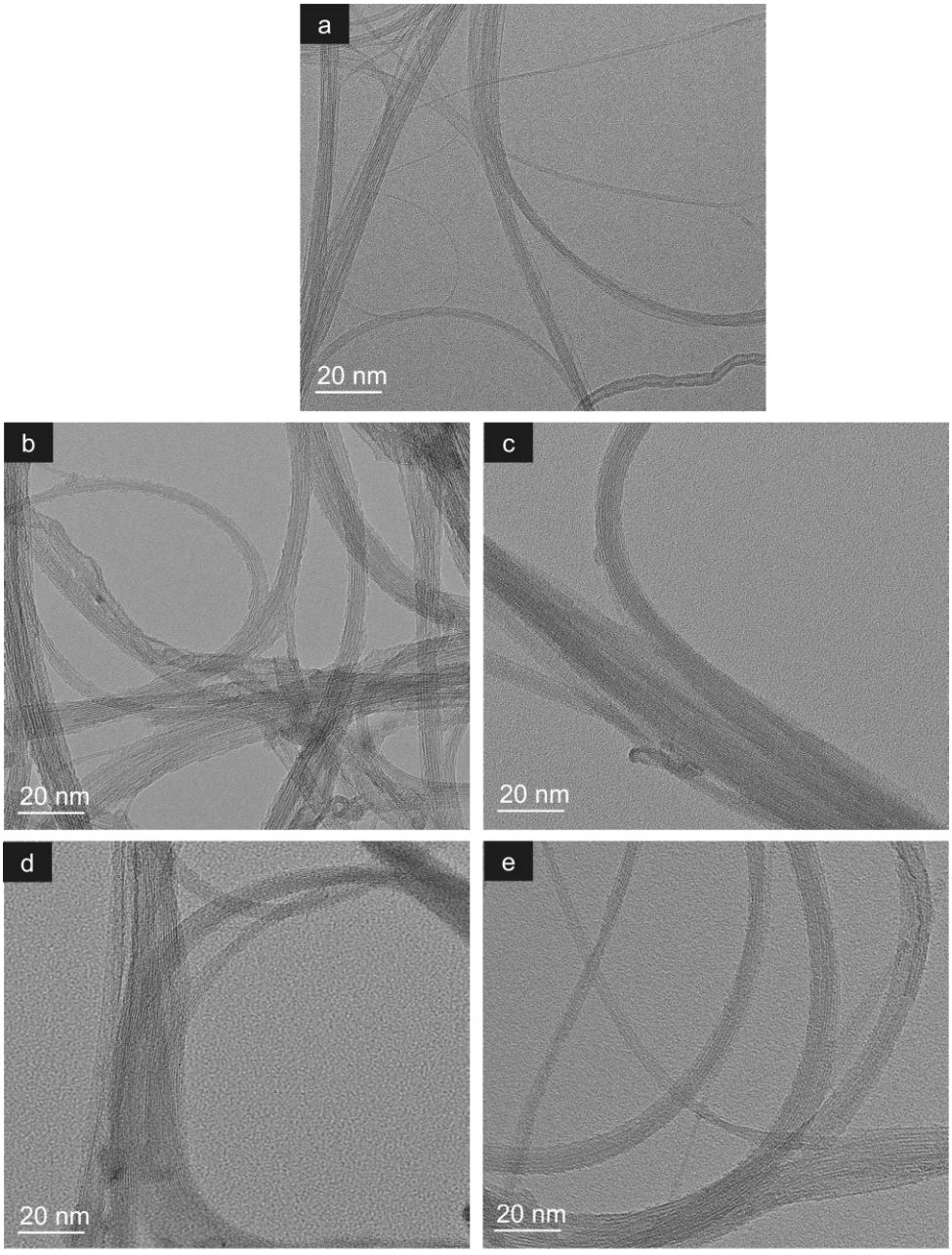

Fig.5. 11. Representative TEM images of (a) pristine single-walled CNTs before and after noncovalent functionalisartion with (b) YPc_2, (c) $LaPc_2$, (d) $GdPc_2$ and (e) $TbPc_2$

Concerning the thermal behaviour of the nanotube and bisphthalocyanine hybrids, the thermograms reveal four thermal events. The first one corresponds to moisture and impurities and in general the other remaining events have been attributed to the oxidative decomposition of MPc_2+SWCNT hybrids. The weight loss around 300 and 460 °C is not only attributed to multi-walled nanotubes but also to the decomposition of bisphthalocyanines and the third ramp or mass change is assigned to the oxidative decomposition of the single-walled carbon nanotubes. It can be seen in Fig.5. 13 that the start and end temperature of thermal degradation of the latter is lower than that of the pristine nanotubes and even coincides with the

decomposition temperatures of the double-decker (Fig.5. 5). One of the possible reasons for this phenomenon is simultaneous formation of rare earth oxides during the degradation process of the bisphthalocyanines present on the surface of the nanotubes. These could act as catalysts in the thermal oxidation of the graphitic material and as a consequence decrease the temperature. This can be explained by the Mars and van Krevelen (MvK) mechanism, which is based on the cyclic reduction-oxidation (Redox) reactions of the active sites. .[41–43] Transition metal oxides and rare earth oxides are known to be active catalysts for the oxidation of carbon compounds (hydrocarbons, [44] CO [45] and aldehydes,[46] specifically), which includes graphene lattice materials. Such catalytic activity is due to the ease of switching between the oxidation states of the metal, an essential feature for MvK.[41–43]

In contrast to the thermal decomposition of 3*d* metal transition phthalocyanines with the nanotubes, especially the hybrid with manganese phthalocyanine (Chapter 3), another factor to consider is the presence of free radicals coming from the double-decker phthalocyanine structure which can jointly contribute to the thermal decomposition of the nanotubes. Estimating the content of bisphthalocyanines in the hybrids by thermal analysis is a complex task. On the other hand, the DTA curves indicate that the thermal oxidation process is exothermic (Fig.5. 13).

5.4. Conclusions

Unsubstituted bisphthalocyanines of yttrium, lanthanum, gadolinium, and terbium were synthesized by a solvothermal method as an alternative approach to conventional synthesis in which the precursor is usually phthalonitrile. Yields of 68% for YPc_2, 43% for $LaPc_2$, 63% for $GdPc_2$ and 62% for $TbPc_2$ were obtained. From EPR results, the bisphthalocyanines contain a dianionic and a monoanionic radial [$M^{3+}(Pc^{2-})$ ($Pc^{\bullet-}$)] ligand. The decomposition of the earth rare double-decker phthalocyanines starts around 350°C. The coordination complexes were identified by infrared, UV-visible and Raman spectroscopy, and elemental analysis.

Single-walled carbon nanotubes were covalently functionalised with the four bisphthalocyanines synthesised by refluxing in butanol. SEM and TEM images show that adsorption of MPc_2 can not only occur on individual nanotubes but also on agglomerates. The bisphthalocyanine radical remains after functionalisation. Thermal oxidation of the hybrids starts and ends at around 300°C and 650°C. Lower temperatures compared to the pristine ones suggest that the oxidation of nanotubes and phthalocyanines is affected by catalytic processes involving the coordination metal, as well as the MnPc+CNT hybrid (Chapter 2). The dispersion of the hybrids depends on the polarity of the solvent and the metal.

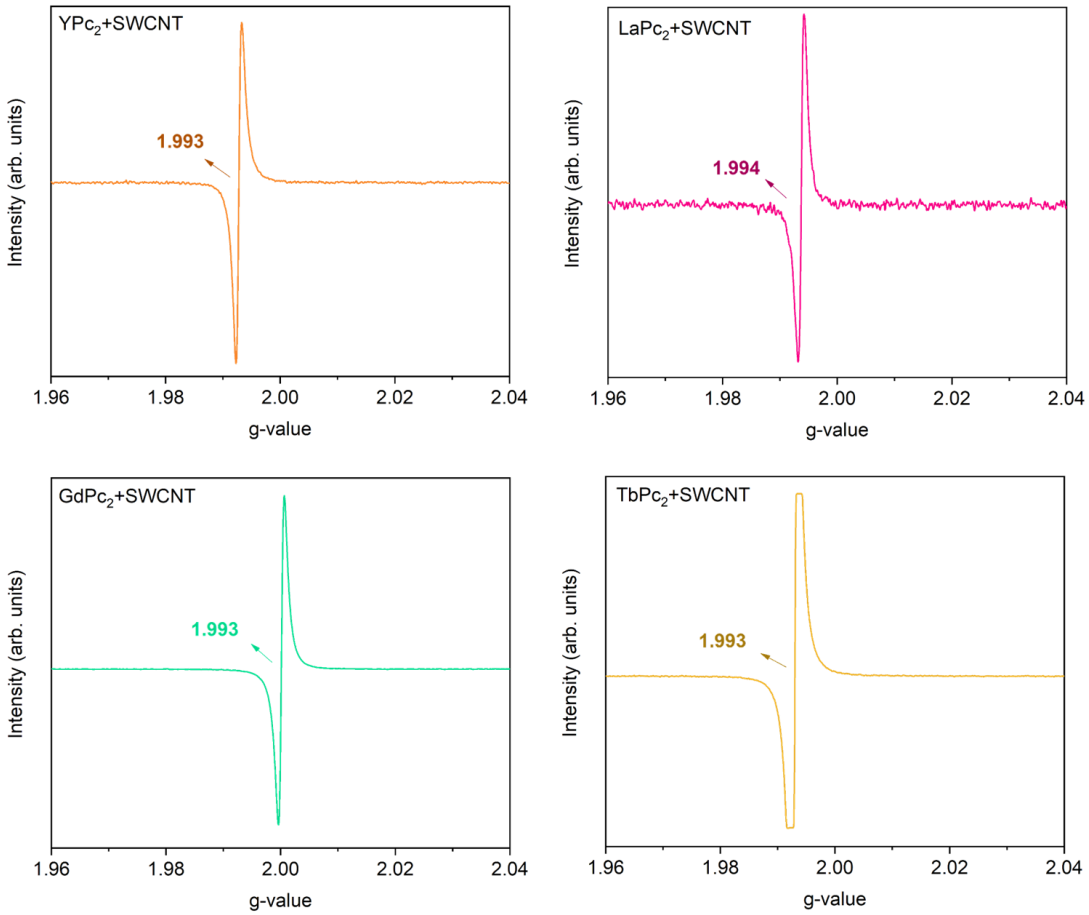

Fig.5. 12. EPR spectra of the four rare earth double-decker phthalocyanines on the surface of carbon nanotubes (MPc_2+SWCNT) at room temperature..

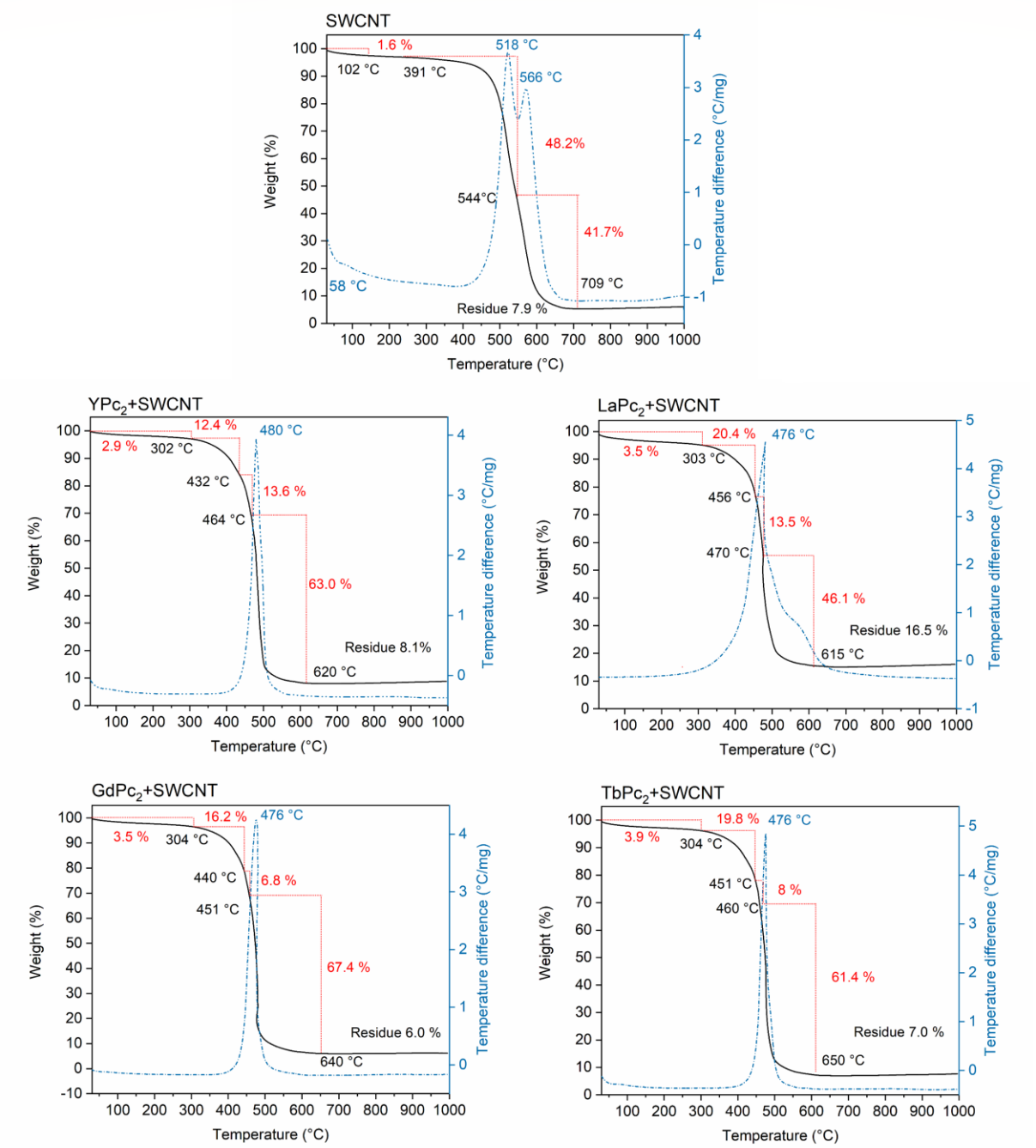

Fig.5. 13. TGA (Black) and DTA (blue) curves of pristine single-walled CNTs and MPc_2+SWCNT hybrids obtained: YPc_2+SWCNT, $LaPc_2$+SWCNT, $GdPc_2$+SWCNT and $TbPc_2$+SWCNT. Air flow100 $mLmin^{-1}$

5.5. References

(1) Pushkarev, V. E.; Tomilova, L. G.; Nemykin, V. N. Historic overview and new developments in synthetic methods for preparation of the rare-earth tetrapyrrolic complexes. *Coord. Chem. Rev.* 2016, *319*, 110–179.

(2) Pushkarev, V. E.; Tomilova, L. G.; Tomilov, Y. V. Synthetic approaches to lanthanide complexes with tetrapyrrole type ligands. *Russ. Chem. Rev.* 2008, *77* (10), 875–907.

(3) Yamamoto, S.; Dudkin, S. V.; Kimura, M.; Kobayashi, N. Phthalocyanine synthesis. In *Handbook of Porphyrin Science: With Applications to Chemistry, Physics, Materials Science, Engineering, Biology and Medicine - Volume 45: Phthalocyanine Synthesis and Computational Design of Functional Tetrapyrroles*; World Scientific Publishing Co., 2019; pp

1–168.
(4) Li, D.; Ge, S.; Sun, G.; He, Q.; Huang, B.; Tian, G.; Lu, W.; Li, G.; Chen, Y.; An, S.; et al. A novel and green route for solvothermal synthesis of manganese phthalocyanine crystals. *Dye. Pigment.* 2015, *113*, 200–204.
(5) Li, D.; Zhang, P.; Ge, S.; Sun, G.; He, Q.; Fa, W.; Li, Y.; Ma, J. A green route to prepare metal-free phthalocyanine crystals with controllable structures by a simple solvothermal method. *RSC Adv.* 2021, *11* (50), 31226–31234.
(6) Xia, D.; Yu, S.; Shen, R.; Ma, C.; Cheng, C.; Ji, D.; Fan, Z.; Wang, X.; Du, G. A novel method for the direct synthesis of crystals of copper phthalocyanine. *Dye. Pigment.* 2008, *78* (1), 84–88.
(7) Ge, S.; Zhang, Y.; Huang, B.; Huang, S.; Tie, W.; Lei, Y.; He, Q.; Tu, G.; Qin, Q.; Niu, S.; et al. Synthesis of highly crystalline copper phthalocyanine needles by solvothermal method. *Mater. Lett.* 2016, *163*, 61–64.
(8) XIA, D.; LI, W.; WANG, X.; YU, S.; FAN, C. xiang; MA, C.; CHENG, C.; FAN, Z.; DU, G.; CONG, F.; et al. Preparation of copper phthalocyanine crystals using solvothermal synthesis. *Chem. Res. Chinese Univ.* 2008, *24* (4), 407–410.
(9) Clarisse, G.; Riou, M. T. Synthesis and characterization of some lanthanide phthalocyanines. *Inorganica Chim. Acta* 1987, *130* (1), 139–144.
(10) Jiang, J.; Arnold, D. P.; Yu, H. Infra-red spectra of phthalocyanine and naphthalocyanine in sandwich-type (na)phthalocyaninato and porphyrinato rare earth complexes. *Polyhedron* 1999, *18*, 2129–2139.
(11) M'Sadak, M.; Roncali, J.; Garnier, F. Rare-earth substitution effect on the electrochemical properties of lanthanide diphthalocyanines. *J. Electroanal. Chem. interfacial Electrochem.* 1985, *189* (1), 99–111.
(12) Lu, F.; Bao, M.; Ma, C.; Zhang, X.; Arnold, D. P.; Jiang, J. Infrared spectra of phthalocyanine and naphthalocyanine in sandwich-type (na)phthalocyaninato and porphyrinato rare earth complexes. part 3. the effects of substituents and molecular symmetry on the infrared characteristics of phthalocyanine in bis(phthal. *Spectrochim. Acta Part A Mol. Biomol. Spectrosc.* 2003, *59* (14), 3273–3286.
(13) Zhang, Y.; Cai, X.; Zhou, Y.; Zhang, X.; Xu, H.; Liu, Z.; Li, X.; Jiang, J. Structures and spectroscopic properties of bis(phthalocyaninato) yttrium and lanthanum complexes: theoretical study based on density functional theory calculations. *J. Phys. Chem. A* 2007, *111* (2), 392–400.
(14) Yara, M. N.; Kandaz, M.; Koca, A.; Salih, B. Functional alcohol-soluble double-decker phthalocyanines : synthesis , characterization, electrochemistry and peripheral metal ion binding. *J. Porphryns phthalocyanines* 2006, *10*, 1022–1033.
(15) Souto, J.; Tomilova^, L.; Aroca, R.; Desaja, J. A. Spectroscopic studies of langmuir-blodgett monolayers of praseodymium bisphthalocyanines. *Langmuir* 1992, *8*, 942–946.
(16) Kratochvílová, I.; Šebera, J.; Paruzel, B.; Pfleger, J.; Toman, P.; Marešová, E.; Havlová; Hubík, P.; Buryi, M.; Vrňata, M.; et al. Electronic functionality of gd-bisphthalocyanine: charge carrier concentration, charge mobility, and influence of local magnetic field. *Synth. Met.* 2018, *236*, 68–78.
(17) Konarev, D. V.; Khasanov, S. S.; Batov, M. S.; Martynov, A. G.; Nefedova, I. V.; Gorbunova, Y. G.; Otsuka, A.; Yamochi, H.; Kitagawa, H.; Lyubovskaya, R. N. Effect of one- and two-electron reduction of terbium(III) double-decker phthalocyanine on single-ion magnet behavior and nir absorption. *Inorg. Chem.* 2019, *58* (8), 5058–5068.
(18) Guilard, R.; Kadish, K. M.; Smith, K. M. *The Porphyrin Handbook*; 2003; Vol. 11.
(19) Chen, X.; Chen, Y.; Bai, M.; Wang, C.; Qi, D.; Liu, Q.; Xu, M.; Jiang, J. Distribution of the unpaired electron in neutral bis(phthalocyaninato) yttrium double-deckers: an experimental and theoretical combinative investigation. *J. Porphyr. Phthalocyanines* 2018, *22* (1–3), 165–172.
(20) Jiang, J.; Bao, M.; Rintoul, L.; Arnold, D. P. Vibrational spectroscopy of phthalocyanine and naphthalocyanine in sandwich-type (na)phthalocyaninato and porphyrinato rare earth complexes. *Coord. Chem. Rev.* 2006, *250* (3–4), 424–448.
(21) Suzuki, A.; Oku, T. Effects of central metal on electronic structure, magnetic properties, infrared and raman spectra of double-decker phthalocyanine. *Appl. Surf. Sci.* 2016, *380*, 127–134.
(22) Zheng, W.; Wang, B. B.; Lai, J. C.; Wan, C. Z.; Lu, X. R.; Li, C. H.; You, X. Z. Electrochromic properties of novel octa-pinene substituted double-decker Ln(III) (Ln = Eu, Er, Lu) phthalocyanines with distinctive near-IR absorption. *J. Mater. Chem. C* 2015, *3* (13), 3072–3080.
(23) Dailey, M.; Besson, C. Selective crystallization of four bis(phthalocyaninato)lanthanoid(III) polymorphs. *CrystEngComm* 2021, *23*, 7151–7161.
(24) Ou, C.; Lv, W.; Chen, J.; Yu, T.; Song, Y.; Wang, Y.; Wang, S.; Yang, G. Structural, photophysical and nonlinear optical limiting properties of sandwich phthalocyanines with different rare earth metals. *Dye. Pigment.* 2021, *184*, 108862.
(25) Erzunov, D. A.; Botnar, A. A.; Domareva, N. P.; Tikhomirova, T. V; Vashurin, A. S. Synthesis, spectroscopic properties and redox behavior kinetics of rare-earth bistetrakis-4-[3-(3,4-dicyanophenoxy)phenoxy]phthalocyaninato metal complexes with Er, Lu and Yb. 2021.
(26) Dyrda, G.; Zakrzyk, M.; Broda, M. A.; Pedziński, T.; Mele, G.; Słota, R. Hydrogen bond-mediated conjugates involving lanthanide diphthalocyanines and trifluoroacetic acid ($LnPc_2$@TFA): structure, photoactivity, and stability. *Molecules* 2020, *25* (16), 1–15.
(27) Słota, R.; Dyrda, G.; Hofer, M.; Mele, G.; Bloise, E.; Del Sole, R. Novel lipophilic lanthanide bis-phthalocyanines functionalized by pentadecylphenoxy groups: synthesis, characterization and uv-photostability. *Mol. 2012, Vol. 17, Pages 10738-10753* 2012, *17* (9), 10738–10753.
(28) Fukuda, T.; Biyajima, T.; Kobayashi, N. A discrete quadruple-decker phthalocyanine. 2010, *132*, 21.
(29) Jiang, J.; Liu, R. C. W.; Mak, T. C. W.; Chan, T. W. D.; Ng, D. K. P. Synthesis, spectroscopic and electrochemical properties of substituted bis(phthalocyaninato)lanthanide(III) complexes. *Polyhedron* 1997, *16* (3), 515–520.
(30) Mele, G.; Garcìa-Lòpez, E.; Palmisano, L.; Dyrda, G.; Słota, R. Photocatalytic degradation of 4-nitrophenol in aqueous suspension by using polycrystalline TiO_2 impregnated with lanthanide double-decker phthalocyanine complexes. *J. Phys. Chem. C* 2007, *111* (17), 6581–6588.
(31) Komijani, D.; Ghirri, A.; Bonizzoni, C.; Klyatskaya, S.; Moreno-Pineda, E.; Ruben, M.; Soncini, A.; Affronte, M.; Hill, S.

Radical-lanthanide ferromagnetic interaction in a Tb(III) bisphthalocyanines complex. *Phys. Rev. Mater.* 2018, *2*, 2.
(32) Seoudi, R.; El-Bahy, G. S.; El Sayed, Z. A. FTIR, TGA and DC electrical conductivity studies of phthalocyanine and its complexes. *J. Mol. Struct.* 2005, *753* (1–3), 119–126.
(33) Ramirez-Calera, I. J.; Meza-Laguna, V.; Gromovoy, T. Y.; Chavez-Uribe, M. I.; Basiuk, V. a.; Basiuk, E. V. Solvent-free functionalization of fullerene C_{60} and pristine multi-walled carbon nanotubes with aromatic amines. *Appl. Surf. Sci.* 2015, *328*, 45–62.
(34) Bassiouk, M.; Basiuk, V. A.; Basiuk, E. V.; Álvarez-Zauco, E.; Martínez-Herrera, M.; Rojas-Aguilar, A.; Puente-Lee, I. Noncovalent functionalization of single-walled carbon nanotubes with porphyrins. *Appl. Surf. Sci.* 2013, *275*, 168–177.
(35) Alzate-Carvajal, N.; Bolivar-Pineda, L. M.; Meza-Laguna, V.; Basiuk, V. A.; Basiuk, E. V.; Baranova, E. A. Oxygen evolution reaction on single-walled carbon nanotubes noncovalently functionalized with metal phthalocyanines. *ChemElectroChem* 2020, *7*, 428–436.
(36) Gonidec, M.; Krivokapic, I.; Vidal-Gancedo, J.; Davies, E. S.; McMaster, J.; Gorun, S. M.; Veciana, J. Highly reduced double-decker single-molecule magnets exhibiting slow magnetic relaxation. *Inorg. Chem.* 2013, *52* (8), 4464–4471.
(37) Ishikawa, N.; Sugita, M.; Wernsdorfer, W. Quantum tunneling of magnetization in lanthanide single-molecule magnets: bis(phthalocyaninato)terbium and bis(phthalocyaninato)dysprosium anions. *Angew. Chemie - Int. Ed.* 2005, *44* (19), 2931–2935.
(38) Gonidec, M.; Davies, E. S.; McMaster, J.; Amabilino, D. B.; Veciana, J. Probing the magnetic properties of three interconvertible redox states of a single-molecule magnet with magnetic circular dichroism spectroscopy. *J. Am. Chem. Soc.* 2010, *132* (6), 1756–1757.
(39) Mahajan, A.; Kingon, A.; Kos Kukovecz, A. ´; Konya, Z.; Vilarinho, P. M. Studies on the thermal decomposition of multiwall carbon nanotubes under different atmospheres. 2012.
(40) Zhang, L. H.; Gong, H.; Wang, J. P. Kinetics and mechanisms of the thermal degradation of amorphous carbon films. *J. Appl. Phys.* 2002, *91* (12), 9646.
(41) Aksel, S.; Eder, D. Catalytic effect of metal oxides on the oxidation resistance in carbon nanotube-inorganic hybrids. *J. Mater. Chem.* 2010, *20* (41), 9149–9154.
(42) Neeft, J. P. A.; Makkee, M.; Moulijn, J. A. Metal oxides as catalysts for the oxidation of graphite. *Carbon N. Y.* 1970, *8* (5), 295–302.
(43) Mckee, D. W. Rare earth oxides as carbon catalysts. *Carbon N. Y.* 1985, *23* (6), 707–713.
(44) Mora-Briseño, P.; Jiménez-García, G.; Castillo-Araiza, C. O.; González-Rodríguez, H.; Huirache-Acuña, R.; Maya-Yescas, R. Mars van krevelen mechanism for the selective partial oxidation of ethane. *Int. J. Chem. React. Eng.* 2019, *17* (7), 1–13.
(45) Doornkamp, C.; Ponec, V. The universal character of the mars and van krevelen mechanism. *J. Mol. Catal. A Chem.* 2000, *162*, 19–32.
(46) Wang, Z.; Yu, H.; Zhang, L.; Guo, L.; Dong, X. Photothermal conversion of graphene/layered manganese oxide 2D/2D composites for room-temperature catalytic purification of gaseous formaldehyde. *J. Taiwan Inst. Chem. Eng.* 2020, *107*, 119–128.

6

Chapter 6

Adsorption of rare-earth double-decker phthalocyanines on single-walled carbon nanotubes: structural analysis and electronic properties by DFT

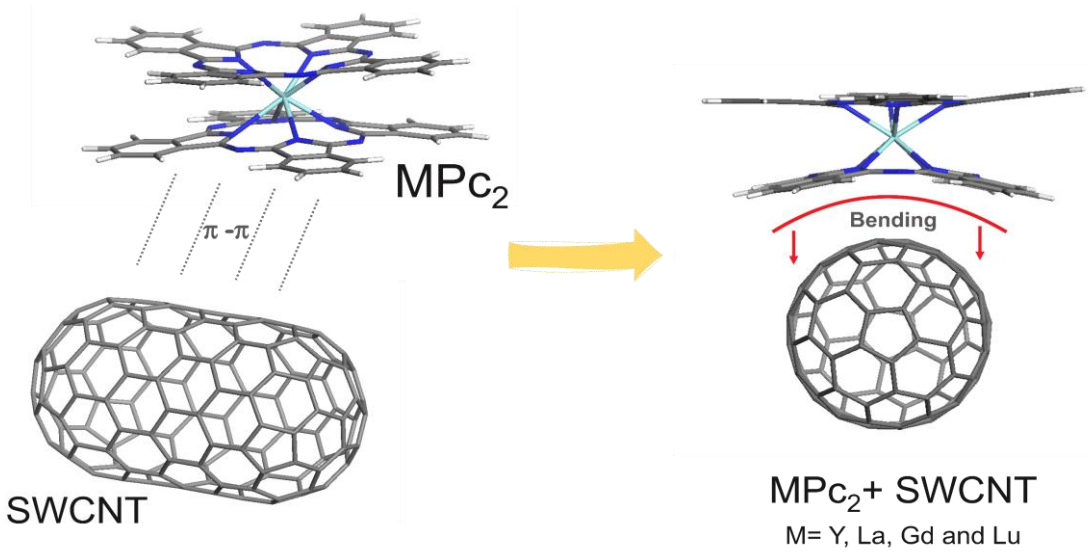

Published as

Lina M. Bolivar-Pineda, Mónica I. Sinecio-Ontivieros and Vladimir A. Basiuk. Mater. Today Commun. 2021, 28, 102667.

Lina M. Bolivar-Pineda, Carlos Uriel Mendoza-Domínguez and Vladimir A. Basiuk. J.Solid State. Sci. Technol, 2022.

Abstract

Molecular modelling of carbon nanotubes and rare earth double-decker phthalocyanines hybrids is challenging due to the presence of 4*f*-electrons. In this chapter a calculation methodology is proposed using basis sets of the Dmol^3 of Material Studio software to analyse trends in structural changes and some electronic properties when a rare earth (Y, La, Gd and Lu) bisphthalocyanine molecule is adsorbed on the surface of two single-walled carbon nanotube models: armchair and zigzag. Density functional theory showed that the height of bisphthalocyanines complexes (MPc_2) when adsorbed on a nanotube (MPc_2+SWCNT) is the structural feature which is most affected by the nanotube model. The formation energy of the MPc_2+SWCNT hybrid depends on the metal atom and the nanotube chirality. YPc_2, $LaPc_2$ and $LuPc_2$ bind stronger to the zigzag nanotube, while for $GdPc_2$, bonding to the armchair nanotube is the stronger one. The HOMO-LUMO gap energy (E_{gap}) shows a correlation between the nature of lanthanide and the nanotube chirality. In the case of adsorption on an armchair nanotube, E_{gap} tends to match the gap of the isolated MPc_2, whereas for adsorption on a zigzag nanotube it is closer to the value for the isolated nanotube model. The spin density is localized on the Pcs ligands, when the bispthalocyanine is on the surface of the armchair nanotube. For bonding to the zigzag nanotube, it extends over both components, except for $LaPc_2$+ZNT where only the spin density is on the nanotube.

6.1. Introduction

Rare-earth double-decker phthalocyanines have attracted great interest due to their remarkable electronic and optical properties, and especially because of their single-molecule magnet (SMM) behaviour. In fact, they show a large magnetic anisotropy, slow relaxation of the magnetic moment and quantum tunnelling of magnetisation, which makes them promising candidates for applications in spintronics and quantum computing. These molecular quantum magnets offer the spin degree of freedom that can be used to control charge transport in conducting systems [1,2].

The self-assembly of bisphthalocyanines on different surfaces has been proposed for the enhancement of magnetic properties, for example, their deposition suggests the survival of a large spin magnetic moment of the rare-earth metal centre [3]. Bisphthalocyanines have been deposited onto the surfaces of copper (111) [3], gold (111) [4–7], nickel [8,9], glass [10] and carbon nanomaterials such as graphene [2,11], highly oriented pyrolytic graphite [12] and carbon nanotubes [1,13–17]. Unfortunately, the properties of SMM films usually change depending on the noble metal and ferromagnetic substrates or the fabrication conditions. The substrate temperature and deposition rate affect the thermodynamics and kinetics for the growth of organic films [10].

In view of their inclusion in spintronic devices, hybrids of MPc_2 with carbon nanomaterials such as graphene and carbon nanotubes have received special attention, since there the weak spin-orbit coupling is expected to result in long spin coherence lifetimes and lengths. [2]In the case of carbon nanotubes, the noncovalent interaction with rare-earth double-decker phthalocyanines through π-π stacking is a way to improve the magnetic measurements and bistability of SMM because the main magnetic properties of rare-earth metal centre are preserved [13].

Considering the reported DFT studies of the metal phthalocyanines interaction with a fullerene and carbon nanotube (including Chapter 4 of this dissertation) the important general conclusion is that the usually planar macrocyclic ring system of MPc suffers a strong bending distortion in order to increase its contact area with the endohedral fullerene $Sc_3N@C_{80}$ [18] or graphene with defects [19,20] or the nanotube sidewall. [21–25] Hence, several questions arise regarding the behaviour of double-decker phthalocyanine analogues. Does their deposition onto the nanotube sidewalls alter their geometry? If there is distortion, how significant is it? Are both Pc ligands affected, and in the same way? Are electronic parameters (for example, HOMO, LUMO and spin density distribution) altered compared to that of isolated MPc_2 complexes? Moreover, what is the influence of the *f*-electrons of the lanthanide core metal of bisphthalocyanines on the properties of the MPc_2+SWCNT hybrid?

Before answering these questions, it should be noted that the geometry optimisations, energetic and electronic characteristics of MPc_2+SWCNT hybrids is much more computationally demanding than the corresponding calculations for a 3*d* transition metal phthalocyanine adsorbed on a SWCNT, for three reasons. Firstly, a second heavy $C_{32}H_{16}N_8$ ligand unit is added to the model; secondly, rare-earth metal atoms have a considerably larger

number of electrons compared to 3*d* transition metals; and thirdly, the calculations must be spin-polarized. Besides that, the systems of major interest, which have especially pronounced magnetic properties, are those incorporating central lanthanides (Eu, Gd and Tb). However, the presence of *f*-electrons implies the existence of a series of almost degenerate states, dramatically complicating self-consistence field (SCF) convergence, not only for these lanthanides, but also for other lanthanides from Ce to Lu. Unless the inclusion of *f*-electron containing lanthanides is critical, a feasible solution capable of providing an insight as regards to the conformational changes in question is the substitution of Ce–Lu atoms with rare earth elements, which do not have *f*-electrons, such as yttrium(III) and lanthanum(III) [26]

With the above considerations in mind, a DFT analysis of the changes in geometry and some electronic properties of yttrium, lanthanum, gadolinium, and lutetium bisphthalocyanines (MPc_2 with M= Y, La, Gd and Lu) when forming non-covalent hybrids with two SWCNT models of different chirality (armchair and zigzag) was performed in the study presented in this chapter.

6.2. Results and discussion

6.2.1. Structural characteristics

To proceed with DFT studies of non-covalent hybrids of double decker phthalocyanines with carbon nanomaterials, it was crucial to optimise the calculation conditions to provide optimised structures of the bisphthalocynines, as close as possible to the ones obtained experimentally by X-ray diffraction. As representative bisphthalocyanines, species with a totally empty ($LaPc_2$, electronic configuration [Xe]4f^0), a half-filled ($GdPc_2$, [Xe]4f^7) and a totally filled ($LuPc_2$, [Xe]4f^{14}) 4*f* shell, as well as an incomplete 4*d*-shell (YPc_2 electron configuration [Kr]4d^{1}5s^2) were considered (Fig.6. 1). Structures calculated with DFT were compared with the following crystal-line phases of the complexes: YPc_2, γ-phase;[6] $LaPc_2$, α-phase;[27]$GdPc_2$, δ-phase[27] and $LuPc_2$, a solvate phase.[28]

The geometry of the isolated YPc_2 molecule, armchair and zigzag carbon nanotubes models, and their hybrids were optimised by the PBE-D functional in conjunction with all three double numerical basis sets available in the DMol^3 module DN, DND and DNP for comparison and to determine if there is an influence of the size of the basis sets. While for this system, no SCF convergence problems were expected when employing the largest basis set, the one in DNP, these problems arose in the case of other rare-earth phthalocyanines (in particular for central lanthanides having several unpaired *f*-electrons). In other word, the larger DNP and DND basis sets (having polarization functions) were found not to be the best choice for the above purpose, due to (often) unresolvable SCF problems and distorted lanthanides double-decker phthalocyanine geometries (represented by $LaPc_2$, $GdPc_2$ and $LuPc_2$), for example, an eclipsed conformation (Fig.6. 2) instead of the typical staggered one (Fig.6. 1).[29] Only the use of a smaller DN basis set helped to complete computations for all lanthanides from La to Lu, as well as to obtain reasonable $LnPc_2$ geometries (see reference 29 for details).

Therefore, to achieve the main goal, the analysis of the structural changes and electronic

properties of $LnPc_2$ phthalocyanines in non-covalently bonded $LnPc_2$+SWCNT hybrids, the DN basis set along with the PBE-D2 functional was employed. Moreover, thermal smearing with a value of 0.0001 Ha was used, this value is very low (equivalent temperature of 31.6 K), but it was impossible to complete the geometry optimization of $LnPc_2$+SWCNT hybrids without thermal smearing (Fermi occupancy). The latter is a computational tool that facilitates convergence to achieve meaningful results, especially for systems containing *f*-elements where a significant number of highly degenerate states close to the Fermi level, dramatically complicates SCF convergence (or simply make it impossible). This applies to all Ln species with partially filled 4*f* orbitals., as explained in detail elsewhere. [30–32].

As regards the nanotube models, those described in Chapter 4 were used to simulate yttrium bisphthalocyanine hybrids (Fig.6. 3a). Table 6. 1 lists the diameter and length of the models optimised by all three basis sets. The values obtained when the DN basis set is used are insignificantly larger, while with DND and DNP basis sets essentially identical values are obtained. In particular, when computed with the DNP basis set, the diameter and length for ANT are 7.060 and 14.123 Å, respectively, and for ZNT, 7.965 and 14.293 Å. For the lanthanide double-decker phthalocyanines hybrids, it was decided to build slightly longer and larger diameter ANT and ZNT models, which are composed of 180 carbon atoms with 8.23 and 7.67 Å diameter and 17.05 and 18.60 Å length, respectively, whose ends are capped with fullerene hemispheres (denoted with * in order to differentiate them: ANT* and ZNT*; Fig.6. 3b).

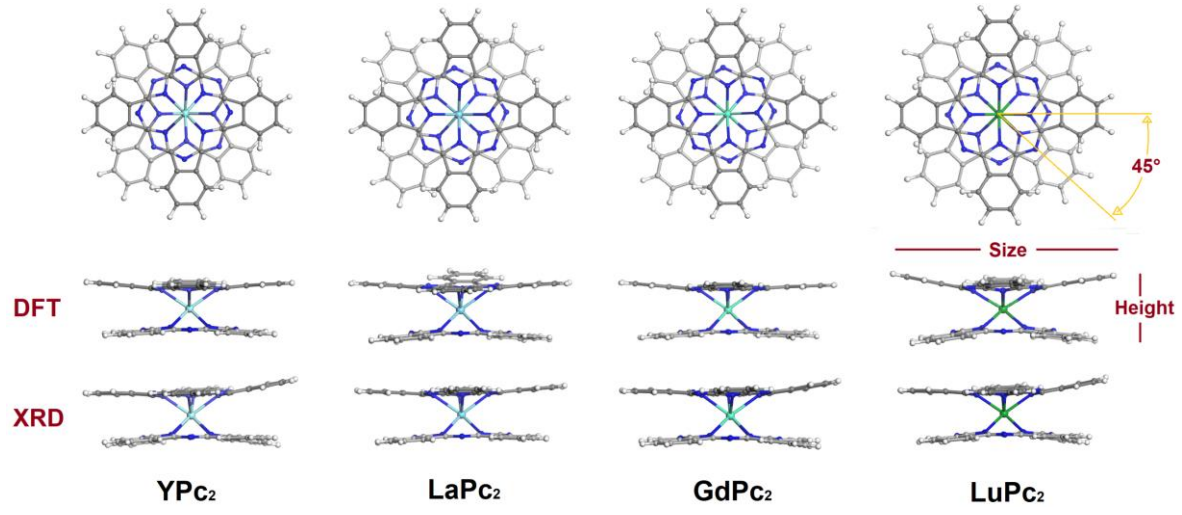

Fig.6. 1. Comparison of DFT-optimised and XRD-derived [6,27,28] structures (side views) for the four rare-earth double-decker phthalocyanines (MPc_2; M= Y, La, Gd and Lu). The optimised geometry of YPc_2 complexes was obtained by DNP with Fermi occupancy (same structure for DND and DN), while for $LaPc_2$, $GdPc_2$ and $LuPc_2$ the DN basis set was used with thermal smearing (0.0001 Ha). It displays size (i.e., width), height and rotation angle (φ) between the two Pc macrocycles (staggered structure) for each complex. Atom colours: gray, carbon; white, hydrogen; deep blue, nitrogen; light blue, yttrium, sky blue, lanthanum, blue turquoise blue, gadolinium; green, terbium.

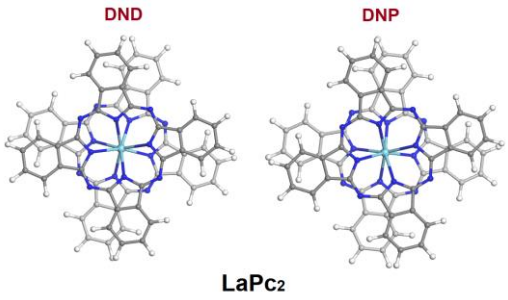

Fig.6. 2. Optimized geometries for lanthanum double-decker phthalocyanine by DND and DNP basis set using Fermi occupancy. Semi-eclipsed structure.

To compare with experimental data and to evaluate the distortion for each MPc_2 in the isolated and the adsorbed state in MPc_2+SWCNT hybrids (Table 6. *2* for YPc_2 and Table 6. 3 for $LnPc_2$) we used several structural parameters: the rotation angle between the two Pc ligands (skew angle; φ), the molecular size (width), height, the N-M distance, and the N-M-N angles. Most of these parameters vary within the same molecule, so we usually present the value as a range.

6.2.1.1. Rotation angle (φ)

As most unsubstituted double-decker phthalocyanines, the ones studied in this PhD project are characterized by a staggered structure (Fig.6. 1), where the mutual rotation angle (φ) between Pc ligands approaches 45°. [29,33] Such a staggered conformation of MPc_2 reduces the overlap between the two electronic clouds and the electrostatic repulsion, leading to a D_{4h} geometry as a result of the Jahn-Teller effect, which forces the molecule to have a less symmetric stable state. [34] The corresponding optimised φ values for YPc_2, $LaPc_2$ and $GdPc_2$ complexes do not show any tangible differences compared to the experimental XRD structures: 0.02° with DN/DND and 0.01° with DNP basis sets for YPc_2, 0.38° for $LaPc_2$ and 0.09° for $GdPc_2$. However, for $LuPc_2$ this angle differs by 4.9° from that deduced from the diffraction. This discrepancy can be attributed to the fact that the experimental value refers to the crystalline phase while the theoretical approach considers an isolated molecule. Also the presence of solvent in the crystal lattice (the reported $LuPc_2$ structure included $[NBu_4]^+$ cation, creating very particular chemical environment). [28] In the phthalocyanines adsorbed on the surface of SWCNT models, the skew angles are not affected: their values vary between 44.8° and 45.0° only, depending on MPc_2 complex, nanotube chirality and of the basis set for the systems with yttrium bisphthalocyanines (Fig.6. 6).

Table 6. 1. Diameter and length (in Å) of isolated ANT and ZNT nanotube models, calculated using PBE GGA functional with Grimme's dispersion correction in conjunction with DN, DND and DNP basis sets for the non-covalent interactions with a yttrium bisphthalocyanine.

Model	Basis set	Diameter (Å)	Length (Å)
ANT	DN	7.088	14.161
	DND	7.059	14.124
	DNP	7.060	14.123
ZNT	DN	7.984	14.338
	DND	7.964	14.299
	DNP	7.965	14.293

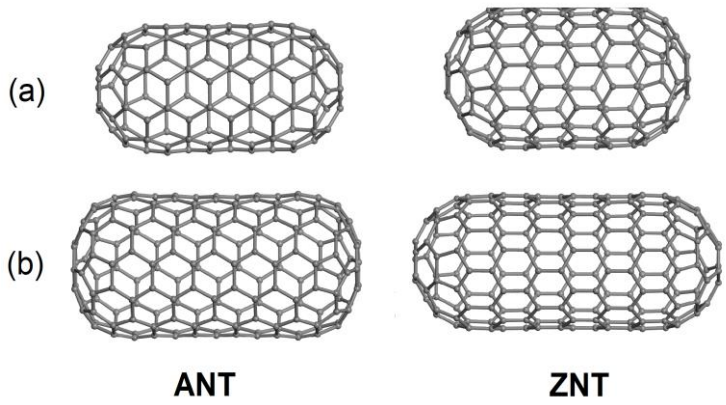

Fig.6. 3. Optimised geometries for armchair and zigzag nanotubes used for non-covalent hybrids with (a) YPc_2 and (b) $LnPc_2$ (Ln = La, Gd and Lu).

In Fig.6. 1 one can see that the two ligands of isolated MPc_2 in XDR and DFT structures are not flat but exhibit a different degree of bending in the isoindole units that generates a certain degree of outward bending (doming toward the central Ln atom). The bending could be caused by some variability in the length of eight M-N coordination bonds, electronic repulsion between the opposite *o*-phenylene rings within the same molecule, π-π stacking and other intermolecular interactions between adjacent bisphthalocyanines in the crystal lattice.[6,27,35].

6.2.1.2. Size

The size (or width) of the isolated optimised MPc_2 molecules, defined as the maximum distance between the two hydrogen atoms at opposite *o*-phenylene moieties of the Pc rings [6,34] (see Fig.6. 1), is overestimated in all cases and fluctuates around 15.0 Å (1.5 nm; Table 6. 2 and Table 6. 3) relative to the experimental data. Hence, the length of the nanotube models is barely sufficient to accommodate one MPc_2 molecule. As seen in Table 6. 2 and Table 6. *3*, the distance between the hydrogen atoms is not the same for all MPc_2 complexes. In particular, the size variation for isolated YPc_2 is larger when the size of the basis set decreases, *i.e.*, 0.111 Å (DN) > 0.047 Å (DND)> 0.015 Å (DNP).

Upon adsorption on the SWCNT models, the *o*-phenylene moieties are attracted to the nanotube sidewall, leading to a more domed geometry of the Pc ligand contacting the SWCNT (Fig.6. 6). The bending distortion is most noticeable when the bisphthalocyanines are adsorbed on small diameter nanotube models. In the case of lanthanide bisphthalocyanines it occurs when they are in contact with the zigzag nanotube, while for yttrium bisphthalocyanines bending is evident for adsorption on the armchair nanotubes (regardless of the basis set size).

In the case of the YPc_2+SWCNT hybrids, the two Pc units are remarkably different in size, unlike the $LnPc_2$+SWCNT. Table 6. 2 shows the average size of each Pc ligand of the yttrium double-decker. The size of the ligand contacting the ANT or ZNT sidewall decreases to 14.8-14.9 Å (first value in the table), i.e., the ligand undergoes distortion bending. As to the second, 'external' Pc ligand, its size remains approximately the same, namely 15.0 Å (second value in

the table). Visually it looks like this ligand becomes flatter upon adsorption (Fig.6. 1 *versus* Fig.6. 6). This impression is due to the diameter and length of the nanotube models that are smaller than the nanotubes used for the $LnPc_2$ complexes, so their distortion of the yttrium bisphthalocyanine structure may be more noticeable due to the curvature of the sidewall and tips.

On the other hand, the size of $LnPc_2$ molecules decreases upon adsorption. However, the size range is much larger than that of the optimised isolated structures or that obtained from experimental data (Table 6. 3). These values are higher than those of yttrium bisphthalocyanine on short nanotube models of smaller diameter.

6.2.1.3. Height

A quantitative evaluation of this distortion can be made by analysing the height of each MPc_2 complex (Table 6. 2 and Table 6. 3), which is measured as the distance between the peripheral hydrogen atoms belonging to the opposing Pc ligands [6,36] (see Fig.6. 1). For the XRD structures of YPc_2, $LaPc_2$, $GdPc_2$ and $LuPc_2$ these height values are, respectively, 2.351-5.094 Å (variation within 2.743 Å), 3.936-4.381 (variation within 0.445 Å), 3.652-4.912 (variation within 1.260 Å) and 3.743-5.141 Å (variation within 1.439 Å). For DFT-optimized MPc_2 geometries, the height variation increases for $LaPc_2$ (from 0.445 to 1.611 Å) but decreases for $GdPc_2$ (from 1.260 to 0.700 Å) and $LuPc_2$ (from 1.439 to 0.652 Å). For YPc_2 it depends on the size of the basis set, the lowest variation being found for DNP (0.254 Å) followed by DND (0.421 Å) and DN (0.652 Å). These results show that the DFT-derived structures tend to be less distorted (Fig.6. 1), flatter and with a more uniform height. A possible reason for this is the absence of adjacent MPc_2 molecules in our DFT calculations.

The height variation of the bisphthalocyanies when interacting with the CNTs models (Fig.6. 6) presents a specific trend for each complex and suggests a higher or lower distortion through the contact with the curved nanotube surface, because of the π-π interactions (Table 6. 2 and Table 6. 3). The calculations with all three basis sets indicate that the height of the YPc_2 molecule increases when adsorbed on the carbon nanotube compared to when it is isolated. For example, with the DNP basis set, this height goes from 0.254 to 0.633 and 0.751 Å for adsorption on the armchair and zigzag models, respectively. $LaPc_2$ shows the same behaviour as YPc_2 on ANT* and ZNT* (from 1.611 to 1.718 and 2.099 Å, respectively). In contrast, the H···H distances in $GdPc_2$ decreases for both hybrids (from 0.700 to 0.646 and 0.591 Å on ANT* and ZNT*), while in the case of $LuPc_2$ the height increases for adsorption on ZNT* but decreases when in contact with ANT* (from 0.625 to 1.100 and 0.602 Å, respectively).

Table 6. 2. Size (in Å), height (in Å) and N-Y-N angles (in degrees) for the isolated YPc_2 molecule and for YPc_2 bound noncovalently to single-walled carbon nanotubes (YPc_2+SWCNT with SWCNT = ANT, ZNT), also listed are the shortest distances: Y···C_{SWCNT}, γ-N···C_{SWCNT} and C_{YPc2}···C_{SWCNT} (in Å) between YPc_2 and SWCNT, calculated using PBE GGA functional with Grimme's dispersion correction in conjunction with DN, DND and DNP basis sets. The structural parameters for the YPc_2 crystal structure as obtained from X-ray diffraction [6] are reported for comparison.

System	Basis set	Size (Å)	Height (Å)	N-Y-N (°)	Y-N (Å)	Y···C_{SWCNT} (Å)	γ-N···C_{SWCNT} (Å)	C_{YPc2}···C_{SWCNT} (Å)
YPc_2 [a]		14.644-14.762	2.351-5.094	109.7-110.6	2.395-2.412			
YPc_2	DN	14.987-15.098	4.151-4.803	113.3-113.7	2.407-2.422			
	DND	14.992-15.039	4.020-4.441	110.7-110.9	2.412-2.417			
	DNP	15.005-15.020	4.062-4.316	110.9-111.0	2.410-2.413			
YPc_2+ANT	DN	14.841; 15.087 [b]	4.390-5.026	112.8-115.1	2.392-2.422	4.386	3.014	3.076
	DND	14.851; 15.031	4.197-4.777	110.6-112.0	2.403-2.417	4.399	3.029	3.081
	DNP	14.805; 15.015	4.297-4.930	110.9-112.2	2.399-2.417	4.430	3.046	3.097
YPc_2+ZNT	DN	14.906; 15.057	4.200-5.140	112.7-115.3	2.392-2.412	4.460	3.060	2.957
	DND	14.916; 15.042	3.963-4.568	110.6-112.0	2.401-2.411	4.507	3.091	2.973
	DNP	14.860; 15.027	4.116-4.867	110.8-112.5	2.396-2.409	4.526	3.095	2.986

[a] Values derived from XRD results

[b] Average size of each Pc ligand of YPc_2 complexes. First value of the ligand in direct contact with the surface of the nanotube

Table 6. 3. Size (in Å), height (in Å), Ln-N bond length (Å) and N-Ln-N angle (in degrees) for the isolated $LnPc_2$ molecules and for LnPc2 bound noncovalently to a single-walled carbon nanotube ($LnPc_2$+SWCNT with SWCNT = ANT, ZNT), also listed are the shortest distances: Ln···C_{SWCNT}, γ-N···C_{SWCNT} and C_{LnPc2}···C_{SWCNT} (in Å), between $LnPc_2$ and SWCNT, calculated using the PBE GGA functional with Grimme's dispersion correction in conjunction with the DN basis set. The structural parameters for the crystal structure of $LnPc_2$ obtained from X-ray diffraction [27,28] are listed for comparison.

System	Size (Å)	Height (Å)	N-Ln-N (◦)	Ln-N (Å)	Ln···C_{SWCNT} (Å)	γ-N···C_{SWCNT} (Å)	C_{LnPc_2}···C_{SWCNT} (Å)
$LaPc_2$ [a]	14.703	3.936-4.381	108.8-108.9	2.421			
$GdPc_2$ [a]	14.679-14.733	3.652-4.912	108.2-108.8	2.422-2.436			
$LuPc_2$ [a]	14.599-14.717	3.743-5.182	110.8-112.0	2.358-2.388			
$LaPc_2$	15.126-15.170	3.803-5.414	107.6-107.3	2.536-2.545			
$GdPc_2$	15.098-15.132	3.858-4.558	107.1-107.6	2.507-2.529			
$LuPc_2$	14.925-15.046	4.358-5.010	114.1-114.2	2.384-2.400			
$LaPc_2$+ANT*	14.838-15.151	4.087-5.805	107.3-107.8	2.522-2.553	4.551	3.107	3.160
$GdPc_2$+ANT*	15.043-15.147	3.920-4.566	111.1-113.2	2.405-2.444	4.597	3.180	3.279
$LuPc_2$+ANT*	14.835-15.052	4.591-5.193	113.6-114.4	2.379-2.405	4.619	3.231	3.218
$LaPc_2$+ZNT*	14.863-15.091	3.899-5.998	107.3-108.7	2.519-2.550	4.692	3.180	3.129
$GdPc_2$+ZNT*	14.839-15.143	4.320-4.911	112.4-114.0	2.411-2.430	4.559	3.192	3.089
$LuPc_2$+ZNT*	14.876-15.030	4.189-5.289	113.6-115.7	2.364-2.391	4.533	3.123	3.076

[a] Values derived from XRD results

6.2.1.4. M-N*iso* bond lengths

The central metal atom of the bisphthalocyanine coordinates with eight isoindole nitrogen atoms (N_{iso}), giving rise to a pseudo-4-fold axis perpendicular to the Pc rings and a distorted square antiprismatic coordination environment around the metal centre. This distortion is a consequence of the non-equal bond lengths between metal atom (M) and each of the eight N_{iso} atoms. The calculated M-N_{iso} bond lengths of the isolated optimised molecular structure are longer than the experimental values. The values for YPc_2 derived with the DND and DNP basis sets are closer or equidistant. Their range is reduced compared to the data calculated DN basis set or to those deduced from XDR (Fig.6. 4a).

The Y-N_{iso} bond length interval calculated on the same theoretical level when YPc_2 is adsorbed on the surface of a carbon nanotube increased with respect to the value for the isolated molecule for all basis sets used. As can be seen in Fig.6. 4a, for the calculation with the DN basis set, some values become smaller. Likewise, the range of Y-N_{iso} bond lengths in the isolated molecule with DNP is 2.410-2.413 Å while for the molecule on the surface of the zigzag nanotube it becomes 2.396-2.409 Å (Table 6. 2). We also note that, Y-N_{iso} lengths for the Pc ligand that is in direct contact with the ANT surface are larger than those of the other ligand and also than those YPc2 on the zigzag nanotube (values calculated with the DNP basis set: 2.411-2.417 Å with DNP for YPc_2+ANT and 2.404-2.409 Å for YPc_2+ZNT). The latter difference is due to the smaller diameter of the nanotube.

The calculated Ln-N_{iso} bond lengths in isolated $LnPc_2$ are 2.536-2.545 Å for $LaPc_2$, 2.507-2.529 Å for $GdPc_2$ and 2.384-2.400 Å for $LuPc_2$, and hence larger than the experimental values deduced from XRD analysis (Table 6. 3). Fig.6. 1b shows how the Ln-N length in each isolated bisphthalocyanine decreases as the Ln atomic number increases, and that this trend is maintained after adsorption on the nanotube sidewall.

6.2.1.5. N-M-M distortion angles

The values of the N-M-N angles formed between the metal atom and two diagonally opposite nitrogen atoms N_{iso} of the coordination sphere (four atoms of nitrogen of the isondole units that coordinated with the central metal, MN4, see Fig.4. 5, are shown in Table 6. 2 and Table 6. 3. For YPc_2, where the experimental values are found in the range 109.7-110.6°, the theoretical ones are always higher, specifically 113.3-113.7° when calculated with the DN basis set, 110.7-110.9° when the DND basis set is used, and 110.9-111.0° for calculation with the DNP basis set. Even though the strongest deviation from the experimental parameters is observed for the calculation with the DN basis set (0.015°), the improvement due to the use of higher-quality DND and DNP basis sets is not strinking, similar to the cases of other geometrical characteristics discussed above (Fig.6. 4a).

On the other hand, compared to the experimental values, the N-Ln-N angles in isolated lanthanide double-decker phthalocyanines were underestimated for $GdPc_2$, and overestimated for $LaPc_2$ and $LuPc_2$ (Fig.6. 4 and Table 6. 3).

The angles of most of the bisphthalocyanines increase after deposition on the surface of each model nanotube with respect to the optimised structure of the isolated molecule, and this independently of the level of calculation (emphasis on systems with YPc_2 molecule). The angles also vary over a greater range, indicating that the molecule becomes more asymmetric and distorted when adsorbed. An exception to this trend is the lanthanum double-decker phthalocyanine on the surface of armchair nanotube, where the values of the angles decrease, as seen in Table 6. 3 and Fig.6. 4b. For $LnPc_2$+SWCNT hybrids, the change in N-Ln-N angle is opposite to that of Ln-N bond lengths: the angles increase from La to Lu. The change becomes more dramatic in the gadolinium hybrids.

6.2.1.6. The closest contact

The attraction between the SWCNT models and the MPc_2 molecules can be characterized in terms of the shortest distances between carbon atoms $C_{MPc2}\cdots C_{SWCNT}$, metal and carbon atoms $M\cdots C_{SWCNT}$, and nitrogen and carbon atoms $\gamma\text{-}N\cdots C_{SWCNT}$ and distances. For the hybrids of the armchair nanotube with lanthanum, gadolinium and yttrium double-decker phthalocyanines (the latter regardless of the basis sets) the closest distance was found between a carbon atom of the nanotube and one of the azomethine nitrogen atoms (γ-N) of the Pc ligand ($\gamma\text{-}N\cdots C_{SWCNT}$), as listed in Table 6.3. This closest distance was determined to be 3.107 Å for $LaPc_2$+ANT* and 3.180 Å for $GdPc_2$+ANT*, and for YPc_2+ANT 3.014 Å as reported in Table 6. 2. For $LuPc_2$+ANT* and for all hybrids of rare-earth bisphthalocyanines and zigzag chiral nanotubes, (MPc_2+ZNT) the closest contact resulted between carbon atoms, $C_{MPc_2}\cdots C_{SWCNT}$.

The shortest distance between the lanthanide of the double-decker and a carbon atom of the nanotube ($Ln\cdots C_{SWCNT}$; Table 6. 3) is one of the structural parameters that is most sensitive to the nanotube model and the Ln species. This distance can be an indirect indicator of the bonding strength. In the $LnPc_2$+ANT* series, it increases as the lanthanide atomic number increases, from 4.551 Å for $LaPc_2$+ANT* to 4.619 Å for $LuPc_2$+ANT*. The opposite behaviour is observed for the $LnPc_2$+ZNT* series, where it decreases from 4.692 Å for $LaPc_2$+ZNT* to 4.533 Å for $LuPc_2$+ZNT*. For hybrids of yttrium bisphthalocyanine and short nanotubes models the distance between the central atom and a carbon atom of the nanomaterial depends on the size of the basis sets: with the larger DNP basis set the distance $Y\cdots C_{swcnt}$ is longer, while with the DN basis set, the distance is shorter (Table 6. 2). An analogous behaviour is found for $\gamma\text{-}N\cdots C_{SWCNT}$ and $C_{YPc2}\cdots C_{SWCNT}$ distances.

6.2.2. Adsorption strength and electronic properties

The formation energies (ΔE), distribution of frontier orbital HOMO and LUMO, HOMO-LUMO gap energies (E_{gap}), the charge, the spin of central metal atom, charge transfer, as well as the spin density distribution were analysed.

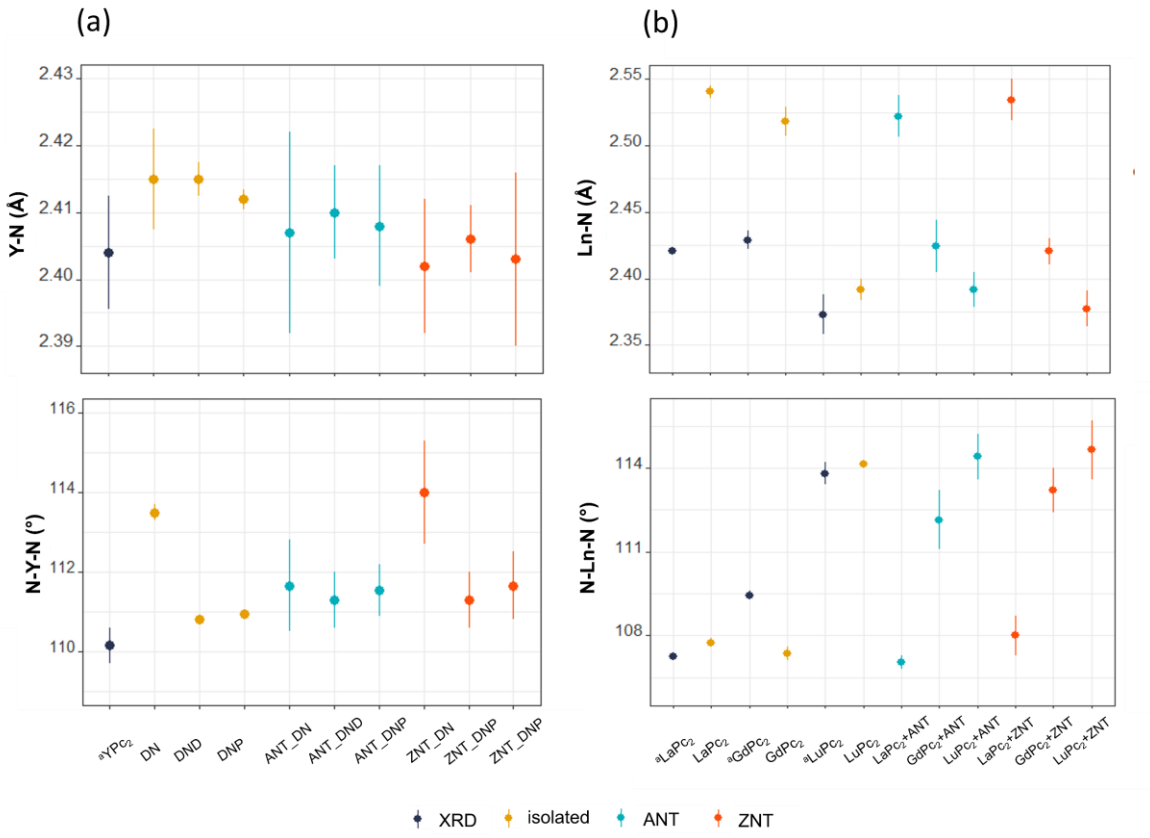

Fig.6. 4. Comparison of the lengths of the bonds between the central metal and the nitrogen atoms of the coordination sphere M-N (Å; top) and of the N-M-N angles (°; bottom) in crystalline rare-earth double-decker phthalocyanines. Data deduced from XRD ($^{a}MPc_2$), in the isolated MPc_2 molecules and calculated for isolated MPc_2 adsorbed on the carbon nanotube sidewalls (MPc_2+SWCNT) are shown, for (a) hybrids of yttrium bisphthalocyanine, where the theoretical values were calculated at the level of PBE-D2 with three numerical basis sets: DN, DND and DNP; (b) for lanthanide bisphthalocyanines, the theoretical structure were optimised at the PBE-D2/DN.

6.2.2.1. Formation energies of MPc_2+SWCNT hybrids

The adsorption strength of the double-decker phthalocyanines complexes on the carbon nanotube surface is mirrored by the formation energy. This energy is strongly related to the chirality of nanotube. The calculated values are reported in Table 6. 4 and Table 6. 5, where one can see that YPc_2, $LaPc_2$, and $LuPc_2$ adsorbed on zigzag nanotubes show more negative energies than for adsorption on ANT: -43.8 (for the DNP basis set), -55.4 and -60.7 kcal/mol vs. -37.1, -52.4 and -55.1 kcal/mol, respectively. An opposite trend can be seen for $GdPc_2$+SWCNT hybrids, though the difference is as small as 1 kcal/mol.

When analysing the influence of the basis set's size with the yttrium double-decker phthalocyanine, the strongest bonding was observed when using the DN basis set, followed by DNP and DND (Table 6. 4). A possible explanation for this trend is the larger orbital cutoff values applied when the latter two basis sets are used, which in turn reduces the polyazamacrocycle bending when the molecule is adsorbed on a SWCNT sidewall. [37] Another point to consider is that the formation energies of the YPc_2+SWCNT hybrids are rather close to the ΔE values

reported previously for the hybrids of 3*d* metal phthalocyanines on the single-walled carbon nanotubes with the same ANT and ZNT models, and which span from -45.4 to -32.7 kcal/mol. [21] This can be interpreted as a minor contribution to the adsorption strength by central metal atom of bisphthalocyanine complex, indicating that the adsorption process is governed by π–π interactions between tetraaza[18]annulene macrocycle and graphene-derived nanotube sidewall. [21]

In the case of lanthanide bisphthalocyanine, the nature of the central metal atom influences the formation energy. The stronger binding with ΔE values of -65.6 and -64.6 kcal/mol was obtained for $GdPc_2$+ANT* and $GdPc_2$+ZNT*, respectively. For both the ANT* and the ZNT* series, Δ*E* increases in the order of $GdPc_2$ < $LuPc_2$ < $LaPc_2$.

6.2.2.2. HOMO-LUMO gap energies

Since it is known that the HOMO-LUMO gap is strongly underestimated when using pure GGA functionals (for example, as compared to hybrid ones such as B3LYP) [38], we analyzed this electronic parameter simply as a measure of changes in the molecule's properties upon adsorption on SWCNT models.

When analyzing frontier orbital energies of isolated YPc_2 (Table 6. 4), one can see that the choice of basis set has a negligible effect. In particular, the calculated HOMO-LUMO gap energy is 0.140 eV for DN, and 0.142 eV for both the DND and DNP basis sets. The short armchair model has semi-conductive behaviour (HOMO-LUMO gap = 0.643 eV with DNP), its gap energy value increases inversely with the basis set size (DN>DND>DNP, see Table 6. 4), whilst the zigzag model shows the opposite trend and is conductive (HOMO-LUMO gap = 0.080 eV with DNP).

The gap energy of isolated $LnPc_2$ molecules slightly decreases in the order of $LuPc_2$ (0.138 eV)>$LaPc_2$ (0.133 eV)>$GdPc_2$ (0. 130 eV), as in earlier calculations with Fermi occupancy. [29]Among the nanotube models, ANT* exhibits a higher band gap than ZNT* (0.551 and 0.001 eV, respectively), similar to the smaller nanotube models with the same chirality that were used to study the non-covalent interactions of 3*d* transition metal [21,22,39] and YPc_2.

Table 6. 4 shows that the basis set size has a negligible effect on the HOMO-LUMO band gap energies of hybrids of yttrium bisphthalocyanines and CNTs. The values obtained for YPc_2+ANT and YPc_2+ZNT with the DNP basis set are 0.140 and 0.059 eV, respectively. For what concerns the gap energy of the $LnPc_2$+SWCNT hybrids, the following observations can be made. For $LnPc_2$+ANT* hybrids E_{gap} becomes slightly larger as the atomic number, and consequently the number of 4*f*-electrons increases: 0.128 eV for $LaPc_2$, 0.131 eV for $GdPc_2$, and 0.134 eV for, $LuPc_2$. For $LnPc_2$+ZNT*, the trend is opposite and the E_{gap} values are smaller by one order of magnitude, namely 0.021, 0.014 and 0.012 eV for $LaPc_2$, $GdPc_2$ and $LuPc_2$.

Overall, ignoring the calculation methodology and comparing the computed gap values of each hybrid with that of the isolated component (Table 6. 4 and Table 6. 5), one can conclude that in the case of rare-earth double-decker bispthalocyanines adsorbed on armchair nanotubes,

E_{gap} tends to approach that of the respective isolated MPc_2, whereas for adsorption on the surface of a zigzag nanotube, it is closer to the band gap of the nanotube. The fact that the gap energy is higher for MPc_2+ANT than for MPc_2+ZNT, also observed in our earlier studies of hybrids with 3*d* transition metal(II) MPc [21,22,39], can be interpreted as an effect of the nanotube chirality, given that the nature of the zigzag models is open-shell.

6.2.2.3. Distribution of frontier orbital HOMO and LUMO

Concerning the distribution of frontier orbitals, Fig.6. 5 illustrates that for isolated YPc_2, $LaPc_2$, $GdPc_2$ and $LuPc_2$ the HOMO and LUMO is localized on the carbon atoms, specifically at the pyrrole unit, as observed earlier for $LnPc_2$ [29] by us and by other research groups at different theoretical levels. [40,41] No contribution from the central metal atom to either HOMO or LUMO was found. The patterns are essentially identical for all theoretical levels tested, at least when the isosurfaces are plotted at 0.03 arb. units. This finding agrees well with experimental data by STM reported for YPc_2. [42]

HOMO and LUMO on the armchair nanotube are found on the sidewall carbon atoms, though both have different distribution patterns (Fig.6. 5). On the zigzag nanotubes, there are some differences that can be attributed to the structural features. HOMO and LUMO of the short model, which interact with YPc_2, are present on the sidewall and tips, meanwhile for the long zigzag model they are concentrated on only one tip of the nanotube (Fig.6. 5).

As shown in Fig.6. 6, the HOMO and LUMO orbital distributions for the MPc_2+SWCNT hybrids depend on the chirality of the nanotube and on the central metal atom. In hybrids with armchair nanotubes, HOMO and LUMO are located on the bisphthalocyanines structure as in isolated MPc_2. In hybrids with zigzag nanotubes, the distribution of the frontier orbitals varies. The HOMO orbital of the YPc_2+ZNT hybrid is localised in both components but the LUMO only on the zigzag nanotube. In $LaPc_2$+ZNT* and $LuPc_2$+ZNT*, the HOMO is localised exclusively on the nanotube and the LUMO on both components; in the case of $LuPc_2$+ZNT* the contribution from the nanotube is more notable. In $GdPc_2$+ZNT*, the HOMO extends over both components and LUMO is localised only on the nanotube, similarly to YPc_2+ZNT*. An additional detail, which can be observed in Fig.6. 6, is that neither HOMO nor LUMO is localized on the central metal atom.

The HOMO-LUMO distribution plots for the YPc_2 hybrids are identical for all three basis sets, DN, DND and DNP.

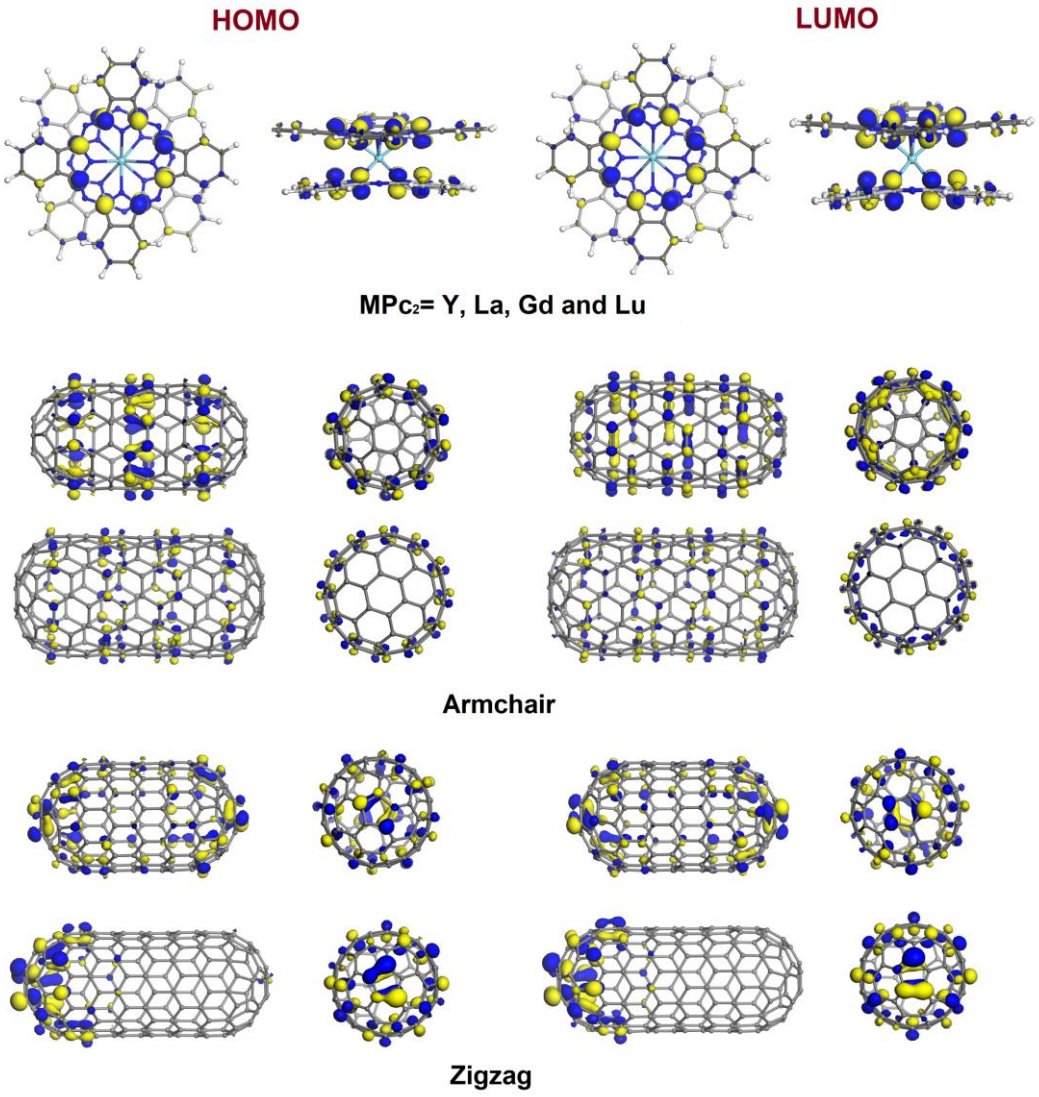

Fig.6. 5. HOMO and LUMO plots (isosurfaces at 0.03 arb.units; two side views) for isolated rare-earth double-decker phthalocyanines (YPc_2, $LaPc_2$, $GdPc_2$ and $LuPc_2$), and for the armchair and zigzag nanotube models employed for thestudy of the formation for hybrids with yttrium (short models), lanthanum, gadolinium and lutetium bisphthalocyanines calculated by the PBE-GGA functional with the DN basis set. HOMO and LUMO plots for yttrium bisphthalocyanines systems were calculated using the DN, DND and DNP basis sets, here results obtained with the DNP geometry are presented (same plots were obtained when DN or DND basis sets were used)

Table 6. 4. Total energies E_{total} (in Ha), formation energies ΔE (in kcal/mol), HOMO, LUMO and HOMO-LUMO gap energies (in eV) for isolated YPc_2, for the nanotube models alone (ANT and ZNT) and for the non-covalently hybrids, as well as charge of Y atom and charge transfer from YPc_2 to SWCNT calculated using PBE GGA functional with Grimme's dispersion correction in conjunction with DN, DND and DNP basis sets. The charge transfer values were obtained from the Mulliken population analysis

[a] The charge transfer is always from YPc_2 to SWCNT model

System	Basis sets	E_{total} (Ha)	ΔE (kcal/mol)	E_{HOMO} (eV)	E_{LUMO} (eV)	E_{gap} (eV)	Y charge (e)	Charge transfer (e) [a]
	DN	-4568.0346443		-5.518	-4.806	0.712		
ANT	DND	-4569.2431383		-5.318	-4.674	0.644		
	DNP	-4569.1629441		-5.354	-4.712	0.643		
	DN	-5329.5208333		-5.795	-5.716	0.079		
ZNT	DND	-5330.9123540		-5.623	-5.544	0.079		
	DNP	-5330.8185875		-5.662	-5.582	0.080		
	DN	-6664.1301901		-4.646	-4.507	0.140	2.074	
YPc_2	DND	-6665.0600567		-4.564	-4.422	0.142	1.966	
	DNP	-6665.1029617		-4.603	-4.461	0.142	1.922	
	DN	-11232.236527	-45.0	-4.874	-4.736	0.138	2.172	0.131
YPc_2+ANT	DND	-11234.361155	-36.4	-4.744	-4.604	0.140	1.980	0.108
	DNP	-11234.324974	-37.1	-4.797	-4.657	0.140	1.963	0.127
	DN	-11993.730585	-49.9	-5.187	-5.129	0.058	2.121	0.520
YPc_2+ZNT	DND	-11996.040216	-42.6	-5.061	-5.001	0.061	1.975	0.454
	DNP	-11995.991383	-43.8	-5.114	-5.055	0.059	1.960	0.489

Table 6. 5. Total energies E_{total} (in Ha) formation energies ΔE (in kcal/mol), HOMO, LUMO and HOMO-LUMO gap energies (in eV) for the isolated $LnPc_2$, SWCNT (ANT and ZNT) and for the non-covalently hybrids, as well as spin and charge of Ln (La, Gd and Lu) and charge transfer from $LnPc_2$ to SWCNT calculated using PBE-GGA functional with Grimme's dispersion correction in conjunction with the DN basis set. The charge transfer values were obtained from the Mulliken population analysis

System	E_{total} (Ha)	ΔE (kcal/mol)	HOMO (eV)	LUMO (eV)	E_{gap} (eV)	Ln charge (e)	Charge transfer (e) [a]	Ln spin (e)
ANT*	-6852.4098123		-5.417	-4.866	0.551			
ZNT*	-6852.3450966		-5.735	-5.734	0.001			
$LaPc_2$	-3388.1293982		-4.845	-4.713	0.133	1.893		0
$GdPc_2$	-3527.7074389		-4.811	-4.680	0.130	1.532		7.006
$LuPc_2$	-3981.3338903		-4.683	-4.545	0.138	1.438		0.002
$LaPc_2$+ANT*	-10240.6227541	-52.4	-5.063	-4.935	0.128	1.924	0.090	0
$GdPc_2$+ANT*	-10380.2217485	-65.6	-4.861	-4.730	0.131	1.487	0.082	7.010
$LuPc_2$+ANT*	-10833.8314531	-55.1	-4.873	-4.740	0.134	1.457	0.079	0.002
$LaPc_2$+ZNT*	-10240.5628015	-55.4	-5.345	-5.324	0.021	1.992	0.377	0
$GdPc_2$+ZNT*	-10380.1555445	-64.6	-5.232	-5.217	0.014	1.472	0.452	7.013
$LuPc_2$+ZNT*	-10833.7757678	-60.7	-5.260	-5.248	0.012	1.431	0.502	0

[a] The charge transfer is always from $LnPc_2$ to SWCNT model

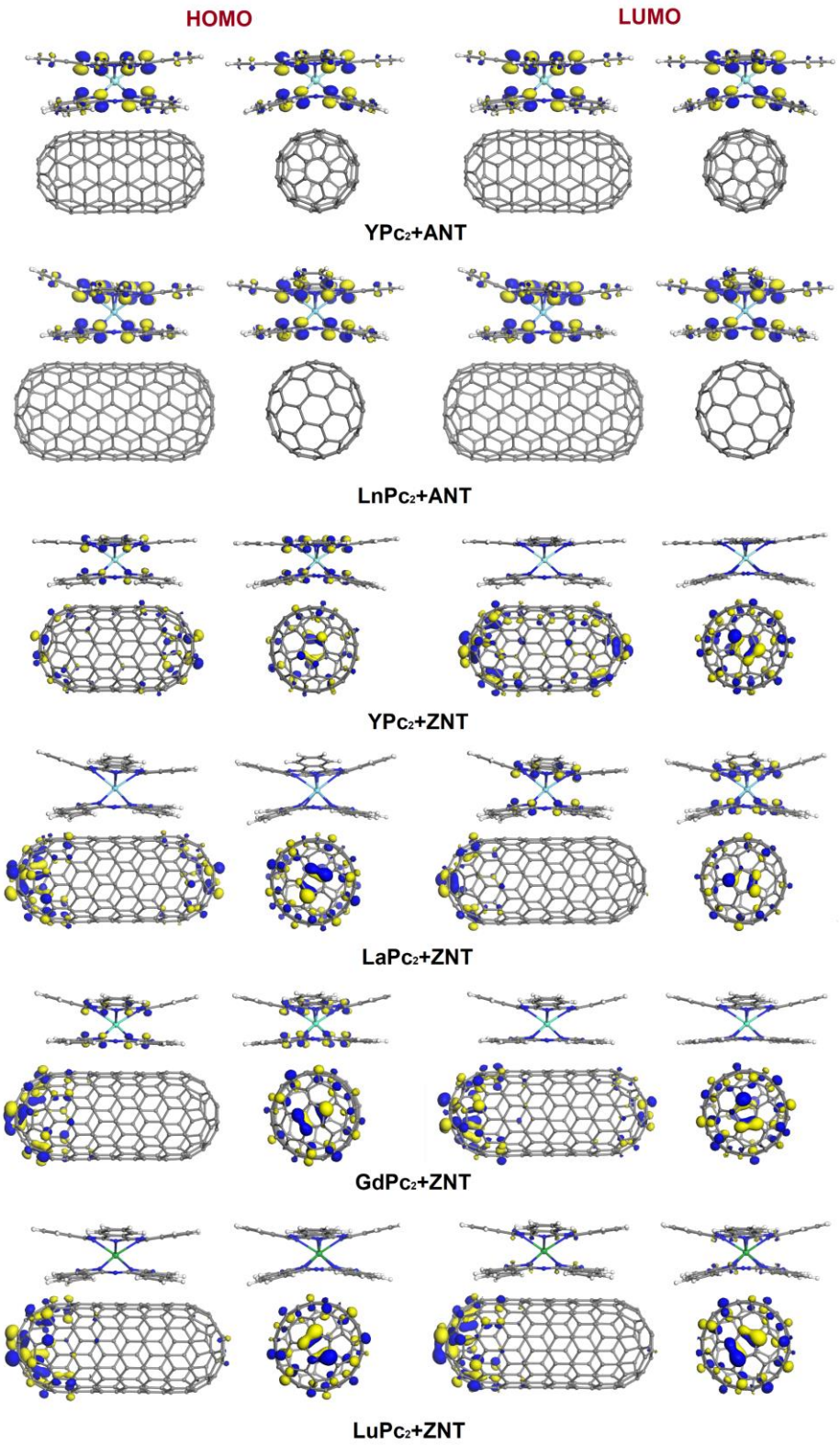

Fig.6. 6. HOMO and LUMO plots (isosurfaces at 0.03 arb. units; two side views) for rare-earth double-decker phthalocyanines (YPc_2, $LaPc_2$, $GdPc_2$ and $LuPc_2$), SWCNT models, and MPc_2+SWCNT hybrids calculated using the PBE GGA functional with Grimme's dispersion correction with the DN basis set, plots for yttrium bisphthalocyanines systems were calculated using the DN, DND and DNP basis set, here the results obtained with the DNP geometry are presented (the same plots were obtained when DN or DND basis sets were employed).

6.2.2.4. Mulliken population analysis

6.2.2.4.1. Charge for central metal

One more aspect of interest we addressed is the charge of metal atom of the bisphthalocyanine, as deduced from the Mulliken population analysis. For YPc_2 complex, that charge depends on the size of the basis set; the charge value decreases both for the isolated molecule and for the hybrids with the nanotubes when the basis set is larger, that is, DNP<DND<DN (Table 6. 4). The charge of the yttrium metal atom decreases when the molecule is deposited on the surface of the nanotube, however it is higher for adsorption on the armchair model (where it decreases from 1.975 to 1.960 *e* when calculated with the DNP basis set) than on the zigzag nanotube.

The charge of La, Gd and Lu in isolated bisphthalocyanines is 1.827, 1.452, and 1.400 *e,* respectively. In the case of hybrids, the changes are rather random (Table 6. 5). For $LaPc_2$+SWCNT* hybrids, there is an increase by 0.031 *e* for $LaPc_2$+ANT* and by 0.099 *e* for $LaPc_2$+ZNT*. When $GdPc_2$+ANT* and $GdPc_2$+ZNT* are formed, the Gd charge decreases by 0.045 and 0.060 *e,* respectively. For $LuPc_2$+SWCNT hybrids, the Lu charge increases by 0.019 *e* for $LuPc_2$+ANT* but decreases insignificantly, by 0.007 *e,* for $LuPc_2$+ZNT*. Regardless of the magnitude, the general trend the same as for isolated phthalocyanines, where the Ln charge decreases in the order of $LaPc_2$ > $GdPc_2$ > $LuPc_2$.

6.2.2.4.2. Charge transfer

Since carbon nanotubes and phthalocyanine hybrids have been considered as supramolecular self-assembled donor-acceptor conjugated systems, the charge transfer between the two components was analysed. [43] From Table 6. 4 and Table 6. 5 it is clear that the direction of charge transfer is from the bisphthalocyanine to the carbon nanotube and depends on the chirality of the nanotube and on the central coordination metal.

Charge transfer from YPc_2 to an armchair nanotube is lower than the adsorption on a zigzag nanotube, regardless of the basis set used for the calculations (Table 6. 4). Calculations with the DN basis set gave the highest charge transfer for both chiralities (0.131 *e* for YPc_2+ANT and 0.520 *e*, for YPc_2+ZNT.

For lanthanide bisphthalocyanines adsorbed on zigzag nanotubes, the charge transfer increases proportionally to the lanthanide atomic number, from 0.377 ($LaPc_2$+ZNT*) to 0.502 *e* ($LuPc_2$+ZNT*) while the increase is inversely proportional to the atomic number when binding to armchair nanotubes, from 0.079 ($LuPc_2$+ANT) to 0.090 *e* ($LaPc_2$+ANT*). Something that can be noted is the relationship between the charge transfer and the Ln···C_{SWCNT} distance: for each set of hybrids per chirality (Table 6. 3), the smaller the Ln···C_{SWCNT} distance, the higher the charge transfer. The charge transfer for hybrids with zigzag nanotubes is always higher.

6.2.2.5. Spin density

The existence of an unpaired electron delocalized over the Pc macrocycles gives rise to a crucial difference between spin density plots obtained for isolated rare-earth bisphthalocyanines (Fig.6. 7) and the ones obtained for conventional single-decker phthalocyanine with *3d* transition metals. [21,22,44,45] The distribution of the spin density in isolated YPc_2 (again, identical for all basis sets), $LaPc_2$ and $LuPc_2$ matches closely the HOMO and LUMO distribution discussed above (Fig.6. 5). In these molecules, the unpaired electrons are found mainly on C atoms of the pyrrole ('spin-up'), with a minor contribution from nitrogen atoms: γ-N and N_{iso} atoms ('spin-down'; oranges lobes). This feature is also present in $GdPc_2$, but the additional main contribution here comes from the metal ('spin-down').

The spin density of the armchair nanotubes with isosurface at 0.01 arb. units is not visible (Fig.6. 7.). The short zigzag model has its spin density distributed over the whole nanotube and' spin-up' prevails, while in the longer model the spin density is only centred on one of the tips and less 'spin-down' contribution is observed.

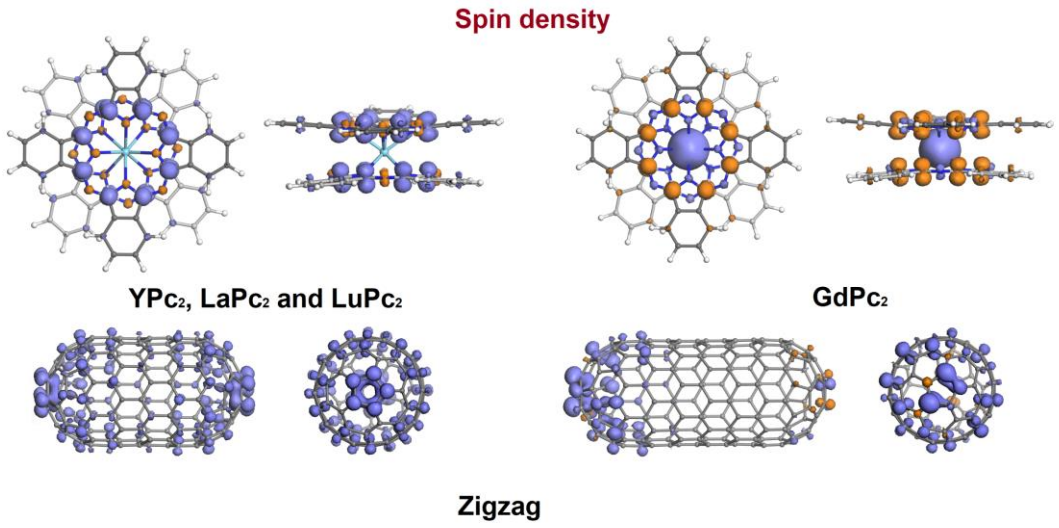

Fig.6. 7. Spin density plots (isosurfaces at 0.01 arb. units) for isolated lanthanide double-decker phthalocyanines (YPc_2, $LaPc_2$, $GdPc_2$ and $LuPc_2$) and zigzag carbon nanotube models (on the right the short model used for depositing YPc_2). Violet and orange lobes correspond to 'spin-up' and 'spin-down' electrons, respectively.

The spin distribution in the hybrids depends not only on the central metal, but also on the nanotube model (Fig.6. 8). For armchair nanotubes (MPc_2+ANT) the spin density remains on the bisphthalocyanine with the same pattern for isolated c MPc_2, whereas the hybrids with zigzag nanotubes exhibit notable differences. In all of them one can observe the presence of unpaired electrons on the closed nanotube ends (as in the isolated ZNT model). An additional detail is that the main cloud found on ZNT is 'spin-up' unpaired electron density. No tangible contribution from the bisphthalocyanine can be found in $LaPc_2$+ZNT*, and only a minor one in YPc_2+ZNT and $LuPc_2$+ZNT*, mainly with 'spin-down' (orange lobes) character. This contrasts with $GdPc_2$+ZNT*, where the spin density distributions of the isolated $GdPc_2$ and of the ZNT* are combined, for $GdPc_2$ the contribution of 'spin-up' (violet lobule) and 'spin-down' on the molecule is reversed when it is deposited on an armchair nanotube.

The features mentioned above for YPc_2+SWCNT hybrids are reproduced with all the basis sets, although the 'spin-down' contribution of the phthalocyanine on the zigzag nanotube is slightly less evident in the calculation with the DN basis set.

Finally, Table 6. 5 specifies the spin of the Ln atoms in isolated and adsorbed double-decker phthalocyanines; one can see that the Ln spin remains relatively constant. For $LaPc_2$ and $LuPc_2$, where the lanthanide(III) ion is in a closed-shell configuration, the spin is always close to zero. On the other hand, for $GdPc_2$ where the 4*f* orbital of gadolinium ion is half-filled, a minor spin transfer of 0.004 and 0.007 *e* from armchair and zigzag carbon nanotubes, respectively, was found. The charge value for Y atoms is zero on all systems independent of calculation method.

6.3. Conclusions

A systematic theoretical analysis of the adsorption of rare-earth bisphthalocyanines on two single-walled carbon nanotube models was performed using the PBE functional together with Grimme dispersion correction. In general, our findings can be described as follows:

The comparison of the four optimised structures of isolated rare-earth bisphthalocyanines with the corresponding structure derived from X-ray diffraction overestimates some structural parameters such as size, M-N_{iso} length and N-M-N angle values at all calculation levels studied. As for the height, the range variation decreases for all the molecules except for $LaPc_2$. Since the XRD data refer to crystals, the differences are attributed to the chemical environment of the crystal lattice.

The optimized structures obtained show that the Pc ligands of the isolated bisphthalocyanine are not flat and present a domed structure. When interacting non-covalently with the carbon nanotubes they undergo an additional distortion to increase the contact area with the nanotube sidewall, resulting in a stronger interaction between the two components. The degree of bending distortion depends on the diameter, length, chirality and coordination metal of the phthalocyanine. The bending is higher for small diameter hybrids for YPc_2 with armchair nanotubes and for lanthanide double-decker phthalocyanines with zigzag nanotubes. For hybrids with longer nanotubes, the size of the macrocycle is not affected as much.

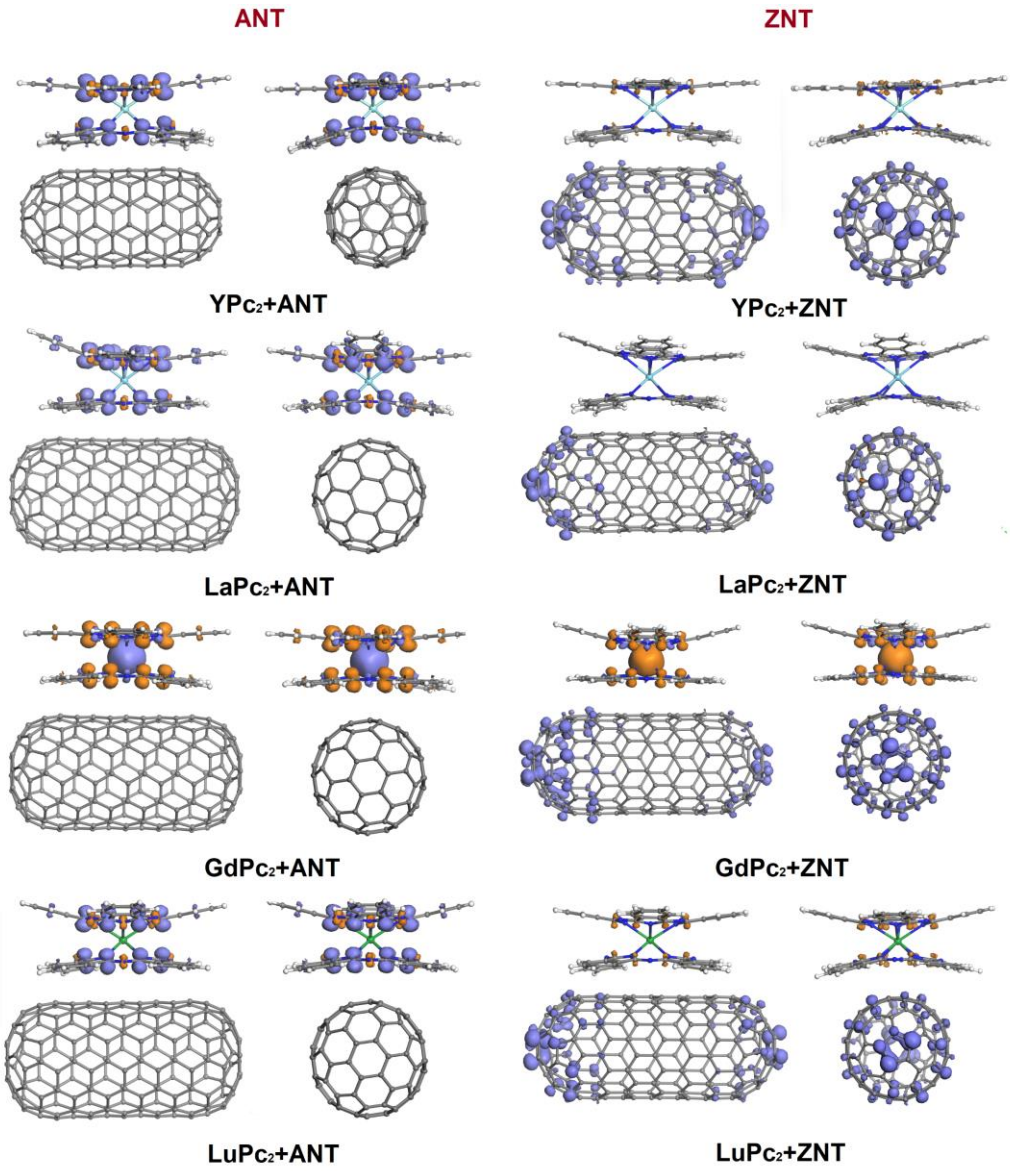

Fig.6. 8 Spin density plots (isosurfaces at 0.01 arb. units) for $MnPc_2$+SWCNT hybrids. Violet and orange lobes correspond to 'spin-up' and 'spin-down' electrons, respectively.

The binding strength or formation energy of nanotube-bisphthalocyanine hybrids depends on the chirality of the nanotube and the coordination metal of the phthalocyanine. Most bisphthalocyanines bind more strongly to zigzag nanotubes.

The HOMO-LUMO gap of the hybrids width correlates with the number of electrons of the lanthanide and nanotube chirality. For $LnPc_2$+ANT E_{gap} increases linearly in the order $LaPc_2$ < $GdPc_2$ < $LuPc_2$, whereas for $LnPc_2$+ZNT the trend is opposite and E_{gap} decreases in the order $LaPc_2$ > $GdPc_2$ > $LuPc_2$. For hybrids with YPc_2, there is no significant influence of the base set size. Adsorption on an armchair nanotube leads to a larger HOMO-LUMO gap compared to the case when MPc_2 binds to a zigzag tube. In the former case, E_{gap} tends to match the gap of isolated MPc_2, whereas in the latter case it is closer to the value for zigzag tube alone.

According to the Mulliken population analysis, the charge transfer in nanotube-bisphthalocyanine hybrids is from the macrocycle to the carbon nanotube. Adsorption on zigzag nanotubes gives rise to the highest charge transfer.

The effect of basis set used in our computations depends on a particular parameter. For YPc_2, the calculated values of molecular size, height and N-Y-N angles tend to decrease with increasing the basis set size (DN > DND > DNP). On the other hand, the ΔE values and the closest contact ($Y\cdots C_{SWCNT}$, $\gamma\text{-}N\cdots C_{SWCNT}$ and $CYPc_2\cdots C_{SWCNT}$) between the two components of the non-covalently bound hybrids tend to increase for larger basis sets (DND and DNP *versus* DN). The opposite behaviour is observed for the charge transfer, which is higher for hybrids optimised with DN and lower for those treated with DNP. The other characteristics (frontier orbital and spin density distribution, as well as HOMO-LUMO gap values) do not exhibit any significant differences when varying the basis set.

The calculation methodology implemented for the calculations of lanthanide bisphthalocyanines using the DN basis set allows further exploration of these double-decker molecules with other carbon allotropes to gain insight into their electronic behaviour, no SCF convergence problems were encountered.

6.4. References

(1) Urdampilleta, M.; Klyatskaya, S.; Cleuziou, J. P.; Ruben, M.; Wernsdorfer, W. Supramolecular spin valves. *Nat. Mater.* 2011, *10* (7), 502–506.

(2) Candini, A.; Klyatskaya, S.; Ruben, M.; Wernsdorfer, W.; Affronte, M. Graphene spintronic devices with molecular nanomagnets. *Nano Lett.* 2011, *11* (7), 2634–2639.

(3) Stepanow, S.; Honolka, J.; Gambardella, P.; Vitali, L.; Abdurakhmanova, N.; Tseng, T. C.; Rauschenbach, S.; Tait, S. L.; Sessi, V.; Klyatskaya, S.; et al. Spin and orbital magnetic moment anisotropies of monodispersed bis(phthalocyaninato)terbium on a copper surface. *J. Am. Chem. Soc.* 2010, *132* (34), 11900–11901.

(4) Komeda, T.; Katoh, K.; Yamashita, M. Double-decker phthalocyanine complex: scanning tunneling microscopy study of film formation and spin properties. *Prog. Surf. Sci.* 2014, *89* (2), 127–160.

(5) Zhang, Y. F.; Isshiki, H.; Katoh, K.; Yoshida, Y.; Yamashita, M.; Miyasaka, H.; Breedlove, B. K.; Kajiwara, T.; Takaishi, S.; Komeda, T. Low-temperature scanning tunneling microscopy investigation of bis(phthalocyaninato)yttrium growth on Au(111): from individual molecules to two-dimensional domains. *J. Phys. Chem. C* 2009, *113* (22), 9826–9830.

(6) Katoh, K.; Yoshida, Y.; Yamashita, M.; Miyasaka, H.; Breedlove, B. K.; Kajiwara, T.; Takaishi, S.; Ishikawa, N.; Isshiki, H.; Yan, F. Z.; et al. Direct observation of lanthanide(III)-phthalocyanine molecules on Au(111) by using scanning tunneling microscopy and scanning tunneling spectroscopy and thin-film field-effect transistor properties ofTb(III)- and Dy(III)-phthalocyanine molecules. *J. Am. Chem. Soc.* 2009, *131* (29), 9967–9976.

(7) Fu, Y.-S.; Rg, J.; Bel, S.; Hla, S.-W.; Dilullo, A.; Hoffmann, G.; Klyatskaya, S.; Ruben, M.; Wiesendanger, R. Reversible chiral switching of bis(phthalocyaninato) terbium(III) on a metal surface. *Nano Lett* 2012, *12*, 3935.

(8) Lodi Rizzini, A.; Krull, C.; Balashov, T.; Kavich, J. J.; Mugarza, A.; Miedema, P. S.; Thakur, P. K.; Sessi, V.; Klyatskaya, S.; Ruben, M.; et al. Coupling single molecule magnets to ferromagnetic substrates. *Phys. Rev. Lett.* 2011, *107* (17), 1–5.

(9) Klar, D.; Klyatskaya, S.; Candini, A.; Krumme, B.; Kummer, K.; Ohresser, P.; Corradini, V.; de Renzi, V.; Biagi, R.; Joly, L.; et al. Antiferromagnetic coupling of $TbPc_2$ molecules to ultrathin Ni and Co films. *Beilstein J. Nanotechnol. 436* 2013, *4* (1), 320–324.

(10) Ruan, L.; Tong, J.; Luo, F.; Wu, Y.; Qin, G.; Jiao, X.; Zhang, X. The magnetic anisotropy of tb-phthalocyanine films effected by molecular orientation. *Appl. Surf. Sci.* 2022, *585* (August 2021), 152445.

(11) Corradini, V.; Candini, A.; Klar, D.; Biagi, R.; De Renzi, V.; Lodi Rizzini, A.; Cavani, N.; Del Pennino, U.; Klyatskaya, S.; Ruben, M.; et al. Probing magnetic coupling between $LnPc_2$ (Ln = Tb, Er) molecules and the graphene/Ni (111) substrate with and without Au-intercalation: role of the dipolar field. *Nanoscale* 2018, *10* (1), 277–283.

(12) Gonidec, M.; Biagi, R.; Corradini, V.; Moro, F.; De Renzi, V.; Del Pennino, U.; Summa, D.; Muccioli, L.; Zannoni, C.; Amabilino, D. B.; et al. Surface supramolecular organization of a terbium(III) double-decker complex on graphite and

its single molecule magnet behavior. *J. Am. Chem. Soc.* 2011, *133* (17), 6603–6612.
(13) Kyatskaya, S.; Mascarós, J. R. G.; Bogani, L.; Hennrich, F.; Kappes, M.; Wernsdorfer, W.; Ruben, M. Anchoring of rare-earth-based single-molecule magnets on single-walled carbon nanotubes. *J. Am. Chem. Soc.* 2009, *131* (42), 15143–15151.
(14) Abdullah, K.; Kong, X.; Imran, M.; Mustafa, G.; Chen, Y. Excellent ambipolar gas sensing response of Eu[Pc(OC_4H_9)$_8$]$_2$/acidified multiwalled carbon nanotubes hybrid at room temperature. *J. Porphyr. Phthalocyanines* 2019, *23* (11–12), 1455–1462.
(15) Apetrei, C.; Nieto, M.; Rodríguez-Méndez, M. L.; De Saja, J. A. Development of lutetium bisphthalocyanine/carbon nanotube Langmuir-Blodgett films. sensing properties. *J. Porphyr. Phthalocyanines* 2011, *15* (9–10), 908–917.
(16) Xu, H. B.; Chen, H. Z.; Shi, M. M.; Bai, R.; Wang, M. A novel donor–acceptor heterojunction from single-walled carbon nanotubes functionalized by erbium bisphthalocyanine. *Mater. Chem. Phys.* 2005, *94* (2–3), 342–346.
(17) Katoh, K.; Sato, J.; Nakanishi, R.; Ara, F.; Komeda, T.; Kuwahara, Y.; Saito, T.; Breedlove, B. K.; Yamashita, M. Terbium(II bis-phthalocyaninato single-molecule magnet encapsulated in a single-walled carbon nanotube. 2021, *9* (33).
(18) Basiuk, V. A.; Tahuilan-Anguiano, D. E. Complexation of free-base and 3*d* transition metal(II) phthalocyanines with endohedral fullerene $Sc_3N@C_{80}$. *Chem. Phys. Lett.* 2019, *722*, 146–152.
(19) Mendoza-Domínguez, C. U.; Basiuk, V. A. Distortion and bonding strength of phthalocyanine molecules adsorbed on topological defects in graphene. *Mater. Chem. Phys.* 2021, *271*, 124963.
(20) Mendoza-Domínguez, C. U.; Basiuk, V. A. Adsorption of yttrium bisphthalocyanine on pristine and defect-contaning graphene models: a DFTstudy. 2022.
(21) Basiuk, E. V.; Huerta, L.; Basiuk, V. A. Noncovalent bonding of *3d* metal(II) phthalocyanines with single-walled carbon nanotubes: a combined DFT and XPS study. *Appl. Surf. Sci.* 2019, *470*, 622–630.
(22) Bolivar-Pineda, L. M.; Basiuk, V. A. Interactions of metal phthalocyanines with Stone-Wales defects on single-walled carbon nanotubes : a theoretical study. *J. Appl. Phys.* 2020, *127* (September 2019), 025302.
(23) Krasnov, P. O.; Basova, T. V.; Hassan, A. Interaction of metal phthalocyanines with carbon zigzag and armchair nanotubes with different diameters. *Appl. Surf. Sci.* 2018, *457*, 235–240.
(24) Correa, J. D.; Orellana, W. Optical response of carbon nanotubes functionalized with (free-base , Zn) porphyrins , and phthalocyanines : a DFT study. *Phys. Rev. B* 2012, *86*, 125417/1-6.
(25) Alvarez, L.; Fall, F.; Belhboub, A.; Le Parc, R.; Almadori, Y.; Arenal, R.; Aznar, R.; Dieudonné-George, P.; Hermet, P.; Rahmani, A.; et al. One-dimensional molecular crystal of phthalocyanine confined into single-walled carbon nanotubes. *J. Phys. Chem. C* 2015, *119* (9), 5203–5210.
(26) Zhang, Y.; Cai, X.; Zhou, Y.; Zhang, X.; Xu, H.; Liu, Z.; Li, X.; Jiang, J. Structures and spectroscopic properties of bis(phthalocyaninato) yttrium and lanthanum complexes: theoretical study based on density functional theory calculations. *J. Phys. Chem. A* 2007, *111* (2), 392–400.
(27) Dailey, M.; Besson, C. Selective crystallization of four bis(phthalocyaninato)lanthanoid(III) polymorphs. *CrystEngComm* 2021, *23*, 7151–7161.
(28) Moussavi, M.; De Cian, A.; Fischer, J.; Weiss, R. Synthesis, structure, and spectroscopic properties of the reduced and reduced protonated forms of lutetium diphthalocyanine. *Inorg. Chem.* 1988, *27* (7), 1287–1291.
(29) Martínez-Flores, C.; Bolívar-Pineda, L. M.; Basiuk, V. A. Lanthanide bisphthalocyanine single-molecule magnets : a DFT survey of their geometries and electronic properties from lanthanum to lutetium. *Mater. Chem. Phys.* 2022, *287*, 126271.
(30) Basiuk, V. A. Electron smearing in DFT calculations : a case study of doxorubicin interaction with single-walled carbon nanotubes. 2011, *111*, 4197–4205.
(31) Basiuk, V. A.; Prezhdo, O. V.; Basiuk, E. V. Thermal smearing in dft calculations: how small is really small? a case of La and Lu atoms adsorbed on graphene. *Mater. Today Commun.* 2020, *25*, 101595.
(32) Basiuk, V. A.; Acevedo-Guzmán, D. A.; Meza-Laguna, V.; Álvarez-Zauco, E.; Huerta, L.; Serrano, M.; Kakazey, M.; Basiuk, E. V. High-energy ball-milling preparation and characterization of Ln_2O_3−graphite nanocomposites. *Mater. Today Commun.* 2021, *26*, 102030.
(33) Woodruff, D. N.; Winpenny, R. E. P.; Layfield, R. A. Lanthanide single-molecule magnets. *Chem. Rev.* 2013, *113* (7), 5110–5148.
(34) Kahlal, S.; Mentec, A.; Pondaven, A.; L'Her, M.; Saillard, J. Y. Substituent effect in unsymmetrical lutetium bisphthalocyanines: a DFT analysis. *New J. Chem.* 2009, *33* (3), 574–582.
(35) Zhang, J. L. Marriage of phthalocyanine chemistry with lanthanides: a single-ion magnet with a blocking temperature up to 25 K *Inorg. Chem. Front.* 2017, *4* (12), 1950–1952.
(36) Kratochvílová, I.; Šebera, J.; Paruzel, B.; Pfleger, J.; Toman, P.; Marešová, E.; Havlová; Hubík, P.; Buryi, M.; Vrňata, M.; et al. Electronic functionality of Gd-bisphthalocyanine: charge carrier concentration, charge mobility, and influence of local magnetic field. *Synth. Met.* 2018, *236*, 68–78.
(37) Basiuk, V. A. Interaction of porphine with closed-end zigzag (6,0) single-walled carbon nanotube: the effect of parameters in $Dmol^3$ DFT calculations. *J. Comput. Theor. Nanosci.* 2008, *5* (11), 2114–2118.

(38) Suzuki, A.; Oku, T. Effects of central metal on electronic structure, magnetic properties, infrared and Raman spectra of double-decker phthalocyanine. *Appl. Surf. Sci.* 2016, *380*, 127–134.
(39) Basiuk, V. A.; Bolivar-Pineda, L. M.; Meza-Laguna, V.; Rybak-Akimova, E. V.; Basiuk, E. V. Carbon nanotubes and graphene promote pyrolysis of free-base phthalocyanine. *J. Phys. Chem. Lett.* 2018, *9* (15), 4420–4427.
(40) Farronato, M.; Bidermane, I.; Lüder, J.; Bouvet, M.; Vlad, A.; Jones, A.; Simbrunner, J.; Resel, R.; Brena, B.; Prévot, G.; et al. New quadratic self-assembly of double-decker phthalocyanine on gold(111) surface: from macroscopic to microscopic scale. *J. Phys. Chem. C* 2018, *122* (46), 26480–26488.
(41) Barhoumi, R.; Amokrane, A.; Klyatskaya, S.; Boero, M.; Ruben, M.; Bucher, J. P. Screening the 4*f*-electron spin of $TbPc_2$ single-molecule magnets on metal substrates by ligand channeling. *Nanoscale* 2019, *11* (44), 21167–21179.
(42) Zhang, Y.; Guan, P.; Isshiki, H.; Chen, M.; Yamashita, M.; Komeda, T. Bis(phthalocyaninato)yttrium grown on Au(111): electronic structure of a single molecule and the stability of two-dimensional films investigated by scanning tunneling microscopy/spectroscopy at 4.8 k. *Nano Res.* 2010, *3* (8), 604–611.
(43) Bottari, G.; De La Torre, G.; Torres, T. Phthalocyanine-nanocarbon ensembles: from discrete molecular and supramolecular systems to hybrid nanomaterials. *Acc. Chem. Res.* 2015, *48* (4), 900–910.
(44) Basiuk, V. A.; Flores-Sánchez, L. J.; Meza-Laguna, V.; Flores-Flores, J. O.; Bucio-Galindo, L.; Puente-Lee, I.; Basiuk, E. V. Noncovalent functionalization of pristine CVD single-walled carbon nanotubes with *3d* metal(II) phthalocyanines by adsorption from the gas phase. *Appl. Surf. Sci.* 2018, *436*, 1123–1133.
(45) Basiuk, V. A.; Basiuk, E. V. Noncovalent complexes of $I_h - C_{80}$ fullerene with phthalocyanines. *Fullerenes , Nanotub. Carbon Nanostructures* 2018, *26*, 69–75.

7

Chapter 7

N-Doped carbon nanofibers from pyrolysis of free-base phthalocyanine

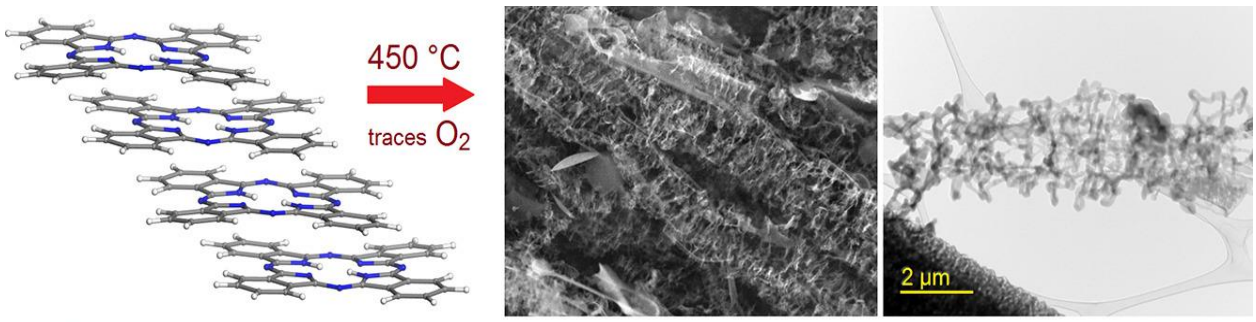

Designed by Dr Vladimir Basiuk

Published as
Vladimir A. Basiuk, Lina M. Bolivar-Pineda, Victor Meza-Laguna, Alexey M. Glushenkov, Billy J. Murdoch and Elena V. Basiuk. Diam. Relat. Mater. 2020, 105, 107812

Abstract

One of the methods for the purification of phthalocyanines is sublimation at temperatures between 400 and 500 °C. However, an attempt to purify free-base phthalocyanine (H_2Pc) at around 450 °C under static vacuum results in the formation of a non-volatile carbonaceous material through oxidative pyrolysis. We used a number of instrumental techniques to characterize its morphology and chemical composition. According to electron microscopy observations, the dominating morphology is fibrous. The estimated length of individual fibres, which appear as rather homogeneous and continuous structures, is several micrometres, with diameters of roughly 200 nm. According to elemental analysis estimates, the per cent contribution of carbon remains approximately the same as in pristine H_2Pc, but about 5.4 at% of nitrogen is substituted by oxygen. Spectroscopic measurements suggest that the oxygen is incorporated into nanofiber structures in the form of different functionalities containing C=O and C–OH bonds. Raman spectroscopy revealed an approximately equal contribution due to sp^3 and sp^2-hybridized carbon atoms, suggesting that the nanofiber thermal stability must be similar to that of defect-containing nanotubes, graphene oxide and nanodiamond. Nevertheless, according to thermogravimetric analysis, nanofibers are at least as thermally stable as graphene and defect-free nanotubes. Density functional theory calculations were employed to suggest possible initial steps of H_2Pc oxidative pyrolysis leading to the formation of nanofibers.

7.1. Introduction

Phthalocyanines, including unsubstituted ones, are found among the most stable organic compounds. [1–4] Despite the rather high molecular weight of Pcs (for example, 514.6 Da for the free-base H_2Pc), many of them are capable of subliming without decomposition in moderate vacuum under temperatures of up to 550 °C, [1–3,5–9] so that even vapor-phase spectral characterisation of Pcs is possible. [5,6,8] Within the group of unsubstituted H_2Pc and its complexes with 3*d* transition metals, such as FePc, CoPc, NiPc, CuPc and ZnPc, it is important to emphasise the contribution of the central atom to their thermal stability and capability to sublime. [8] However, it turns out that the free ligand H_2Pc is not the least thermally stable of this group, being superior to Pc complexes with Mn(II)[8], Cd(II) and Sn(II) [3]. In other words, the principal factor which defines the stability of Pcs is *p*-hyperconjugation within the extended aromatic polyazamacrocyclic system.

In the context of the present section and bearing in mind the methodology of non-covalent hybrids formation with 3*d* metal phthalocyanines and carbon nanotubes by sublimation under undemanding conditions as described in Chapter 3, there is one more interesting aspect where two such different types of materials meet, again related to carbon nanostructures. Furthermore, it is also directly related to pyrolysis phenomena. For more than two decades, in to design simple and efficient approaches to the synthesis of nitrogen-doped MWCNTs and similar carbon nanostructures, several research teams have described the nanotube fabrication processes based on pyrolytic decomposition of metal Pc. [10–19] The starting compounds employed essentially comprise three 3*d* transition metal(II) complexes: namely, FePc [12–19] , CoPc [11,16,18] and NiPc [10,11,16]. The medium and temperature conditions are variable. In particular, MWCNT can be grown under evacuation [10,19] or in vials sealed under vacuum,[18] as well as under acetylene [15] or argon/hydrogen atmosphere [11–14,16,17]. The temperatures of Pc pyrolysis are typically of 800-1000 °C, in extreme cases spanning from 700 °C [10] to 1100 °C [14].

To the best of our knowledge, free-base H_2Pc does not appear on the list of possible starting materials for carbon nanotube fabrication. The reason is obvious: while the latter is a catalytic process, H_2Pc incorporates no metal, which could serve as a catalyst for efficient CNTs growth. Our interest in the free base, within the context of nanotube chemistry, was dictated by quite different considerations. The gas-phase functionalisation of CNTs with unsubstituted phthalocyanines via physical vapor deposition proposed by us recently [20–22] is particularly straightforward and successful when commercially available and moderate-price complexes such as MnPc, FePc, CoPc, NiPc, CuPc and ZnPc are used, which can sublime without decomposition. For certain applications phthalocyanines containing other central metal atoms can be of importance. However, either their thermal stability is insufficient for safe physical vapor deposition and/or their availability is limited. In this case, the prior gas-phase functionalisation of CNTs with H_2Pc followed by its liquid-phase complexation with a metal salt of choice could be a pathway to a broader variety of nanotube-supported unsubstituted Pcs complexes.

Recently we attempted to achieve the goal of noncovalent SWCNTs functionalisation with

metal-free H_2Pc, [23] under the same conditions as those found to be optimal for the deposition of its metal derivatives (temperature of 450 °C and vacuum of ca. 10^{-2} Torr).[20–22] The result turned out to be totally unexpected. A minor fraction of phthalocyanine ligand was, as expected, successfully deposited onto SWCNTs (synthesised by a CVD process), thus yielding the target functionalised material. However, a significant amount of H_2Pc underwent pyrolytic degradation where phthalonitrile, known as the most common starting material for Pc synthesis, was a main decomposition product. In addition to CVD SWCNT, this effect was observed for CVD MWCNT and graphene. [23] The explanation we offered for this anomalous thermal behaviour of H_2Pc is based on its covalent attachment to the topological defects (which are ubiquitous in all carbon nanomaterials derived from graphene honeycomb lattice and exhibit considerable reactivity toward NH and NH_2 groups via nucleophilic addition process), followed by the disintegration of chemisorbed intermediates formed into lower-molecular-weight species, where phthalonitrile dominates.

The experiments described in Ref. [23] gave rise to one more change finding, which was not immediately analysed and interpreted. It has to do with an experimental error in handling the vacuum system. The main requirement for valid comparison of the results was constant evacuation. This included the blank experiments on H_2Pc sublimation in the absence of carbon nanomaterials, which, under the correct dynamic vacuum of 10^{-1}-10^{-2} Torr, must result in almost quantitative phthalocyanine recovery. In some blank experiments, however, the evacuation was interrupted by mistake, and H_2Pc was unable to sublime: the sample remained in the heated zone at 450 °C, losing the characteristic deep violet coloration and acquiring black appearance typical for CNTs, graphene powder and amorphous carbon.

The goal of the present chapter is to present the characterisation of the morphology and chemical composition of the above product of H_2Pc pyrolysis by means of several instrumental techniques, and to roughly estimate the span of conditions for its formation.

7.2. Experimental section

7.2.1. H_2Pc pyrolysis

Free-base phthalocyanine H_2Pc (β-form, 98% purity) was purchased from Sigma-Aldrich. For each experiment, about 200 mg of H_2Pc was used. The tubular quartz reactor employed for most pyrolysis experiments was described previously in Chapter 3. Phthalocyanine was placed onto the bottom of a quartz reactor. This can be done either directly, or with H_2Pc wrapped into aluminium foil to prevent it blowing away upon evacuation: both options provide similar results. After pumping the system out to a vacuum of about 10^{-2} Torr at room temperature, the valve of the reactor was closed, and the furnace was switched on. The tests were performed at four selected temperatures of 350, 400, 450 and 500 °C. The duration of experiments was recorded from the moment when the temperature stabilised: it was 2, 5, 10 and 15 h. The sample notation was based on temperature and duration of the experiment: for example, the sample treated at 450 °C for 10 h is denoted as P-450-10.

In addition to the main series of experiments in which a quartz reactor was employed, for comparison, we have done several additional tests with H_2Pc heating in a vacuum-sealed vial and in a Pyrex beaker.

7.3. Results and discussion

7.3.1. Characterisation

As mentioned evacuation to 10^{-1}-10^{-2} Torr was interrupted by mistake. As a result, phthalocyanine was unable to sublime and remained in the heated zone at 450 °C, losing the characteristic deep violet coloration and acquiring black appearance typical for CNTs, graphene powder and amorphous carbon. Further attempts to sublime the material formed at 450 °C or even higher temperature under the correct vacuum were unsuccessful.

Bearing in mind the reports by other research groups on CNTs fabrication by means of pyrolytic decomposition of metal Pc at 700-1100 °C, [10–19] we analysed the possibility of the formation of similar carbon nanostructures using electron microscopy techniques, namely SEM and HRTEM. The general sample morphology was characterised by SEM, in comparison with that for pristine H_2Pc crystals (β-form). As one can see in Fig.7. 1a-c, the latter are needle-shaped of roughly 10^1-10^3 mm length and 1-10 mm width. The microstructure of pyrolysates, exemplified here by P-450-10 sample (Fig.7. 1g-l), reflects to a great degree the dimensions of H_2Pc crystals, which is especially evident in Fig.7. 1g-i. However, instead of a solid appearance, pyrolysate particles are mostly observed as sponge-like agglomerates of irregularly shaped fibres. At some sites of the sample, a continuous and denser morphology of agglomerates dominates, with less evident presence of the formations matching the shape and dimensions of H_2Pc crystals (Fig.7. 1j-l). (It is likely that the more ordered structures were simply crushed during SEM sample preparation, or during pyrolysate extraction from the reactor.) Additionally, one should mention a minor presence of platelet-like formations, like the one seen in top-left part of Fig.7. 1i.

Even though SEM revealed a fibrous morphology of pyrolysates, similar to MWCNTs, this technique is unable to discern whether the fibres have an inner cavity. To provide further structural details, we employed transmission electron microscopy. A series of representative HRTEM images of characteristic formations found in P-450-10 sample is shown in Fig.7. 2. In line with the results of SEM imaging (Fig.7. 1g-i), the dominating morphology is a fibrous one, with clear separations between individual fibres (Fig.7. 2a-c). The estimated length of the latter is several micrometres, with diameters of roughly 200 nm. While these dimensions match, in principle, those of common MWCNT, neither inner cavities nor concentric walls can be discerned here. Instead, the nanofibres appear as rather homogeneous and continuous structures. At other sites of P-450-10 sample (Fig.7. 2h,i), similar nanofibers are densely packed into micrometre-sized globular formations, which apparently match the morphology observed by SEM in Fig.7. 1j-l. As minor components, we also observed fused agglomerates of relatively compact nanoparticles (Fig.7. 2d-e), as well as rod-like formations (Fig.7. 2g), which

are generally reminiscent of MWCNTs, but have larger, micrometre-scale dimensions (including the diameter).

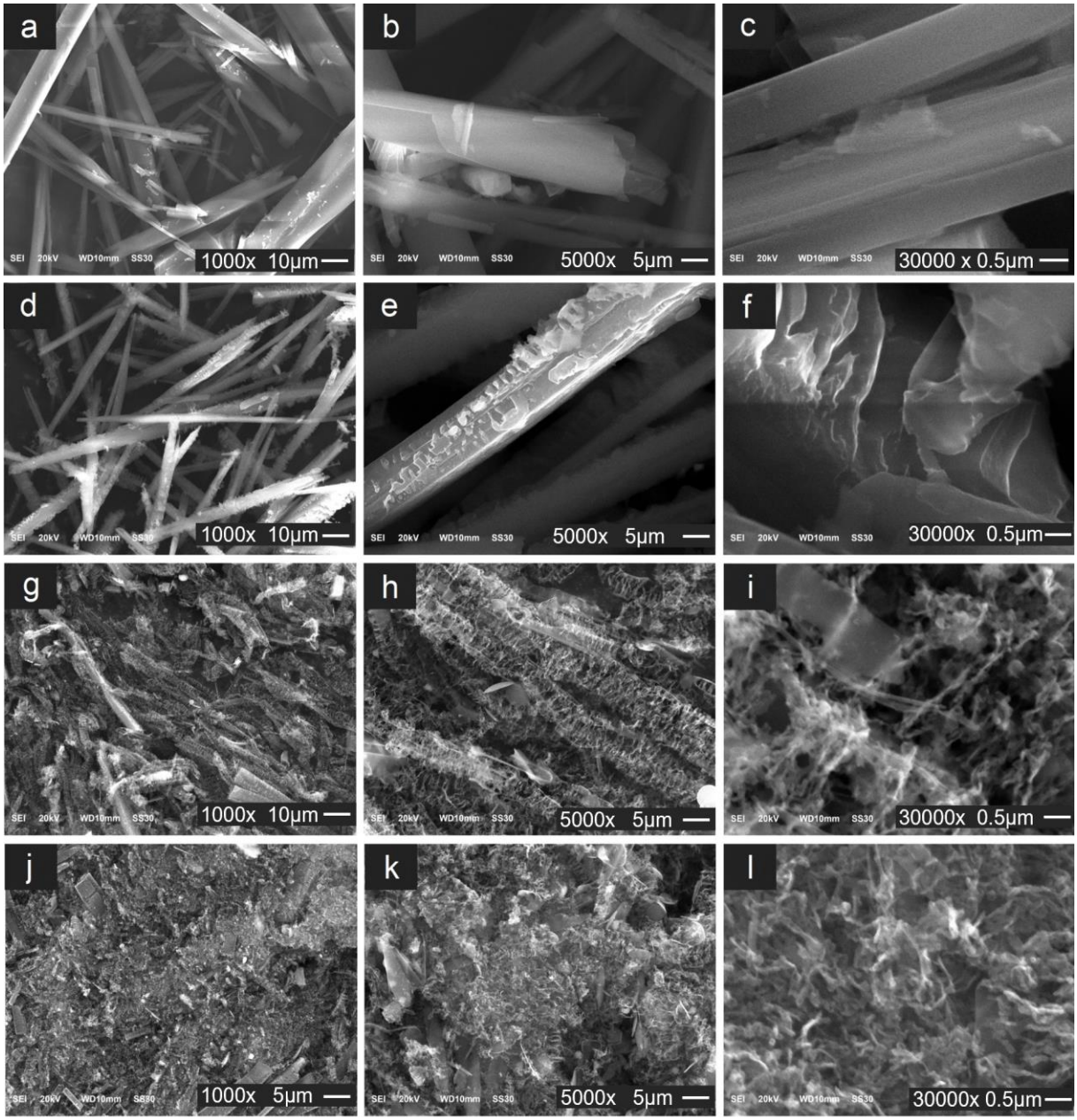

Fig.7. 1. Comparison of representative SEM images, at different magnifications, for (a-c) pristine H_2Pc crystals, (d-f) P-400-10 sample and (g-l) P-450-10 sample. For P-450-10 sample, two general types of morphology were analysed: (g-i) the one matching the shape of starting H_2Pc crystals, and (j-l) mostly disordered and denser morphology. Scale bars: (a,d,g,j) 10 µm, (b,e,h,k) 5 µm and (c,f,i,l) 0.5 µm.

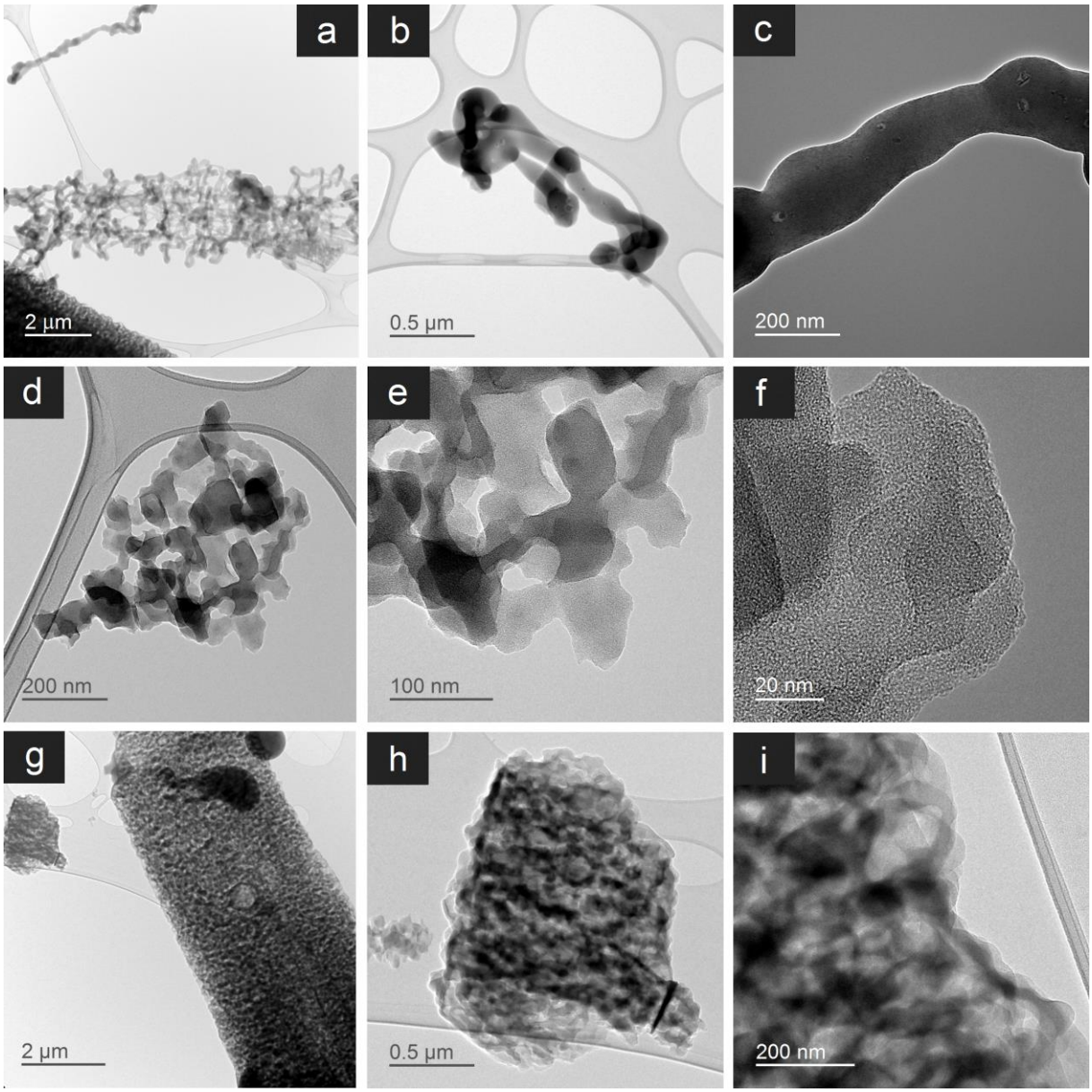

Fig.7. 2. Representative HRTEM images, at different magnifications, of characteristic formations found in P-450-10 sample: (a-c) the dominating fibrous structures, with clear separations between individual fibres; (d-e) fused agglomerates of relatively compact nanoparticles; (g) a micrometre-sized rod; (h,i) a micrometre-sized globular formation composed of densely packed nanofibers.

An important question to answer is under what conditions (temperature, pyrolysis duration and vacuum) the above structures can efficiently form. As was specified in the experimental section, a series of tests was performed at four selected temperatures of 350, 400, 450 and 500 °C, with heating durations of 2, 5, 10 and 15 h (from the moment when the temperature stabilised). The temperature of 350 °C was too low, where no changes in H_2Pc crystal morphology were detected by SEM even after 15 h, regardless of whether the experiment was carried out in the quartz reactor under vacuum or in a Pyrex beaker under air (Fig.7. 3a).

Another extreme is the heating at 500 °C, where already after 2 h, more than a half of the starting phthalocyanine sublimed, leaving a minor amount (of ca. 10% of the starting reagent) at the bottom of the reactor (Fig.7. 3b). In other words, the residence time of H_2Pc in the hot zone at 500 °C is insufficient. Morphological changes were observed starting with 400 °C. At the same time, H_2Pc crystals kept their integrity, and even after 10 h (quartz reactor under vacuum), only signs of their corrosion were observed by SEM, as can be seen from Fig.7. 1d-f. The temperature at which the rates of H_2Pc pyrolysis and sublimation can roughly equilibrate is 450 °C. Interestingly, the product morphology generally does not depend on the heating duration, remaining essentially the same in the experiments performed at 2, 5, 10 and 15 h. The yields were poorly reproducible and fluctuated from 3 to 90%, which can be explained by impossibility to reproduce air leaks after closing the vacuum line. Nevertheless, the residual pressure turns out to be incomparably lower with respect to the atmospheric one: in a blank experiment with an empty sublimation system (without H_2Pc and heating), it does not increase to more than 4 Torr at 10 h after interrupting evacuation. For comparison, heating in a Pyrex beaker under air at 450 °C results in gradual burning of H_2Pc, where the amount of solid residue after 2, 5, 6 and 9-h heating was found to be about 23, 14, 1 and 0%, respectively, of starting phthalocyanine weight. On the other hand, H_2Pc heated at 450 °C in a small (compared to the size of quartz reactor) vacuum-sealed vial did not undergo evident changes. The above observations point to the crucial role of minor amounts of air oxygen in the H_2Pc pyrolysis process, supplied to the sublimation system due to air leaks.

It is logical to expect that, as a result, oxygen covalently bonds to phthalocyanine macrocycles and/or to the products of their thermal transformations. In this case, it must be readily detected by spectroscopic techniques, first, by EDS coupled to SEM. In neat H_2Pc (brute formula $C_{32}H_{18}N_8$), the C:N atomic ratio is 4:1 (or 80:20 to sum up to 100 at %), with no structural oxygen present. According to EDS analysis of P-450-10 sample probed at 19 different sites (representative results are shown in Fig.7. 4a), the content of C, N and O turned to be 71.13-93.76, 0-31.54 and 3.64-7.26 at %, respectively, with the corresponding averaged values of 79.27, 14.60 and 5.40 at %. In other words, the per cent contribution of carbon remains approximately the same as in pristine H_2Pc, but about 5.4 at% of nitrogen is substituted by oxygen. In line with the results of SEM imaging of P-400-10 sample (Fig.7. 1d-f), which is a product of the very early steps of H_2Pc pyrolysis, the average O content is much lower than for the P-450-10 sample. Namely, the average content of C, N and O was found to be 77.6, 19.27 and 3.01 at% from EDS analysis probed at 11 sites (representative results are exemplified in Fig.7. 4b) gave generally broader ranges of 71.27-83.56, 7.26-25.13 and 0.94-9.12 at%, respectively. These the above values reflect the surface composition of H_2Pc crystals, whose interiors remain intact.

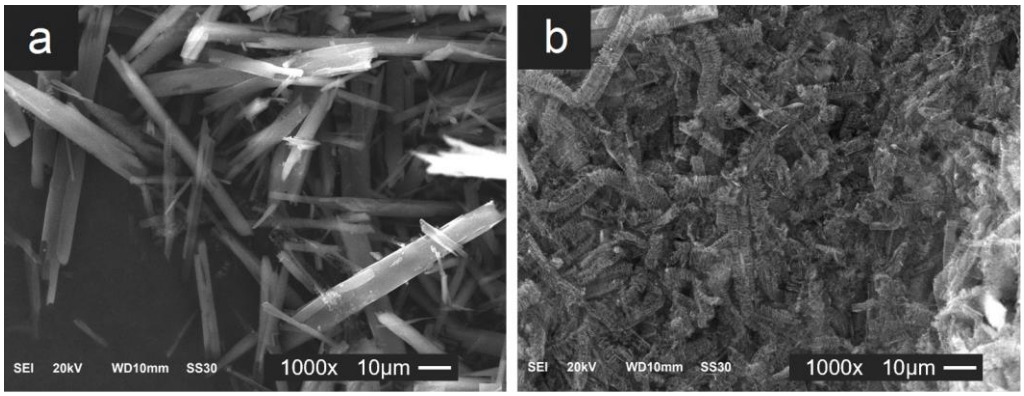

Fig.7. 3. Representative SEM images for: (a) P-350-10 sample for the experiment performed in a Pyrex beaker under air; (b) P-500-2 sample for the experiment carried out in the quartz reactor under vacuum.

To give an insight into the chemical nature of new structural features resulting from H_2Pc pyrolysis, we employed FTIR and XPS spectroscopies. As one can see from Fig.7. 5a, the main infrared spectral features of pristine H_2Pc in the lower-frequency region are the bands at 712-727 (γ_{CH}), 870 (in-plane vibration), 1000 (N–H in-plane bending), 1092 (C–H in-plane deformation), 1187 (C–N in-plane bending), 1318 (δ_{NH}), 1437 (CC stretching in isoindole moieties), 1500 (C=N stretching) and 1608 cm^{-1} (C=C deformation of macrocyclic system).[24] The lower-intensity higher-frequency modes are due to aromatic ν_{CH} vibrations at 3011 and 3048 cm^{-1}, as well as ν_{NH} vibrations at 3288 cm^{-1}. In the spectrum of the P-450-10 sample, the latter higher-frequency features do not exhibit substantial changes; nevertheless, the general background in this region is dominated by a low-intensity diffuse absorption band centred at ca. 3500 cm^{-1}, which is indicative of the formation of O–H functionalities. In a similar way, FTIR spectrum of the P-450-10 sample in the lower-frequency region shares most features with the spectrum of pristine H_2Pc. At the same time, the signals tend to notably broaden due to the appearance of a large number of closely related structural elements. In addition, here one can see at least two new features. The first one is a broad and intense band at 1590 cm^{-1}, which apparently combines aromatic ν_{CC}, $\nu_{C=N}$, $\nu_{C=O}$ in quinones and/or conjugated ketones, and d_{NH} vibrations in secondary amines. [25,26] The second feature at 1723 cm^{-1} corresponds to $\nu_{C=O}$ vibrations in COOH groups. What was totally unexpected is the appearance of a clearly distinguishable nitrile ($\nu_{C\equiv N}$) band at 2227 cm^{-1}, along with a small peak at 2165 cm^{-1} attributable to $\nu_{C\equiv C}$ vibrations.

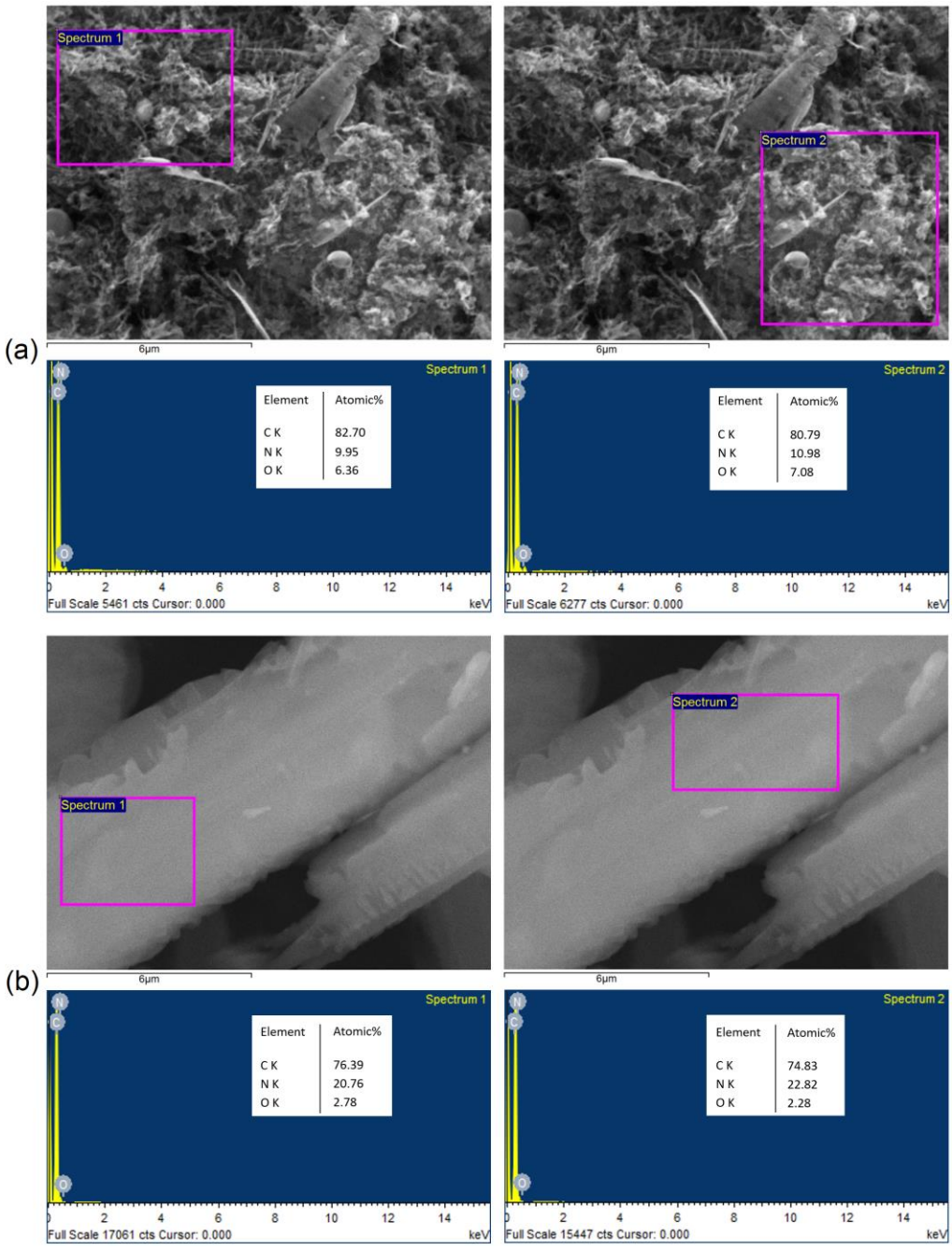

Fig.7. 4. Representative EDS results (C, N and O at%) for different selected SEM areas of (a) P-450-10 sample and (b) P-400-10 sample.

The deconvolution of C 1*s* and N 1*s* peaks in XPS spectra of P-400-10 and P-450-10 samples (Fig.7. 5b) reveals a series of characteristic components found in the XPS spectrum of pristine H_2Pc. [27] The common C 1s features are the lowest energy peak at 284.7 eV due to sp^2 carbon atoms in phenylene rings, the one at 286.3 eV corresponding to C atoms connected to two nitrogen atoms (N–C–N) and its satellite at 287.5-288.0 eV. One should note that C=O groups may also show a C 1*s* peak in the latter region, which would agree with the above interpretation of FTIR spectra, and that some contribution in the C 1s spectrum of P-400-10 at

~286 eV can be due to C–O bonds. In addition, the intermediate-energy peak at 285.5-285.8 eV, detected for both pyrolysates, can be attributed to C atoms in a broken macrocyclic system. A special similarity between pristine and pyrolysed H_2Pc can be observed in the case of N 1s deconvolution, where all three materials exhibit two peaks at 398.6-398.7 and 400.1-400.2 eV due to *meso*-bridging and central nitrogen atoms, respectively.[27] As expected, the most interesting result is observed in O 1s spectra of the two pyrolysed samples. They are very different from one other. In the case of the P-400-10 sample, one can clearly separate two peaks at 531.6 and 533.8 eV. The former can be assigned to carbonyl groups C=O: such a peak can be found in XPS spectra of oxidised carbon nanomaterials including MWCNT [28] and graphene oxide (GO). [29] The presence of the higher-energy peak at 533.8 eV was interpreted elsewhere in different ways: for example, it was attributed to carboxylic functionalities in GO, [30–32] as well as to C–O(H) and ether groups. [28,29] Interestingly, in the O 1s deconvolution for the P-450-10 sample, corresponding to a more developed degree of pyrolysis, only one peak at 532.5 eV can be found. Again, different assignments can be suggested: in particular, to C=O/O–C=O groups, [30–32]or to a combination of COOH, anhydride, ester and lactone functionalities. [28]

The most striking changes due to pyrolysis were observed by Raman spectroscopy. As it is evident from Fig.7. 5c, almost no Raman features of pristine H_2Pc can be found in the spectrum of the P-450-10 sample. Instead, two broad bands appear, which are centred at 1337 and 1585 cm^{-1}. This resulting general appearance of Raman spectrum is very typical and familiar within the area of carbon nanomaterials: the two modes observed are called disorder (D) and graphite (G) bands, which correspond to sp^3 and sp^2-hybridised carbon atoms. They can be found in the spectra of essentially all nanocarbons, at variable I_D/I_G intensity ratios, and at Raman shifts fluctuating within a few tens of cm^{-1}. Particular values of the latter are as follows (D and G band, respectively): for CVD single-walled CNTs with defects, 1332-1351 and 1583-1590 cm^{-1} [20,21,33]; for MWCNT, 1334-1355 and 1562-1604 cm^{-1} [33–36]; for graphene, 1339 and 1572 cm^{-1} [37]; for GO, 1338-1355 and 1565-1590 cm^{-1} [31,32,38]; for nanodiamond, 1320 and 1590 cm^{-1} [32,39]. Furthermore, related nitrogen-doped materials exhibit a very similar spectral pattern, with the following examples of Raman shifts for D and G band, respectively: CNTs, 1360 and 1580 cm^{-1} [40]; carbon nanoparticles, 1350 and 1585 cm^{-1} [41]; graphene, 1330 and 1580 cm^{-1} [42]. In the present case (Fig.7. 5c), an I_D/I_G intensity ratio close to 1 is indicative of an approximately equal contribution due to sp^3 and sp^2-hybridised atoms.

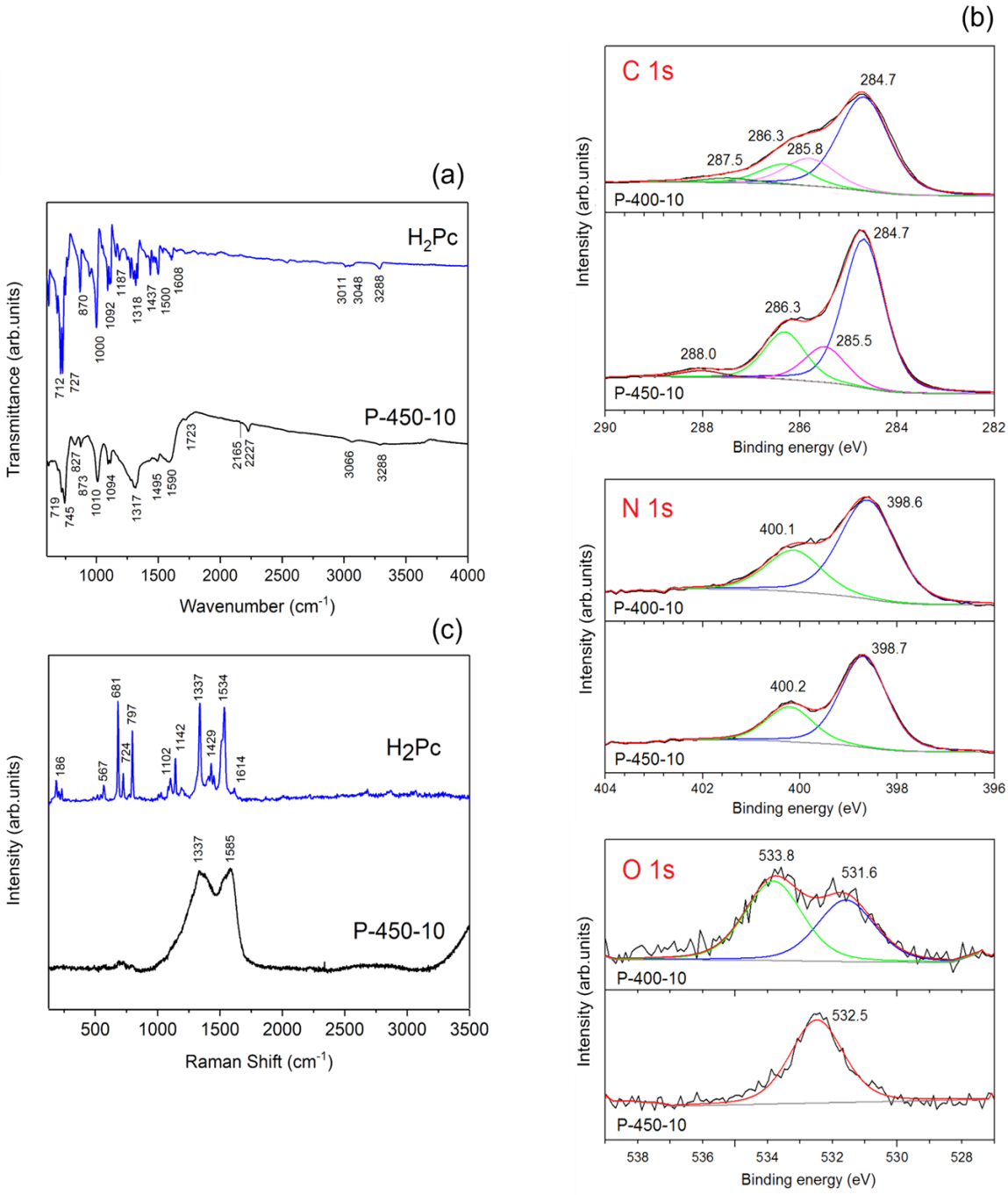

Fig.7. 5. (a) Comparison of FTIR spectra of pristine H_2Pc and P-450-10 sample. (b) Deconvolution of C1*s*, N1*s* and O 1*s* components in XPS spectra of P-400-10 and P-450-10 samples. (c) Comparison of Raman spectra of pristine H_2Pc and P-450-10 sample.

To more closely relate the products of H_2Pc pyrolysis to a particular nanocarbon form, we compared TGA and DTA curves measured for the P-450-10 sample with those obtained for pristine H_2Pc (Fig.7. 6a). As a general rule, when the presence of sp^3-hybridised C atoms is insignificant, nanomaterial decomposes completely at 750-800 °C (for TGA measurements in

air atmosphere), as is observed for graphene [37] and purified SWCNT [33,43]. In contrast, a high content of sp^3-hybridised C atoms, which manifest itself in Raman spectra as a high-intensity D band, strongly reduces the final decomposition temperature in air to roughly 600 °C as this is the case of the multi-walled CNTs, [32–36] GO [31,32,38] and nanodiamond [32,39]. From the TGA curve presented in Fig.7. 6b, the material constituting the P-450-10 sample is at least as thermally stable as graphene and defect-free single-walled CNTs, exhibiting a final decomposition temperature of 827 °C. Here, the first minor weight loss of 4.5% is due to impurities adsorbed from air (including water), which is followed by two almost indistinguishable steps starting at 435 and 683 °C, with the corresponding DTA maxima at 574 and 778 °C. From comparison with the results of SEM and TEM imaging, one can suggest that these two steps match the existence of nanofiber phases of lower (Fig.7. 1g-i and Fig.7. 2a-c) and higher (Fig.7. 1j-l and Fig.7. 2h,i) packing density, respectively. In the case of neat H_2Pc, the first slight weight loss of 4.5% (apparently due to impurities) is followed by three main steps at 481-549 (25.2%), 549-620 (30.8%) and 620-860 °C (39.7%), with the corresponding DTA peaks at 543, 596 and 759 °C. The first two weight losses are very steep, whereas the third one is very similar to the main weight loss observed for the P-450-10 sample, both in terms of the slope and the final decomposition temperature. One can suggest that the residue formed after reaching ca. 600 °C is most likely very similar in structure and composition to the nanostructured products of the H_2Pc pyrolysis (to the P-450-10 sample in particular). Overall, the TGA/DTA results were unexpected given the high content of sp^3-hybridised carbon atoms in pyrolysed H_2Pc found by Raman spectroscopy.

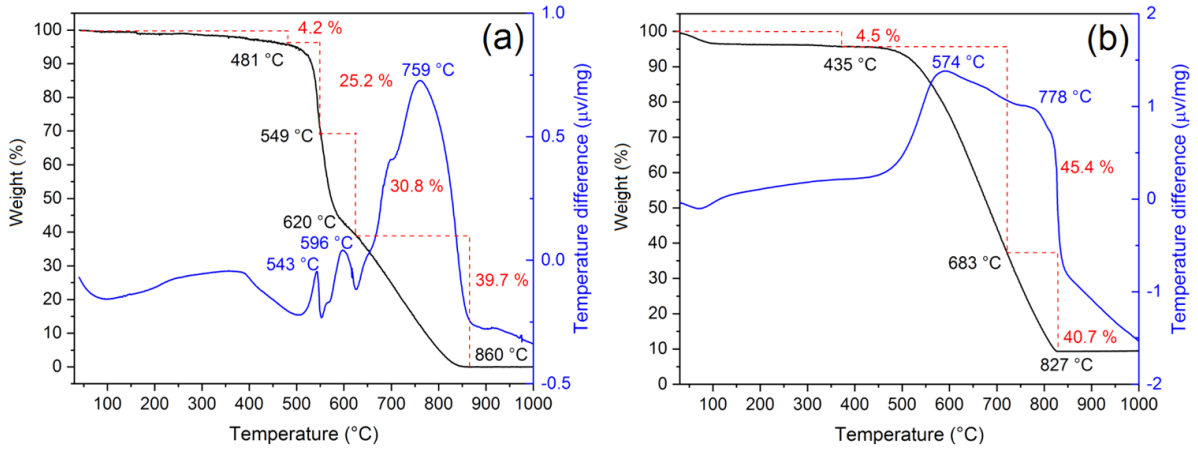

Fig.7. 6. Comparison of TGA and DTA curves for (a) pristine H_2Pc and (b) P-450-10 sample.

7.3.2. Explanation by DFT

Due to the high complexity of the phthalocyanine molecule and the need to consider intermolecular interactions in the solid phase, it is virtually impossible to suggest a straightforward mechanism of H_2Pc oxidative pyrolysis. What we have attempted to do, employing DFT calculations (at the PBE-D/DNP level of theory), is to predict its very first steps: namely, how the interaction of macrocyclic molecules found on the surface of *b*-form of crystalline H_2Pc with molecular oxygen can generate reactive chemical species, capable of further high-temperature transformations. First, one has to identify possible sites within an isolated H_2Pc molecule, which can serve as a target for nucleophilic attack by a O_2 molecule. Fig.7. 7a shows the electrostatic potential distribution in H_2Pc along with atomic charges obtained from Mulliken population analysis. One can see that the most positively charged atoms (and thus, the most plausible sites for nucleophilic O_2 addition) are the C atoms of 16-membered macrocyclic system. All of them are connected to two adjacent N atoms of the macrocycle and have an atomic charge from 0.263 (two pyrrole rings without H atom) to 0.291 (two pyrrole rings with H atom), providing an important contribution into both LUMO and HOMO orbitals of the phthalocyanine system (Fig.7. 7b). In turn, logically, the latter type of C atoms can attract an O_2 nucleophile more efficiently.

In a second step, we investigated the behaviour of the product of O_2 addition onto the site identified above. Due to computational limitations, the model system considered included only two phthalocyanine molecules (referred to as $2H_2Pc$; Fig.7. 8a) laying at the crystal surface, with the same mutual orientation as the one observed in the b-crystalline form. In the optimised geometry of $2H_2Pc$, all intermolecular separations are >3.1 Å, except for one distance of 3.061 Å (dotted line). The LUMO isosurface plot shown on the right of Fig.7. 8a indicates the possible site of nucleophilic attack by an O_2 molecule (red arrows). After the addition of O_2 onto the superior (that is, found on crystal surface) phthalocyanine molecule, the pyrrole ring where O_2 was attached undergoes strong distortion from the macrocyclic plane, so that its N(H) atom approaches (dotted line) one of the H(C) atoms of the subsurface molecule (Fig.7. 8b). The formation energy for this species (denoted as $2H_2Pc+O_2$) is 37.27 kcal/mol, i.e., the process is endothermic. To form a new N–H bond between the latter two atoms, a few existing covalent bonds have to be broken (marked with solid red lines) to avoid hypervalency. In the resulting structure ($2H_2Pc+O_2$_b; Fig.7. 8c), whose formation is highly endothermic (73.36 kcal/mol), the surface macrocycle turns out to be strongly distorted, and both surface and subsurface molecules become reactive due to the appearance of several sites with high unpaired electron density (spin density plot on the right of Fig.7. 8c). The most important factor for inducing further pyrolytic transformations is a radical character of the subsurface phthalocyanine species, acquired as a result of H atom abstraction by the surface H_2Pc molecule.

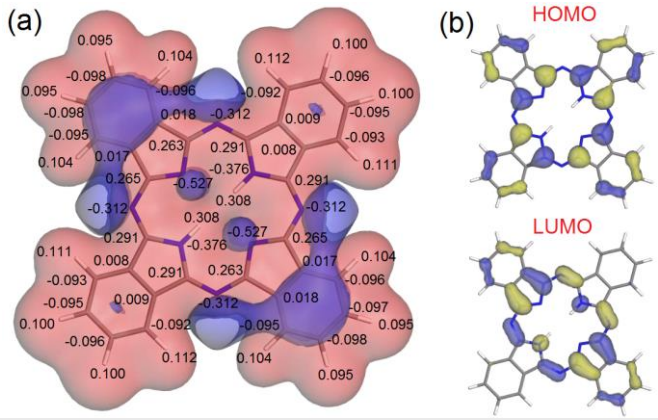

Fig.7. 7. Isosurface plots computed for isolated H_2Pc molecule: (a) electrostatic potential (isosurface at 0.016 arb. units.), with red and blue lobes corresponding to positive and negative potential, respectively, and atomic charges obtained from Mulliken population analysis; (b) frontier orbitals (isosurfaces at 0.03 arb. units.).

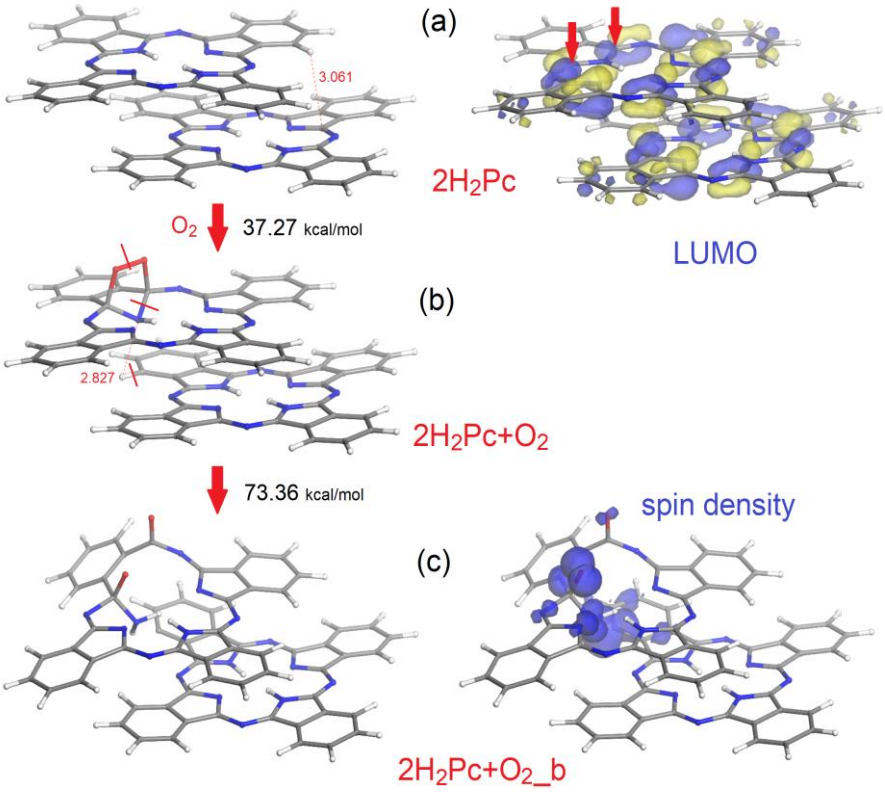

Fig.7. 8. Proposed initial steps of H_2Pc oxidative pyrolysis. (a) The model system has two phthalocyanine molecules ($2H_2Pc$) with a mutual orientation as in the β-crystalline form. The distance of 3.061 Å (dotted line) is the only approach between the two molecules which is closer than typical separations of >3.1 Å. The LUMO isosurface (at 0.03 a.u.) plot shown on the right indicates a possible site of nucleophilic attack with O_2 molecule (red arrows). (b) The product of nucleophilic addition of O_2 onto the surface phthalocyanine molecule of $2H_2Pc$ model. The pyrrole ring where O_2 attached undergoes strong distortion from macrocyclic plane, so that its N(H) atom approaches (dotted line) one of H(C) atoms of the subsurface molecule. To form a new N–H bond between the latter two atoms, a few existing covalent bonds have to be broken (marked with the solid red lines). In the resulting structure **(c)** the surface macrocycle turns out to be strongly distorted, and both molecules become reactive due to the presence of several sites with high unpaired electron density (spin density isosurface at 0.03 arb. units. on the right).

7.4. Conclusions

Heating free-base phthalocyanine H_2Pc at temperatures around 450 °C under static vacuum prevents its sublimation recovery, but instead results in the formation of a carbonaceous material through oxidative pyrolysis. According to electron microscopy observations, the dominating morphology of pyrolysate is fibrous, usually with clear separations between individual fibres. The estimated length of the latter is several micrometres, with diameters of roughly 200 nm. While these dimensions match, in principle, those of common MWCNT, neither inner cavities nor concentric walls can be discerned by TEM. Instead, the nanofibers appear as rather homogeneous and continuous structures. According to elemental analysis by SEM-coupled EDS, the per cent contribution of carbon remains approximately the same as in pristine H_2Pc, but about 5.4 at% of nitrogen is substituted by oxygen. FTIR and XPS spectroscopy suggest that the oxygen is incorporated into the nanofiber structure in the form of different functionalities containing C=O and C–OH bonds, which might include COOH, anhydride, ester and lactone groups. Raman spectroscopic measurements revealed an approximately equal contribution due to sp^3 and sp^2-hybridised carbon atoms, which suggests that the thermal stability of nanofibers must be similar to that of defect-containing CNTs, graphene oxide and nanodiamond, whose final decomposition temperature in air is roughly 600 °C. Nevertheless, as follows from the TGA and DTA curves obtained, N-doped nanofibers are at least as thermally stable as graphene and defect-free SWCNT, exhibiting a final decomposition temperature of 827 °C.

DFT calculations suggest that the oxidative pyrolysis of b-crystalline form of H_2Pc can be initiated through nucleophilic addition of an O_2 molecule onto one of the pyrrole rings of the phthalocyanine molecule laying at the crystal surface.

7.5. References

(1) Dahlen, M. A. A new class of synthetic pigments and dyes. *Ind. Eng. Chem.* 1939, *31*, 8339–8847.
(2) Lever, A. B. P. The phthalocyanines. *Adv. Inorg. Chem. Radiochem.* 1965, *7* (C), 27–114.
(3) Barrett, P. A.; Dent, C. E.; Linstead, R. P. Phthalocyanines. part VII. phthalocyanine as a co-ordinating group. a general investigation of the metallic derivatives. *J. Chem. Soc.* 1936, *382(0)*, 1719–1736.
(4) Guilard, R.; Kadish, K. M.; Smith, K. M. *The Porphyrin Handbook*; 2003; Vol. 11.
(5) Eastwood, D.; Edwards, L.; Gouterman, M.; Steinfeld, J. Spectra of porphyrins.past VII. vapor absorption and emission of phthaloocyanines. *J. Mol. Spectrosc.* 1966, *20*, 381–390.
(6) Edwards, L.; Gouterman, M. Porphyrins: XV. vapor absorption spectra and statability: phthalocyanines. *J. Mol. Spectrosc.* 1970, *33*, 292–310.
(7) Wagner, H.; Loutfy, R.; Hsiao, C.-K. *Purification and Characterization of Phthalocyanines*; 1982; Vol. 17.
(8) MacKay, A. Heats of sublimation of phthalocyanines. *Aust. J. Chem.* 1973, *26*, 2425–2433.
(9) Williams, G.; Dafydd, L.; Watts, A.; Mcmurray, N. Latent fingermark visualisation using reduced-pressure sublimation of copper phthalocyanine. *Forensic Sci. Int.* 2011, *204*, e28–e31.
(10) Yudasaka, M.; Kikuchi, R.; Ohki, Y. Nitrogen-containing carbon nanotube growth from ni phthalocyanine by chemical vapor deposition. *Carbon N. Y.* 1997, *35*, 195–201.
(11) Wang, X. B.; Liu, Y. Q.; Zhu, D. B. Honeycomb-like alignments of carbon nanotubes synthesized by pyrolysis of a metal phthalocyanine. *Appl. Phys. A Mater. Sci. Process.* 2000, *71*, 347–348.
(12) Wang, X.; Hu, W.; Liu, Y.; Long, C.; Xu, Y. Bamboo-like carbon nanotubes produced by pyrolysis of iron (II) phthalocyanine. *Carbon N. Y.* 2001, *39*, 1533–1536.
(13) Huang, S.; Dai, L.; Mau, A. Synthesis and structures of aligned branched carbon nanotubes produced by pyrolysis of

iron (II) phthalocyanine. *Phys. B* 2002, *323*, 336–338.
(14) Huang, S.; Dai, L. Microscopic and macroscopic structures of carbon nanotubes produced by pyrolysis of iron phthalocyanine. *J. Nanoparticle Res.* 2002, *4*, 145–155.
(15) Liu, B. C.; Lee, T. J.; Lee, S. H.; Park, C. Y.; Lee, C. J. Large-scale synthesis of high-purity well-aligned carbon nanotubes using pyrolysis of iron (II) phthalocyanine and acetylene. *Chem. Phys. Lett.* 2003, *377*, 55–59.
(16) Kim, N. S.; Lee, Y. T.; Park, J.; Han, J. B.; Choi, Y. S.; Choi, S. Y.; Choo, J.; Lee, G. H. Vertically aligned carbon nanotubes grown by pyrolysis of iron, cobalt, and nickel phthalocyanines. *J. Phys. Chem. B* 2003, *107* (35), 9249–9255.
(17) Song, J.; Sun, M.; Chen, Q.; Wang, J.; Zhang, G.; Xue, Z. Field emission from carbon nanotube arrays fabricated by pyrolysis of iron phthalocyanine. *J. Phys. D. Appl. Phys.* 2004, *37* (1), 5–9.
(18) Zhi, L.; Gorelik, T.; Friedlein, R.; Wu, J.; Kolb, U.; Salaneck, W. R.; Müllen, K. Solid-state pyrolyses of metal phthalocyanines: a simple approach towards nitrogen-doped CNTs and metal/ carbon nanocables. *SamII* 2005, *1*, 798–801.
(19) Milev, A. S.; Tran, N.; Kannangara, G. S. K.; Wilson, M. A. Polymorphic transformation of iron-phthalocyanine and the effect on carbon nanotube synthesis. 2008, 5339–5347.
(20) Basiuk, V. A.; Flores-Sánchez, L. J.; Meza-Laguna, V.; Flores-Flores, J. O.; Bucio-Galindo, L.; Puente-Lee, I.; Basiuk, E. V. Noncovalent functionalization of pristine cvd single-walled carbon nanotubes with *3d* metal(II) phthalocyanines by adsorption from the gas phase. *Appl. Surf. Sci.* 2018, *436*, 1123–1133.
(21) Alzate-Carvajal, N.; Bolivar-Pineda, L. M.; Meza-Laguna, V.; Basiuk, V. A.; Basiuk, E. V.; Baranova, E. A. Oxygen evolution reaction on single-walled carbon nanotubes noncovalently functionalized with metal phthalocyanines. *ChemElectroChem* 2019, *7*, 428–436.
(22) Basiuk, E. V.; Huerta, L.; Basiuk, V. A. Noncovalent bonding of *3d* metal(II) phthalocyanines with single-walled carbon nanotubes: a combined dft and xps study. *Appl. Surf. Sci.* 2019, *470*, 622–630.
(23) Basiuk, V. A.; Bolivar-Pineda, L. M.; Meza-Laguna, V.; Rybak-Akimova, E. V.; Basiuk, E. V. Carbon nanotubes and graphene promote pyrolysis of free-base phthalocyanine. *J. Phys. Chem. Lett.* 2018, *9* (15), 4420–4427.
(24) Verma, D.; Dash, R.; Katti, K. S.; Schulz, D. L.; Caruso, A. N. Role of coordinated metal ions on the orientation of phthalocyanine based coatings. *Spectrochim. Acta - Part A Mol. Biomol. Spectrosc.* 2008, *70*, 1180–1186.
(25) Coates, J. Interpretation of infrared spectra, a practical approach. *Encycl. Anal. Chem.* 2006, 1–23.
(26) Cyran, J. D.; Nite, J. M.; Krummel, A. T. Characterizing anharmonic vibrational modes of quinones with two-dimensional infrared spectroscopy. *J. Phys. Chem. B* 2015, *119* (29), 8917–8925.
(27) Niwa, Y.; Kobayashi, H.; Tsuchiya, T. X-ray photoelectron spectroscopy of tetraphenylporphin and phthalocyanine. *J. Chem. Phys.* 1974, *60* (3), 799–807.
(28) Wu, S.; Wen, G.; Schlögl, R.; Su, D. S. Carbon nanotubes oxidized by a green method as efficient metal-free catalysts for nitroarene reduction. *Phys. Chem. Chem. Phys.* 2015, *17* (3), 1567–1571.
(29) Yang, D.; Velamakanni, A.; Bozoklu, G.; Park, S.; Stoller, M.; Piner, R. D.; Stankovich, S.; Jung, I.; Field, D. A.; Ventrice, C. A.; et al. Chemical analysis of graphene oxide films after heat and chemical treatments by X-ray photoelectron and micro-raman spectroscopy. *Carbon N. Y.* 2009, *47* (1), 145–152.
(30) Axet, M. R.; Dechy-Cabaret, O.; Durand, J.; Gouygou, M.; Serp, P. Coordination chemistry on carbon surfaces. *Coord. Chem. Rev.* 2016, *308*, 236–345.
(31) Basiuk, V. a.; Alzate-Carvajal, N.; Henao-Holguín, L. V.; Rybak-Akimova, E. V.; Basiuk, E. V. Coordination functionalization of graphene oxide with tetraazamacrocyclic complexes of nickel(II): generation of paramagnetic centers. *Appl. Surf. Sci.* 2016, *371*, 16–27.
(32) Alzate-Carvajal, N.; Basiuk, E. V.; Meza-Laguna, V.; Puente-Lee, I.; Farías, M. H.; Bogdanchikova, N.; Basiuk, V. A. Solvent-free one-step covalent functionalization of graphene oxide and nanodiamond with amines. *RSC Adv.* 2016, *6* (114), 113596–113610.
(33) Basiuk, V. a.; Henao-Holguín, L. V.; Álvarez-Zauco, E.; Bassiouk, M.; Basiuk, E. V. Gas-phase noncovalent functionalization of carbon nanotubes with a Ni(II) tetraaza[14]annulene complex. *Appl. Surf. Sci.* 2013, *270*, 634–647.
(34) Ramirez-Calera, I. J.; Meza-Laguna, V.; Gromovoy, T. Y.; Chavez-Uribe, M. I.; Basiuk, V. a.; Basiuk, E. V. Solvent-free functionalization of fullerene c60 and pristine multi-walled carbon nanotubes with aromatic amines. *Appl. Surf. Sci.* 2015, *328*, 45–62.
(35) Henao-Holguín, L. V.; Meza-Laguna, V.; Gromovoy, T. Y.; Basiuk, E. V.; Rivera, M.; Basiuk, V. A. Solvent-free covalent functionalization of fullerene c60and pristine multi-walled carbon nanotubes with crown ethers. *J. Nanosci. Nanotechnol.* 2016, *16* (6), 6173–6184.
(36) Basiuk, E. V.; Ramírez-Calera, I. J.; Meza-Laguna, V.; Abarca-Morales, E.; Pérez-Rey, L. A.; Re, M.; Prete, P.; Lovergine, N.; Álvarez-Zauco, E.; Basiuk, V. A. Solvent-free functionalization of carbon nanotube buckypaper with amines. *Appl. Surf. Sci.* 2015, *357*, 1355–1368.
(37) Basiuk, E. V; Basiuk, V. A.; Martínez, M. H.; Álvarez, E. z; Heano, V. L.; Puente, I. Noncovalent functionalization of graphene with ani(ii) tetraaza[14]annulene complex. *DaltonTransactions* 2014, *43*, 7413–7428.

(38) Alzate-Carvajal, N.; Acevedo-Guzmán, D. A.; Meza-Laguna, V.; Farías, M. H.; Pérez-Rey, L. A.; Abarca-Morales, E.; García-Ramírez, V. A.; Basiuk, V. A.; Basiuk, E. V. One-step nondestructive functionalization of graphene oxide paper with amines. *RSC Adv.* 2018, *8* (28), 15253–15265.

(39) Basiuk, E. V.; Santamaría-Bonfil, A.; Meza-Laguna, V.; Gromovoy, T. Y.; Alvares-Zauco, E.; Contreras-Torres, F. F.; Rizo, J.; Zavala, G.; Basiuk, V. A. Solvent-free covalent functionalization of nanodiamond with amines. *Appl. Surf. Sci.* 2013, *275*, 324–334.

(40) Rajesh, J. A.; Pandurangan, A. Lanthanum nickel alloy catalyzed growth of nitrogen-doped carbon nanotubes by chemical vapor deposition. *RSC Adv.* 2014, *4* (39), 20554–20566.

(41) Bhattacharjya, D.; Park, H. Y.; Kim, M. S.; Choi, H. S.; Inamdar, S. N.; Yu, J. S. Nitrogen-doped carbon nanoparticles by flame synthesis as anode material for rechargeable lithium-ion batteries. *Langmuir* 2014, *30* (1), 318–324.

(42) Kumar, N. A.; Nolan, H.; McEvoy, N.; Rezvani, E.; Doyle, R. L.; Lyons, M. E. G.; Duesberg, G. S. Plasma-assisted simultaneous reduction and nitrogen doping of graphene oxide nanosheets. *J. Mater. Chem. A* 2013, *1* (14), 4431–4435.

(43) Bassiouk, M.; Basiuk, V. A.; Basiuk, E. V.; Álvarez-Zauco, E.; Martínez-Herrera, M.; Rojas-Aguilar, A.; Puente-Lee, I. Noncovalent functionalization of single-walled carbon nanotubes with porphyrins. *Appl. Surf. Sci.* 2013, *275*, 168–177.

Outlook

The research presented in this dissertation describes non-covalent interactions of single-walled carbon nanotubes with four transition metal phthalocyanines and four rare earth double-decker phthalocyanines characterized using a set of analytical techniques. Additionally, it provides an overview of the self-assembly of the macrocycles on a curved surface, the influence of the nature of the coordinated metal, structural defects and chirality of the nanotubes on certain electronic properties and structural changes of the phthalocyanines on the nanotube by molecular simulation. Despite this, some experimental aspects remain to be performed as follows:

- To explore the self-assembly of transition metal phthalocyanines on the surface of nanotubes by STM and compare them with the results obtained by molecular mechanics. Characterisation by STM is complicated by the curved surface of the nanotubes and the fact that the functionalised nanotubes remain in agglomerates rather than individual nanotubes.

- The observed electrocatalytic activity of hybrids with cobalt and nickel phthalocyanine and the straightforward method of their synthesis opens the possibility of exploring the proposed materials for applications in anion exchange membrane water electrolysis (AEMWE).

- To study the surface of carbon nanotubes functionalised with rare-earth double-decker phthalocyanines by XPS, HRTEM and STM. Since the bisphthalocyanines are considered single-molecule magnets, it is of interest to determine the magnetic properties for possible application in spintronic devices.

List of publications

Carlos. U. Mendoza-Domínguez, **L. M. Bolívar-Pineda** and V. A. Basiuk. Effect of structural defects in graphene on the geometry and electronic properties of adsorbed lanthanide bispthalocyanines: A DFT study. Computational Materials Science. Submitted. **2023.**

L. M. Bolívar-Pineda, Carlos. U. Mendoza-Domínguez and V. A. Basiuk Adsoprtion of lanthanide double-decker phthalocyanines on single walled carbon nanotubes: structural changes and electronic properties as studied by density functional theory. Journal of Molecular Modeling. Submitted. **2022**.

C. Martínez-Florez, **L. M. Bolívar-Pineda** and V. A. Basiuk. Lanthanide bispthalocyanine single-molecule magnets: A DFT survey from lanthanum to lutetium. Materials Chemistry and Physics. **2022**. 287. 126271.

L. M. Bolívar-Pineda, M.I. Ontiveros, and V. A. Basiuk. Distorsion of yttrium bisphthalocyanine (YPc_2) upon noncovalent interaction with carbon nanotubes: A DFT study. Materials Today communications. **2021**. 28. 102667.

N. Alzate-Carvajal, **L. M. Bolívar-Pineda**, V. Meza-Laguna, V. A. Basiuk, E. V. Basiuk and E. A. Baranova. Oxygen evolution noncovalently functionalized with metal phthalocyanines. CHEMELECTROCHEM. **2020**. 7. 428-436.

L. M. Bolívar-Pineda and V. A. Basiuk. Interactions of metal phthalocyanines with Stone-Wales defects on single-walled carbon nanotubes: A theorical study. Journal of Applied Physics. **2020**. 127. 025302.

V. A. Basiuk. **L. M. Bolívar-Pineda,** V. Meza-Laguna, A. M. Glushenkov. B. J. Murdoch and E. V. Basiuk. N-doped carbon nanofibers from pyrolysis of free-base phthalocyanine. Diamond & Related Materials. **2020**. 105. 107812.

Conferences

2022, Reunión Mexicana de Fisicoquímica Teórica. Cuernavaca, Morelos, Mexico. Poster.

2022, 32nd International Conference on Diamond and Carbon Materials (ICDCM). Lisbon, Portugal. Poster.

2022, ZIAM PhD Colloquium. University of Groningen. Groningen, The Netherlands. Talk.

2022, Vlieland 2022. The Netherlands. Poster.

2022, International meeting on chemistry of carbon nanomaterials (ChemOnTube). San Sebastián, Spain. Awarded Poster.

2021, International Nanoscience Student Conference (INASCON). Tel Aviv, Israel. Poster.

2021, Webinar for the Amazonia. Universidad de la Amazonia. Florencia, Colombia. Talk.

2019, IX Simposio de Química Aplicada (IX SIQUIA) y I Congreso Internacional de Nanoquímica, Nanofísica y Nanomedicina (I CINNN) (Symposium and international congress). Armenia. Quindío, Colombia. Talk.

"Everything will be okey", Dad

Journal of Applied Physics ARTICLE scitation.org/journal/jap

Interactions of metal phthalocyanines with Stone-Wales defects on single-walled carbon nanotubes: A theoretical study

Cite as: J. Appl. Phys. **127**, 025302 (2020); doi: 10.1063/1.5128629
Submitted: 20 September 2019 · Accepted: 21 December 2019 ·
Published Online: 8 January 2020

Lina M. Bolivar-Pineda and Vladimir A. Basiuk[a)]

AFFILIATIONS

Instituto de Ciencias Nucleares, Universidad Nacional Autónoma de México, Circuito Exterior C.U, Ciudad de México 04510, Mexico

Note: This paper is part of the Special Topic on Defects in Semiconductors 2020.
[a)]**Author to whom correspondence should be addressed:** basiuk@nucleares.unam.mx

ABSTRACT

A density functional theory (DFT) analysis of the influence of Stone-Wales (SW) defect incorporated into an armchair and zigzag single-walled carbon nanotube (SWCNT) models (ANT and ZNT, respectively) functionalized noncovalently with unsubstituted nickel(II) and cobalt(II) phthalocyanines (MPcs, where M = Ni^{2+}, Co^{2+}) as representative Pcs was performed at the PBE-D/DNP level of theory. The data obtained (bonding and frontier orbital energies, geometries, charge and spin distribution, etc.) were compared with the DFT results for similar systems based on defect-free nanotube models. SW defect was incorporated into each nanotube model in different orientations with respect to SWCNT axis, depending on whether the (7,7) junction is tilted (ANT_SW-T and ZNT_SW-T models), parallel (ANT_SW-P), or perpendicular (ZNT_SW-P) with respect to the SWCNT axis. The formation energy of SW defect-containing SWCNTs depends on the defect orientation and nanotube chirality, decreasing in the order of ANT_SW-P > ZNT_SW-T > ANT_SW_T > ZNT_SW-P; in all cases, HOMO-LUMO gap narrowing was observed. Phthalocyanine molecules in MPc + SWCNT_SW complexes undergo strong bending distortion in order to increase the area of their contact with the nanotube sidewall. As compared to NiPc and CoPc dyads with defect-free nanotubes, formation energy ΔE decreased (that is, bonding strength increased) for three complexes, for four complexes an opposite effect was found, and in one case the variation was negligible. For most dyads, gap narrowing was observed, as compared to both defect-free complexes and SW defect-containing isolated nanotube models.

I. INTRODUCTION

The covalent and noncovalent functionalization of carbon nanotubes (CNTs), of both multiwalled and single-walled CNTs (MWCNTs and SWCNTs, respectively), with macrocyclic compounds such as phthalocyanines (Pcs), has been addressed in numerous studies due to a broad spectrum of applications such nanohybrid materials can offer. They include Li/$SOCl_2$ batteries,[1] nonlinear optical materials,[2] catalysts for the CO_2[3] and O_2[4,5] reduction reactions, photovoltaic and photoelectronic devices,[6–9] molecular spin-valves,[10] as well as electrochemical sensors for a variety of gases and solutes.[11,12] Performance of all the above functional materials and devices relies upon the particular distribution and position of Pc molecules on CNT sidewalls (especially in the case of noncovalent functionalization, when π-π stacking interactions between the aromatic rings are explored), the nature of central metal atoms in the Pc molecules, as well as the CNT size and chirality.[13] In this context, it is necessary to take into account that carbon nanotubes (as any graphene-derived materials) do not possess a perfect structure, since they usually include different types of topological defects incorporated during their growth (synthesis) or purification, irradiation, or chemical workup. The most important of them to mention are vacancies, Stone-Wales (SW) defects, octagon-pentagon pairs, as well as adatoms, all of which can significantly change the electrical, chemical, and mechanical properties of carbon nanomaterials.[14–18]

The formation of SW defect consists in the 90° rotation of only two carbon atoms (C–C) in the plane of hexagonal network,

creating two pairs of five-membered and seven-membered rings (5775). As a result, this defect is the only mechanism of defect generation that does not alter the nature of sp^2 backbone.[15,18–20] The abundance of SW defects might be desirable for many novel chemicals and electronic applications employing CNT network formation. The defect formation and its effects on the structural and electronic properties of nanotubes have been examined theoretically by a number of researchers[14,16,20–27] who have demonstrated that incorporation of SW defects can reduce or close the bandgap in large-bandgap CNTs and therefore increase their metallic character,[16,23,28] or on the contrary, it can induce bandgap opening in narrow-bandgap carbon nanotubes. Naturally, the number of SW defects and their orientation in the tube can further enhance the change from a semiconductor nanotube to a metallic conductor, as well as modify its chirality and diameter.[14,24] Other previous related studies showed that the nanotube stability increases as the defects are found closer to the open end of the single-walled carbon nanotube (SWCNT)[15] and that C–C bonds associated with SW defects are more reactive compared to those in a perfect hexagon,[20,27] thus enhancing the adsorption of ozone,[26] Ni atoms,[27] and alkanethiol molecules,[29] as well as in covalent bond formation when interacting with carboxyl groups,[30] methylene CH_2,[20] and amine groups.[31,32]

In spite of the importance of all the phenomena mentioned above, the relevant information on the influence of SW defects on structural, chemical, and physical properties for a wide variety of hybrid systems based on CNTs is relatively scarce and at times controversial. This is especially true for nanotubes noncovalently functionalized with such important compounds as Pcs. For example, a few studies (including our own reports) addressed the adsorption of Pcs on defect-free carbon nanotubes,[13,33–36] but only one was focused on the adsorption of free-base phthalocyanine (H_2Pc) on SW defect-containing SWCNT models.[19] One should specially emphasize that versatile experimental characterization of carbon nanohybrids noncovalently functionalized with organic compounds is not an easy task and commonly requires the participation of a large set of analytical techniques. Nevertheless, even in this case, the data provided are often insufficient to make well-grounded conclusions on the mechanisms of interaction of organic functionalizing species with a carbon nanomaterial.[35] Under such circumstances, it is necessary to employ theoretical tools, in particular, density functional theory (DFT) calculations, which are capable of providing valuable information on the geometry, stability, and electronic characteristics of Pc–carbon nanocluster (for example, carbon nanotubes[34–36] and fullerenes[37–39]).

The goal of the present paper was to carry out a DFT analysis of the influence of SW defect incorporated into armchair and zigzag SWCNT models functionalized noncovalently with unsubstituted nickel(II) and cobalt(II) phthalocyanines (MPcs, where M = Ni^{2+}, Co^{2+}) as representative Pcs. The data obtained are compared with our previous DFT results reported for similar dyads of MPcs with defect-free nanotube models.[34]

II. METHODS

To carry out a valid comparison of DFT calculations on MPc hybrid systems with SW defect-containing nanotube (MPc + SWCNT_SW) models, the same computational methodology was applied as in the previous analysis of MPcs adsorbed on defect-free SWCNT models (MPc + SWCNT).[34] The DFT functional of choice was Perdew-Burke-Ernzerhof (PBE) in combination with a long-range dispersion correction by Grimme (PBE-D), due to the need to account for dispersion interactions, which is very important in noncovalently bonded molecular systems. The software package employed for calculations was the Materials Studio 6.0 (from Accelrys, Inc.) including DMol^3 module, with numerical DNP basis set, having a polarization *d*-function added on all nonhydrogen atoms and a polarization *p*-function added on all H atoms. This approach has been successfully applied to describe different types of bonding (covalent and noncovalent) between tetraazamacrocyclic (including porphyrins and Pcs) and many other compounds with fullerene, graphene, graphene oxide, nanodiamond, and carbon nanotube models.[35,37–43] In all calculations, we used the "all-electron" core treatment with Fermi orbital occupation (no thermal smearing). A global orbital cutoff was set to 4.7 Å; "fine" quality and convergence criteria (energy gradient, 10^{-5} Ha; maximum force, 0.002 Ha/Å; maximum displacement, 0.005 Å; self-consistent field tolerance, 10^{-6}) were the settings we used for full geometry optimization and calculations of electronic parameters. For open-shell systems containing cobalt, the calculations were spin-unrestricted with maximum step size of 0.1 Å, whereas for closed-shell systems with nickel the latter was set to 0.02 Å and the calculations were spin-restricted.

The formation energies for SW defects were calculated as

$$\Delta E_{SW} = E_{def} - E_{perf}, \quad (1)$$

where E_{def} and E_{perf} are the total energies of the nanotube with and without defects, respectively.[44,45] The formation energies $\Delta E_{MPc+SWCNT}$ (hereafter, simply ΔE) for the noncovalent dyads of MPcs with SWCNT models were calculated using the following general equation:

$$\Delta E_{MPc+SWCNT} = E_{MPc+SWCNT} + (E_{SWCNT} + E_{MPc}), \quad (2)$$

where E_i is the corresponding absolute energy.

III. RESULTS AND DISCUSSION

A. Stone-Wales defects in SWCNT models

The carbon nanotube models employed to study the influence of SW defect on the noncovalent interactions of SWCNTs with CoPc and NiPc were derived from the armchair (5,5) and zigzag (10,0) nanotubes (ANTs and ZNTs, respectively), which are composed of 120 and 140 carbon atoms, and whose ends are capped with C_{60} and C_{80} (spherical with I_h symmetry) fullerene hemispheres, respectively.[34–36,46,47] The incorporation of SW defect in the nanotube is possible in two different ways depending on the defect orientation with respect to the SWCNT axis (Fig. 1). In one of them, the (7,7) junction is tilted with respect to the SWCNT axis; correspondingly, the defects are referred to as SW-T, and nanotube models as ANT_SW-T and ZNT_SW-T. The other two alternative models contain SW defect with the (7,7) junction parallel in ANT and perpendicular in ZNT with respect to the nanotube

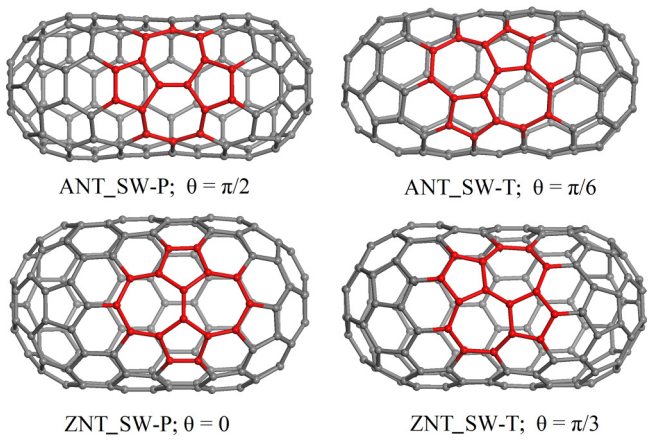

FIG. 1. Optimized geometries for armchair (ANT) and zigzag (ZNT) nanotube models, incorporating SW defects in parallel (in ANT) or perpendicular (in ZNT) and tilted orientation (SW-P and SW-T, respectively) of the (7,7) junction with respect to the nanotube axis. Two pentagonal and two heptagonal rings forming SW defect (16 carbon atoms) are highlighted in red. θ is the angle between the rotating C–C bond in the pristine SWCNT and the nanotube axis.

axis (SW-P notation in both cases; ANT_SW-P and ZNT_SW-P models). These nanocluster models were used in the recent analysis of adsorption of base-free phthalocyanine on SWCNTs with SW defects.[19]

In the present study, the structures of isolated four models of defective nanotubes were fully optimized, and their computed properties including geometric parameters (bond lengths, bond angles, and dihedral angles); formation energies; HOMO, LUMO, and LUMO-HOMO gap energies; and Mulliken charge distribution were compared to those of defect-free ANT and ZNT nanotubes. The calculated energy of SW defect formation for any particular CNT with diameter d increases monotonically with the angle θ made by the rotating C–C bond with the tube axis in perfect nanotube. Their values were calculated by taking into account the total energies as presented in Table I and those published previously for defect-free ANT and ZNT:[34] they are 71.02 (ANT_SW-P; θ = π/2), 49.39 (ANT_SW_T; θ = π/6), 63.84 (ZNT_SW-T; θ = π/3), and 33.93 kcal/mol (ZNT_SW-P; θ = 0). Pan *et al.*,[24] as well as Kabir and Van Vliet,[44] when considering a series of periodic nanotube models with chiralities (*n*,0) and (*n*,*n*), reported on a similar behavior as a function of the orientation of SW dislocation dipole θ and diameter. In particular, they indicated that the greater the diameter the greater the formation energy for any particular θ or orientation of SW defect, converging toward the value calculated for graphene (114.38 kcal/mol).[44] For the periodic nanotube models with particular chiralities (10,0) and (5,5), the same authors[44] reported SW defect formation energies between ca. 67 and 85 kcal/mol (depending on the angle θ), which can be considered rather close to our values, taking into account the differences between models (periodic vs cluster) and theoretical levels.

One of the first visible changes due to the incorporation of pentagons and heptagons as imperfections in the sp^2 hexagonal lattice is the distortion of curvature of the nanotubes[48,49] after

TABLE I. Total energies (in Ha) for separated components and noncovalent hybrids MPc + SWCNT_SW; formation energies ΔE (in kcal/mol) for the hybrids; HOMO, LUMO, and HOMO-LUMO gap energies (in eV); the shortest M···C_{SWCNT}, N···C_{SWCNT}, and C_{MPc}···C_{SWCNT} distances (in Å) between MPc and SWCNT; as well as N-M-N angles in MPc components, calculated by using PBE general gradient approximation functional with Grimme's dispersion correction in conjunction with DNP basis set.

System	E_{total}, Ha	ΔE, kcal/mol	E_{HOMO}, eV	E_{LUMO}, eV	E_{gap}, eV	M···C_{SWCNT}, Å	N···C_{SWCNT}, Å	C_{MPc}···C_{SWCNT}, Å	N-M-N, deg
ANT_SW-P	−4 569.096 332 1		−5.105	−4.789	0.316 (0.648)[a]				
ANT_SW-T	−4 569.130 818 1		−5.333	−4.757	0.576 (0.648)				
ZNT_SW-P	−5 330.818 355 5		−5.652	−5.563	0.089 (0.388)				
ZNT_SW-T	−5 330.770 686 4		−5.571	−5.443	0.128 (0.388)				
CoPc	−3 048.558 986 1		−5.043	−4.021	1.023				179.2, 179.3
NiPc	−3 174.108 102 3		−5.064	−3.601	1.463				179.4, 179.8
CoPc + ANT_SW-P	−7 617.713 681 1	−36.62 (−35.73)[a]	−4.923	−4.647	0.276 (0.609)	3.020 (2.969)[a]	3.050 (3.106)[b]	2.951	178.4, 179.2
CoPc + ANT_SW-T	−7 617.750 155 4	−37.87 (−35.73)	−5.134	−4.604	0.530 (0.609)	2.899 (2.969)	3.035[c]	3.018	179.1, 179.4
CoPc + ZNT_SW-P	−8 379.440 507 0	−39.64 (−40.03)	−5.370	−5.291	0.079 (0.065)	2.951 (3.069)	3.070 (3.091)[b]	3.042	175.6, 179.4
CoPc + ZNT_SW-T	−8 379.390 118 0	−37.93 (−40.03)	−5.308	−5.268	0.039 (0.065)	3.137 (3.069)	3.034 (3.091)[b]	2.941	178.1, 178.5
NiPc + ANT_SW-P	−7 743.255 949 9	−32.33 (−33.07)	−4.877	−4.599	0.278 (0.610)	3.141 (3.043)	3.085 (3.186)[b]	2.982	176.4, 179.8
NiPc + ANT_SW-T	−7 743.291 598 8	−33.06 (−33.07)	−5.118	−4.570	0.547 (0.610)	3.004 (3.043)	3.095[c]	3.085	177.2, 177.3
NiPc + ZNT_SW-P	−8 504.982 947 1	−38.00 (−37.61)	−5.375	−5.289	0.086 (0.070)	3.004 (3.106)	3.110 (3.133)[b]	3.051	174.2, 179.3
NiPc + ZNT_SW-T	−8 504.934 337 0	−37.41 (−37.61)	−5.325	−5.263	0.062 (0.070)	3.150 (3.106)	3.129[c]	3.007	177.3, 178.2

[a]For comparison, ΔE, E_{gap}, and M···C_{SWCNT} values obtained previously for the defect-free structures[34] are presented in parenthesis.
[b]The shortest distance N···C_{SWCNT} is formed with one of the γ-N atoms, with the shortest distance N···C_{SWCNT} for the N atom of MN_4 coordination sphere is given in parenthesis.
[c]The shortest distance N···C_{SWCNT} is formed with the N atom of MN_4 coordination sphere.

geometry optimization, as can be seen in Fig. 1. The presence of these defects generates an increase and/or decrease simultaneously in the diameter of nanotube within the same structure.[50,51] The variation in diameter depends on a particular orientation of [7,7] C–C bond, whereas in a defect-free closed-end nanotube, the diameter is a function of the size of the fullerene cap only. The correlation between the angle θ of rotating C–C [6,6] bond and ΔE_{SW} value can be explained qualitatively in terms of the curvature-induced rehybridization upon the defect formation. The Coulomb repulsion inside the nanotube increases with increasing curvature, leading to significant rehybridization within σ and π orbitals. The real hybridization in CNTs is intermediate between sp^2 and sp^3, that is, $sp^{2+\tau}$.[44] For a particular CNT with diameter d, the rehybridization τ decreases with increasing θ. For the defect-containing structure (SWCNT_SW), the local curvature at the site of C–C bond rotation increases for higher θ and correspondingly τ decreases, which in turn increases ΔE_{SW}[44] (Table I). Also, when comparing the length of the rotating C–C bond for nanotubes without and with the defect, we find it to be shorter in the latter case (Table II). The resulting difference ($\Delta b = b_{perf} - b_{def}$) is larger for larger θ values: ANT_SW-P ($\theta = \pi/2$) > ANT_SW-T ($\theta = \pi/6$) and ZNT_SW-T ($\theta = \pi/3$) > ZNT_SW-P ($\theta = 0$). Thus, the structures ANT_SW-T and ZNT_SW-P are lower in energy than ANT_SW-P and ZNT_SW-T models due to comparatively higher rehybridization. This phenomenon was observed for periodic nanotube models (with no closed ends).[44]

Another type of geometric parameters convenient for the characterization of structural changes due to SW defect is dihedral or torsion angles (ϕ). Figure 2 shows the fragments (16 carbon atoms) of geometries optimized for defect-free ANT and ZNT and those incorporating Stone-Wales defects in different orientations, along with the set of values of dihedral angles for each fragment. One can see that in defect-free ANT, the angles perpendicular to nanotube axis [ϕ_p; for example, C(1)–C(2)–C(3)–C(15) in ANT-P] have zero values, whereas "horizontal" angles [ϕ_h; exemplified by C(14)–C(1)–C(2)–C(3) in ANT-P] parallel to the nanotube axis vary between −21.9° and 21.9° for both perpendicular (ANT-P) and tilted orientations (ANT-T) of the central C–C bond. In the case of zigzag chirality (ZNT-P and ZNT-T), ϕ_p varies between −20.7° and 20.9° and ϕ_h between −5.6° and 6.8°. The introduction of an SW defect results in generally strong distortion of dihedral angles, which can be illustrated by the following ranges for each particular SWCNT model: for ANT_SW-P, ϕ_p between −48.5° and 48.8°, and ϕ_h between −26.6° and 26.7°; for ANT_SW-T, ϕ_p between −13.1° and 14.8°, and ϕ_h between −29.8° and 30.6°; for ZNT_SW-P, ϕ_p between −24.0° and 24.1°, and ϕ_h between −16.7° and 15.0°; for ZNT_SW-P, ϕ_p between −40.5° and 26.2°, and ϕ_h between −32.1° and 20.1°. At the same time, the corresponding bond angle distortion turns to be relatively small in all cases.

TABLE II. Carbon-carbon bond lengths before (SWCNT) and after rotation (SWCNT_SW) for zigzag and armchair nanotubes studied here. Bond lengths for different defect orientations are shown. The difference between bond lengths for pristine and defected structures is calculated as ($\Delta b = b_{perf} - b_{def}$).

SWCNT	[6,6] C–C bond, Å	SWCNT_SW	[7,7] C–C bond, Å	$\Delta b = b_{perf} - b_{def}$
ANT-P	1.4400	ANT_SW-P	1.3620	0.0780
ANT-T	1.4200	ANT_SW-T	1.3980	0.0220
ZNT-P	1.4150	ZNT_SW-P	1.3780	0.0370
ZNT-T	1.4280	ZNT_SW-T	1.3470	0.0810

The difference between HOMO and LUMO levels represents the bandgap energy.[50,52] Since bandgap is one of the critical parameters in the design of CNT-based systems for electronic applications, its behavior upon SW defect formation is of special interest.[43] Table I compares bandgap values for ANT and ZNT models without and with SW defects. Regardless of nanotube chirality and defect orientation, gap narrowing is observed. For SW-P models, gap energy decreases from 0.648 (defect-free ANT) and 0.388 eV (defect-free ZNT) to 0.316 and 0.089 eV, respectively; for the corresponding SW-T models, the decrease is less significant to 0.576 and 0.128 eV, respectively. In other words, the least effect is found for ANT_SW-T. Besides that, armchair (5,5) nanotube models studied systematically exhibit a broader bandgap as compared to zigzag (10,0) models, which can be attributed not only to chirality, but to diameter (and consequently sidewall curvature) as well.[51] One can add that in chemical terms, a smaller HOMO-LOMO gap implies higher reactivity and correspondingly lower stability.[14]

Incorporation of SW defect results in frontier orbital redistribution, which is illustrated by HOMO-LUMO plots in Fig. 3. Its extent depends on the particular nanotube model. The most pronounced changes can be found for HOMO of ANT_SW-P and LUMO of ANT_SW-T (as compared to the lobe shape in parent defect-free model), where the most visible feature is large lobes localized on SW defect.

One more aspect of interest we addressed is the atomic charge redistribution caused by the defect incorporation, by using the Mulliken population analysis. The results presented in Fig. 2 include both individual charges on the 16 carbon atoms participating in SW defect formation and the total charge on this structural unit. The latter is positive in all cases before C–C bond rotation, from 0.012 to 0.056 e. They remain to be positive for three of four defect-containing structures, with the largest changes found for ZNT_SW-T (from 0.026 to 0.054 e) and the smallest one for ANT_SW-P (from 0.028 to 0.030 e). In other words, in the above two transformations, electron acceptor properties increase. In the remaining two cases of ANT_SW-T and ZNT_SW-P, a gain in electrons is observed, from 0.012 to −0.016 e and from 0.056 to 0.031 e, respectively; that is, SW defect in ZNT_SW-P remains to be an electron acceptor, contrary to its counterpart in ANT_SW-T, whose total charge becomes negative (like it was found elsewhere[53] for 585 defects). Noteworthy, the C atoms of [7,7] junction in most SW defect units keep the positive sign of charge of [6,6] bond atoms in defect-free nanotubes with the exception of ZNT_SW-P. In the case of ANT_SW_P and ZNT_SW-T, the positive charge increased, whereas in ANT_SW-T it decreased. It is also interesting to note that heptagon ring atoms tend to gain electrons, whereas pentagons generally lose them. Such charge redistribution is a factor that influences the reactivity and explains the mechanisms of covalent and noncovalent interaction with various chemical species.[54,55]

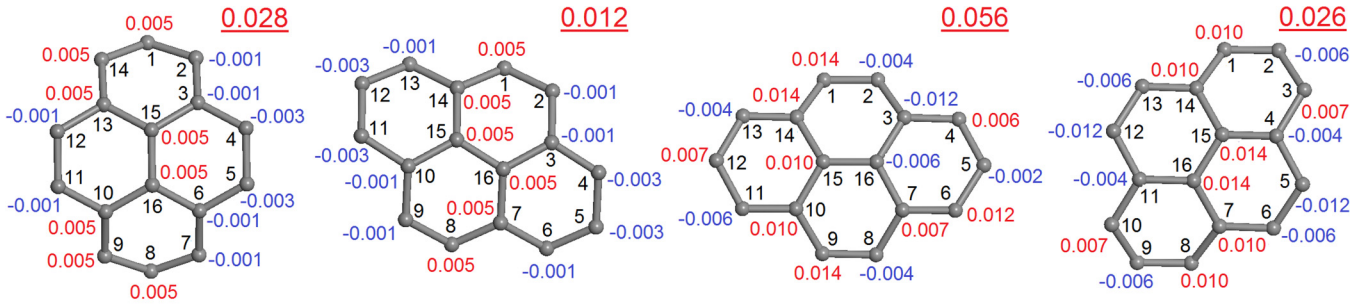

ANT-P

1-2-3-15	= 0.0
3-4-5-6	= 0.0
6-16-15-3	= 0.0
16-6-7-8	= 0.0
8-9-10-16	= 0.0
10-11-12-13	= 0.0
13-15-16-10	= 0.0
15-13-14-1	= 0.0
14-1-2-3	= 21.2
14-13-15-3	= 21.2
15-3-4-5	= 21.8
5-6-16-15	= 21.9
16-6-7-8	= 21.2
10-9-8-7	= 21.2
16-10-11-12	= 21.2
12-13-15-16	= 21.2
13-14-1-2	= -21.2
2-3-15-13	= -21.2
4-5-6-16	= -21.8
4-3-15-16	= -21.9
6-7-8-9	= -21.2
6-16-10-9	= -21.2
15-16-10-11	= -21.2
11-12-13-15	= -21.2

ANT-T

1-2-3-16	= 0.0
3-4-5-6	= 0.0
6-7-16-3	= 0.0
15-16-7-8	= 0.0
8-9-10-15	= 0.0
10-11-12-13	= 0.0
13-14-15-10	= 0.0
16-15-14-1	= 0.0
14-1-2-3	= 21.2
14-15-16-3	= 21.2
16-3-4-5	= 21.8
5-6-7-16	= 21.9
10-15-16-7	= 21.2
7-8-9-10	= 21.2
15-10-11-12	= 21.8
12-13-14-15	= 21.9
15-14-1-2	= -21.2
2-3-16-15	= -21.2
7-16-3-4	= -21.9
4-5-6-7	= -21.8
9-10-15-16	= -21.2
16-7-8-9	= -21.2
14-15-10-11	= -21.9
11-12-13-14	= -21.8

ZNT-P

1-2-3-16	= 16.9
3-4-5-6	= 6.8
7-16-3-4	= -12.7
15-16-7-8	= 20.9
9-10-15-16	= -19.3
13-14-15-10	= 19.5
11-12-13-14	= 20.7
15-14-1-2	= -18.5
14-1-2-3	= 0.8
14-15-16-3	= -0.6
16-3-4-5	= 2.1
5-6-7-16	= -5.6
7-8-9-10	= 0.4
10-15-16-7	= -0.7
15-10-11-12	= -0.7
12-13-14-15	= 0.4
2-3-16-15	= -17.0
1-14-15-16	= 18.4
4-5-6-7	= -5.1
3-16-7-6	= 14.3
16-7-8-9	= -20.7
15-10-9-8	= 19.5
14-15-10-11	= -19.3
13-12-11-10	= 20.9

ZNT-T

1-2-3-4	= 20.9
15-4-5-6	= 16.9
6-7-16-15	= 18.4
11-16-7-8	= 19.5
8-9-10-11	= 20.9
16-11-12-13	= 16.9
13-14-15-16	= 18.4
1-14-15-4	= 19.5
14-1-2-3	= -0.7
3-4-15-14	= 0.4
16-15-4-5	= 0.8
5-6-7-16	= -0.6
7-8-9-10	= -0.7
10-11-16-7	= 0.4
15-16-11-12	= 0.8
12-13-14-15	= -0.6
2-3-4-15	= -20.7
4-5-6-7	= -17.0
7-16-15-4	= -18.5
16-7-8-9	= -19.3
9-10-11-16	= -20.7
11-12-13-14	= -17.0
14-15-16-11	= -18.5
15-14-1-2	= -19.3

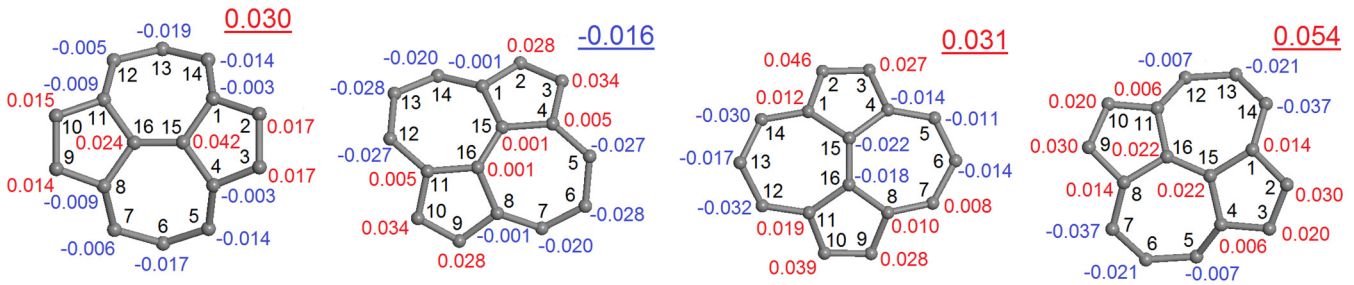

ANT_SW-P

1-2-3-4	= 0.0
3-4-15-1	= 15.1
15-4-5-6	= -24.7
6-7-8-16	= 25.6
11-16-8-9	= -13.6
8-9-10-11	= -0.1
16-11-12-13	= -25.7
13-14-1-15	= 24.8
2-3-4-15	= -9.1
15-1-2-3	= 9.0
4-5-6-7	= -26.6
7-8-16-15	= -48.5
16-8-9-10	= 8.2
10-11-16-8	= 13.5
11-12-13-14	= -26.5
16-15-1-14	= -45.2
4-15-1-2	= -15.1
5-6-7-8	= 26.4
8-16-15-4	= 2.3
9-10-11-16	= -8.1
11-16-15-1	= -2.5
15-16-11-12	= 48.8
12-13-14-1	= 26.7
16-15-4-5	= 13.5

ANT_SW-T

2-3-4-15	= -9.7
4-15-1-2	= 7.0
4-5-6-7	= -2.3
7-8-16-15	= 4.9
11-16-8-9	= 7.0
9-10-11-16	= -9.7
11-12-13-14	= -2.3
14-1-15-16	= 4.9
1-2-3-4	= 14.8
3-4-15-1	= 1.6
5-6-7-8	= -29.8
8-16-15-4	= -22.0
8-16-11-10	= 1.6
8-9-10-11	= 14.8
12-13-14-1	= -29.8
1-15-16-11	= 22.0
15-1-2-3	= -13.1
16-15-4-5	= -0.4
6-7-8-16	= 30.6
15-4-5-6	= 22.2
16-8-9-10	= -13.1
12-11-16-15	= -0.4
16-11-12-13	= 22.2
13-14-1-15	= 30.6

ZNT_SW-P

2-3-4-15	= 3.8
15-1-2-3	= -5.4
4-5-6-7	= 8.0
8-16-15-4	= 0.4
16-8-9-10	= -5.4
9-10-11-16	= 5.3
12-13-14-1	= -24.0
1-15-16-11	= 1.2
1-2-3-4	= 1.0
4-15-1-2	= 7.6
15-4-5-6	= 2.3
6-7-8-16	= -4.6
8-9-10-11	= 0.0
11-16-8-9	= 8.6
16-11-12-13	= 1.9
13-14-1-15	= -1.8
3-4-15-1	= -7.0
16-15-4-5	= -8.1
5-6-7-8	= -6.9
7-8-16-15	= 8.4
10-11-16-8	= -8.4
15-16-11-12	= -16.7
11-12-13-14	= 24.1
14-1-15-16	= 15.0

ZNT_SW-T

1-2-3-4	= -15.4
3-4-15-1	= 5.4
16-15-4-5	= 26.2
6-7-8-16	= -3.5
8-9-10-11	= -15.4
10-11-16-8	= 5.4
12-11-16-15	= 26.2
13-14-1-15	= -3.5
2-3-4-15	= 5.9
15-1-2-3	= 17.9
4-5-6-7	= 2.5
7-8-16-15	= -32.1
9-10-11-16	= 5.9
16-8-9-10	= 17.9
11-12-13-14	= 2.5
14-1-15-16	= -32.1
4-3-2-1	= -14.3
15-4-5-6	= -40.5
5-6-7-8	= 25.4
8-16-15-4	= 20.1
11-16-8-9	= -14.3
16-11-12-13	= -40.5
12-13-14-15	= 25.4
1-15-16-11	= 20.1

FIG. 2. Fragments (16 carbon atoms; other atoms are omitted for clarity) of geometries optimized for defect-free ANT and ZNT (top structures) and those incorporating Stone-Wales defects in different orientations (bottom structures), along with the values of dihedral angles (in degrees; only atom numbers without "C" symbols are shown for simplicity) and Mulliken population charges. The numbers in blue denote negative charges, and in red, positive charges of carbon atoms. The underlined values (upper right corner of each fragment) specify the total charge on the 16 atoms.

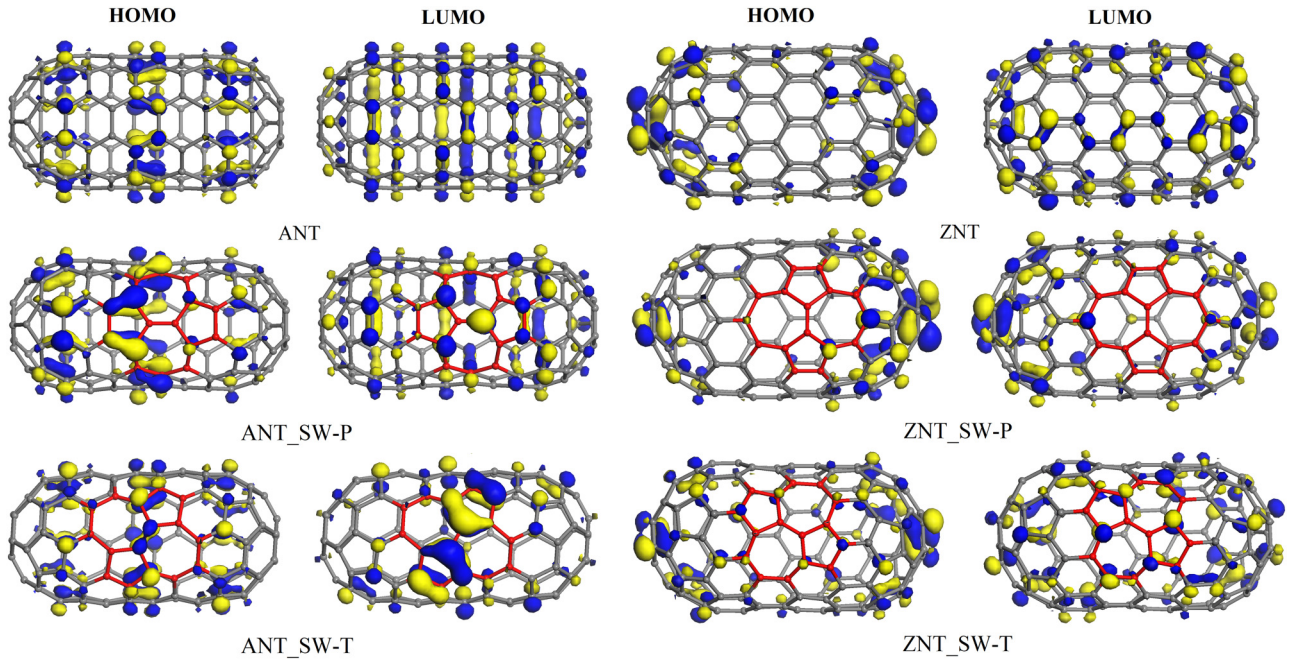

FIG. 3. HOMO and LUMO plots (isosurfaces at 0.03 a.u.) for Stone-Wales defect-containing armchair (ANT) and zigzag (ZNT) nanotube models. Two pentagonal and two heptagonal rings forming SW defect (16 carbon atoms) are highlighted in red.

B. MPc + SWCNT_SW dyads

The length of nanotube models with SW defect employed in our calculations is barely enough to accommodate one MPc molecule, with its overwhelming part contacting the tubular part. We made attempts to use longer models; however, this dramatically increased computational cost and, most importantly, caused serious convergence problems, especially in the case of open-shell systems. The choice of spin-restricted vs unrestricted calculations on MPc + SWCNT_SW hybrids was based on the spin state of the central metal atom in MPc component, that is, for Ni-containing systems closed-shell calculations were performed, whereas those including Co atoms were treated as open-shell systems.

To analyze the influence of SW defect on different parameters characterizing the noncovalent interaction of SWCNTs with CoPc and NiPc, a comparison was done with the results of previous DFT computations on the adsorption of the same phthalocyanines with defect-free ANT and ZNT.[34] The data obtained are summarized in Table I, which shows the total energies for separated components and noncovalent hybrids MPc + SWCNT_SW; formation energies ΔE for the hybrids; HOMO, LUMO, and HOMO-LUMO gap energies; the shortest $M\cdots C_{SWCNT}$, $N\cdots C_{SWCNT}$, and $C_{MPc}\cdots C_{SWCNT}$ distances between MPc and SWCNT; as well as N-M-N angles in metal phthalocyanine molecules.

The optimized geometries of all MPc + SWCNT_SW hybrids considered here exhibit the important feature typical for noncovalent complexes of phthalocyanines with a variety of nanotubes, including both cluster[19,35] and periodic models[13,33,56] of different diameters and chiralities, studied at different levels of DFT. It consists in strong bending distortion of a usually planar macrocyclic ring system in order to increase the area of its contact with the nanotube sidewall, as illustrated in Fig. 4. The degree of distortion can be quantitatively interpreted by comparing the values of

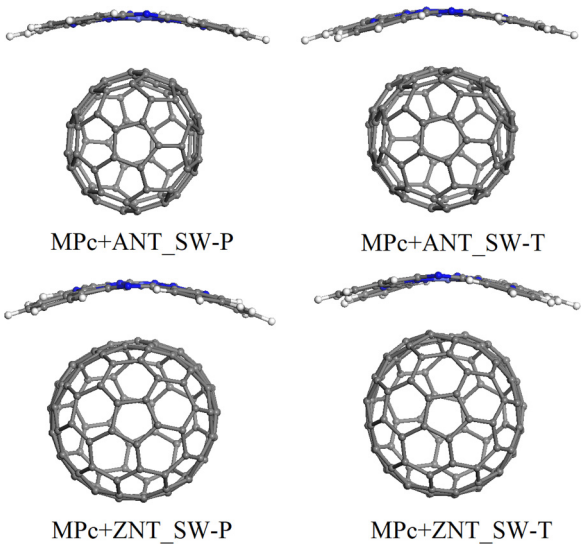

FIG. 4. Optimized geometries for noncovalent dyads MPc + SWCNT_SW, illustrating bending distorsion of the macrocycle ring plane.

N-M-N angles (diagonally opposite nitrogen atoms of the coordination sphere MN_4) in isolated MPc, which are approximately 179°–180°, with those in macrocycle adsorbed on SWCNT (Table I). One can see that the strongest distortion occurs for both dyads with ZNT_SW-P, where N-M-N angle decreases to 175.6° in CoPc and to 174.2° in NiPc. The strong noncovalent interactions between SWCNT and phthalocyanine make the central metal atom move slightly toward the nanotube sidewall out of the macrocyclic plane. This behavior is similar to the one observed for MPc dyads with defect-free SWCNT models,[34] including the fact that the distortion is generally greater on ZNT.

The shortest distance between metal and carbon atoms of nanotube defect ($M\cdots C_{SWCNT}$; Table I) spans from 2.899 Å in CoPc + ANT_SW_T to 3.150 Å in NiPc + ZNT_SW-T. Compared to the corresponding distances in hybrids with defect-free nanotubes, they tend to slightly increase for ANT_SW-P and ZNT_SW-T (roughly by 0.05–0.10 Å) and to decrease in the case of ANT_SW-T and ZNT_SW-P (by 0.07–0.12 Å). The longest $M\cdots C_{SWCNT}$ distances were found in the complexes of the zigzag model with SW-T defects of 3.137 Å for CoPc and 3.150 Å for NiPc. The nitrogen atoms forming shortest $N\cdots C_{SWCNT}$ distances can be those belonging to MN_4 coordination sphere or γ-N atoms

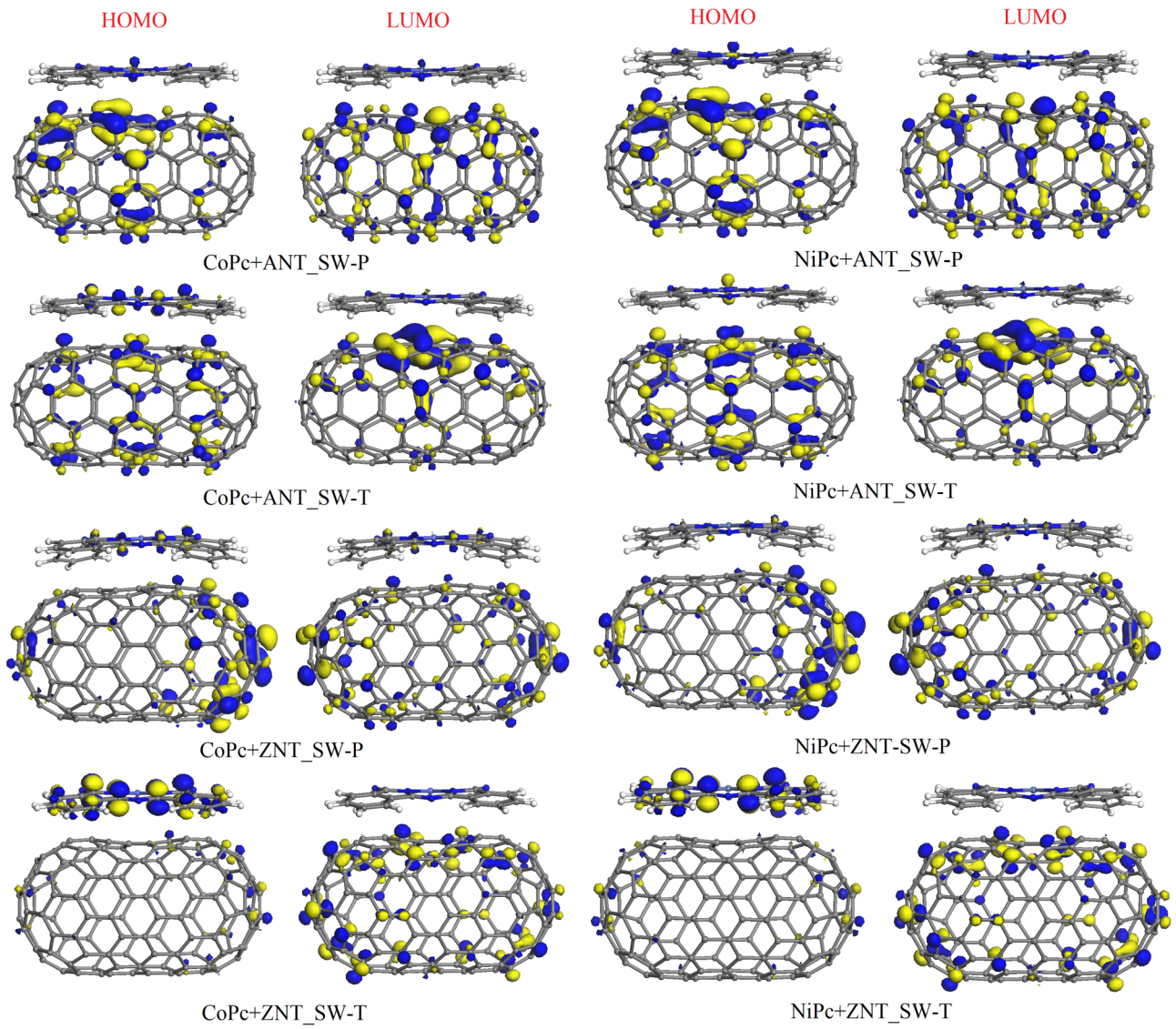

FIG. 5. HOMO and LUMO plots (isosurfaces at 0.03 a.u.) for the noncovalent complexes of CoPc and NiPc with Stone-Wales defect-containing armchair (ANT) and zigzag (ZNT) nanotube models.

(the latter situation being observed more frequently), with the separations of 3.035–3.186 or 3.034–3.110 Å, respectively. The closest contact between heteroatoms in MPc and SWCNT is not always M···C_{SWCNT}: in three complexes (CoPc + ZNT_SW-T, NiPc + ANT_SW-P, and NiPc + ZNT_SW-T) of eight, it is N···C_{SWCNT}. Furthermore, in half of the dyads, C_{MPc}···C_{SWCNT} turns to be the shortest separation: namely, for CoPc + ANT_SW-P (2.951 Å), CoPc + ZNT_SW-T (2.941 Å), NiPc + ANT_SW-P (2.982 Å), and NiPc + ZNT_SW-T (3.007 Å).

The most important issue we intended to address is how SW defect incorporation influences the strength of MPc bonding to SWCNTs. Compared to MPc complexes with defect-free nanotubes,[34] ΔE values decrease (that is, bonding strength increases) for three complexes CoPc + ANT_SW-P, CoPc + ANT_SW-T, and NiPc + ZNT_SW-P by 0.89, 2.14, and 0.39 kcal/mol, respectively (Table I). For four complexes CoPc + ZNT_SW-T, CoPc + ZNT_SW-P, NiPc + ANT_SW-P, and NiPc + ZNT_SW-T, an opposite effect was found, where ΔE increases by 0.39, 2.1, 0.74, and 0.2 kcal/mol. In the case of NiPc + ANT_SW-T, the variation is negligible (an increase by 0.01 kcal/mol). In general, binding for ANT models is stronger (by 1.25 kcal/mol for CoPc and 0.73 kcal/mol for NiPc) with SW_T defect than with SW-P, in contrast to ZNT nanotubes where the interaction with SW-P is stronger (by 1.71 kcal/mol for CoPc and 0.59 kcal/mol for NiPc) than that with SW_T, similar to the adsorption of free-base H_2Pc on the same nanotube models.[19] In other words, the interaction strength depends on both SWCNT chirality and orientation of SW defect, matching the order of defect formation energies of ANT_SW-P > ANT_SW_T and ZNT_SW-T > ZNT_SW-P (see Sec. III A).

We also analyzed the calculated HOMO, LUMO, and HOMO-LUMO gap energies (Table I) as well as the corresponding orbital plots (Fig. 5). Compared to the gap width calculated for CoPc and NiPc with defect-free SWCNTs,[34] SW defect-containing complexes exhibit variable behavior. For most (six of eight) dyads, gap narrowing can be observed, which is the least for NiPc + ZNT_SW-T (by 0.008 eV) and the most considerable one for CoPc + ANT_SW-P (by 0.333 eV). The two exceptions are complexes with ZNT_SW-P, where E_{gap} insignificantly increased by 0.014 (CoPc) and 0.016 eV (NiPc). In terms of magnitude of the change, the strongest one is found for both complexes with ANT_SW-P, for which gap energy reduces more than by half: by 0.333 (CoPc) and 0.332 eV (NiPc). When comparing gap energies for MPc + SCWNT_SW complexes with those of the respective isolated nanotube models, one can see that noncovalent bonding with phthalocyanines tends to narrow HOMO-LUMO gap; the exception is NiPc + ANT_SW-T, where E_{gap} increases insignificantly, by 0.001 eV. As a whole, regardless of the presence of defect, the gap is considerably broader for all hybrids with ANT than that with ZNT, matching E_{gap} of the corresponding isolated nanotube models. Further differences between them depend more on SW defect orientation, rather than on the central metal atom.

A closely related aspect is frontier orbital distribution. In CoPc and NiPc hybrids with defect-free ANT and ZNT, both HOMO and LUMO are localized mainly on carbon nanoclusters.[34] The presence of SW defect gives rise to variation in HOMO-LUMO distribution in all dyads (Fig. 5), but to a different degree, depending on a particular system. For most of them, the above pattern with HOMO and LUMO observed mainly on SWCNT remains. Additionally, a variable minor fraction of both orbitals can be found on MPc, being most evident for HOMO in CoPc + ANT_SW-T. Only the two complexes with ZNT_SW-T exhibit behavior contrasting with the others. Here, HOMO is shifted almost completely to MPc, and LUMO is localized exclusively (for the given isosurface value of 0.03 a.u.) on nanotube, which corresponds to the most common pattern for noncovalent hybrids of porphyrins and phthalocyanines with carbon nanoclusters (nanotubes and fullerenes), thus being indicative of weak charge transfer.[35,39]

Finally, for open-shell systems containing paramagnetic CoPc, we analyzed spin density plots (Fig. 6). The parent defect-free complexes CoPc + ANT and CoPc + ZNT[34] had two very different patterns of spin distribution. The "typical" one, in which unpaired electron density is localized exclusively on the central Co atom, was found only on the zigzag nanotube, whereas in the former, spin density was totally shifted to the donor nitrogen atoms. In the present study, all the dyads (including ANT-based ones) match the "typical" pattern of CoPc + ZNT.[34] An additional feature found in CoPc + ANT_SW-P, CoPc + ANT_SW-T, and CoPc + ZNT_SW-P is the appearance of minor spin lobes on carbon atoms of the

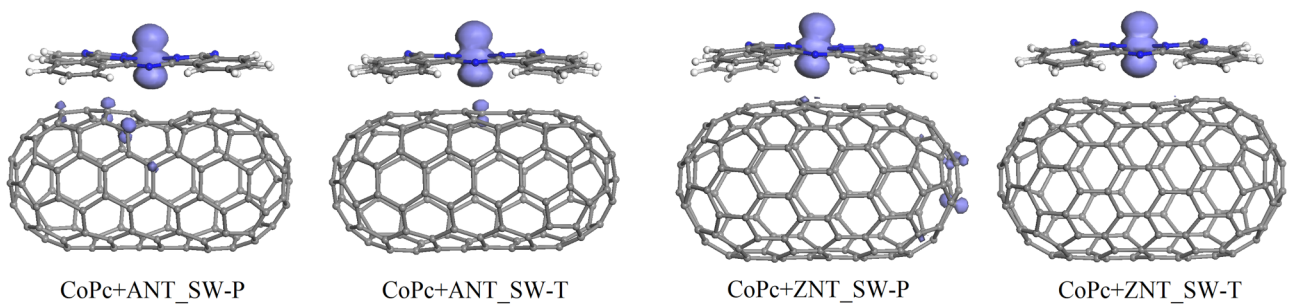

FIG. 6. Spin density plots (isosurfaces at 0.01 a.u.) for open-shell noncovalent complexes of CoPc with Stone-Wales defect-containing armchair (ANT) and zigzag (ZNT) nanotube models.

SWCNT model, at the site of contact between the interacting units (CoPc + ANT_SW-P and CoPc + ANT_SW-T) or even as far from it as at the closed nanotube cap (CoPc + ZNT_SW-P).

IV. CONCLUSIONS

The main results can be summarized as follows:

- The formation energy of SW defect-containing SWCNTs depends on the defect orientation and nanotube chirality, decreasing in the order of ANT_SW-P (71.02 kcal/mol) > ZNT_SW-T (63.84 kcal/mol) > ANT_SW_T (49.39 kcal/mol) > ZNT_SW-P (33.93 kcal/mol).
- In all cases, HOMO-LUMO gap narrowing is observed. For SW-P models, gap energy decreases from 0.648 (defect-free ANT) and 0.388 eV (defect-free ZNT) to 0.316 and 0.089 eV, respectively; for the corresponding SW-T models, the decrease is less significant, to 0.576 and 0.128 eV.
- Phthalocyanine molecules in MPc + SWCNT_SW complexes undergo strong bending distortion in order to increase the area of their contact with the nanotube sidewall, like in the case of similar dyads with defect-free nanotubes.[13,19,33–35,56]
- As compared to NiPc and CoPc complexes with defect-free nanotubes, formation energy ΔE decreases (that is, bonding strength increases) for three complexes CoPc + ANT_SW-P, CoPc + ANT_SW-T, and NiPc + ZNT_SW-P by 0.89, 2.14, and 0.39 kcal/mol, respectively. For four complexes CoPc + ZNT_SW-T, CoPc + ZNT_SW-P, NiPc + ANT_SW-P, and NiPc + ZNT_SW-T, an opposite effect was found, where ΔE increases by 0.39, 2.1, 0.74, and 0.2 kcal/mol. In the case of NiPc + ANT_SW-T, the variation is negligible (an increase by 0.01 kcal/mol).
- For most dyads, gap narrowing can be observed, which is the smallest for NiPc + ZNT_SW-T (by 0.008 eV) and the largest for CoPc + ANT_SW-P (by 0.333 eV), as compared to the defect-free systems. For the complexes with ZNT_SW-P, E_{gap} insignificantly increased by 0.014 (CoPc) and 0.016 eV (NiPc). As compared with gap energies of the respective isolated nanotube models, noncovalent bonding with phthalocyanines also tends to narrow the HOMO-LUMO gap.

ACKNOWLEDGMENTS

Financial support from the National Autonomous University of Mexico (UNAM, Grant No. DGAPA-IN203219) and from the National Council of Science and Technology of Mexico (CONACYT, Grant No. 250655) is greatly appreciated. L.M.B.-P. is indebted to the Doctorate Degree Program in Chemical Sciences of UNAM and to CONACyT for Ph.D. scholarship.

REFERENCES

[1]Z. Xu, H. Li, H. Sun, Q. Zhang, and K. Li, Chin. J. Chem. **28**, 2059 (2010).
[2]L. Zhang, H. Yu, L. Liu, and L. Wang, J. Compos. Mater. **48**, 959 (2014).
[3]X. Zhang, Z. Wu, X. Zhang, L. Li, Y. Li, H. Xu, X. Li, X. Yu, Z. Zhang, Y. Liang, and H. Wang, Nat. Commun. **8**, 14675 (2017).
[4]H. Li, Z. Xu, K. Li, X. Hou, G. Cao, Q. Zhang, and Z. Cao, J. Mater. Chem. **21**, 1181 (2011).
[5]X. Yan, X. Xu, Q. Liu, J. Guo, L. Kang, and J. Yao, J. Power Sources **389**, 260 (2018).
[6]L. Cao, H. Z. Chen, H. B. Zhou, L. Zhu, J. Z. Sun, X. Bin Zhang, J. M. Xu, and M. Wang, Adv. Mater. **15**, 909 (2003).
[7]S. Campidelli, B. Ballesteros, A. Filoramo, D. Díaz-Díaz, G. de la Torre, T. Torres, G. M. A. Rahman, C. Ehli, D. Kiessling, F. Werner, V. Sgobba, D. M. Guldi, C. Cioffi, M. Prato, and J.-P. Bourgoin, J. Am. Chem. Soc. **130**, 11503 (2008).
[8]G. Bottari, G. De Torre, D. M. Guldi, and T. Torres, Chem. Rev. **110**, 6768 (2010).
[9]K. Sanusi, E. K. Amuhaya, and T. Nyokong, J. Phys. Chem. C **118**, 7057 (2014).
[10]M. Urdampilleta, S. Klyatskaya, J. P. Cleuziou, M. Ruben, and W. Wernsdorfer, Nat. Mater. **10**, 502 (2011).
[11]P. Jha, M. Sharma, A. Chouksey, P. Chaturvedi, D. Kumar, G. Upadhyaya, J. S. B. S. Rawat, and P. K. Chaudhury, Synth. React. Inorg. Met.-Org. Nano-Met. Chem. **44**, 1551 (2014).
[12]Y. Wang, N. Hu, Z. Zhou, D. Xu, Z. Wang, Z. Yang, H. Wei, E. S. W. Kong, and Y. Zhang, J. Mater. Chem. **21**, 3779 (2011).
[13]P. O. Krasnov, T. V. Basova, and A. Hassan, Appl. Surf. Sci. **457**, 235 (2018).
[14]Q. X. Zhou, C. Y. Wang, Z. B. Fu, Y. J. Tang, and H. Zhang, Front. Phys. **9**, 200 (2014).
[15]F. Ding, Phys. Rev. B Condens. Matter Mater. Phys. **72**, 245409 (2005).
[16]J.-C. Charlier, Acc. Chem. Res. **35**, 1063 (2002).
[17]X. Qin, Q. Meng, and W. Zhao, Surf. Sci. **605**, 930 (2011).
[18]H. A. Johll and R. Low, Procedia Eng. **93**, 2 (2014).
[19]V. A. Basiuk and E. Chávez-Colorado, Diam. Relat. Mater. **97**, 107443 (2019).
[20]H. F. Bettinger, J. Phys. Chem. B **109**, 6922 (2005).
[21]Y. Miyamoto, A. Rubio, S. Berber, M. Yoon, and D. Tománek, Phys. Rev. B Condens. Matter Mater. Phys. **69**, 121413(R) (2004).
[22]L. G. Zhou and S.-Q. Shi, Appl. Phys. Lett. **83**, 1222 (2003).
[23]H. J. Choi, J. Ihm, S. G. Louie, and M. L. Cohen, Phys. Rev. Lett. **84**, 2917 (2000).
[24]B. C. Pan, W. S. Yang, and J. Yang, Phys. Rev. B Condens. Matter Mater. Phys. **62**, 12652 (2000).
[25]J. C. Charlier, T. W. Ebbesen, and P. Lambin, Phys. Rev. B **53**, 11108 (1996).
[26]S. Picozzi, S. Santucci, L. Lozzi, L. Valentini, and B. Delley, J. Chem. Phys. **120**, 7147 (2004).
[27]S. H. Yang, W. H. Shin, and J. K. Kang, J. Chem. Phys. **125**, 084705 (2006).
[28]S. Azadi, R. Moradian, and A. M. Shafaee, Comput. Mater. Sci. **49**, 699 (2010).
[29]S. Roh, J. Oh, Y. Choi, D. Sohn, W. Kim, C. Cho, W. Yi, J. Yoo, C. Lee, and J. Kim, J. Vac. Sci. Technol. B **22**, 1411 (2004).
[30]C. Wang, G. Zhou, H. Liu, J. Wu, Y. Qiu, B. L. Gu, and W. Duan, J. Phys. Chem. B **110**, 10266 (2006).
[31]M. A. Turabekova, T. C. Dinadayalane, D. Leszczynska, and J. Leszczynski, J. Phys. Chem. C **116**, 6012 (2012).
[32]B. Ben Doudou, J. Chen, A. Vivet, C. Poîlane, and M. Ayachi, Phys. E Low-Dimensional Syst. Nanostruct. **44**, 120 (2011).
[33]J. D. Correa and W. Orellana, Phys. Rev. B **86**, 125417/1 (2012).
[34]E. V. Basiuk, L. Huerta, and V. A. Basiuk, Appl. Surf. Sci. **470**, 622 (2019).
[35]E. Chávez-Colorado and V. A. Basiuk, Struct. Chem. **28**, 1765 (2017).
[36]V. A. Basiuk, L. J. Flores-Sánchez, V. Meza-Laguna, J. O. Flores-Flores, L. Bucio-Galindo, I. Puente-Lee, and E. V. Basiuk, Appl. Surf. Sci. **436**, 1123 (2018).
[37]V. A. Basiuk and E. V. Basiuk, Fuller. Nanotub. Carbon Nanostruct. **25**, 410 (2017).
[38]V. A. Basiuk and D. E. Tahuilan-Anguiano, Chem. Phys. Lett. **722**, 146 (2019).
[39]V. A. Basiuk and E. V. Basiuk, Fuller. Nanotub. Carbon Nanostruct. **26**, 69 (2018).
[40]V. A. Basiuk and L. V. Henao-Holguín, J. Comput. Theor. Nanosci. **11**, 1609 (2014).
[41]M. Bassiouk, E. Álvarez-Zauco, and V. A. Basiuk, Appl. Surf. Sci. **275**, 374 (2013).

[42]V. A. Basiuk, E. V. Rybak-Akimova, and E. V. Basiuk, RSC Adv. **7**, 17442 (2017).
[43]Y. Matsuda, J. Tahir-Kheli, and W. A. Goddard, J. Phys. Chem. Lett. **1**, 2946 (2010).
[44]M. Kabir and K. J. Van Vliet, J. Phys. Chem. C **120**, 1989 (2016).
[45]Q. Lu and B. Bhattacharya, Nanotechnology **16**, 555 (2005).
[46]V. A. Basiuk, Int. J. Quantum Chem. **111**, 4197 (2011).
[47]V. A. Basiuk, L. M. Bolivar-Pineda, V. Meza-Laguna, E. V. Rybak-Akimova, and E. V. Basiuk, J. Phys. Chem. Lett. **9**, 4420 (2018).
[48]J. H. Lehman, M. Terrones, E. Mansfield, K. E. Hurst, and V. Meunier, Carbon **49**, 2581 (2011).
[49]I. Zsoldos, Nanotechnol. Sci. Appl. **3**, 101 (2010).
[50]J. A. Talla, Comput. Condens. Matter **19**, e00378 (2019).
[51]P. Partovi-Azar and A. Namiranian, J. Phys. Condens. Matter **24**, 035301 (2012).
[52]H. Cui, Q. Li, G. Qiu, and J. Wang, MRS Commun. **8**, 189 (2018).
[53]J.-W. Li, Y.-Y. Liu, L.-H. Xie, J.-Z. Shang, Y. Qian, M.-D. Yi, T. Yu, and W. Huang, Phys. Chem. Chem. Phys. **17**, 4919 (2015).
[54]W. Zhang, W. C. Lu, H. X. Zhang, K. M. Ho, and C. Z. Wang, Carbon **110**, 330 (2016).
[55]C. N. He, W. Q. Huang, L. Xu, Y. C. Yang, B. X. Zhou, G. F. Huang, P. Peng, and W. M. Liu, Sci. Rep. **6**, 22267 (2016).
[56]L. Alvarez, F. Fall, A. Belhboub, R. Le Parc, Y. Almadori, R. Arenal, R. Aznar, P. Dieudonné-George, P. Hermet, A. Rahmani, B. Jousselme, S. Campidelli, J. Cambedouzou, T. Saito, and J. L. Bantignies, J. Phys. Chem. C **119**, 5203 (2015).

Materials Today Communications 28 (2021) 102667

Contents lists available at ScienceDirect

Materials Today Communications

journal homepage: www.elsevier.com/locate/mtcomm

Distortion of yttrium bisphthalocyanine (YPc_2) upon noncovalent interaction with carbon nanotubes: A DFT study

Lina M. Bolivar-Pineda, Mónica I. Sinecio-Ontiveros, Vladimir A. Basiuk [*,1]

Instituto de Ciencias Nucleares, Universidad Nacional Autónoma de México, Circuito Exterior C.U., Ciudad de México 04510, Mexico

ARTICLE INFO

Keywords:
Carbon nanotubes
Yttrium bisphthalocyanine
Noncovalent interaction
Distortion
Density functional theory

ABSTRACT

We performed a DFT analysis of the changes in geometry and some electronic properties of yttrium bisphthalocyanine YPc_2 when forming noncovalent hybrids with two single-walled carbon nanotube models, having armchair (ANT) and zigzag (ZNT) chiralities. The Perdew-Burke-Ernzerhof functional in combination with a long-range dispersion correction by Grimme (PBE-D) and the double numerical basis sets of variable size (DN, DND and DNP) was used. We found that YPc_2 molecule suffers binding distortion in order to increase the area of contact with nanotube sidewall, which enhances interaction between the two components. YPc_2 bonding is stronger with ZNT nanotube, of −43.8 kcal/mol, *vs.* −37.1 kcal/mol for YPc_2 + ANT complex (as calculated with DNP basis set). The height of bisphthalocyanine molecule in the dyads dramatically increases compared to that calculated for isolated YPc_2, whereas the calculated N-Y-N angles in YN_4 coordination change very insignificantly. In all cases, a minor HOMO-LUMO gap narrowing is observed. For YPc_2 + ANT the gap tends to match the one for isolated YPc_2, whereas for YPc_2 + ZNT it is much closer to the band gap of ZNT. The calculated HOMO, LUMO and spin density plots are analyzed.

1. Introduction

Phthalocyanine (Pc) and its substituted derivatives have attracted a great interest in recent years, owing to their unique physicochemical properties resulting from their extended aromatic conjugation system, as well as the ability to coordinate with a variety of metal ions [1]. Depending on the oxidation state and size (i.e., ionic radius) of the central metal (M), single-decker phthalocyanines (also called monophthalocyanines, MPcs), double-decker (bisphthalocyanines; MPc_2), triple-decker (M_2Pc_3), etc., structures can be formed. In addition, Pcs can have peripheral substituentes, which can be crucial to modify such properties as solubility [2–7].

The conventional single-decker phthalocyanines MPcs are 2D macrocyclic planar aromatic molecules (where Pc^{2-} is phthalocyaninate anion $C_{32}H_{16}N_8^{2-}$) with D_{4h} symmetry, which consists of four isoindole units connected through nitrogen atoms known as azomethine nitrogens (γ-N). The ligand Pc^{2-} is capable of binding various divalent transition (especially 3*d*) metal cations M(II) (Fig. 1a) [5–7]. Phthalocyanines are characterized by high thermal and chemical stability: many of them do not decompose up to 550 °C and can sublimate. Furthemore, they have the ability to self-assemble into stacks through π-π supramolecular interactions, and possess remarkable optical and catalytic properties [6–11].

The coordination with large metal ions such as rare earths comprising lanthanides (Ln), yttrium (Y) and scandium (Sc) produces double-decker structures, where the rare-earth ion is sandwiched between two phthalocyanine ligands, with face-to-face stacking, forming a structure with (ideally) D_{4d} symmetry (Fig. 1b) [12–14]. The neutral forms of these molecules are generally radical complexes (as confirmed by electron paramagnetic resonance studies). Bisphthalocyanines composed of a trivalent central metal M^{3+}, a dianionic macrocycle Pc^{2-} and a monoanionic radical ligand $Pc^{\bullet-}$ (that is, $[M^{3+}(Pc^{2-})(Pc^{\bullet-})]$) represent an important family of compounds not only due to the fact that they share unique properties of MPcs, but also because they can behave as single-molecule magnets (SMMs). The latter circumstance makes them especially attractive for the development of spintronic devices for high-density and energy-efficient information storage and processing [12,15–18]. SMMs are high-spin molecules with strong easy-axis magnetic anisotropy, exhibiting slow magnetization relaxation at a certain blocking temperature (T_B). One of the problems is that most SMMs, show

* Corresponding author.
E-mail address: basiuk@nucleares.unam.mx (V.A. Basiuk).
[1] ORCID: 0000-0001-7864-9203

https://doi.org/10.1016/j.mtcomm.2021.102667
Received 11 May 2021; Received in revised form 17 July 2021; Accepted 19 July 2021
Available online 21 July 2021

behavior similar to that of a macroscopic magnet, having T_B below 3 K [15,19,20]. Previous attempts to solve it focused on designing and using polymetallic transition complexes. Nevertheless, the increased total spins were usually accompanied by more symmetric structures that often counteract the anisotropies, creating a small energy barrier [19, 21]. As an alternative, rare-earth bisphthalocyanines, which are mononuclear complexes, display the highest T_B reported to date, up to approximately 54 K, as a consequence of their well-defined anisotropy, which is in turn caused by the ligand field created by the two Pc rings between which a magnetic ion is intercalated [19,20,22]. Moreover, the unpaired electron delocalized in MPc_2 makes the molecules suitable for ligand-mediated interactions with variable substrates [16]. The latter aspect was addressed in a number of studies, where MPc_2 complexes were deposited onto the surfaces of copper (111) [23], gold (111) [2, 24], nickel [20], and carbon nanomaterials comprising graphene [16, 25], highly oriented pyrolytic graphite [26] and carbon nanotubes (CNTs) [27–30].

The noncovalent functionalization of CNTs with MPc_2 complexes through π-π stacking is a way to refine the magnetic measurements and improve the magnetic bistability of SMMs by preserving the large spin magnetic moment of the rare-earth metal center and thus the general characteristics of SMMs, since (on the contrary) the adsorption on noble metal and ferromagnetic surfaces provokes variations in the magnetic properties of SMMs [27,31]. On the other hand, CNTs are especially interesting and important substrates due to their physical and electronic properties. However, unfortunately, the deposition of sandwich-type rare-earth Pc complexes on nanotubes (MPc_2 + CNTs) turns to be the least explored [27–30], including theoretically. Among earlier reports related to the hybrids of Pcs with carbon nanoclusters one should mention the density functional theory (DFT) studies on noncovalent MPc dyads with fullerenes [32,33] and single-walled carbon nanotubes (SWCNTs), in which both cluster [34–36] and periodic models with different nanotube diameters and chirality [37–39] at different DFT theoretical levels were employed. The most important general conclusion of all the above works is that the usually planar macrocyclic ring system of MPc suffers a strong bending distortion in order to increase the area of its contact with the fullerene cage or nanotube sidewall.

Hence, several questions can arise regarding the behavior of double-decker phthalocyanine analogues. In particular, does their deposition onto nanotube sidewalls alter the complex geometry? If it causes distortion, how significant this distortion is? Are both Pc ligands affected, and in the same way? Are electronic parameters (for example, HOMO, LUMO and spin density distribution) altered compared to that of isolated MPc_2 systems?

The possibility to answer the above questions by using experimental tools is minimal to null. One can only appeal to theoretical techniques, like in the case of conventional MPc complexes of 3*d* transition metals and free-base H_2Pc [34–39]. At the same time, the task becomes much more computationally demanding, for three reasons. First, the second heavy $C_{32}H_{16}N_8$ ligand unit is added to the model. Second, rare-earth metal atoms have a considerably larger number of electrons compared to 3*d* transition metals. And third, the calculations have to be necessarily spin-polarized. Besides that, the systems of major interest, which have especially pronounced magnetic properties, would be those incorporating central lanthanides (Eu, Gd and Tb). However, not only for these, but also for other lanthanides from Ce to Lu, the presence of *f*-electrons implies the existence of a series of almost degenerate states, dramatically complicating self-consistence field (SCF) convergence. Unless the inclusion of *f*-electron containing lanthanides is critical, a feasible solution capable of providing an insight as regards the conformational changes in question is the substitution of Ce–Lu atoms with rare earth elements, which do not have *f*-electrons, such as yttrium(III) and lanthanum(III) [40].

With the above considerations in mind, in the present report we attempted a DFT analysis of the changes in geometry and some electronic properties of yttrium bisphthalocyanine YPc_2 when forming noncovalent hybrids with two SWCNT models of different (armchair and zigzag) chiralities.

2. Computational methods

The computational technique of choice for all geometry optimizations and calculations of electronic parameters was the general gradient approximation (GGA) functional by Perdew-Burke-Ernzerhof (PBE) in combination with a long-range dispersion correction by Grimme (PBE-D; also referred to as PBE-D2) [41,42], due to the need to account for dispersion interactions, which is very important when noncovalently bonded molecular systems are analyzed. The PBE-D calculations were performed by using the numerical-based DFT module DMol^3 available as a part of the Materials Studio 6.0 software package from Accelrys, Inc. [43]. Three double numerical basis sets were tested to analize possible effects of the basis set size on the calculation accuracy (first of all, on the optimized geometries): DN, without polarization functions included (equivalent of 6–31G); DND, which adds a polarization *d*-function on all non-hydrogen atoms only (equivalent of 6–31G(d)); and DNP, which has a polarization *d*-function added on all non-H atoms, as well as a polarization *p*-function added on all hydrogen atoms (equivalent of 6–31G(d, p)). In addition to different numerical basis sets employed in DMol^3, another important adjustable parameter is the global orbital cutoff (or real space cutoff). The global orbital cutoff is applied to the generation of the numerical basis sets to limit the range of the numerical integrations and reduce the computational cost, as justified by the fact that the charge density decreases quickly as the distance from an atomic nucleus increases [44]. The real space cutoff values used in the present study were 4.2, 4.8 and 5.6 Å for DN, DND and DNP basis set, respectively, as defined by the presence of Y atom (electron configuration [Kr] $4d^15s^2$). The calculation quality corresponding to the use of DN, DND and DNP basis set is referred to as 'coarse', 'medium' and 'fine'. In the

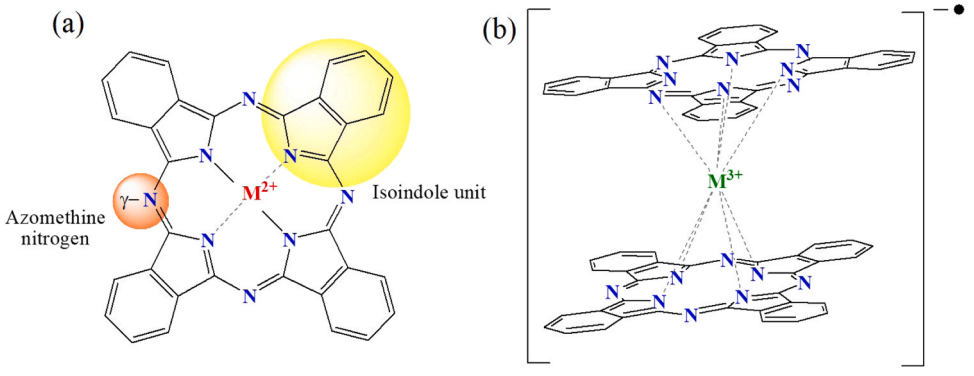

Fig. 1. Structure of (a) M(II) monophathalocyanine (b) M(III) bisphthalocyanine.

latter case (DNP) it implies the following convergence criteria: energy gradient, 10^{-5} Ha; maximum force, 0.002 Ha/Å; maximum displacement, 0.005 Å; self-consistent field (SCF) tolerance, 10^{-6}. This set of computational parameters is similar to the one used previously to describe different types of bonding (both noncovalent and covalent) between phthalocyanines and carbon nanotubes and other carbon allotropes (see, for example, [9,10,34,36,45]). All the calculations were spin-unrestricted, and the core treatment was all-electron with Fermi orbital occupation. The maximum step size allowed was 0.3 Å.

The formation energies $\Delta E_{YPc2+SWCNT}$ (ΔE hereafter for simplicity) for the noncovalent hybrids of YPc_2 with SWCNT models were calculated according to the general equation:

$$\Delta E_{YPc2+SWCNT} = E_{YPc2+SWCNT} - (E_{YPc2} + E_{SWCNT})$$

where E_i is the corresponding absolute energy.

3. Results and discussion

3.1. Yttrium bisphthalocyanine YPc_2

Prior to the analysis of yttrium bisphthalocyanine behavior on the surface of carbon nanotubes via noncovalent functionalization, we analyzed the geometry of isolated YPc_2 molecule optimized by the PBE-D functional in conjunction with all three double numerical basis sets available in the DMol^3 module (DN, DND and DNP), for comparison. (Cartesian coordinates for optimized geometries of all the structures studied are listed at the end of Electronic Supplementary Information (ESI).) While for this particular system no SCF convergence problems were expected when employing the largest one, DNP, they might arise in the case of other rare-earth phthalocyanines (in particular, for central lanthanides having several unpaired *f*-electrons), especially when their noncovalent bonding with extended carbon nanoclusters (SWCNT and graphene sheet models) is studied. In that case, a basis reduction to DND and even DN might be desirable to unavoidable, under the condition that it can yield sufficiently accurate/realistic geometry (unfortunately, systematic information on how the choice of basis set influences the results of this sort is relatively scarce [46,47]).

The calculated structural parameters analyzed for isolated YPc_2 (Tables 1 and S1 of ESI) included molecular size (width), height, rotation angle between the two Pc ligands, and N-Y-N angles, which were compared to the corresponding values obtained experimentally by X-ray diffraction (XRD) [48]. Also, the HOMO, LUMO, and HOMO-LUMO band gap energies (E_{gap}; Tables 2 and S2 of ESI) for the double-decker phthalocyanine were computed, as well as spin density distribution in YPc_2 was plotted.

As an example, Fig. 2 shows the optimized structure of YPc_2 obtained when using DNP basis set. For all basis sets, the Y^{3+} ion is sandwiched between two phthalocyanine ligands rotated by an angle of 45.0° with respect to each other, forming a characteristic staggered structure (Fig. 2a). In other words, the difference with the XRD structure in these terms, where the rotation angle is 44.9° [48], is negligible. Other basis set effects on the YPc_2 geometry can be appreciated from Table S3 of ESI. The central atom coordinates with eight isoindole nitrogen atoms (N_{iso}), giving rise to a pseudo-4-fold axis perpendicular to the Pc rings and a distorted square antiprismatic coordination environment around the metal center. This distortion is a consequence of the non-equal bond distances between Y atom and each of the eight N_{iso} atoms. The Y-N_{iso} bond lengths obtained with all basis sets employed are slightly longer (within 0.03 Å only) compared to the experimental values by XRD: while the latter are found in the range of 2.395–2.412 Å, the ranges for

Table 2
Total energies (in Ha) for isolated components and noncovalent hybrids YPc_2 + SWCNT (SWCNT = ANT, ZNT), formation energies ΔE (in kcal/mol) for the hybrids, HOMO, LUMO and HOMO-LUMO gap energies (in eV), calculated by using PBE GGA functional with Grimme's dispersion correction in conjunction with DNP basis set.

System	E_{total} (Ha)	ΔE (kcal/mol)	E_{HOMO} (eV)	E_{LUMO} (eV)	E_{gap} (eV)
ANT	-4569.1629441		-0.197	-0.173	0.643
ZNT	-5330.8185875		-0.208	-0.205	0.080
YPc_2	-6665.1029617		-0.169	-0.164	0.142
YPc_2 + ANT	-11234.324974	-37.1	-0.176	-0.171	0.140
YPc_2 + ZNT	-11995.991383	-43.8	-0.188	-0.186	0.059

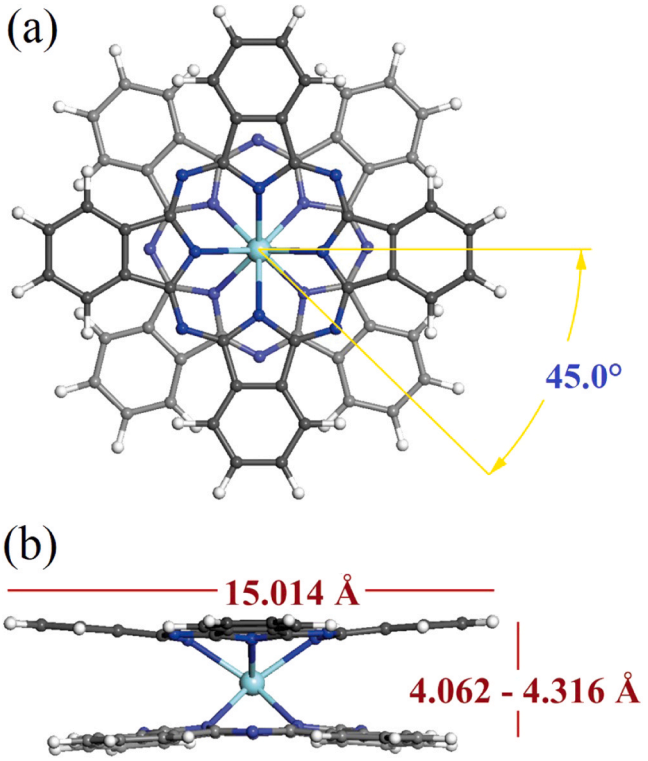

Fig. 2. Top (a) and side (b) views of YPc_2 geometry optimized by using PBE GGA functional with Grimme's dispersion correction in conjunction with the DNP basis set, showing its size (i.e., width), height and twisted angle between the two Pc macrocycles. Atom colors: gray, carbon; white, hydrogen; deep blue, nitrogen; light blue, yttrium.

Table 1
Size (in Å), height (in Å) and N-Y-N angles (in degrees) for isolated YPc_2 molecule and in the noncovalent hybrids YPc_2 + SWCNT (SWCNT = ANT, ZNT), as well as the shortest $Y\cdots C_{SWCNT}$, $\gamma\text{-}N\cdots C_{SWCNT}$ and $C_{\ddot{Y}Pc}C_{SWCNT}$ distances (in Å) between YPc_2 and SWCNT, calculated by using PBE GGA functional with Grimme's dispersion correction in conjunction with DNP basis set. Structural parameters for YPc_2 crystal structure obtained by X-ray diffraction (XRD)[48] are specified for comparison.

System	Size (Å)	Height (Å)	N-Y-N (°)	$Y\cdot C_{SWCNT}$ (Å)	$\gamma\text{-}N\cdots C_{SWCNT}$ (Å)	$C_{\ddot{Y}Pc2}C_{SWCNT}$ (Å)
YPc_2 (XRD)	14.727	2.351–5.094	109.7–110.6			
YPc_2	15.014	4.062–4.316	110.9–111.0			
YPc_2 + ANT	14.805; 15.015	4.297–4.930	110.8–112.2	4.430	3.046	3.097
YPc_2 + ZNT	14.860; 15.027	4.116–4.867	110.8–112.5	4.526	3.095	2.986

DN, DND and DNP basis sets are 2.407–2.422, 2.412–2.417 and 2.410–2.413 Å, respectively (Table S3).

Another important parameter is the height of YPc_2 molecule, which is measured as the distance between peripheral hydrogen atoms belonging to opposite Pc ligands. Depending on the basis set, it comprises the range of 4.151–4.803 Å for DN, 4.020–4.441 Å for DND, and 4.062–4.316 Å for DNP, compared to 2.351–5.094 Å in the experimentally reported structure [48] (Tables 1 and S1 of ESI). The disparity of the height values in each case is a consequence of the repulsive interaction between the two macrocycles, in particular between the benzene rings. On the other hand, it is evidently less significant in the calculated structures, which can be explained by the absence of adjacent YPc_2 molecules, contrary to the crystalline phthalocyanine. From Fig. 2b one can also see that the two Pc ligands have somewhat different shapes: one macrocycle is more domed (likely due to Y-N_{iso} bond contraction and electronic repulsion between the o-phenylene rings, which leads to a bending of the isoindole units), and the other Pc ligand is flatter [49]. Viewed in this way, the staggered conformation of YPc_2 reduces the overlap between the two electronic clouds and the electrostatic repulsion, leading to a D_{4h} geometry as a result of the Jahn-Teller effect, which forces the molecule to have a less symmetric stable state. As regards the size (or width; Fig. 2b) of YPc_2 molecule, defined as the maximum distance between the two hydrogen atoms at opposite o-phenylene moieties of Pc rings [48,49], it is overestimated in all cases (Tables 1 and S1 of ESI). The difference with respect to the experimental value from XRD (14.727 Å) increases as the basis set size decreases, that is, in the series of DN (15.056 Å) > DND (15.016 Å) > DNP (15.014 Å).

The degree of bending of each Y-coordinated Pc unit can be quantitatively evaluated from the angles N-Y-N formed between the metal atom and two diagonally opposite nitrogen atoms N_{iso} of YN_4 coordination sphere. Due to the minor asymmetry caused by the Jahn-Teller effect, the N-Y-N angles slightly vary in both XRD and calculated structures. From Table 1 one can see that the experimental values are found in the range of 109.7–110.6°, and the theoretical ones are always higher, of 113.3–113.7° for DN, 110.7–110.9° for DND, and 110.9–111.0° for DNP. Even though the strongest deviation from the experimental parameters is observed for DN basis set, the improvement due to the use of higher-quality DND and DNP basis sets is not dramatical, similarly to the cases of other geometrical characteristics discussed above.

The general computation quality for YPc_2 geometry can be assessed through a graphical comparison of calculated versus experimental bond lengths and angles, as it is shown in Fig. 3 and S1 of ESI. One can see that the correlation coefficients (CCs) are rather high, where the lowest value of 0.995 was found for bond angles calculated when using DN basis set, with a minor improvement to 0.997 in the case of DND and DNP. On the other hand, CC values of 0.999 for bond lengths were obtained by employing all three basis sets.

When analyzing frontier orbital energies of YPc_2 (Tables 2 and S2 of ESI), one can see that the choice of basis set has a negligible effect. In particular, the calculated HOMO-LUMO gap energy is 0.140 eV for DN, and 0.142 eV for both DND and DNP basis sets. Likewise, the patterns of HOMO-LUMO distribution in YPc_2 (exemplified in Fig. 4 for DNP basis set) are essentially identical for all theoretical levels tested. No contribution to both HOMO and LUMO was found from the central Y atom, but instead the main lobes are localized on the carbon atoms of isoindole pentagonal rings. This feature agrees well with experimental and theoretical data reported elsewhere [50].

The existence of unpaired electron delocalized over Pc macrocycles gives rise to a crucial difference between spin density plots obtained here for YPc_2 (again, identical for all basis sets; exemplified in Fig. 4 for DNP) and the ones obtained for conventional single-decker phthalocyanine complexes with 3*d* transition metals [9,32,33,36,45]. As a matter of fact, the spin distribution presented in Fig. 4 is a close match of the HOMO-LUMO plots discussed above. From comparison between the two types of plots it appears that the HOMO and LUMO lobes coincide with the 'spin-up' electron density. At the same time, additional 'spin-down' density (orange lobes) is clearly seen on all nitrogen (both N_{iso} and γ-N) atoms.

3.2. YPc_2+SWCNT hybrids

For the simulation of the noncovalent interactions between YPc_2 and SWCNTs, we employed two fulleroid models of different chirality, same as the ones used in our previous works [9,34–36,45]: armchair (5,5) and zigzag (10,0), referred to as ANT and ZNT (Fig. 5), which are composed of 120 and 140 carbon atoms, and whose ends are capped with C_{60} and I_h-C_{80} fullerene hemispheres, respectively. The geometries of isolated ANT and ZNT models were optimized by applying all three basis sets. Comparison of their diameter and length (Table S4 of ESI) shows that the dimensions calculated are insignificantly larger when DN is used, being essentially identical for the cases of DND and DNP. In particular, as computed with DNP basis set, the diameter and length for ANT are 7.060 and 14.123 Å, respectively, and for ZNT, 7.965 and 14.293 Å. That is, the length of both nanotube models is barely sufficient to accommodate one YPc_2 molecule.

The main geometric and electronic parameters for noncovalent YPc_2 + ANT and YPc_2 + ZNT complexes calculated by varying the basis set are summarized in Tables S1 and S2 of ESI, with Tables 1 and 2 extracting the values obtained by using DNP. As it was observed previously [9,34–38,45], one of the typical structural features of noncovalent hybrids of *3d* transition metal(II) phthalocyanine complexes (M(II) = Mn, Fe,

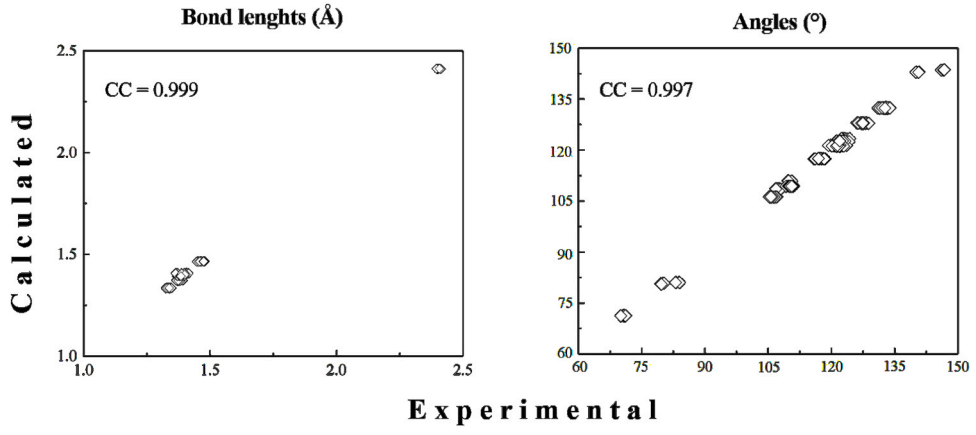

Fig. 3. Graphic interrelation between the bond lengths and angles in YPc_2 molecule, obtained by computer modeling (DNP basis set) and their experimental counterparts from XRD diffraction data. CC, correlation coefficient.

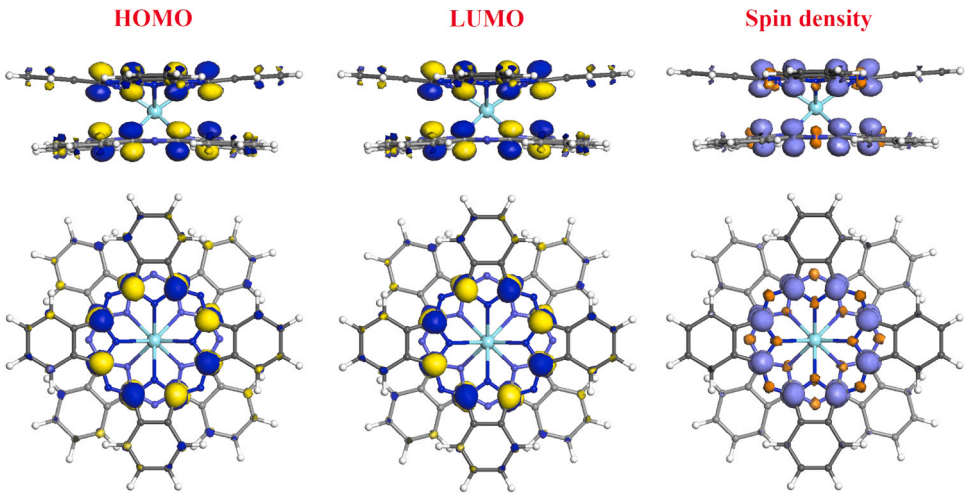

Fig. 4. HOMO, LUMO (isosurfaces at 0.03 a.u.; side and top views) and spin density plots (isosurfaces at 0.01 a.u.) for yttrium double-decker phthalocyanine, calculated by using PBE GGA functional with Grimme's dispersion correction in conjunction with DNP basis set. (Same plots were obtained when DN or DND basis sets are used.) In spin density plots, violet and orange lobes correspond to spin-up and spin-down electrons, respectively.

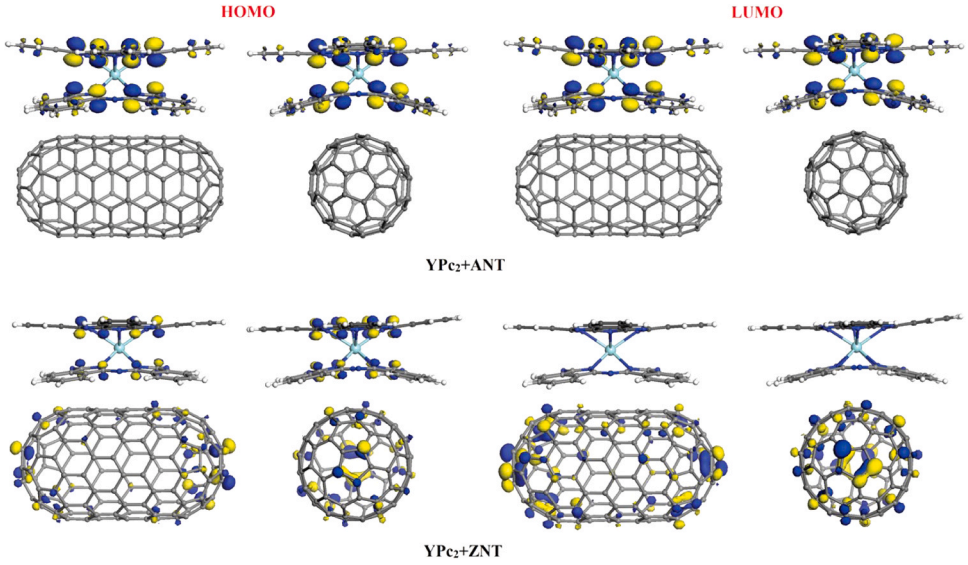

Fig. 5. HOMO and LUMO plots (isosurfaces at 0.03 a.u.; two side views) for YPc_2 + ANT and YPc_2 + ZNT noncovalent complexes, calculated by using PBE GGA functional with Grimme's dispersion correction in conjunction with DNP basis set. (Same plots were obtained when DN or DND basis sets are used.).

Co, Ni, Cu, Zn) with SWCNTs is the strong bending distortion of macrocyclic system, by means of which the area of Pc contact with nanotubes sidewall is increased. This bending due to non-parallel π-π interactions between the two extended π-systems [51] ocurrs to a variable degree, depending on the central atom. In the present case of YPc_2 adsorption on ANT and ZNT models, both macrocyclic rings of the bisphthalocyanine suffer distortion, which can be appreciated from Fig. 5. The degree of bendidng can be quantitatively interpreted by comparing the size, height and N-Y-N angles for isolated YPc_2 molecule and for that forming YPc_2 + SWCNT hybrids.

The size of isolated YPc_2 molecules optimized with all basis sets is approximately 15.0 Å (Tables 1 and S1 of ESI), which refers to both phthalocyanine ligands. For YPc_2 + SWCNT complexes, the two Pc units exhibit notably different sizes. The span of the ligand contacting ANT and ZNT sidewall decreases to 14.8–14.9 Å (the first values in Tables 1 and S1), as a result of attraction of *o*-phenylene moieties to nanotube surface, leading to a more pronounced domed geometry of Pc macrocycle compared to that observed in isolated YPc_2. In the particular case of ANT and ZNT models employed, the nanotube diameter (7.060 and 7.965 Å, respectively, for DNP basis set) is considerably smaller than the size of phthalocyanine ligand. Of the two YPc_2 + SWCNT complexes, the one formed by ANT exhibits somewhat stronger bending (regardless of the basis set size), evidently due to its smaller diameter compared to that of ZNT. As to the second, 'external' Pc ligand, its size remains approximately the same, of 15.0 Å (the second values in Tables 1 and S1), though visually it makes an impression of becoming flatter than before complexation (Figs. 5 and 6 *versus* Fig. 4).

The height of bisphthalocyanine molecule in YPc_2 + SWCNT dyads dramatically increases compared to that calculated for isolated YPc_2, for example, from 4.062–4.316 to 4.297–4.930 (YPc_2 + ANT) and 4.116–4.867 Å (YPc_2 + ZNT), as obtained at the highest theoretical level. On the other hand, the calculated N-Y-N angles in YN_4 coordination change very insignificantly: at the same PBE-D/DNP level of theory, they increase from 110.9° to 111.0° in isolated YPc_2 to 110.8–112.2° in YPc_2 + ANT and 110.8–112.5° in YPc_2 + ZNT (compared to 109.7–110.6° found by XRD in bisphthalocyanine crystals). In these terms, there is almost no difference between the two hybrids.

Some other structural and electronic characteristics of YPc_2 +

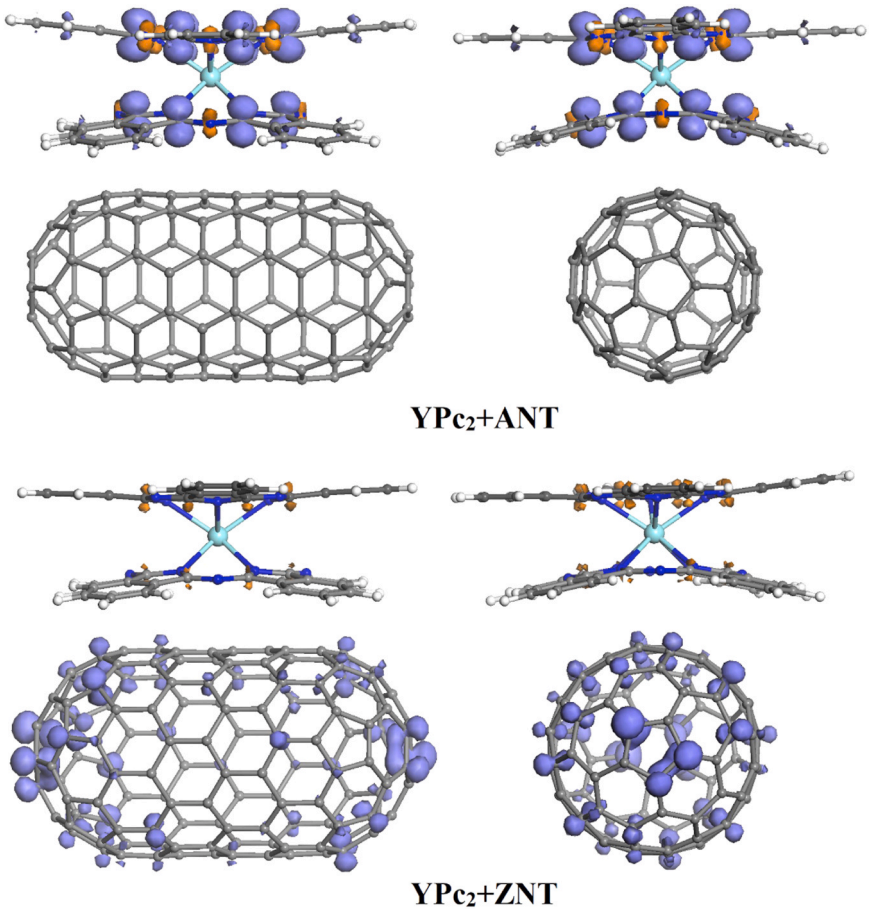

Fig. 6. Spin density plots (isosurfaces at 0.01 a.u.; two side views) for YPc_2 + ANT and YPc_2 + ZNT noncovalent complexes, calculated by using PBE GGA functional with Grimme's dispersion correction in conjunction with DNP basis set. (For YPc_2 + ANT, same plots were obtained when DN or DND basis sets are used.) Violet and orange lobes correspond to spin-up and spin-down electrons, respectively.

SWCNT dyads do depend on the nanotube model, for example, the shortest distances between the interacting components. Comparing the distances obtained with each basis set, all close approaches are systematically shorter when computed with DN. For YPc_2 + ANT, regardless of the basis set, the closest approach (Table S1) is between the nanotube carbon atoms and azomethine nitrogen atoms of Pc (γ-N$\cdots$C$_{SWCNT}$), whereas for YPc_2 + ZNT the shortest distance is found between the carbon atoms (C$_{YPc2}$C$_{SWCNT}$). The attraction between SWCNT and bisphthalocyanine cause the yttrium atom to approach nanotube sidewall at Y$\cdots$C$_{SWCNT}$ distance of 4.386–4.430 Å (depending on the basis set) in YPc_2 + ANT, whereas in YPc_2 + ZNT it is by roughly 0.1 Å longer, from 4.460 to 4.526 Å.

While, in principle, Y$\cdots$C$_{SWCNT}$ separations could serve as an indirect indicator of the bonding strength, the calculated formation energies ΔE (Table S2) are systematically more negative for YPc_2 + ZNT dyad: for example, −43.8 *vs.* −37.1 kcal/mol for YPc_2 + ANT (for DNP basis set; Table 2). The strongest bonding was observed when using DN, followed by DNP and DND. A possible explanation for this trend is larger orbital cutoff values applied when the latter two basis sets are used, reducing the polyazamacrocycle bending when adsorbed on a SWCNT sidewall [52]. Overall, the above formation energies are rather close to the ΔE values reported previously for M(II)Pc + SWCNT complexes with the same ANT and ZNT models, which span from −45.4 to −32.7 kcal/mol [45]. This can be interpreted as a minor significance of the chemical nature of central metal atom of phthalocyanine complex for the binding strength, but instead that the adsorption process is governed by the π—π interactions between tetraaza [18]annulene macrocycle and graphene-derived nanotube sidewall [9,45]. (The contribution of dispersion term in the total energy calculations is specified for each system in Table S5 of ESI.).

Since it is known that HOMO-LUMO gap is strongly underestimated when using pure GGA functionals (for example, as compared to hybrid ones such as B3LYP [53]), we analyzed this electronic parameter simply as a measure of changes upon YPc_2 adsorption on SWCNT models. As one can see from Table S2, the choice of basis set has a little effect on the frontier orbital and HOMO-LUMO band gap energies. The latter values obtained for YPc_2 + ANT and YPc_2 + ZNT dyads with DNP basis set are 0.140 and 0.059 eV, respectively. Comparing them with the values computed for isolated components (at the same theoretical level; Table 2), which are 0.142 eV for YPc_2, 0.643 eV for ANT, and 0.080 eV for ZNT, one can conclude that in the case of YPc_2 + ANT the gap tends to match the one for isolated YPc_2, whereas for YPc_2 + ZNT it is much closer to the band gap of ZNT. Apparently, the latter result is attributable to an open-shell nature of the zigzag model.

As a consequence, the HOMO and LUMO plots shown in Fig. 6 turn to be very different for YPc_2 + ANT and YPc_2 + ZNT complexes. In the former case, they are essentially identical to the ones presented in Fig. 5 for isolated double-decker phthalocyanine: both HOMO and LUMO are localized on YPc_2 with no traces of any orbital (at least when the isosurfaces are plotted at 0.03 a.u.) present on ANT. While some contribution of HOMO can be seen on phthalocyanine component in YPc_2 + ZNT, a comparable contribution to this frontier orbital is due to ZNT. As regards LUMO of this dyad, it is localized exclusively on the nanotube component. A similar pattern was reported, for example, for noncovalent CuPc + ZNT complex [45].

Like in the case of isolated double-decker phthalocyanine (Fig. 4),

the spin distribution for YPc_2 + ANT and YPc_2 + ZNT dyads exemplified in Fig. 6 for DNP basis set has very much to do with the corresponding HOMO-LUMO plots (Fig. 5). The evident reason is that it is unpaired electron cloud which is responsible for the phthalocyanine reactivity in both electrophylic and nucleophylic processes, which is reflected in the frontier orbital distribution. Therefore, in YPc_2 + ANT all the spin density remains on Pc component, whereas in YPc_2 + ZNT it is almost an exact match of its LUMO plot shown in Fig. 5. An additional detail is that the main cloud found on ZNT is represented by 'spin-up' unpaired electron density, with a barely noticeable contribution from 'spin-down' density localized on the C atoms of phthalocyanine macrocycle (this feature is reproduced when all the basis sets are used, being slightly less evident with DN; Fig. S2 of ESI). Thus, the spin density plots found for both YPc_2 + SWCNT dyads are strikingly different from those described previously for most M(II)Pc + SWCNT complexes derived from paramagnetic central 3*d* metals, for which the unpaired electron density is found mostly on metal [9,36,45].

4. Conclusions

The data obtained show that YPc_2 molecule interacting noncovalently with SWCNTs undergoes binding distortion in order to increase the area of contact with nanotube sidewall, which results in a stronger interaction between the two components. YPc_2 bonding is stronger with ZNT nanotube, of − 43.8 kcal/mol, *vs.* −37.1 kcal/mol for YPc_2 + ANT complex (as calculated with DNP basis set). The height of bisphthalocyanine molecule in the dyads dramatically increases compared to that calculated for isolated YPc_2, from 4.062–4.316 to 4.297–4.930 (YPc_2 + ANT) and 4.116–4.867 Å (YPc_2 + ZNT), as obtained at the highest theoretical level. At the same time, the calculated N-Y-N angles in YN_4 coordination change very insignificantly. The closest contacts in YPc_2 + SWCNT hybrids depend on the nanotube model, being γ-N$\cdots C_{SWCNT}$ for ANT, and $C_{\ddot{Y}Pc2}C_{SWCNT}$ for ZNT. The data related to frontier orbital energies/plots and spin density distribution are model-sensitive as well. In all cases, a minor HOMO-LUMO gap narrowing is observed. For YPc_2 + ANT the gap tends to match the one for isolated YPc_2, whereas for YPc_2 + ZNT it is much closer to the band gap of ZNT, which might be attributed to an open-shell nature of the zigzag model studied. Both HOMO and LUMO are found on YPc_2 in YPc_2 + ANT (with the same distribution as in isolated bisphthalocyanine); in YPc_2 + ZNT, HOMO is localized on both interacting components, and LUMO, only on the nanotube. The spin distribution plots have very much to do with the corresponding HOMO-LUMO plots: in YPc_2 + ANT all the spin density remains on phthalocyanine component, whereas in YPc_2 + ZNT it is almost an exact match of its LUMO plot.

The effect of basis set used in our computations depends on a particular parameter and system analyzed. In the case of isolated YPc_2, the calculated values of molecular size, height and N-Y-N angles are slightly larger compared to the experimental ones from XRD structure, tending to decrease with increasing the basis set (DN > DND > DNP). The basis set effect on the calculated Y-N_{iso} distances and SWCNT model dimensions is even less notable. On the other hand, the ΔE values and the closest contacts ($Y\cdots C_{SWCNT}$, γ-N$\cdots C_{SWCNT}$ and $C_{\ddot{Y}Pc2}C_{SWCNT}$) for the noncovalent complexes tend to increase for larger basis sets (DND and DNP *versus* DN). The other characteristics (frontier orbital and spin density distribution, as well as HOMO-LUMO gap values) do not exhibit any significant differences when varying the basis set.

Overall, the bending distortion upon adsorption of macrocyclic compounds on CNT sidewalls appears to be a rather common phenomenon, since it is observed not only for extended phthalocyanine systems [9,34–38,45,51], which belong to the class of tetraaza[18]annulenes, but also for much simpler tetraaza [14] annulenes [54].

CRediT authorship contribution statement

Lina M. Bolivar-Pineda: Data curation, Formal analysis, Validation, Visualization, Investigation, Writing – original draft. **Mónica I. Sinecio-Ontiveros:** Data curation, Formal analysis. **Vladimir A. Basiuk:** Conceptualization, Methodology, Supervision, Writing – review & editing, Supervision, Funding.

Declaration of Competing Interest

The authors declare that they have no known competing financial interests or personal relationships that could have appeared to influence the work reported in this paper.

Data availability

The raw/processed data required to reproduce these findings cannot be shared at this time due to technical and time limitations (their total size of a few GB). In addition, these data form part of an ongoing study.

Acknowledgments

Financial support from the National Autonomous University of Mexico (UNAM, grant DGAPA-IN203219) is greatly appreciated. L. M. B.-P. is indebted to the Doctorate Degree Program in Chemical Sciences of UNAM and to CONACyT for PhD scholarship. M. I. S.-O. thanks the Master Degree Program in Chemical Sciences of UNAM and to CONACyT for MSc scholarship.

Appendix A. Supporting information

Supplementary data associated with this article can be found in the online version at doi:10.1016/j.mtcomm.2021.102667.

References

[1] G. de la Torre, C.G. Claessens, T. Torres, Phthalocyanines: old dyes, new materials. Putting color in nanotechnology, Chem. Commun. (2007) 2000–2015, https://doi.org/10.1039/b614234f.
[2] T. Komeda, K. Katoh, M. Yamashita, Double-decker phthalocyanine complex: scanning tunneling microscopy study of film formation and spin properties, Prog. Surf. Sci. 89 (2014) 127–160, https://doi.org/10.1016/j.progsurf.2014.03.001.
[3] V.E. Pushkarev, L.G. Tomilova, V.N. Nemykin, Historic overview and new developments in synthetic methods for preparation of the rare-earth tetrapyrrolic complexes, Coord. Chem. Rev. 319 (2016) 110–179, https://doi.org/10.1016/j.ccr.2016.04.005.
[4] V.E. Pushkarev, L.G. Tomilova, Y.V. Tomilov, Synthetic approaches to lanthanide complexes with tetrapyrrole type ligands, Russ. Chem. Rev. 77 (2008) 875–907, https://doi.org/10.1070/rc2008v077n10abeh003879.
[5] D. Luneau, Molecular magnets, Curr. Opin. Solid State Mater. Sci. 5 (2001) 123–129, https://doi.org/10.1016/S1359-0286(00)00043-7.
[6] R. Sk, A. Deshpande, Unveiling the emergence of functional materials with STM: metal phthalocyanine on surface architectures, Mol. Syst. Des. Eng. 4 (2019) 471–483, https://doi.org/10.1039/c9me00014c.
[7] A. Şenocak, E. Demirbaş, M. Durmuş, 23. Phthalocyanine-nanocarbon materials and their composites: preparation, properties, and applications, in: A. Khan, M. Jawaid, Inamuddin, A.M. Asiri (Eds.), Nanocarbon and its Composites, Woodhead Publishing Elsevier, 2019, pp. 677–709, https://doi.org/10.1016/b978-0-08-102509-3.00023-7.
[8] J. Mack, N. Kobayashi, Low symmetry phthalocyanines and their analogues, Chem. Rev. 111 (2011) 281–321, https://doi.org/10.1021/cr9003049.
[9] V.A. Basiuk, L.J. Flores-Sánchez, V. Meza-Laguna, J.O. Flores-Flores, L. Bucio-Galindo, I. Puente-Lee, E.V. Basiuk, Noncovalent functionalization of pristine CVD single-walled carbon nanotubes with 3d metal(II) phthalocyanines by adsorption from the gas phase, Appl. Surf. Sci. 436 (2018) 1123–1133, https://doi.org/10.1016/j.apsusc.2017.12.122.
[10] V.A. Basiuk, L.M. Bolivar-Pineda, V. Meza-Laguna, E.V. Rybak-Akimova, E. V. Basiuk, Carbon nanotubes and graphene promote pyrolysis of free-base phthalocyanine, J. Phys. Chem. Lett. 9 (2018) 4420–4427, https://doi.org/10.1021/acs.jpclett.8b02141.
[11] D. Eastwood, L. Edwards, M. Gouterman, J. Steinfeld, Spectra of porphyrins.Past VII. Vapor absorption and emission of phthaloocyanines, J. Mol. Spectrosc. 20 (1966) 381–390.
[12] M. Bouvet, P. Gaudillat, J.M. Suisse, Lanthanide macrocyclic complexes: from molecules to materials and from materials to devices, J. Porphyr. Phthalocyanines 17 (2013) 628–635, https://doi.org/10.1142/S1088424613300048.
[13] M. Sumimoto, Y. Kawashima, K. Hori, H. Fujimoto, Theoretical study on the stability of double-decker type metal phthalocyanines, M(Pc)2 and M(Pc)2+ (M = Ti, Sn and Sc): a critical assessment on the performance of density functionals,

Phys. Chem. Chem. Phys. 17 (2015) 6478–6483, https://doi.org/10.1039/c4cp05645k.
[14] R. Murdey, M. Bouvet, M. Sumimoto, S. Sakaki, N. Sato, Direct observation of the energy gap in lutetium bisphthalocyanine thin films, Synth. Met. 159 (2009) 1677–1681, https://doi.org/10.1016/j.synthmet.2009.05.002.
[15] L. Bogani, W. Wernsdorfer, Molecular spintronics using single-molecule magnets, Nanosci. Technol. 7 (2009) 194–201, https://doi.org/10.1142/9789814287005_0020.
[16] V. Corradini, A. Candini, D. Klar, R. Biagi, V. De Renzi, A. Lodi Rizzini, N. Cavani, U. Del Pennino, S. Klyatskaya, M. Ruben, E. Velez-Fort, K. Kummer, N.B. Brookes, P. Gargiani, H. Wende, M. Affronte, Probing magnetic coupling between LnPc2 (Ln = Tb, Er) molecules and the graphene/Ni (111) substrate with and without Au-intercalation: role of the dipolar field, Nanoscale 10 (2018) 277–283, https://doi.org/10.1039/c7nr06610d.
[17] D.N. Woodruff, R.E.P. Winpenny, R.A. Layfield, Lanthanide single-molecule magnets, Chem. Rev. 113 (2013) 5110–5148, https://doi.org/10.1021/cr400018q.
[18] X. Chen, Y. Chen, M. Bai, C. Wang, D. Qi, Q. Liu, M. Xu, J. Jiang, Distribution of the unpaired electron in neutral bis(phthalocyaninato) yttrium double-deckers: an experimental and theoretical combinative investigation, J. Porphyr. Phthalocyanines 22 (2018) 165–172, https://doi.org/10.1142/S1088424618500219.
[19] J.L. Zhang, Marriage of phthalocyanine chemistry with lanthanides: a single-ion magnet with a blocking temperature up to 25 K, Inorg. Chem. Front. 4 (2017) 1950–1952, https://doi.org/10.1039/c7qi00502d.
[20] A. Lodi Rizzini, C. Krull, T. Balashov, J.J. Kavich, A. Mugarza, P.S. Miedema, P. K. Thakur, V. Sessi, S. Klyatskaya, M. Ruben, S. Stepanow, P. Gambardella, Coupling single molecule magnets to ferromagnetic substrates, Phys. Rev. Lett. 107 (2011) 1–5, https://doi.org/10.1103/PhysRevLett.107.177205.
[21] N. Ishikawa, M. Sugita, T. Ishikawa, S.Y. Koshihara, Y. Kaizu, Lanthanide double-decker complexes functioning as magnets at the single-molecular level, J. Am. Chem. Soc. 125 (2003) 8694–8695, https://doi.org/10.1021/ja029629n.
[22] A.I.A. Abd El-Mageed, T. Ogawa, Supramolecular structures of terbium(III) porphyrin double-decker complexes on a single-walled carbon nanotube surface, RSC Adv. 9 (2019) 28135–28145, https://doi.org/10.1039/c9ra05818d.
[23] S. Stepanow, J. Honolka, P. Gambardella, L. Vitali, N. Abdurakhmanova, T. C. Tseng, S. Rauschenbach, S.L. Tait, V. Sessi, S. Klyatskaya, M. Ruben, K. Kern, Spin and orbital magnetic moment anisotropies of monodispersed bis (Phthalocyaninato)terbium on a copper surface, J. Am. Chem. Soc. 132 (2010) 11900–11901, https://doi.org/10.1021/ja105124r.
[24] Y.F. Zhang, H. Isshiki, K. Katoh, Y. Yoshida, M. Yamashita, H. Miyasaka, B. K. Breedlove, T. Kajiwara, S. Takaishi, T. Komeda, Low-Temperature scanning tunneling microscopy investigation of bis(phthalocyaninato)yttrium growth on au (111): from individual molecules to two-dimensional domains, J. Phys. Chem. C 113 (2009) 9826–9830, https://doi.org/10.1021/jp902410q.
[25] A. Candini, S. Klyatskaya, M. Ruben, W. Wernsdorfer, M. Affronte, Graphene spintronic devices with molecular nanomagnets, Nano Lett. 11 (2011) 2634–2639, https://doi.org/10.1021/nl2006142.
[26] M. Gonidec, R. Biagi, V. Corradini, F. Moro, V. De Renzi, U. Del Pennino, D. Summa, L. Muccioli, C. Zannoni, D.B. Amabilino, J. Veciana, Surface supramolecular organization of a terbium(III) double-decker complex on graphite and its single molecule magnet behavior, J. Am. Chem. Soc. 133 (2011) 6603–6612, https://doi.org/10.1021/ja109296c.
[27] S. Kyatskaya, J.R.G. Mascarós, L. Bogani, F. Hennrich, M. Kappes, W. Wernsdorfer, M. Ruben, Anchoring of rare-earth-based single-molecule magnets on single-walled carbon nanotubes, J. Am. Chem. Soc. 131 (2009) 15143–15151, https://doi.org/10.1021/ja906165e.
[28] K. Abdullah, X. Kong, M. Imran, G. Mustafa, Y. Chen, Excellent ambipolar gas sensing response of Eu[Pc(OC4H9)8]2/acidified multiwalled carbon nanotubes hybrid at room temperature, J. Porphyr. Phthalocyanines 23 (2019) 1455–1462, https://doi.org/10.1142/S1088424619501554.
[29] M. Urdampilleta, S. Klyatskaya, J.P. Cleuziou, M. Ruben, W. Wernsdorfer, Supramolecular spin valves, Nat. Mater. 10 (2011) 502–506, https://doi.org/10.1038/nmat3050.
[30] C. Apetrei, M. Nieto, M.L. Rodríguez-Méndez, J.A. De Saja, Development of lutetium bisphthalocyanine/carbon nanotube Langmuir-Blodgett films. Sensing properties, J. Porphyr. Phthalocyanines 15 (2011) 908–917, https://doi.org/10.1142/S108842461100377X.
[31] G. Serrano, S. Wiespointner-Baumgarthuber, S. Tebi, S. Klyatskaya, M. Ruben, R. Koch, S. Müllegger, Bilayer of terbium double-decker single-molecule magnets, J. Phys. Chem. C. 120 (2016) 13581–13586, https://doi.org/10.1021/acs.jpcc.6b03676.
[32] V.A. Basiuk, D.E. Tahuilan-Anguiano, Complexation of free-base and 3d transition metal(II) phthalocyanines with endohedral fullerene Sc3N@C80, Chem. Phys. Lett. 722 (2019) 146–152, https://doi.org/10.1016/j.cplett.2019.03.019.
[33] V.A. Basiuk, E.V. Basiuk, Noncovalent complexes of Ih−C80 fullerene with phthalocyanines, Fuller. Nanotub. Carbon Nanostruct. 26 (2018) 69–75, https://doi.org/10.1080/1536383X.2017.1356823.
[34] V.A. Basiuk, E. Chávez-Colorado, Adsorption of free-base phthalocyanine on Stone-Wales defect-containing carbon nanotubes: a DFT study, Diam. Relat. Mater. 97 (2019), 107443, https://doi.org/10.1016/j.diamond.2019.107443.
[35] E. Chávez-Colorado, V.A. Basiuk, Noncovalent interactions of free-base phthalocyanine with elongated fullerenes as carbon nanotube models, Struct. Chem. 28 (2017) 1765–1773, https://doi.org/10.1007/s11224-017-0955-6.
[36] L.M. Bolivar-Pineda, V. Basiuk, Interactions of metal phthalocyanines with Stone-Wales defects on single-walled carbon nanotubes: a theoretical study, J. Appl. Phys. 127 (2020), 025302, https://doi.org/10.1063/1.5128629.
[37] P.O. Krasnov, T.V. Basova, A. Hassan, Interaction of metal phthalocyanines with carbon zigzag and armchair nanotubes with different diameters, Appl. Surf. Sci. 457 (2018) 235–240, https://doi.org/10.1016/j.apsusc.2018.06.282.
[38] J.D. Correa, W. Orellana, Optical response of carbon nanotubes functionalized with (free-base, Zn) porphyrins, and phthalocyanines: a DFT study, Phys. Rev. B 86 (2012), 125417, https://doi.org/10.1103/PhysRevB.86.125417.
[39] L. Alvarez, F. Fall, A. Belhboub, R. Le Parc, Y. Almadori, R. Arenal, R. Aznar, P. Dieudonné-George, P. Hermet, A. Rahmani, B. Jousselme, S. Campidelli, J. Cambedouzou, T. Saito, J.L. Bantignies, One-dimensional molecular crystal of phthalocyanine confined into single-walled carbon nanotubes, J. Phys. Chem. C 119 (2015) 5203–5210, https://doi.org/10.1021/acs.jpcc.5b00168.
[40] Y. Zhang, X. Cai, Y. Zhou, X. Zhang, H. Xu, Z. Liu, X. Li, J. Jiang, Structures and spectroscopic properties of bis(phthalocyaninato) yttrium and lanthanum complexes: theoretical study based on density functional theory calculations, J. Phys. Chem. A 111 (2007) 392–400, https://doi.org/10.1021/jp066157g.
[41] J.P. Perdew, K. Burke, M. Ernzerhof, Generalized gradient approximation made simple, Phys. Rev. Lett. 77 (1996) 3865–3868.
[42] S. Grimme, T.O. Chemie, O.I.D.U. Münster, Semiempirical GGA-type density functional constructed with a long-range dispersion correction, J. Comput. Chem. 27 (2006) 1787–1799, https://doi.org/10.1002/jcc.
[43] B. Delley, From molecules to solids with the DMol3 approach, J. Chem. Phys. 113 (2000) 7756–7764, https://doi.org/10.1063/1.1316015.
[44] Y. Luo, S. Yin, W. Lai, Y. Wang, Effects of global orbital cutoff value and numerical basis set size on accuracies of theoretical atomization energies, Theor. Chem. Acc. 133 (2014) 1580, https://doi.org/10.1007/s00214-014-1580-8.
[45] E.V. Basiuk, L. Huerta, V.A. Basiuk, Noncovalent bonding of 3d metal(II) phthalocyanines with single-walled carbon nanotubes: a combined DFT and XPS study, Appl. Surf. Sci. 470 (2019) 622–630, https://doi.org/10.1016/j.apsusc.2018.11.159.
[46] N.A. Benedek, I.K. Snook, K. Latham, I. Yarovsky, Application of numerical basis sets to hydrogen bonded systems: a density functional theory study, J. Chem. Phys. 122 (2005), 144102, https://doi.org/10.1063/1.1876152.
[47] V.A. Basiuk, L.V. Henao-Holguín, Effects of orbital cutoff in DMol3 DFT calculations: a case study of meso-tetraphenylporphine-C60 complex, J. Comput. Theor. Nanosci. 10 (2013) 1266–1272, https://doi.org/10.1166/jctn.2013.2840.
[48] K. Katoh, Y. Yoshida, M. Yamashita, H. Miyasaka, B.K. Breedlove, T. Kajiwara, S. Takaishi, N. Ishikawa, H. Isshiki, F.Z. Yan, T. Komeda, M. Yamagishi, J. Takeya, Direct observation of lanthanide(III)-phthalocyanine molecules on Au(111) by using scanning tunneling microscopy and scanning tunneling spectroscopy and thin-film field-effect transistor properties of Tb(III)- and Dy(III)-phthalocyanine molecules, J. Am. Chem. Soc. 131 (2009) 9967–9976, https://doi.org/10.1021/ja902349t.
[49] S. Kahlal, A. Mentec, A. Pondaven, M. L'Her, J.Y. Saillard, Substituent effect in unsymmetrical lutetium bisphthalocyanines: a DFT analysis, N. J. Chem. 33 (2009) 574–582, https://doi.org/10.1039/b810131k.
[50] Y. Zhang, P. Guan, H. Isshiki, M. Chen, M. Yamashita, T. Komeda, Bis (phthalocyaninato)yttrium grown on Au(111): electronic structure of a single molecule and the stability of two-dimensional films investigated by scanning tunneling microscopy/spectroscopy at 4.8 K, Nano Res. 3 (2010) 604–611, https://doi.org/10.1007/s12274-010-0021-9.
[51] P. Tian, B. Zhang, J. Chen, J. Zhang, L. Huang, R. Ye, B. Bao, M. Zhu, Curvature-induced electronic tuning of molecular catalysts for CO_2 reduction, Catal. Sci. Technol. 11 (2021) 2491–2496, https://doi.org/10.1039/d0cy01589j.
[52] V.A. Basiuk, Interaction of porphine with closed-end zigzag (6,0) single-walled carbon nanotube: the effect of parameters in DMol3 DFT calculations, J. Comput. Theor. Nanosci. 5 (2008) 2114–2118, https://doi.org/10.1166/jctn.2008.1106.
[53] A. Suzuki, T. Oku, Effects of central metal on electronic structure, magnetic properties, infrared and Raman spectra of double-decker phthalocyanine, Appl. Surf. Sci. 380 (2016) 127–134, https://doi.org/10.1016/j.apsusc.2016.02.026.
[54] V.A. Basiuk, Interaction of tetraaza[14]annulenes with single-walled carbon nanotubes: a DFT study, J. Phys. Chem. B 108 (2004) 19990–19994, https://doi.org/10.1021/jp046197p.